Mikrofluidische Strategien zur Synthese von definierten, plasmonischen Nanopartikeln für bioanalytische Anwendungen

Dissertation

(kumulativ)

zur Erlangung des akademischen Grades *doctor rerum naturalium*
(Dr. rer. nat.)

vorgelegt dem Rat der Chemisch-Geowissenschaftlichen Fakultät

der Friedrich-Schiller-Universität Jena

von Master of Science (M.Sc.) Matthias Thiele geboren am 18. August 1986 in Weimar.

1. Gutachter: Prof. Dr. Volker Deckert (Jena)

2. Gutachter: apl. Prof. Dr. Wolfgang Fritzsche (Jena)

Tag der Verteidigung: 24.04.2018

Kurzfassung/ Abstract

Die dargelegte Arbeit beschäftigt sich mit der Untersuchung zur gezielten Herstellung von plasmonischen Nanopartikeln mit Hinblick auf deren sensorische Anwendung. In der Arbeit werden die Limitationen von klassischen Synthesverfahren untersucht, um mikrofluidische Lösungsstrategien zu entwickeln. Der Fokus liegt dabei auf der Herstellung von formanisotropen plasmonischen Nanopartikeln mit großen Sensitivitäten, wie beispielsweise Silbernanoprismen. Als zentrales Thema steht die optimale Kombination verschiedener Methoden im Vordergrund, wodurch effiziente und hochreproduzierbare Synthesen ermöglicht werden. Darauf aufbauend konnte eine mikrofluidische Syntheseplattform realisiert werden, die ein leistungsfähiges Parameterscreening hinsichtlich Inkubationszeiten der einzelnen Syntheseschritte, der formabhängigen Additiven und der finalen Partikelgrößen für sphärische und anisotrope Nanopartikel ermöglicht. Neben kontrollierten Prozessbedingungen kennzeichnet das System einen reduzierten Ressourcen- und Zeitverbrauch und ermöglicht die parallele Herstellung von Goldnanopartikeln, mit sphärischer, kubischer oder Stäbchengeometrie. Die synthetisierten Nanopartikel zeichnen sich schließlich durch ihre optischen Eigenschaften als Transducer in neuartigen optofluidischen und getaperten Lichtwellenleitern aus, wobei sie selbst nach postsynthetischen Stabilisierungsprozessen eine hohe Sensitivität aufweisen. In diesem Zusammenhang sind die publizierten Artikel, die auf den hier vorgestellten Forschungsergebnissen basieren, richtungsweisend für die nächste Generation der Nanopartikelsynthese und deren Applikationen.

Schlüsselwörter: *Mikrofluidik, Mikromischer, plasmonische Nanopartikel, anisotrope Nanopartikel, Lichtwellenleiter*

The present work deals with the investigation of systematic production of plasmonic nanoparticles regarding their sensoric applications. Within the work the limitations of classical synthesis methods will be addressed to develop microfluidic approaches. The focus lies in the fabrication of shape anisotropic plasmonic nanoparticles with high sensitivities like silver nanoprisms. A central issue is the clever combination of several methods to enable an efficient and highly reproducible synthesis. Based on this, a microfluidic synthesis platform was realized that allow an effective parameter screening regarding the incubation time of each single synthesis step, the shape dependent additives and the final particle sizes for spherical and anisotropic nanoparticles. Beside the controlled process conditions, the system is characterized by the reduction of consumed resources and time and further enables the parallel production of gold nanoparticles with spherical, cubed or rod geometries. Based on their optical features, the synthesized nanoparticles are utilized as transducers in novel optofluidic and tapered fibers, whereby the sensitivity of the nano-

particles stays high even after post-synthetic stabilization processes. In this regard, displays the publications based on the results in the presented work display the direction for the next generation of nanoparticle synthesis and their applications.

Keywords: *microfluidic, micromixer, plasmonic nanoparticles, anisotropic nanoparticles, optical fibers*

Inhaltsverzeichnis

Abkürzungsverzeichnis

Abkürzung	Bedeutung	Übersetzung/ Bemerkung
µSEED	microfluidic-Seeds	mittels mikrofluidischem Verfahren hergestellte Seeds
$AgNO_3$	Silbernitrat	
bSEED	batch-Seeds	mittels Batchverfahren hergestellte Seeds
c	Lichtgeschwindigkeit	
CF	Continuous Flow	kontinuierlicher Fluss (mikrofluidisches Verfahren)
CFD	Computational Fluid Dynamics	numerische Strömungsmechanik
CMC	Critical Micelle Concentration	kritische Konzentration zur Mizellenbildung
CTAB	Cetyltrimethylammoniumbromid	quartäre Ammoniumverbindung mit Alkylgruppe (C-16); Bromid als Gegenion
CTAC	Cetyltrimethylammoniumchlorid	quartäre Ammoniumverbindung mit Alkylgruppe (C-16); Chlorid als Gegenion
D	Diffusionskoeffizient	Maß für die Beweglichkeit von Teilchen/ Molekülen
d	Dicke	zum Beispiel Kanaldicke oder Lamellenstärke
DB	Dropbled based	tropfenbasierte Mikrofluidik
DCS	Differential Centrifugal Sedimentation	Dichtegradientenzentrifugation
DDT	Dichlordiphenyltrichlorethan	
De	Dean-Zahl	dimensionslose Kennzahl zur Beschreibung der Strömung in gekrümmten Kanal
DFM	Dean-Flow-Mischer	auf den Deaneffekt basierender Mikromischer
dl	Diffusionslänge	Entfernung, die ein Teilchen durch Diffusion zurücklegt
f	Frequenz	
FOM	Figure Of Merit	Bewertungsfaktor
FWHM	Full Width at Half Maximum	Halbwertsbreite
GS1,2	Growth Step 1, 2	Wachstumsschritt 1, 2
$HAuCl_4$	Tetrachlorgoldsäure	Goldsäure
LBL	Layer-by-Layer	monomolekulares Beschichtungsverfahren

LSPR	Localized Surface Plasmon Resonance	lokalisierte Oberflächenplasmonenresonanz
ME	Mixing Elements	Mischelement
MTAB	Tetradecyltrimethylammonium bromide	quartäre Ammoniumverbindung mit Alkylgruppe (C14)
N	Number	Anzahl (Bsp. Lamellenanzahl)
NIR	Near-infrared	nahes Infrarotlicht
OD	optische Dichte	
PAH	Poly(allylamine hydrochloride)	
PDDA	Polydiallyldimethylammonium	
PE	Polyethylene	
PEG	Polyethylenglycol	
PNIPAM	Poly(N-isopropylacrylamide)	temperaturabhängiges Polymer/ Hydrogel
POC	Point-of-Care	Vor-Ort-Analyseverfahren
POEGMA	Poly(oligo(ethylene glycol)ethyl ether methacrylate	temperatur- und pH-wertabhängiges Polymer/ Hydrogel
PSS	Polystyrenesulfonat	
PVA	Polyvinylalkohol	
Q	Quantity	Flussrate
Re	Reynoldszahl	dimensionslose Kennzahl, die das Verhältnis von Trägheits- zu Zähigkeitskräften und damit das Turbulenzverhalten in Kanälen angibt
REM	Rasterelektronenmikroskopie	
RI	Refractive Index	Brechungsindex; dimensionslose Zahl, welche die Lichtausbreitung durch ein Medium darstellt
RIU	Refractive Index Unit	virtuelle Einheit zur Quantifizierung der Brechungsindexänderung
S	Sensitivität	Verhältnis aus Wellenlängenänderung zu Brechungsindexänderung
S_B	Bulksensitivität	Sensitivität, bezogen auf die Veränderung in der direkten Partikelumgebung
S_S	Oberflächensensitivität	Sensitivität, bezogen auf ein chemisches Bindungsereignis an der Partikeloberfläche

S1, S2, S3	Spritze 1, 2, 3	verwendete Spritzen für die Spritzenpumpe
SAR	Split And Recombine	Teilung und Neuformierung
SCF	suspended-core-fibre	optische Faser, bei denen der lichtleitende Faserkern quasi frei hängt und von freien Kanälen umgeben wird
SDS	Sodium Dodecyl Sulfate	Natriumdodecylsulfat
SF	Segmented Flow	segmentierter Fluss (mikrofluidisches Verfahren)
SI	Système international d'unités	internationales Einheitensystem
TSC	Trisodium citrate	Natriumcitrat
t	Diffusionszeit	
TEM	Transmissionselektronenmik-roskop	
UV	Ultraviolet	
λ	Lamda	Wellenlänge
λ_{max}	Lamda_max	Resonanzwellenlänge

Vorwort und Übersicht

Der Vortrag Richard Feynmanns mit dem Titel *„There is plenty of room at the bottom"* kann als die Geburtsstunde der Nanotechnologie angesehen werden. In dem 1959 am CALTEC gehaltenen Plädoyer an die Technologie im Nanometerbereich[a] geht der spätere Nobelpreisträger auf Chancen und Herausforderungen ein, welche durch die bewusste Gestaltung und Manipulation von Nanostrukturen möglich werden. Seine Vision wurde schließlich die Schlüsseltechnologie des 21. Jahrhunderts und erhielt Einzug in viele Industrie- und Forschungsbereiche. In seinem Vortrag beschreibt er eine Abkehr der bis dahin geltenden „Top-down"-Methode hin zu „Bottom-up"-Verfahren und der damit einhergehenden Realisierung von schnelleren, kleineren und leistungsfähigeren Maschinen. Am Beispiel biologischer Selbstassemblierungsprozesse zieht er Parallelen zur Erzeugung von Komponenten durch gezieltes Zusammenlagern ihrer kleinsten Bestandteile. Die vorliegende Arbeit soll an diesem Bottom-up-Ansatz anknüpfen und beschäftigt sich mit der Herstellung von Nanoobjekten aus ihren Grundelementen, den Atomen. Angefangen mit klassischen Laborreaktoren mit Dimensionen im cm^3 Bereich (Batchreaktor) liegt der Fokus der Arbeit auf der Verwendung mikrofluidischer Bauelemente mit Kanalstrukturen im μm^3 Maßstab, zur Herstellung von metallischen Nanopartikeln mit Abmessungen im nm^3 Bereich. Die Nanopartikel können wiederum durch ihre speziellen optischen Eigenschaften als Signalwandler kleinste Moleküle bis in den Subnanometerbereich detektieren. Die dimensionsübergreifenden Maßstäbe spielen dabei eine zentrale Rolle, da insbesondere unter Verwendung mikrofluidischer Komponenten die großen Herausforderungen der Nanopartikelherstellung beherrscht werden können. Durch die Vereinigung verschiedener mikrofluidischer Techniken in Kombination mit weiteren Methoden wird in dieser Arbeit das Potenzial zur effizienten Kontrolle von Partikelherstellungs- und Wachstumsprozessen gezeigt. Dadurch ist eine kontrollierte und reproduzierbare Herstellung von verschiedenen Nanopartikelgeometrien mit einstellbaren optischen Eigenschaften und hohen Ausbeuten möglich. Mit diesen maßgeschneiderten Nanopartikeln können neue einzigartige Eigenschaften von Nanoobjekten realisiert werden, was der Visionär Feynman postulierte, als er sagte *„… I can hardly doubt that when we have some control of the arrangement of things on a small scale we will get an enormously greater range of possible properties …."*

---

[a] Das Wort Nano leitet sich vom griechischen Wort *nanos* ab und bedeutet „Zwerg". Es wird als Präfix für SI-Einheiten verwendet, um entsprechend kleine Werte auszudrücken. Im Beispiel für die Längeneinheit Meter bedeutet 1 nm = 0,000000001 m ($\hat{=} 10^{-9}$ m)

„Big is beautiful, but small is powerful" (Autor Unbekannt)

*„Ich bin immer noch verwirrt, aber auf einem höheren Niveau." (Enrico Fermi)*

gewidmet meiner Familie

und meinen Freunden

1. Einleitung

1.1. Einführung/ Introduction

Unter dem Begriff Nanopartikel versteht man ein Teilchen, bei dem alle drei räumlichen Dimensionen im Nanometerbereich liegen [1]. Damit schließen Nanopartikel die Lücke zwischen der Mikrometerskala (>1 µm) und der atomaren Skala (<1 nm) und werden daher häufig als Mediator zwischen diesen beiden Welten betrachtet [2-5]. Besonders Edelmetall-Nanopartikel aus Gold und Silber sind derzeit Gegenstand intensiver Forschung. Der Grund sind ihre außergewöhnlichen Eigenschaften (katalytisch, elektrisch und optisch), die sich stark von denen ihres makroskopischen Pendants aufgrund ihrer „eingesperrten Elektronen" unterscheiden [6]. Wissenschaftliche Untersuchungen reichen dabei zurück bis 1857, als Michael Faraday erstmals die purpurne rote Farbe mit der Partikelgröße von Goldnanopartikeln in Zusammenhang brachte und ihre Streueigenschaften (siehe Abbildung 1) untersuchte [7]. Aufbauend auf diesen Niederschriften schaffte es später der Chemiker Richard Zsigmondy 1902, Partikelsuspensionen[b], bestehend aus noch feineren Goldnanopartikeln, herzustellen und die Theorie Faradays zu beweisen. Dafür nutzte er das von ihm und Henry Siedentopf in Jena entwickelte Ultramikroskop (Dunkelfeldmik-
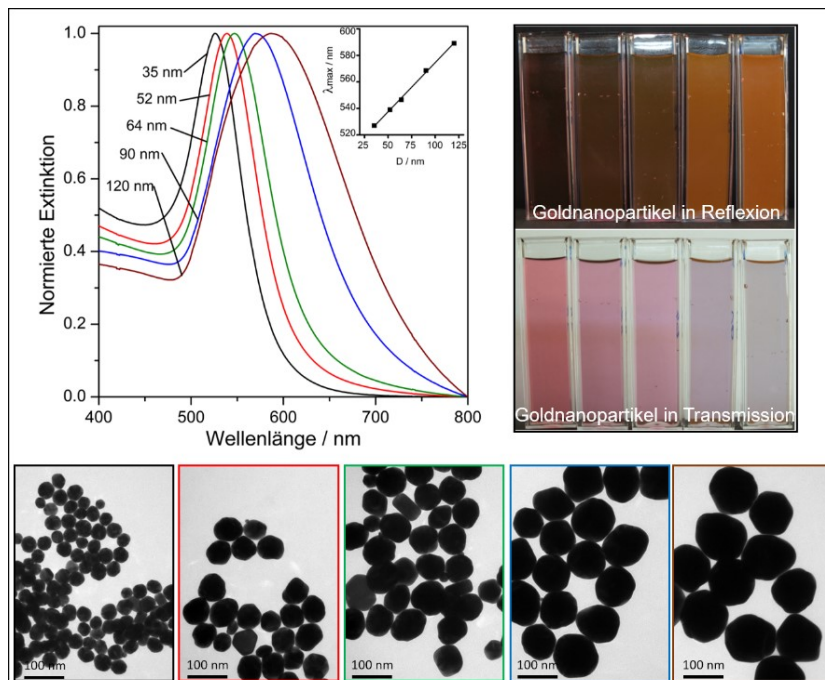
Abbildung/ Figure 1: *Optisches Spektrum mit Reflexions- und Transmissionsbild (optische Dichte OD = 0,5) sowie zugehörige TEM-Aufnahmen von Goldnanopartikeln in verschiedenen Größen.*

---

[b] Eine Suspension oder auch kolloidale Lösung (griech. *kólla* (Leim) und *eidos* (Aussehen/ Form) ist ein Spezialfall der Dispersion (heterogenes Gemisch aus nicht mischbaren Stoffen) und beschreibt Nanometer bis Mikrometer große Teilchen in fester oder flüssiger Form, die in einem sie umgebenden und in sich geschlossenen Medium, dem Dispersionsmedium, fein verteilt sind.

roskop), welches ausschließlich das vom Partikel gestreute Licht zeigt und dadurch eine hohe Auflösung auf Einzelpartikelebene erlaubt [8]. Unter anderem ist es diesem Durchbruch in der Lichtmikroskopie zu verdanken, dass sich im Verlauf des 20. Jahrhunderts die Anzahl der Wissenschaftler, welche sich mit kolloidalen[b] Systemen beschäftigten, drastisch gesteigert hat [9]. Besonders hervorzuheben sind dabei die Untersuchungen zur gezielten Größenherstellung von kolloidalem Gold, die von Turkevich 1951 publiziert und von Frens 1973 verfeinert wurden und Kolloidchemikern heute generell als „Turkevich-Frens"-Methode ein Begriff sind [10, 11]. Der Trend setzte sich über die Jahrtausendwende fort und eröffnete den metallischen Kolloidsystemen immer mehr Applikationsfelder, basierend auf ihren speziellen optischen Eigenschaften. Da diese durch chemische Zusammensetzung und geometrische Faktoren der Partikel genau eingestellt und determiniert werden, sich jedoch auch durch die Änderung der Partikelumgebung beeinflussen lassen, werden metallische Nanopartikel für Biosensoren verwendet [12, 13]. Darüber hinaus finden sie Verwendung zum Markieren von Zellen [14, 15], dem gezielten Manipulieren und Schneiden von DNA [16, 17], als Positioniermaschinen[18], sowie als molekularer Signalverstärker [19-21]. Demgegenüber beschäftigt sich die vergleichsweiche recht junge Technologie der Mikroreaktionstechnik mit Reaktionen und Prozessen in miniaturisierten verfahrenstechnischen Anlagen [22]. Dabei werden die Manipulation und der Transport von Fluiden auf engstem Raum mithilfe von mikrostrukturierten Elementen als Mikrofluidik zusammengefasst. Entgegen klassischen, chemischen Reaktionskolben im Litermaßstab oder großindustriellen Reaktoren im Kubikmeter-Maßstab, kommen hier miniaturisierte Durchlaufreaktoren (Mikroreaktoren) im Mikro- oder Nanoliterbereich zum Einsatz. Dadurch verändern sich nicht nur die Dimensionen und Skalierungen, sondern auch die Art der Prozessführung. Während in klassischen Reaktoren ein finales Volumen durch die schrittweise Zugabe der Edukte erreicht wird (diskontinuierlich), sind es in der Mikrofluidik miniaturisierte kontinuierliche Prozesse [23-25]. Reaktionen können in Echtzeit verfolgt [26, 27], dokumentiert [28] und mit Hilfe eines Regelkreislaufes koordiniert und schließlich automatisiert werden. Grundlage dafür bildet vor allem die verringerte laterale Dimension der Mikroreaktoren. Das Oberflächen-Volumenverhältnis wird erhöht und das effektive Volumen verringert, wodurch kürzere Diffusionswege realisiert werden können, was zu einem verbesserten Material- und Wärmetransport und damit zu effizienteren Mischvorgängen führt [29]. Infolgedessen kann eine schnellere Änderung der Reaktionsparameter ermöglicht werden, wodurch man eine schnelle Rückkopplung erhält und somit einen flexibleren Gesamtprozess erreicht. Die mikrofluidische Prozessführung ermöglicht im Hinblick auf die Syntheseparameter eine leistungsfähige Hochdurchsatzanalyse (*High-Throughput-Screening*) [30], was unter anderem wirtschaftliche Vorteile mit sich bringt [31]. Darüber hinaus sind die Verringerung von verwendeten Chemikalien- und Materialienmengen sowie benötigter Energie von wirtschaft-

lichem, aber auch von sicherheitstechnischem Interesse. Entgegen klassischen verfahrenstechnischen Anlagen werden mikrofluidische Aufbauten dabei nicht volumenorientiert hochskaliert (*upscaling*), wodurch alle erwähnten dimensionsbedingten Vorteile verloren gingen. Vielmehr kommt es zu einem „*numbering-up*", einer gesteigerten Anzahl der parallellaufenden Anlagen, wodurch sich die Produktionsflexibilität (hinsichtlich Ausfällen, neuen Reaktionen, geänderten Anforderungen) erhöht und ein schneller Transfer von Forschung in die Produktion realisiert werden kann [23, 24, 29]

The term nanoparticle describes a certain particle, which displays all three dimensions of the nanometer range [1]. Nanoparticles are able to close the gap between the micrometer (>1 µm) and atomic scale (<1 nm) and can therefore serve as a mediator between these two worlds [2-5]. In particular, noble metal nanoparticles made of gold and silver are part of intense research these days. The reason for this lies in their extraordinary properties (catalytic, electronic, and optical) which strongly differ from their macroscopic pendants based on their "confined electrons" [6]. Scientific investigations reach back until 1857, when Michael Faraday postulated the relation between the purple red color of the solution and the size of the gold nanoparticles for the first time and further examined their scattering characteristics (Figure 1) [7]. Based on Faradays protocols, in 1902 the chemist Richard Zsigmondy developed particle suspensions that contain even finer gold nanoparticles and thus he verified Faradays theory. He used the ultramicroscope (darkfield microscope), which was developed by him and Henry Siedentopf in Jena, to solely visualize the scattered light from the particle and hence reach an optical resolution on single nanoparticle level [8]. This breakthrough in the optical light microscopy is, among other things, the reason for the increasing interest of researchers in the 20th century on the topic of colloidal systems [9]. Of particular note is the study of defined colloidal sized gold nanoparticles, which was published by Turkevich in 1951 and improved by Frens in 1973. Nowadays colloidal chemists know this procedure as the "Turkevich-Frens-method" [10, 11]. After the new Millennium, the trend continued and initiated new application fields for the colloidal metallic system based on their particular optical characteristics. Caused on the issue, that their optical properties can be exactly adjusted and determined by the chemical composition and the geometrical parameters, but are still affected by changes in the particle surrounding, the metallic nanoparticles will be used for biosensors [10-13]. Furthermore, they are utilized to tag cells [14, 15], to selectively manipulate and cut DNA [16, 17], as position devices [18] and to enhance molecular signals [19-21]. In contrast, the comparatively young technology of microreaction technology deals with reactions and processes in miniaturized plant constructions [22]. Thus, the manipulation and the transport of fluids in tiny spaces with the help of microstructured elements are summarized as microfluid-

ics. Contrary to classical chemical reaction flasks using liter scale or major industrial reactors using cubic meter scale, microfluidics miniaturized flow-through reactors (microreactors) apply micro or nanoliter scale. As a result, not only the dimensions and scaling changes, but also the general way of processing. While in conventional reactors a final volume will be achieved by the stepwise adding of educts (discontinuous), miniaturized continuous processes will be used in microfluidics[23-25]. Reactions can be tracked [26, 27] and recorded [28] in real-time as well as coordinated and finally automated with the help of a feedback loop system. The fundament for this is chiefly based on the decreased dimensions of the microreactors. The effective volume will be increased by decreasing the surface to volume ratio, whereby the diffusion paths will be reduced which results into an improved material and heat transport that enhances the mixing process [29]. Consequently, a rapid change of the reaction parameters can be realized, whereby a faster feedback is reached that results in a highly flexible entire process. Regarding the synthesis parameters the microfluidic process enables an efficient high-throughput-screening [30] that improves economic aspects [31]. Moreover, the reduction of used chemicals, material amounts as well as required energy are of economic and safety related interest. Because in case of losing the above-mentioned dimension-dependent advantages, the microfluidic plants will not be volume-oriented scaled-up like classical batch plants. In fact, it will use the numbering-up method, an increased quantity of parallel working microreactors. This method increases the flexibility during production (regarding failures, new reactions, changed requirements) and allows a faster transfer from research into the commercial production [23, 24, 29].

1.2. Motivation

Die Eigenschaften von metallischen Nanopartikeln sind auch über das reine Forschungsbestreben hinaus für industrielle Anwendungen interessant [32]. Dementsprechend gibt es vermehrt Unternehmen, welche Nanopartikelsuspensionen kommerziell vertreiben (*Nanopartica, Nanocomposix, Nanopartz, BBI, mkNano, Nanoprobes, Creative Diagnostics, PlasmaChem, Creative Diagnostics*). Jedoch sind kommerziell erhältliche kolloidale Lösungen meist teuer und ihre Zusätze bzw. Additive oft unklar, so dass keine Rückschlüsse auf den Herstellungsweg und die auf der Partikeloberfläche befindliche Chemie gemacht werden können. Auch ist der Vertrieb von konventionell erhältlichen, plasmonischen Nanopartikeln (abgesehen von verschiedenen Größen) auf sphärische und stäbchenförmige Nanopartikel limitiert. Aber gerade formanisotrope[c] und komplexere plasmonische Strukturen sind interessant für katalytische und optische Anwendungen. Dabei werden diese Nanostrukturen derzeitig meist über Top-down-Verfahren herge-

---

[c] Anisotropie bezeichnet ein richtungsabhängiges Ereignis (z.B. Partikelwachstum). Der Begriff formanisotrope Nanopartikel bezieht sich auf jegliche Partikelformen, die von einer sphärischen Geometrie abweichen.

stellt, die von ihrer lückenlosen Produktionskette, der hohen Parallelisier- und Reproduzierbar-keit, aber vor allem von ihren etablierten Verfahren profitieren. Dem gegenüber stehen die Bot-tom-up-Methoden, die sich durch ihren geringen Bedarf an Personal, Equipment, Zeit und Kos-ten auszeichnen. Die damit einhergehende hohe Effektivität wird durch ihren „aufbauenden" Charakter untermauert, wodurch kleinere und maßgeschneiderte, zum Beispiel monokristalline Nanostrukturen, hergestellt werden können. Die vorliegende Dissertation beschäftigt sich daher mit der chemischen Synthese von formanisotropen metallischen Nanostrukturen. Es soll gezeigt werden, dass durch Kombination mikrofluidischer Prozesse metallische Nanopartikel mit geziel-ten optischen Eigenschaften definiert hergestellt werden können. Dabei soll verdeutlicht werden, dass aufgrund der hohen Reproduzierbarkeit, der kontrollierten Prozessführung und der damit verbundenen hohen Ausbeute vor allem mehrstufige Syntheseprotokolle (Abbildung 2) von den mikrofluidischen Prozessen profitieren. Durch entsprechendes Adaptieren geeigneter Mikromi-scher oder Methoden auf die jeweiligen Reaktionsbedingungen lässt sich somit jeder Wachs-tumsschritt optimieren und damit der Materialverbrauch senken, aber auch die Flexibilität des Gesamtsystems bezüglich der Herstellung von formanisotropen Nanopartikeln erhöhen. Darüber hinaus soll das Potenzial der hergestellten Nanopartikel in neuartigen Sensoranwendungen deutlich gemacht werden. Eine Übersicht über die gesamten in der Arbeit enthaltenen Nanopar-tikel und miteinander verflochtenen Prozessschritte ist schematisch in Abbildung 2 dargestellt.
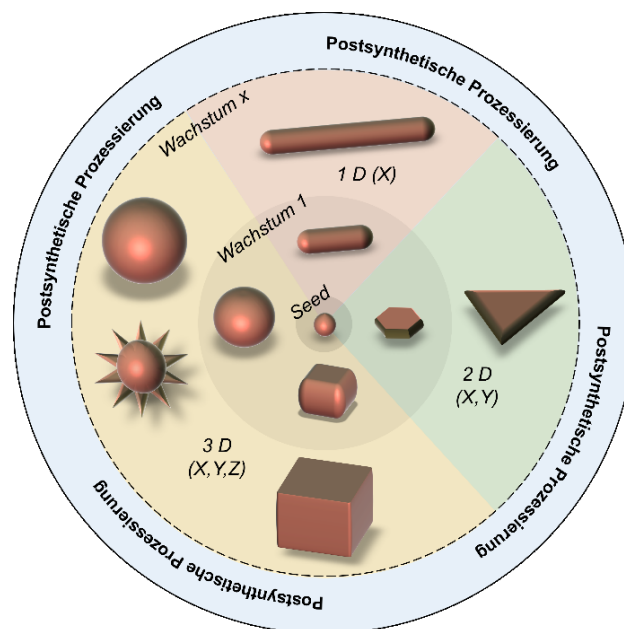

Abbildung 2: *Schematische Einteilung und Übersicht über die hergestellten Nanopartikelformen.*

2. Grundlagen

2.1. Optische Eigenschaften metallischer Nanopartikel und deren Verwendung in der Biosensorik

Die optischen Eigenschaften metallischer Nanopartikel sind unter anderem auf ihre Nanoskaligkeit und das damit verbundene „Einsperren" der Leitungsbandelektronen zurückzuführen [6]. Bei der Interaktion der Nanopartikel mit eingehender elektromagnetischer Strahlung kommt es zu einer frequenzabhängigen kollektiven Auslenkung der Leitungsbandelektronen, wobei die Amplitude durch die Polarisierbarkeit des Materials vorgegeben ist. Es entstehen sogenannte Plasmonen[d], weshalb diese Art der Nanoteilchen auch als plasmonische Nanopartikel bezeichnet wird. Im Fall der Resonanz (Resonanzfrequenz[e]) ist die Auslenkung und das damit verbundene Dipolmoment am höchsten. Das induzierte Dipolmoment erzeugt dabei ein evaneszentes[f] Feld auf der Partikeloberfläche. Die Intensität dieses Feldes, welches sich senkrecht zur Partikeloberfläche und damit in das umliegende Dielektrikum ausbreitet, unterliegt einem exponentiellen Abfall (1/e) [33]. Somit sind die höchsten Feldintensitäten direkt an der Nanopartikeloberfläche lokalisiert [34]. Beim Resonanzverhalten spricht man von lokalisierter Oberflächenplasmonenresonanz (engl. *localized surface plasmon resonance*; LSPR) [12], welche stark von der chemischen Beschaffenheit (Materialzusammensetzung und Kristallinität) [33], den geometrischen Faktoren (Größe und Form) [35] und vom umgebenden Dielektrikum (Brechungsindex) abhängt [34]. Durch die Kontrolle dieser Faktoren können verschiedenen Resonanzwellenlängen (LSPR-Bande, λ_{max}) realisiert werden, was in Abbildung 1 für verschieden große sphärische Goldnanopartikel dargestellt ist. Da die chemische Beschaffenheit sowie die Geometrie nach der jeweiligen Herstellung determiniert sind, können diese als intrinsisch bezeichneten Faktoren nicht mehr oder nur schwer nach der Synthese modifiziert werden. Demgegenüber kann jedoch der Brechungsindex bzw. die Umgebung der Partikel relativ einfach verändert werden [36]. Diese fundamentale Eigenschaft wird für biosensorische Anwendungen ausgenutzt, wobei die plasmonischen Nanopartikel als optischer Signalwandler (Transducer[g]) für Brechungsindexänderungen

---

[d] Plasmonen sind quantenmechanische Quasiteilchen, welche quantisierte Oszillationen der Ladungsträgerdichte (Elektronengas) in Festkörpern darstellen.

[e] In der Plasmonik wird eher die Wellenlänge λ als die Frequenz f angegeben. Über den Zusammenhang λ = c / f kann zwischen beiden Größen umgerechnet werden. Dabei steht c für die Lichtgeschwindigkeit im Vakuum und beträgt 299.792.458 m/s.

[f] Evaneszenz (lat. *Evanescere*, „verschwinden") beschreibt ein an eine Oberfläche gebundenes Feld.

[g] Transducer stellen Vermittler oder Wandler dar, die ein physikalisches oder chemisches Signal in ein anderes umsetzen können. Im Fall von plasmonischen Nanopartikeln wird meist ein chemisches Signal (beispielsweise die Anbindung von Molekülen auf der Partikeloberfläche) in ein optisches Signal (die Verschiebung der Resonanzwellenlänge) umgewandelt.

im Umgebungsmedium fungieren [12]. Ein großes Potenzial liegt dabei in der Detektion von Molekülen (Molekül-Molekül Interaktion), da die Eindringtiefe der Plasmonen in das Medium um den jeweiligen Nanopartikel und die Größe der zu detektierenden Spezies in der gleichen Größenordnung liegt. Dadurch können sie markierungsfrei[h] ein chemisches Bindungsereignis an der Partikeloberfläche oder das schlichte Verändern der gesamten Partikelumgebung detektieren, indem sich ihre LSPR-Bande auf spezifische Weise verschiebt [34, 37-39]. Ein ähnlicher Effekt tritt ein, wenn die Partikel in unmittelbare Nähe zueinander oder zu einem weiteren optischen Element, wie beispielsweise ein Fluoreszenzmolekül, kommen. Im Fall von Resonanzübereinstimmung kommt es zu einer Resonanzkopplung [40] untereinander oder aber zu einer Feldverstärkung [2]. Vor allem die plasmonenverstärkte Ramanspektroskopie (*Plasmon Enhanced Raman Spectroscopy* – PERS) [2] und Fluoreszenzeffekte, wie beispielsweise *metal-enhanced fluorescence* (MEF) [41, 42], *surface enhanced Raman scattering* (SERS) [43, 44] und *tip-enhanced Raman spectroscopy* (TERS), [3, 19, 45] profitieren von diesem Effekt. In Abbildung 3 sind die beschriebenen plasmonischen Sensorprinzipien schematisch gegenübergestellt. Um jedoch mit plasmonischen Nanopartikeln hochempfindlich Moleküle detektieren zu können, ist neben der Spezifität, welche durch die fixierten Erkennungsmoleküle an der Partikeloberfläche bestimmt wird, die Sensitivität ein entscheidendes Kriterium. Dabei bezeichnet die Sensitivität S die spektrale Verschiebung der Resonanzwellenlänge in Abhängigkeit zur Änderung des Brechungsindexes. Je höher diese Verschiebung ist, desto sensitiver können Umgebungsänderungen, entweder durch direktes Anbinden an der Partikeloberfläche (Oberflächensensitivität; S_S), oder durch Verändern des Brechungsindex um den Nanopartikel (Bulksensitivität; S_B) detektiert werden [34, 37, 46]. Wie die LSPR-Bande selbst, haben die intrinsischen Faktoren auch einen
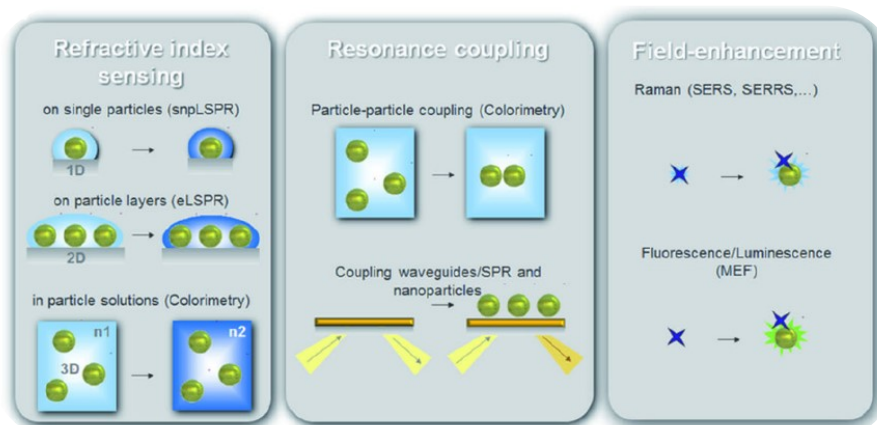

Abbildung 3: *Übersicht von Sensorprinzipien, basierend auf plasmonischen Nanopartikeln. [49]*

---

[h] Markierungsfrei oder labelfrei bezeichnet die Detektion des nachzuweisenden Analyten, ohne diesen selbst vorher zu markieren.

Einfluss auf die Sensitivität. So ist die Bulksensitivität (S_B) für größere Partikel generell höher [47, 48]. Gleiches gilt aufgrund geringerer materialspezifischer Dämpfungseigenschaften [33] für die Interaktion von Materie und Licht für plasmonische Nanopartikel aus Silber im Vergleich zu denen aus Gold [46]. Auch besitzen formanisotrope Nanopartikel neben mehreren LSPR-Banden, die auf verschiedene Resonanzmoden zurückzuführen sind, eine höhere Sensitivität (vor allem S_s) als ihr sphärisches Pendant [37]. Diese Eigenschaft beruht auf der verstärkten Ausprägung und der damit einhergehenden starken Fokussierung der Oberflächenplasmonen an Spitzen und Kanten [50, 51]. Das wiederum ist ein für die Nahfeldkopplung entscheidender Effekt [52], da er abermals eine Feldverstärkung, sogenannte „Hot Spots" [53], an den beschriebenen charakteristischen Strukturen, ermöglicht [40, 54, 55]. Die Herstellung formanisotroper Nanostrukturen ist jedoch sehr komplex. Der folgende Abschnitt beschäftigt sich daher mit den Grundlagen der Nanopartikelsynthese.

2.2. Herstellung von metallischen Nanopartikeln

Die nasschemische Herstellung von plasmonischen Nanopartikeln ist eine kolliodale Synthese[b], gehört zu den Bottom-up-Verfahren und basiert auf der Reduktion von in Lösung vorliegenden Metallionen. Dabei wird eine Vorstufenverbindung (*Präkursor*), meist ein Metallsalz (z.B. Tetrachlorgoldsäure für Gold und Silbernitrat für Silber), als Ausgangsstoff verwendet. Durch Reaktion der Metallionen mit einem Reduktionsmittel können dessen Elektronen vom Metallion aufgenommen und das Metallion zu Atomen reduziert werden [6, 56, 57]. Als Reduktionsmittel werden häufig Natriumborhydrid ($NaBH_4$) [58, 59], Hydroxylamin (NH_2OH) [60], Ascorbinsäure (AA, C_6H_8O) [61-64], Natriumcitrat ($Na_3C_6H_5O_7$) [11, 65, 66] oder verschiedene Alkohole [67], Aldehyde [68] und Saccharide [69] verwendet [56]. In der Regel sind in der Syntheselösung weiterhin Stabilisierungsmoleküle vorhanden, welche einen direkten Einfluss auf die Nanopartikel bzw.
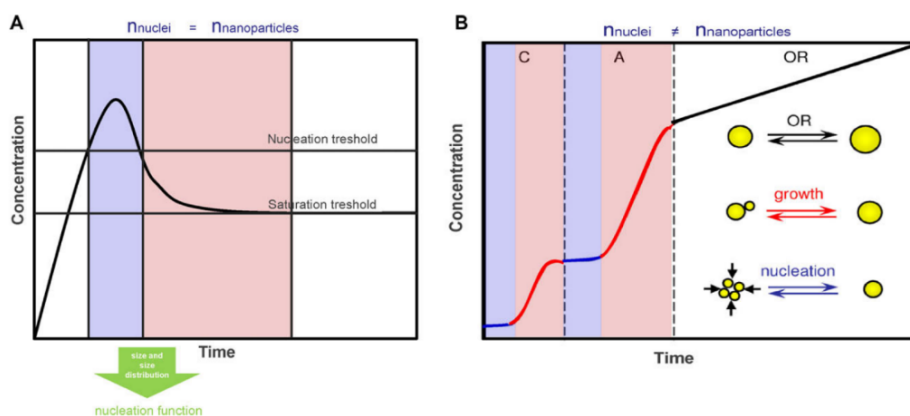

Abbildung 4: *Vergleich der Modelle zur Nanopartikelsynthese. Beim klassischen Modells nach LaMer werden die Anzahl der Nanopartikel durch die Anzahl der Nuclei terminiert (a). In der korrigierten Version von Polte sind dagegen die Anzahl der Nuclei und die finale Nanopartikelanzahl nicht identisch (b) [49].*

den Kristallisationsprozess haben. So adsorbieren diese Moleküle auf der Partikeloberfläche und stabilisieren die Nanopartikel elektrostatisch (Bsp. Citrationen) durch repulsive Kräfte oder sterisch durch räumliche Abschottung voneinander. Für letzteres gibt es verschiedene Möglichkeiten. Beispielsweise können Polymere (PEG; PVA, PVP, PSSS) [70-73] DNA [74, 75], Tenside (CTAB, CTAC, MTAB) [76-78] und organische Liganden [59, 79, 80] verwendet werden [81, 82]. Durch gezieltes Variieren der beschriebenen Zusätze können diese aber auch die Kristallbildung [72], das optische Ansprechverhalten und die finale Form der Nanopartikel beeinflussen [82], was in Tabelle 1 (Kapitel 3.5) zusammengefasst ist. Bei zu starker Dezimierung oder Vernachlässigung der Stabilisierungsmoleküle kommt es jedoch zur Agglomeration[i] oder sogar zur Aggregation[j] [1] der Nanopartikel und damit zur Präzipitation, was häufig eine Zerstörung der kolloidalen Lösung zur Folge hat. Destabilisierung kann jedoch auch induziert sein und wie in Abbildung 3 für kolorimetrisches Detektieren[k] verwendet werden [83, 84]. Die eigentliche Synthese, also die gezielte Bildung von Nanopartikeln, bzw. die Erzeugung einer neuen festen Phase lässt sich dabei in zwei Schritte einteilen: (I) die Keimbildung (*Nuclei*) und dessen Entwicklung in stabile Kristallkeime (*Seeds*) sowie (II) das generelle Wachstum der Kristallkeime zu den finalen Nanokristallen [6]. Abhängig von den herzustellenden Nanopartikeln, kann das Wachstum aus mehreren einzelnen Wachstumsschritten bestehen. Dabei steht der ursprünglich 1950 entwickelten Theorie zur Keimbildung nach LaMer [85], das derzeitig allgemein akzeptierte Modell entgegen (Abbildung 4). Nach LaMer kommt es zur Bildung eines Nukleus aufgrund des Erreichens einer kritischen Konzentration von Metallatomen (basierend auf der fortlaufenden Reduktion des Präkursors) und damit zur homogenen Selbstnukleation. Aufgrund dieser kommt es jedoch zum rapiden Abfall der in der Lösung vorhandenen Metallatomkonzentration, wodurch die Nukleation beendet und ausschließlich ein heterogenes Wachstum der gebildeten Nuclei durch die noch in der Lösung vorhandenen Metallatome stattfinden kann. Damit sind die Konzentration und die Größe der späteren Nanopartikel durch die Anzahl an gebildeten Nuclei determiniert (Nukleationsfunktion) [86]. Diese sind wiederum abhängig von der Dauer der kritischen Nukleationszeit, welche durch die Auswahl an verschieden starken Reduktionsmitteln und der damit verbundenen Reduktionsgeschwindigkeit des Präkursors zu Metallatomen kontrolliert werden kann. So ist NaBH$_4$ zum Beispiel ein sehr starkes Reduktionsmittel und

---

[i] Unter Agglomeration versteht man eine reversible lockere Zusammenlagerung von Partikeln aufgrund Destabilisieren der Effekte und das daraus resultierende Überwiegen von attraktiven Kräften (Bsp. *Van-der-Waals-Kräfte*). Es handelt sich um einen reversiblen Prozess, bei dem die resultierende externe Oberfläche ähnlich der Summe der Einzeloberflächen ist.

[j] Eine Aggregation ist eine irreversible starke Zusammenlagerung von Partikeln aufgrund kovalenter Bindungen. Die entstehende resultierende externe Oberfläche ist hierbei kleiner als die Summe der Einzeloberflächen.

[k] Kolorimetrie bezeichnet die Konzentrationsbestimmung einer Substanz basierend auf einen Farbumschlag der Partikelsuspension.

bildet sehr schnell (< 100 ms) [27, 87] viele Nuclei, die aufgrund des hohen Metallatomumsatzes während der Nukeationsphase anschließend nur sehr wenig wachsen. Abhängig von den Zusätzen können somit Goldnanopartikel zwischen 1,2 und 10 nm hergestellt werden [56]. Im Gegensatz dazu ist Natriumcitrat ein sehr schwaches Reduktionsmittel, dass Metallpräkursor ausschließlich unter starker Energiezufuhr (z.B. durch Erhitzen) und längere Zeit (etwa 60 sec) zu ihren atomaren Spezies reduzieren kann [88, 89]. Hier wird der beschriebene Vorgang, der auf Turkevich und Frens zurückgeht, besonders deutlich. Die einzelnen Synthesephasen und damit die Nukleationsfunktion können durch verschiedene Verhältnisse von Reduktionsmittel zu Metallkonzentration eingestellt werden [11, 90]. Dementsprechend können Goldnanopartikel von 10 nm [91] bis zu 200 nm [92] hergestellt werden, die jedoch eine relativ breite Größenverteilung aufweisen. So beschreibt das Modell von LaMer zwar relativ ausführlich die Nukleationspase, hat jedoch Defizite hinsichtlich der Beschreibung von Wachstums- und Reifungsprozessen[l]. Hier setzt die Theorie des *„Aggregativen-Synthesprozesses"* [86], basierend auf der Ausarbeitung jüngster experimenteller Ergebnisse von Polte und Kollegen, an (Abbildung 4b) [57]. Dabei ist auch hier der Nukleationsprozess vom verwendeten Reduktionsmittel abhängig. So sind bei Verwendung von $NaBH_4$ 0,8 nm große Nuclei bereits nach etwa 100 ms erreicht [27], was für Natriumcitrat erst nach etwa 60 sec der Fall ist [89]. Direkt im Anschluss kommt es jedoch zum Vereinigen (Koaleszenz[m]) der entstandenen Nuclei, da sie aufgrund ihrer geringen Größen und der damit einhergehenden großen Oberflächen nicht ausreichend stabil sind [87, 93]. Das Resultat ist ein vergrößerter Partikeldurchmesser bei paralleler Verringerung der Partikelanzahl. Dieser Prozess dauert für $NaBH_4$ ca 100 ms und für Natriumcitrat etwa 20 min. Bei Verwendung von Letzterem als Reduktionsmittel kommt es jedoch nochmals zu einem langsamen und schnellen Wachstumsprozess, der zu berücksichtigen ist [86, 89]. Die beschriebenen Prozesse laufen für Gold- und Silbernanopartikel in ähnlicher Weise ab, wobei das Wachstum bei Silbernanopartikeln durch einen weiteren metastabilen Zustand geprägt ist, der auf einem reaktionsbedingten Gleichgewicht zwischen in Lösung vorhandenen Kolloiden und unverbrauchtem Präkursor basiert. [6] Durch die Zugabe geeigneter Liganden ist es jedoch möglich, auch diese Synthese zu kontrollieren [72]. Dabei kann neben der anfangs beschriebenen Stabilisierung auch die Nanopartikelgröße und deren Form über Liganden gesteuert werden.

---

[l] Hier ist insbesondere die Ostwald-Reifung gemeint, bei der ein Materiestrom von kleineren zu größeren Kolloiden vorliegt. Es kommt folglich zum Schrumpfen der kleineren und zum Wachsen der größeren Partikel, wobei die kleinen Partikel ab einem bestimmten Radius instabil werden und sich schließlich völlig auflösen. Daraus resultiert eine generelle Verringerung der Kolloidanzahl und somit die Minimierung der freien Energie des kolloidalen Systems [57]

[m] Koaleszenz (lat. *coalescere* - Zusammenwachsen) bezeichnet den Zusammenschluss/Verschmelzen von dispergierenden Teilchen

2.3. Mikrofluidik und Mikroreaktoren

In der Mikrofluidik spielen Mikroreaktoren mit meist hierarchisch angeordneten und dem Einsatzgebiet angepassten Strukturelementen[n] die Hauptrolle gefolgt von den peripheren Elementen (z.B. Spritzenpumpe, Spritzen, Verbindungselemente, Anschlüsse, Zu- und Ableitungen usw.) [23]. Auch wenn streng genommen Mikrotiterplatten und nanoskalige Kavitäten ebenfalls zu den Mikroreaktoren gehören, haben sie in der Mikrofluidik eine eher untergeordnete Rolle, da ein entscheidendes Kriterium gerade der manipulative Fluidtransport ist [94]. Diesbezüglich lassen sich mikrofluidische Verfahren in zwei Kategorien unterteilen, in (I) die kontinuierliche und (II) die tropfenbasierte Mikrofluidik [95]. Bei der kontinuierlichen Prozessführung fließen die Fluide in der Regel als permanente Phase durch den Mikroreaktor (CF – *Continuous Flow*) [22, 29, 95]. Die tropfenbasierte Mikrofluidik beruht dagegen auf einem Mehrphasensystem (mindestens zwei). Hier trennen die nicht mischbaren Phasen kleine Reaktionsräume (Segmente) auf, die perlenschnurartig im Mikrosystem transportiert und manipuliert werden können [30]. Dadurch entsteht ein segmentierter Fluss (SF – *Segmented Flow*), bei dem jedes Segment eine in sich geschlossene, einzelne Reaktionskammer darstellt [96, 97]. Abgesehen von ihrer Prozessführung lassen sich Mikroreaktoren jedoch generell durch ihre Wirkprinzipien eingliedern [23, 24]. Einen speziellen Typ stellen Mikromischer dar, die, basierend auf ihren Funktionselementen, verschiedene Fluidspezies effektiv miteinander mischen können. Dabei kann der Mischvorgang sowohl aktiv induziert (z.B. elektrodynamisch, elektrokinetisch, dielektrophoretisch, magnetisch), als auch passiv (ohne Zugabe externer Energie) realisiert werden [98, 99]. Unabhängig von der zugrundeliegenden Art hat der physikalische Prozess des Mischens dabei das Ziel, eine gleichmäßige Verteilung verschiedener Spezies in einer Mixtur in kürzester Zeit zu erreichen [100]. Der fundamentale Mischprozess basiert auf der molekularen Diffusion, die auf dem Fick'schen Gesetz beruht und durch die vereinfachte Abhängigkeit

$$t \sim d_l^2 / D$$

dargestellt wird. Die Diffusionszeit t hängt dabei antiproportional vom Diffusionskoeffizient D und direkt vom quadrat der Diffusionslänge d_l ab. Dementsprechend sind Diffusionsvorgänge für kleine Abstände höchst effizient, jedoch langsam und ineffektiv für größere Distanzen[o]. Die Aufgabe von Mikromischern ist es daher, aus verhältnismäßig großen Volumina kleinere Volumenelemente zu generieren, um somit die effektiven Diffusionswege zu verkürzen [23]. Erreicht wird dieses

---

[n] Die Mikrostrukturierung definiert dabei ein Funktionselement, welches mit der zugehörigen Mikroperipherie eine Reaktionseinheit bildet. Alle Reaktionseinheiten ergeben im Zusammenspiel den Mikroreaktor [24].

[o] Beispielsweise benötigt ein kleines, in Wasser gelöstes organisches Molekül 5 s für eine Diffusionstrecke von 100 µm, jedoch nur 50 ms für eine Strecke von 10 µm [23].

Ziel entweder durch laminares oder durch turbulentes Mischen. Beim Konzept des laminaren Mischens wird die Gesamtheit der zu mischenden Fluide sukzessive durch Teilung und Neuformierung (*Split-and-Recombine, SAR*) zu regulären, alternierenden und parallellaufenden Lamellen forciert. Das dabei entstehende Multilaminationsmuster zeichnet sich, aufgrund der vielen schmalen Lamellen und der daraus resultierenden großen Grenzflächen, durch kurze Diffusionswege aus [23]. Die Prozessparameter zur optimalen Durchmischung müssen dabei jedoch meist empirisch ermittelt werden. Beim turbulenten Mischen werden im gesamten Mischelement strukturbedinge Verwirbelungen erzeugt, so dass lokale Unterschiede eliminiert und die Fluide global betrachtet homogen verteilt sind. Dafür muss die Fluidgeschwindigkeit auf die vorherrschende Mischergeometrie abgestimmt werden, da in den kleinen Kanälen Wirbel erst ab einer kritischen Flussrate entstehen. Unterhalb dieser Flussrate herrscht ein laminares Strömungsregime, welches an dieser Stelle keine ausreichende Durchmischung erlaubt [99, 100]. Um für die verschiedenen Mischergeometrien den Übergang zwischen laminarer und turbulenter Strömung zu quantifizieren, bedient man sich verschiedener dimensionsloser Kennzahlen, die Aussagen über das im Mikromischer vorherrschende Strömungsverhalten zulassen. Die *Reynoldszahl* (Re) beschreibt beispielsweise das Verhältnis zwischen Trägheits- und Zähigkeitskräften und berechnet sich wie folgt:

$$\mathrm{Re} = \frac{\rho * v * d}{\eta}$$

Dabei stellt ρ die Dichte und η die dynamische Viskosität des Mediums dar, v die Strömungsgeschwindigkeit und d die charakteristische Länge (meist hydraulischer Durchmesser d_h). Überschreitet die Reynoldszahl einen kritischen Wert (Re_{krit}), so kommt es von einem laminaren in einen turbulenten Fluidstrom [23, 24]. Für T-Mischer, einem klassischen Mischer bei dem das Mischelement ein einfaches T darstellt (zwei orthogonal aufeinander stehende Kanäle), ist das zum Beispiel ab einem Wert von Re > 200 der Fall [101, 102]. Komplexere Mikromischer haben jedoch ein anderes Verhalten, so dass für jeden Mischertyp andere Kennzahlen berechnet werden müssen [102]. Beispielsweise wird in gewundenen Kanälen neben der Reynoldszahl die *Dean-Zahl* (De) angegeben, um die Existenz bzw. die Stärke der durch die Umlenkung des Fluidstroms entstandenen Wirbel im Kanal zu quantifizieren (siehe Kapitel 3.2 Abbildung 8) [103, 104]. Für eine ausreichende Durchmischung sollte De > 150 und Re > 100 sein, wobei die Dean-Zahl über den Krümmungsradius R und den hydraulischen Durchmesser des Kanals folgendermaßen berechnet wird:

$$\mathrm{De} = \mathrm{Re} \sqrt{\frac{d_h}{2*R}} \text{ [105]}.$$

Bei allen Mikromischern ist ein einheitliches Verweilzeitverhalten entscheidend, wobei vor allem kurze Verweilzeiten speziell für schnelle Reaktionen gewährleistet werden können. Der Vorteil, geringe Mengen sehr präzise zu mischen, spielt vor allem bei gefährlichen Reaktionen eine große Rolle und unterstreicht weiterhin die ökologischen und ökonomischen Aspekte. Die Grundlage dafür sind die verringerten Dimensionen und der damit einhergehenden minimierte Material-, Chemikalien- und Energieverbrauch [23, 106]. Vor allem mit SF-Verfahren können effizient Hochdurchsatzscreenings gemacht werden [107]. Darüber hinaus erlauben Mikromischer im Vergleich zu herkömmlichen Durchfluss- und Batchanlagen eine schnelle Anpassung an sich ändernde Reaktionsbedingungen, wodurch sie für online-monitoring-Prozesse prädestiniert und daher ideal für Automatisierungsprozesse geeignet sind. Anders als klassische Verfahren werden Mikromischer nicht nach dem Prinzip des *scale-up* (die volumenmäßige Erhöhung des Durchlaufs), sondern nach dem Prinzip des *numbering-up* (die Anzahl der parallellaufenden Mikromischer wird erhöht) betrieben. Durch diese einfache und günstige parallele Replikation bleiben sämtliche Prozessparameter bei erhöhter Ertragsproduktion gleich und die Flexibilität somit erhalten [23, 24].

2.4. Stand der Technik

Während die Arbeiten von Faraday und Turkevich sich noch auf die thermodynamisch favorisierte, sphärische Form der plasmonischen Nanopartikel beschränkten, versuchten Wissenschaftler in den 1990er Jahren verstärkt auch formanisotrope Nanopartikel herzustellen [108-112]. Durch Verwendung der in Tabelle 1 (Kapitel 3.5) aufgelisteten Zusätze konnten dabei verschiedene Kristallfacetten gezielt blockiert und damit ein gerichtetes Wachstum induziert werden. Aufgrund der teilweise unklaren chemischen Vorgänge bei der Herstellung und der damit einhergehenden, mäßigen Prozesskontrolle war der Erfolg hinsichtlich der zu erreichenden Geometrien und Ausbeuten jedoch mäßig. Erst nachdem Jana 2001 das effiziente Verfahren der mehrstufigen Synthese [60] für formanisotrope Goldnanopartikel publizierte und damit einen Meilenstein setzte [113, 114], konnte die Palette verschiedener Nanopartikelformen stets erweitert und deren Syntheseausbeute erhöht werden [6, 115-117]. Dabei beruht das Verfahren der keimbasierten Synthese (*seed-mediated synthesis)* auf dem strikten Trennen der Synthese (Keimbildungsprozessen) von der anschließenden heterogenen Keimbildung mit gezielten Wachstum. In diesem Zusammenhang konnte Wagner 2004 erstmals zeigen, dass sphärische Goldnanopartikel im Mikromischer effektiv wachsen können [118]. Grundlage und Fundament dazu war jedoch die Synthese der Seeds im Batchreaktor. Ein Jahr später konnte auch eine effiziente Synthese von sphärischen Goldseeds im Mikromischer gezeigt werden [119]. Gleiches gelang erstmals Lin für Silbernanopartikel [120]. 2010 gelang es dann Polte und Kollegen, die Reaktionen der Keimbil-

dung, aber auch der Wachstumsschritte durch Verwendung von Mikromischern und in-situ Charakterisierung teilweise aufzuklären [27]. Trotz Limitationen hinsichtlich Nanopartikelsynthese in Batchreaktoren und des großen Potenzials der Mikrofluidik demgegenüber entwickelte sich jedoch erst im letzten Jahrzehnt die mikrofluidische Synthese zu einer leistungsfähigen Herstellungsmethode für plasmonische Nanopartikel mit ausreichender Qualität für die Untersuchung von Form-Eigenschafts-Beziehungen. In Tabelle 2 (Anhang) sind Meilensteine der mikrofluidischen Synthese von plasmonischen Nanopartikeln zusammengefasst. Darüber hinaus beschäftigen sich verschiedene Reviews [121, 122] bzw. deren Unterkapitel [22, 95] mit dieser Thematik. Dabei liegt der Fokus auf verschiedenen Aspekten. Im speziellen Fall der formanisotropen Synthese beziehen sich die meisten aktuellen Arbeiten auf die Synthese im segmentierten Fluss (SF). Hier stechen vor allem die Arbeiten der Forschungsgruppen der TU-Ilmenau [107, 123-127] und der Universität Singapur [128-131] hervor. Die kontinuierliche Synthese mithilfe von Mikromischern wurde hingegen wenig thematisiert. Meist beziehen sich diese Synthesen auf die simple Miniaturisierung in ein schlichtes Durchflussrohr [120, 132-135], wobei das große Potenzial kontinuierlicher mikrofluidischer Verfahren dabei nicht ausgeschöpft werden kann. Der Fokus dieser Arbeit widmet sich hauptsächlich der Schließung dieser Lücke und soll dazu beizutragen, das Gesamtbild der mikrofluidischen Nanopartikelsynthese zu verstehen und zu vervollständigen.

3. Eigene Arbeiten

In diesem Kapitel werden die Ergebnisse vorgestellt, die im Rahmen dieser Dissertation entstanden sind. Der erste Abschnitt bezieht sich dabei auf die Herausforderungen und die daraus resultierenden Lösungsstrategien mit Bezug zu mikrofluidischen Verfahren für eine effiziente Herstellung von plasmonischen Nanopartikeln. In den darauffolgenden drei Abschnitten werden die Lösungsstrategien aufgegriffen und systematisch untersucht. Neben der Keimbildung und dem formkontrollierten Wachstum spielt die Kombinatorik verschiedener Methoden für die jeweilig stattfindenden Prozesse eine entscheidende Rolle. Untersucht wird dieser Zusammenhang insbesondere anhand der Synthese von formanisotropen metallischen Nanopartikeln. Der letzte Abschnitt beschäftigt sich mit der postsynthetischen Prozessierung (Stabilisierung) der hergestellten Nanopartikel und ihrem Potenzial für sensorische Applikationen.

3.1. Herausforderungen bei der Herstellung metallischer Nanopartikel und deren weiterer Prozessierung [MT1]

Bei der Arbeit mit metallischen Nanopartikeln, insbesondere bestehend aus Gold, Silber, Platin und Palladium, sieht man sich häufig mit dem Vorurteil der hohen Chemikalienkosten konfrontiert. Dabei werden bei der schrittweisen chemischen Reduktion von Metallionen im wässrigen Medium nur wenige mg des Metallsalzes benötigt[p]. Die kolloidale Synthese benötigt hierfür ein Metallsalz, einen Elektronendonator (Reduktionsmittel), sowie Stabilisierungsmoleküle. Das Zusammenspiel dieser Faktoren hat einen imminenten Einfluss auf die herzustellenden plasmonischen Nanopartikel, wobei die genau ablaufenden Prozesse bereits unter 2.2 beschrieben sind. Die sich daraus ergebende Vielseitigkeit bei der Synthese erlaubt ein genaues Einstellen der Partikelparameter und dabei insbesondere der Plasmonenresonanz. In Abbildung 5 sind verschiedene Nanopartikelarten mit der dazugehörigen Lage ihrer LSPR-Banden im elektromagnetischen Spektrum dargestellt. Für diese Arbeit sind dabei vor allem plasmonische Nanopartikel interessant, deren LSPR-Maximum im Bereich des sichtbaren Lichts liegt. Diesbezüglich konnten maßgeschneiderte Partikel hergestellt werden, wovon einige in Abbildung 6 dargestellt sind. Neben unterschiedlichen Partikelgrößen (siehe Abbildung 1 für Gold) konnten verschiedene formisotrope und -anisotrope Nanopartikel als auch unterschiedliche Materialzusammensetzungen realisiert werden. Wobei die Vielseitigkeit der kolloidalen Synthese ein genaues Verständnis und Kontrolle der ablaufenden sensiblen Prozesse nach sich zieht, da besonders die Herstellung

---

[p] Für die Herstellung von 100 ml einer 10 nm Goldnanopartikelsuspension mit 10 nm großen Partikeln und einer OD von etwa 1,5 wird 1 mg Goldsäure benötigt. Bei einem Kaufpreis von 634 € / 5 g [136] entstehen Goldkosten von etwa 0,13 € für die Partikelsuspension. Der Preis für eine vergleichbare kommerziell erhältliche kolloidale Lösung von Goldnanopartikeln liegt dagegen bei etwa 190 € (100 ml; OD = 1) [137].
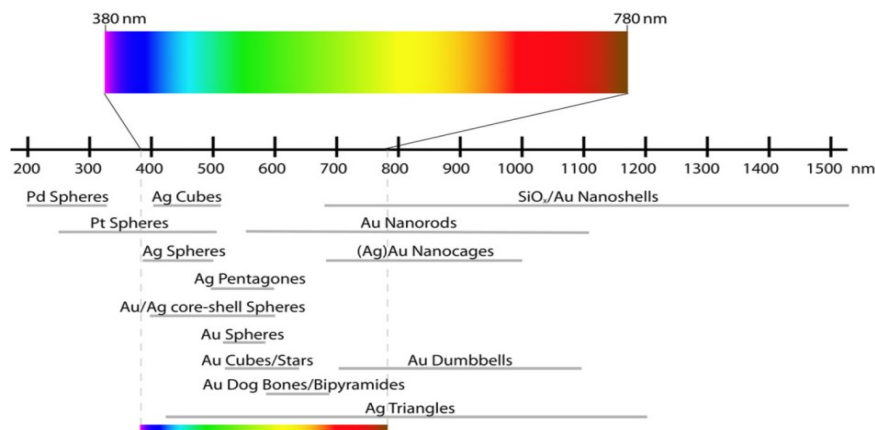
Abbildung 5: *Übersicht der spektralen Bandbreite der lokalisierten Plasmonenreso-
nanz für verschiedene metallische Nanopartikel im UV-Vis und NIR-Bereich. [MT1]*

formanisotroper Nanopartikel unter geringer Ausbeute und Reproduzierbarkeit leidet. Dabei un-
terliegt ihre Herstellung generell demselben Mechanismus wie sphärischen Nanopartikeln (siehe
Kapitel 2.2). Jedoch müssen hier neben mehreren aufeinander folgenden Prozessschritten noch
weitere Additive zugegeben werden, die ein anisotropes Wachsen, also eine gerichtete Ausprä-
gung der Dimensionen ermöglichen bzw. unterstützen. Beide Faktoren sind neben der ohnehin
nicht trivialen Herstellung von plasmonischen Nanopartikeln abermals potenzielle Fehlerquellen.
Da bei einer mehrstufigen Herstellung jeder Prozessschritt auf den vorangegangenen aufbaut,
ist es entscheidend, dass jeder einzelne Schritt optimal verläuft. Aus Seeds mit einer breiten
Größenverteilung lassen sich weder qualitativ hochwertige plasmonische Nanopartikel erzeugen,
noch kann von einem reproduzierbaren Vorgang gesprochen werden. Erschwerend kommt hin-
zu, dass jeder Prozessschritt andere Bedingungen und teilweise verschiedene Zusätze erfordert,
zum einem zur Stabilisierung der Nanopartikel, zum anderen auch zur Erzeugung definierter
geometrischer Strukturen mit den gewünschten optischen Eigenschaften. Zur Herstellung aniso-
troper Nanopartikel sind Additive (Tabelle 1 in Kapitel 3.5) obligatorisch, wobei vor allem
Surfaktanten[q] eine große Bedeutung spielen. Sie bilden zwar einen Komplex mit dem Metallion
und kontrollieren dabei dessen Reduktion [140], fungieren aber hauptsächlich als Kristallfacet-
tenblocker, die sich bevorzugt an bestimmte Facetten anlagern und diese während des Wachs-
tums blockieren. Die blockierten Facetten entwickeln sich langsamer als die freien und es kommt
so zum gerichteten Wachstum. Dieser Vorgang basiert entweder darauf, dass dichter besetzte
Oberflächen stärker gegenüber Metallatomanlagerung abgeschirmt sind als weniger dichtbesetz-
te Facetten [141, 142], oder auf der lokalen Verschiebung des Oberflächenpotenzial durch die

---

[q] Surfaktant (engl. surfactant - ***surf**face **act**ive **agent***) sind Tensid ähnliche, grenzflächenaktive Stoffe, die sich an die
Oberfläche der Nanopartikel (Phasengrenze fest-flüssig) anlagern und diese hinsichtlich physikochemischer Eigen-
schaften verändern. Ab einer bestimmten Konzentration (*CMC – critical micelle concentration*) bilden sich durch
Selbstassemblierungsprozesse Mizellen aus. Die CMC gilt dabei als Mindestanforderung zur Stabilisierung von Nano-
partikeln und beträgt für CTAB zwischen 0,9 und 1 mM. [138] und für CTAC etwa 1,4 mM [139].

Besetzung und der damit einhergehenden facettenabhängigen elektrostatischen Abschirmung [57, 87]. In jedem Fall hat der Vorgang einen starken Einfluss auf den Syntheseablauf und er bedarf einer genauen Kontrolle, da sich die Reaktionskinetik ändert und sich das thermodynamische Gleichgewicht verschiebt. Ein Lösungsansatz ist die erwähnte Aufspaltung der Gesamtsynthese in mehrere Schritte (keimbasierte Synthese) und die gezielte Optimierung jedes Prozessschrittes. Das optimale Verfahren beruht auf der Herstellung von Seedpartikeln, die stufenweise zum Wachstum gebracht werden. Dabei wird die Wachstumslösung immer wieder mit den aus der vorherigen Reaktion resultierenden Partikeln okuliert. Somit kann die gesamte Synthese mehrere Wachstumsschritte mit jeweils spezifischen und unterschiedlichen Zusätzen und Kinetiken aufweisen. Dabei sind der Zeitpunkt der Additivzugabe und deren Konzentration entscheidend. Nach der Nanopartikelherstellung tritt die postsynthetische Prozessierung in den Vordergrund. Hier spielen vor allem die Langzeitstabilisierung, der Ligandenaustausch und die biologisch-chemische Modifizierung, beispielsweise für die optische Sensorik, eine zentrale Rolle (siehe Tabelle 1 in Kapitel 3.5). In den folgenden Abschnitten wird darauf eingegangen, ob und wie mikrofluidische Verfahren die genannten Herausforderungen der Herstellung lösen und wie die Nanopartikel stabilisiert werden können, um sie für biosensorische Anwendungen zu nutzen.
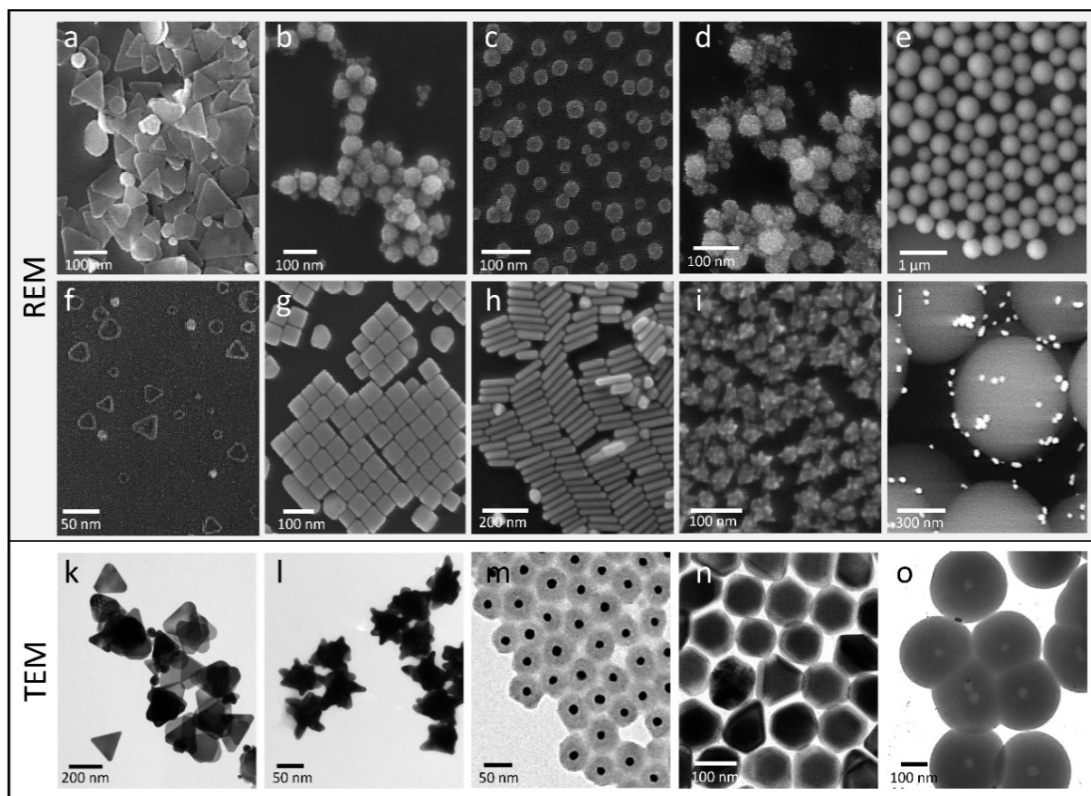

Abbildung 6: *Elektronenmikroskopieaufnahmen (REM: a - j und TEM: k - o) von Nanopartikeln verschiedener Morphologie und Zusammensetzungen, die im Rahmen der Promotion hergestellt wurden. Silberdreicke (a, k), Platinpartikel (b), Palladiumpartikel (c), Titanoxidpartikel mit Stickstoffdotierung (d), Silicapartikel (e), Goldrahmen (f), Goldwürfel (g), Goldstäbchen (G), Goldsterne (i, l) Goldinseln auf Silicapartikeln (j), und Kernhülle-Partikel: Goldkerne ummantelt von Silikat (m) und Silber (n) sowie Silberkerne mit Silikathülle (o).*

3.2. Mikrofluidik als effizientes Werkzeug zur Kontrolle der Keimbildung [MT2, MT3, MT4]

Um mikrofluidische Verfahren für die Synthese plasmonischer Nanopartikel zu verwenden, ist ein generelles Umdenken nötig. Die konventionelle Batchsynthese, bei der die Chemikalien nacheinander zugegeben werden, muss in einen kontinuierlichen Prozess überführt werden. Schematisch ist das in Abbildung 7 zur Herstellung kleiner Goldkeime dargestellt. Durch die kontinuierliche Prozessführung kommt es zu keiner Limitierung der Reaktanden mehr, so dass (theoretisch) durchgehend Nanopartikel synthetisiert werden können. Die Volumina müssen dafür in Flussraten überführt werden, so dass sich die Endkonzentrationen der eingesetzten Chemikalien ausschließlich aus ihren Flussratenverhältnissen ergeben. Dabei muss die verwendete Mikrofluidik zum Vorhaben exakt angepasst werden. Der Mikromischer (im Fall von CF-Verfahren) muss geeignete Fluidanschlüsse (Anzahl Zu- und Abgänge) besitzen und die Wirkungsweise sowie der Arbeitsbereich müssen zu der ablaufenden Reaktion passen (siehe Kapitel 2.3). Dementsprechend kommen für verschiedene Reaktionen unterschiedliche Mikromischer zum Einsatz. Im Hinblick auf die Synthese von plasmonischen Nanopartikeln ist die Keimbildungsphase unter Verwendung von Natriumborhydrid als Reduktionsmittel ein kritischer Schritt. Wie bereits erläutert, verläuft diese Reaktion für Gold in 100 ms ab [27]. Für ein optimales und effizientes Mischen unter diesen Bedingungen eignet sich der Dean-Flow-Mischer (DFM), dessen geometrische und fluidtechnische Parameter in Abbildung 8 zusammengefasst sind. Der Simulation zufolge stellen sich ab einer Flussrate von 23 μl/s, einer Reynoldszahl von Re = 150 und einer Dean-Zahl von De = 156 ausreichend sekundäre Verwirbelungen ein, um die beiden Edukte zu mischen. Ab dieser Gesamtflussrate kommt es demnach zu Turbulenzen im Kanal, die auf der rotationsartigen Trajektion des schnelleren Kernfluids an den Kanalkrümmungen (Mäander) basieren und damit das langsamere Außenfluid verdrängen. Die Mischeffizienz konnte dabei mit Erhöhung der Flussrate noch gesteigert und die Ergebnisse experimentell validiert werden, so dass der Arbeitspunkt des Mikromischers ab einer Gesamtflussrate von mindestens 30 μl/s und einer Fluid-
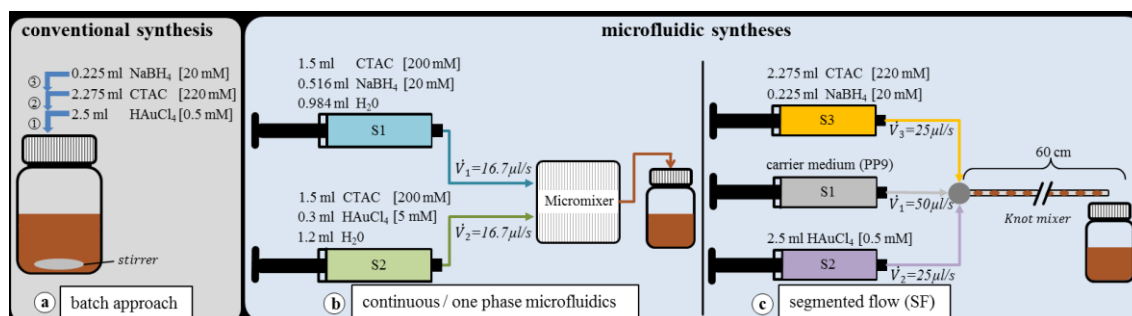

Abbildung 7: *Übersicht der Synthesemethoden mit dem diskontinuierlichen Batchverfahren (a) und den beiden mikrofluidischen Methoden der kontinuierlichen Phase (b) und dem segmentierten Flussverfahren (c) zur Herstellung von kleinen Goldnanopartikeln (AuSeeds). S1, S2 und S3 steht für die jeweilige Spritze 1, 2 oder 3 [MT3].*
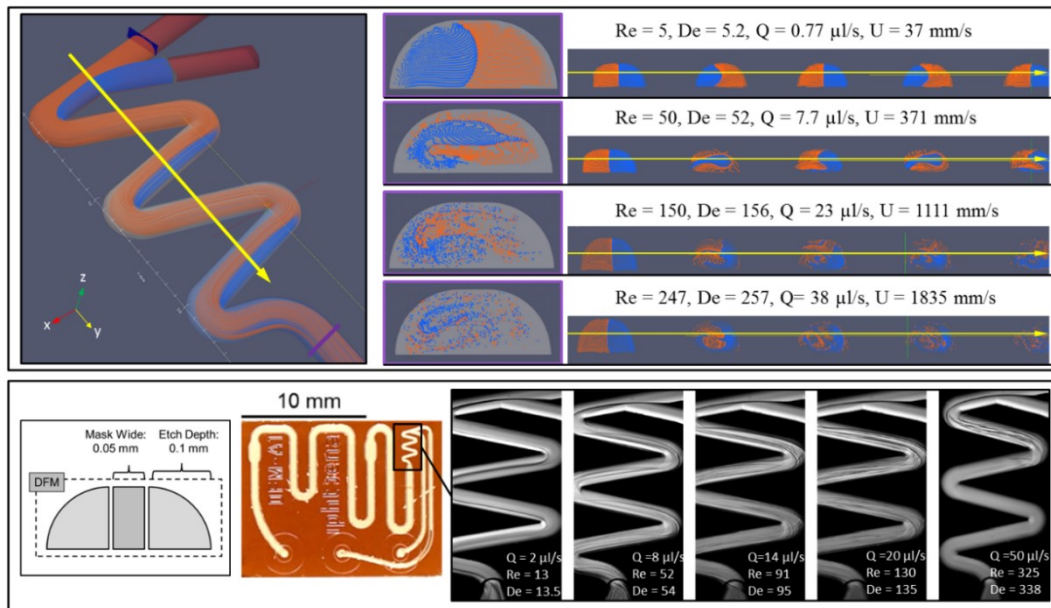
Abbildung 8: *Charakterisierung des Dean-Flow-Mikromischers (DFM). Im oberen Teil sind die CFD Simulationen dargestellt, wobei links die gesamte Mischzone und in der Mitte der Fluidausgangsbereich dargestellt ist. Im rechten Teil ist der gesamte simulierte Mischprozess entlang des Kanals (der gelbe Pfeil markiert die genaue Position) für verschiedene Flussraten dargestellt. Im unteren Teil sind die experimentellen Ergebnisse, beginnend mit den geometrischen Parametern, einer Aufnahme des Mikromischers und Bildern des vorherrschenden Laminationsmusters bei steigender Flussrate (Q), gezeigt. [MT4]*

geschwindigkeit (im Mäander) von etwa 1450 mm/s festgemacht werden konnte. Die effektive Mischzeit liegt dementsprechend im Bereich von 4 ms. Diesbezüglich eignet sich der DFM als Mikromischer für die komplexen Anforderungen der Nukleation und wurde zur Herstellung von definierten Gold und Silberkeimen verwendet. Für beide Metalle konnte hinsichtlich Partikelgröße und Partikelgrößenverteilung eine Verbesserung erreicht werden. Die Seedsynthese hat als allgemeines Ziel, möglichst kleine Partikel mit schmaler Größenverteilung herzustellen. In Abbildung 9 sind die Ergebnisse der Partikelsynthese unter Verwendung des DFMs dargestellt. Als Referenz wurde eine Batchsynthese mit demselben Protokoll und Chemikalien durchgeführt. Im direkten Vergleich wird deutlich, dass die mikrofluidisch hergestellten Nanopartikel zum einen kleiner und zum anderen homogener in ihrer Größenverteilung sind. Für Silber wurden mikrofluidisch 4,7 (± 0,6) nm große Seeds anstelle von 6,1 (± 2,5) nm erreicht und für Gold konnten mittels DFM 2,91 (± 0,7)[r] nm große Seeds anstelle von 3,56 (± 0,9)[r] nm großen aus dem Batchverfahren synthetisiert werden. Darüber hinaus konnte gezeigt werden, dass sich auch die SF-Methode als weiteres mikrofluidisches Verfahren zur Partikelsynthese eignet. Mit 2,55 (± 0,6)[r] nm konnten auch hier sehr kleine und homogene Seedpartikel aus Gold hergestellt werden. Dabei hat der mikrofluidische Ansatz des SF Vor- und Nachteile. Beispielsweise werden

---

[r] Die Halbwertbreite (FWHM) wurde über die folgende Beziehung in die Standardabweichung (σ) umgerechnet: $FWHM = 2\sqrt{2 * ln\,2}\ \sigma$
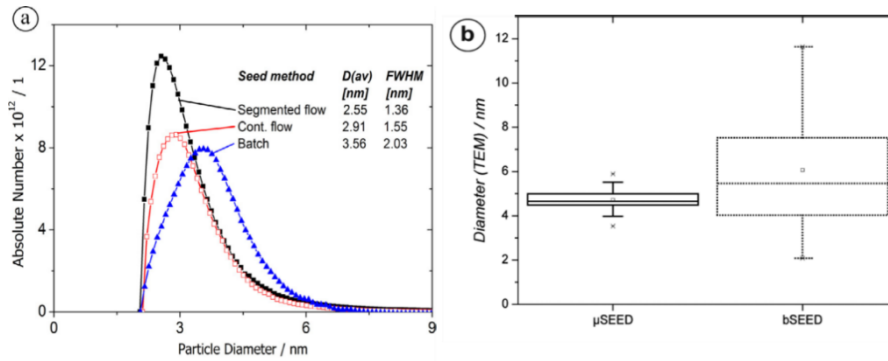
Abbildung 9: *Vergleich mikrofluidisch (µSEED) und nach klassischem Batchverfahren (bSEED)) hergestellter Seedpartikel. Für Gold (a) wurden die Größen mittels Dichtegradientenzentrifuge (DCS) ermittelt und für Silber (b) wurden TEM-Bilder ausgewertet. [MT2 & MT3]*

durch das Mehrphasensystem kleine Reaktionskammern im Bereich von 200 nl erzeugt, so dass eine größere Produktion langwierig ist und die aufgesammelten Phasen nach der Synthese noch separiert werden müssen. Vorteilig ist jedoch, dass die in sich geschlossenen wässrigen Segmente dabei vollständig von der organischen Phase abgeschirmt werden, so dass es nicht zum Ablagern von Material an den Kanalwänden und damit zum Zusetzen des Kanals (*Reaktorfouling* [143]) kommen kann. Beim Verwenden des DFM hingegen kommen, aufgrund der negativen Oberflächenladung der Kanalwände, sämtliche in der Lösung enthaltenen Spezies mit ihr in Berührung, wodurch diese für die positiv geladenen Metallionen als Kristallisationskeim fungiert [119, 144]. Folglich kommt es, wie in Abbildung 10b für die Herstellung von Goldkeimen gezeigt, zu Ablagerung an den Kanalwänden. Dabei tritt jedoch keine vollständige Blockierung des Kanals auf, sondern lediglich eine Verengung des Kanalquerschnitts. Für die Herstellung von Silberseeds konnte so eine 10-%-ige Verringerung des Durchmessers nach 12 min Synthese und 50 ml hergestellten Silberkeimen festgemacht werden. Die Kanalverkleinerung fördert dabei zwar aufgrund der erhöhten Fluidgeschwindigkeit die Durchmischung (Ansteigen von Re- und De-Zahl) und kann mit Aqua Regia regeneriert werden, jedoch bleiben der Materialverlust und die damit einhergehende Minimierung der Partikelausbeute. Der Prozess des Reaktorfoulings konnte jedoch erfolgreich unterbunden werden, indem den Reaktionslösungen Tenside, wie CTAB oder CTAC, zugegeben wurden. Beide Tenside bestehen aus einer Alkylgruppe mit 16 Kohlenstoffatomen (hydrophober Teil) sowie einer quartären Ammoniumverbindung (hydrophiler Teil), die als Gegenion Bromid (CTAB) oder Chlorid (CTAC) hat. Die hydrophilen Köpfe des Surfaktants lagern sich an der Glasoberfläche an und passivieren die Kanalwandungen. Das Resultat ist in Abbildung 10 a dargestellt, wo auch nach mehr als 10-minütiger kontinuierlicher Synthese die Mischzone transparent und folglich ohne Ablagerungen bleibt. Darüber hinaus hat der Einsatz von Surfaktanten neben der Passivierung der Kanaloberfläche das Potenzial zur Herstellung formanisotroper Nanopartikel, worauf im folgenden Kapitel näher eingegangen wird.
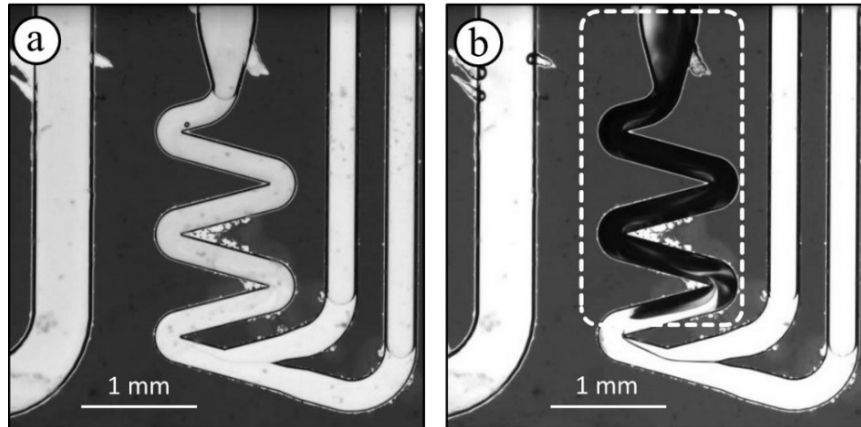
Abbildung 10: *Mischzone des Dean-Flow-Mischers nach über 10-minütiger Synthese von Goldkeimen. Die Flussraten und die verwendeten Chemikalien sind bis auf die Verwendung von 100 mM CTAC (a) und dessen Substitution mit Wasser (b) identisch. CTAC als Surfactant passiviert die Kanaloberflächen, so dass es nicht zu Goldablagerungen (schwarz gefärbter Bereich) im Kanal kommt. [MT3]*

3.3. Kombination verschiedener Synthesemethoden zur Herstellung formanisotroper plasmonischer Nanopartikel [MT2; MT3; MT4]

Bei der Synthese formanisotroper Metallnanopartikel laufen verschiedene Reaktionen ab. Neben der beschriebenen zeitlichen Trennung von Keimbildungs- und Wachstumsphase sind sowohl die Reihenfolge der Chemikalien, als auch ihre zeitliche Abfolge entscheidend. Trotz ihrer eingeschränkten Mischeffizienzen lässt sich bei klassischen Batchansätzen zumindest die Reihenfolge der Chemikalienzugabe durch schrittweises Pipettieren einfach realisieren. Aufgrund des kontinuierlichen Verfahrens muss für mikrofluidische Ansätze jedoch anders vorgegangen werden. Wie in den Abbildungen 7b und 7c dargestellt, ist es möglich einige Reaktanden bereits als Mastermix vorzumischen und damit die Spritzen zu befüllen. Generell entscheidend ist jedoch, dass die jeweilige Metallvorstufenverbindung und das Reduktionsmittel (für Seedpartikel Natriumborhydrid) räumlich voneinander getrennt sind und erst im Mischelement des Mikromischers miteinander in Kontakt kommen. Für die Herstellung von Silbernanoprismen, bzw. deren postsynthetische Prozessierung zu Goldnanorahmen, stellte sich jedoch heraus, dass diese Trennung nicht ausreicht. Zwar konnten, wie im vorherigen Kapitel beschrieben, mikrofluidisch kleine und homogene Seedpartikel hergestellt werden, jedoch ist hier für das weitere Wachstum entscheidend, dass die Keime bereits während der Synthese mit PSSS (*Poly sodium 4-styrenesulfonat*) als Facettenblocker inkubiert werden. Dabei ist zum einem wichtig, dass PSSS mit NaBH$_4$ reagieren kann, bevor Silberkeime gebildet werden und zum anderem, dass Citrat als Stabilisierungsreagenz vorliegt, sobald Nanopartikel entstanden sind. Die Chemikalienreihenfolge ist dementsprechend äußerst kritisch. Hinzu kommt, dass sich die zu verwendenden Volumina und Konzentrationen um eine Dimension, sowie die einzelnen Reaktionsgeschwindigkeiten drastisch
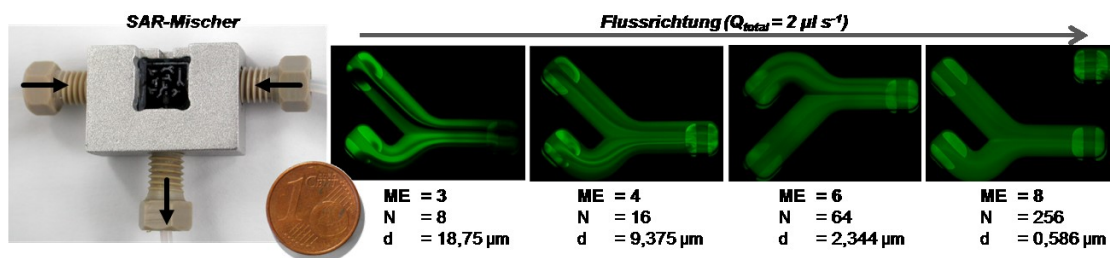
Abbildung 11: *Aufnahme des Split and Recombine (SAR) ROSAR-Mikromischers mit zugehörigen fortlaufenden Multilaminationsmustern für die Gesamtflussrate Q_{total} = 2 µl/ s. Nach jedem Mischelement (ME) wird die Lamellenzahl (N) verdoppelt und die Lamellenstärke (d) halbiert.*

unterscheiden. Um die Synthese jedoch in einen kontinuierlichen mikrofluidischen Prozess zu überführen war es nötig, den Syntheseprozess um einen Schritt zu erweitern. Dementsprechend wurde ein Vormischprozess initiiert, der die im Sekundenbereich liegende schnelle Reaktion von PSSS mit $NaBH_4$ bei geringer Flussrate effizient mischt, sowie die mäßig schnelle Reaktion von TSC (*Trinatriumcitrat*) und $AgNO_3$ (*Silbernitrat*) unter hoher Gesamtflussrate vermischt und damit reaktive Zwischenprodukte erzeugt (eine Übersicht der Edukte und Flussraten befindet sich in Tabelle 2 aus der Publikation [MT2]). Weil die Mischung von TSC mit $AgNO_3$ als verhältnismäßig unkritischer Prozess angesehen werden kann, konnte hier ein einfacher T-Mischer verwendet werden, dessen Reynoldszahl mit ca. Re = 190 ausreicht, um die beiden Edukte zu mischen. Anders verhält es sich dagegen beim Mischen von PSSS und $NaBH_4$, wo aufgrund der geringen Flussraten ein T-Mischer oder ein DFM ineffizient ist. Hier eignet sich ein Multilaminationsmischer, dessen Vorteil im effektiven Mischen von Chemikalien mit langsamen Flussraten liegt (siehe Kapitel 2.3). Die Ergebnisse der empirischen Ermittlung in Abbildung 11 zeigen, dass der SAR ROSAR-Mikromischer bereits bei einer Gesamtflussrate von 2 µl/s zwei Substanzen effektiv miteinander mischt. Erkennbar ist diese Mischung am Ausbleiben der charakteristischen Laminationsmuster und der damit einhergehenden homogenen Chemikalienverteilung nach 8 Mischelementen. Nach der Erzeugung der beiden reaktiven Zwischenprodukte ist der nächste Schritt die eigentliche Synthese der Silberseedpartikel. Dabei besteht die Herausforderung darin, die unterschiedlichen Flussraten der beiden Intermediate (das Flussratenverhältnis beträgt etwa 18) zu handhaben und somit $NaBH_4$ und $AgNO_3$ effektiv miteinander zu mischen, ohne dass es zur Transportlimitierung[s] kommt. Hier eignet sich wiederum der DFM, bei dem eine Gesamtflussrate von mindestens 30 µl/s anliegen muss (Abbildung 8). Im Vergleich zu anderen Mischern hat der DFM dabei den Vorteil, dass lediglich eine der beiden zulaufenden Flussraten hoch sein muss, um die sekundären Wirbel auszubilden, während die andere wesentlich geringer sein kann. Mit dem beschriebenen mikrofluidischen System, bestehend aus drei verschiedenen

---

[s] Bei der Transportlimitierung läuft die chemische Reaktion schneller ab, als neues Material zur Verfügung gestellt werden kann. Der limitierende Faktor des Umsatzes ist nicht die Reaktion, sondern der Transport.
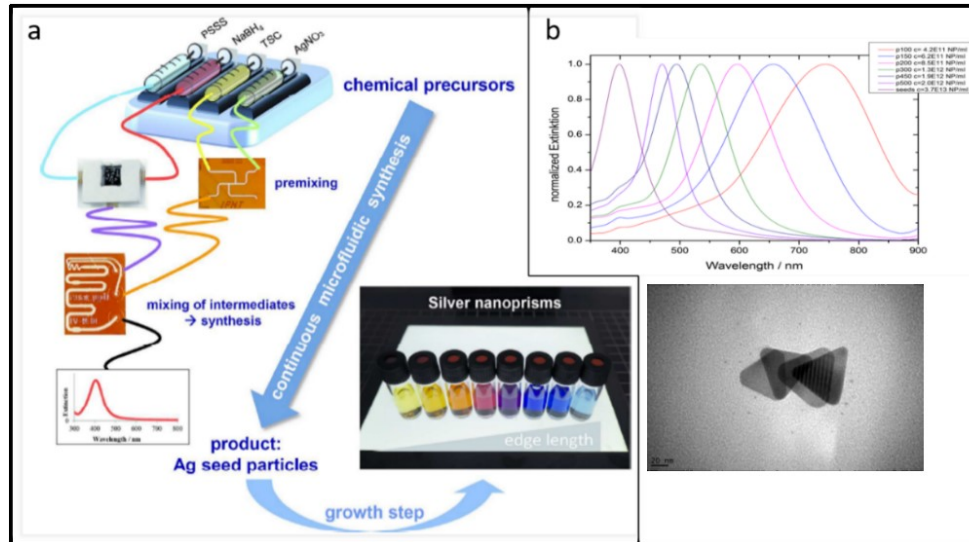
Abbildung 12: *Das Gesamtsystem zur Herstellung von Silberprismen besteht aus zwei Stufen: 1. Die kontinuierliche mikrofluidische Synthese der Seeds teilt sich dabei erneut in einen Vormischprozess, bestehend aus zwei Mikromischern (SAR und T-Mischer) und den eigentlichen Syntheseprozess unter Verwendung des Dean-Flow-Mischer (DFM) auf. 2. Bei der anschließenden Wachstumsstufe im Becherglas (Batch) wachsen die Seeds zu Silberprismen (a). Durch Verwendung unterschiedlicher Seedkonzentrationen kann die Größe und damit auch die spektrale Lage (bzw. die Farbe) der kolloidalen Lösung systematisch eingestellt werden. Dabei gilt, je weniger Seeds eingesetzt werden, desto Länger wird die Kantenlänge der Silberprismen, was zu einer Rotverschiebung der LSPR-Bande führt (b).*

Mikromischern, ist es möglich, definierte und kleine Silberseedpartikel, mikrofluidisch zu erzeugen (Abbildung 9b) und diese anschließend zu Silberprismen mit definierten Kantenlängen und definierter LSPR-Bande wachsen zu lassen. Anders als die Synthese der Seeds ist das Wachstum zu Prismen ein reaktionslimitierter[t] Prozess (>30 s), der lediglich eine moderate Mischung erfordert, weil hier ein recht mildes Reduktionsmittel (Ascorbinsäure) verwendet wird. Daher ist es sinnvoll und ausreichend, diesen Prozess im Batchreaktor durchzuführen. Mit den mikrofluidisch hergestellten Seedpartikeln lassen sich verschieden große Silberprismen reproduzierbar herstellen, deren spektrale Lage und damit auch Größe mit der zum Wachstum verwendeten Seedpartikelmenge korreliert (Abbildung 12). Für seedbasierte Wachstumsprozesse gilt dabei generell, je kleiner die Menge der verwendeten Seeds bzw. deren Konzentration bei sonst gleichen Bedingungen ist, desto größer werden die aus ihnen resultierenden Nanopartikel. Auffällig ist jedoch, dass die Ausbeute von Silberprismen, die mittels µSEEDs hergestellt wurden, wesentlich höher ist (93%) als jene mittels bSEEDs (70%). Das Gesamtsystem zur Silberprismenherstellung ist schematisch in Abbildung 12a dargestellt und beruht letztendlich auf dem Zusammenspiel von CF betriebenen mikrofluidischen Prozessen (drei verschiedene Mikromischer) und dem klassisch chemischen Ansatz im Batchreaktor. Aus diesem Resultat ergibt sich die Annahme, dass eine Kombination verschiedener Verfahren besonders für die Herstellung

---

[t] Als reaktionslimitiert wird ein Prozess bezeichnet, bei dem ein ständiges Überangebot an Material zur Verfügung steht. Der chemische Umsatz hängt nicht von Transport- oder Mischprozessen ab, sondern von der Reaktionskinetik.
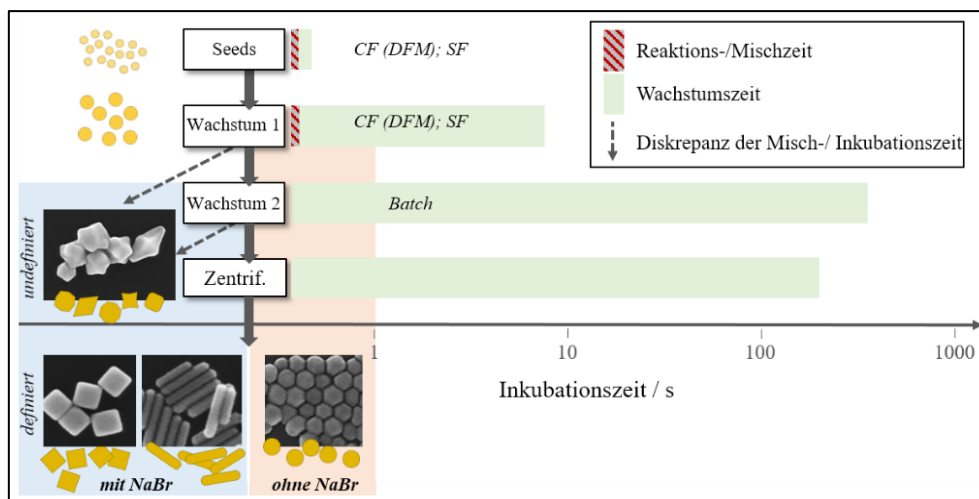
Abbildung 13: *Schema der Seed-basierten-Synthese von anisotropen Goldnanopartikeln. Da die Mischzeiten für die Seedsynthese sowie den ersten Wachstumsschritt (GS 1) im Bereich von Millisekunden liegen, sind mikrofluidische Verfahren dem klassischen Batchansatz vorzuziehen. Darüber hinaus erlauben diese eine genaue Einstellung der Verweilzeit über das Verhältnis Flussrate : Kanallänge und können somit reproduzierbare Inkubationszeiten frei von subjektiven Einflüssen gewährleisten. Das akkurate Einhalten der Inkubationszeiten in Kombination mit NaBr (blaue Box) stellte sich als kritischer Parameter für die Herstellung definierter anisotroper Nanopartikel heraus. Bei Nichtbeachten der Inkubationszeit (gestrichelte Pfeile) kommt es zu undefinierten Partikelformen, wobei das Auslassen von NaBr im zweiten Wachstumsschritt zu quasisphärischen Nanopartikeln führt (orange Box). Der zweite Wachstumsschritt umfasst indes mehrere Minuten und kann effizient im Batch realisiert werden.*

formanisotroper Nanopartikel wesentlich effizienter ist als die strikte Prozessierung der Schritte mit dem gleichen Verfahren. Deutlich wird dieser Effekt weiterhin anhand der logarithmischen Zeitskala in Abbildung 13 für die komplexe Herstellung von Goldnanowürfeln (und anderen anisotropen Goldnanopartikeln, siehe Kapitel 3.4). Das Schema fasst anschaulich zusammen, dass sich die einzelnen Reaktionsschritte für die Herstellung der Goldnanowürfell hinsichtlich Inkubationszeit um mehrere Dimensionen unterscheiden. Da Mikromischer jedoch für die effiziente Durchmischung und Kontrolle von schnellen Reaktionen konzipiert werden, können sie ihre Vorteile bei Reaktionen im Minutenbereich nicht ausspielen. Beispielsweise sollte die Seedsynthese, wie in Kapitel 3.2 beschrieben, innerhalb von 100 ms erfolgen und konnte effizient mikrofluidisch (mittels DFM und SF) umgesetzt werden. Das anschließende Mischen der Seeds mit der ersten Wachstumslösung (GS 1) erzeugt angereicherte Seeds, von denen ein kleiner Teil nach einigen Sekunden in einen zweiten Wachstumsansatz (GS 2) übertragen wird [145]. Dabei wird für den Transfer der angereicherten Seeds in GS 2 das gleiche Volumen genutzt, welches ursprünglich auch für die Seeds verwendet wurde. Da es sich hierbei um nur wenige Mikroliter handelt (25 µl bis 100 µl abhängig von der zu erreichenden Partikelgröße), kann jedoch nahezu der gesamte 10 ml GS 1-Ansatz (beinhaltet $HAuCl_4$) aufgrund der Überschreitung der Inkubationszeit nicht zur weiteren Prozessierung verwendet werden. Allein aus ökonomischer Sicht sind mikrofluidische Verfahren für diesen Schritt besonders geeignet, weil das aktivierte Volumen (Mischung aus Seeds, Reduktionsmittel und $HAuCl_4$) von GS 1 durch die miniaturisierten Kanäle
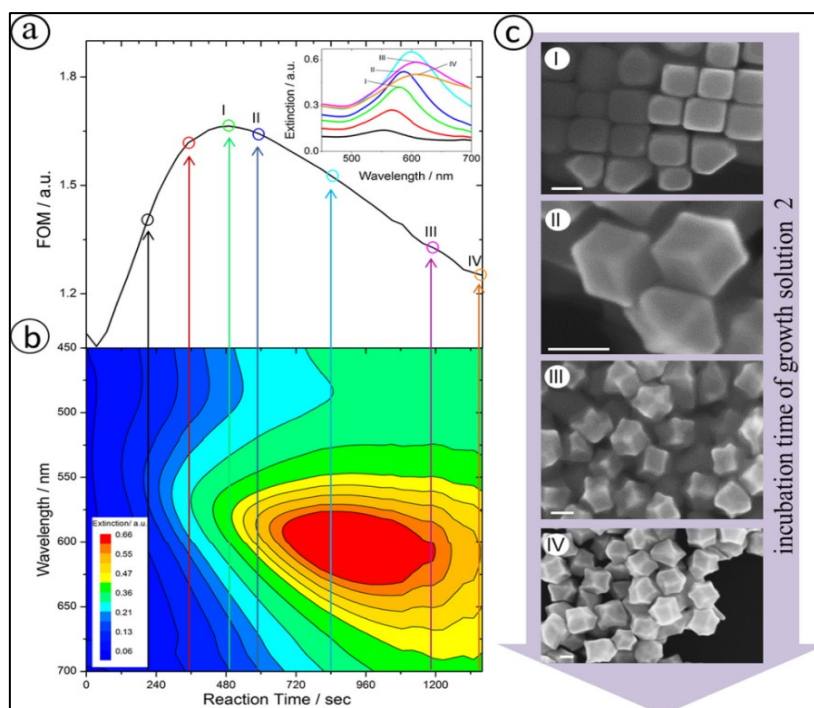
Abbildung 14: *Die Kinetik des zweiten Wachstumsschrittes (b) ist schwer zu verifizieren ist, sodass aus den Einzelspektren ein Bewertungsfaktor (FOM) erzeugt wurde (a). Dessen Korrelation mit den zugehörigen REM-Bildern (c) erlaubt zukünftig eine rein spektroskopische Einschätzung der auszubildenden Würfelform. Für einzelne diskrete Werte der FOM sind die Spektren extrahiert im Insert dargestellt (farbliche Zuordnung), wobei an den Positionen I bis IV die jeweiligen REM-Bilder (Maßstabskala entspricht 50 nm) die Entwicklung der Goldnanopartikel darstellen. [MT3]*

wesentlich geringer ist und besser kontrolliert werden kann als beim Batchprozess. Beim SF-Verfahren verhält sich jedes Segment wie ein einzelner, aber miniaturisierter Batchreaktor mit einem Volumen von etwa 200 nl. Der Aufbau ist dabei ähnlich wie für die Seedsynthese (Abbildung 7c), jedoch unter Verwendung anderer Chemikalien (siehe Tabelle 1 in [MT3]). Beim CF-Verfahren unter Verwendung des DFM als Mikromischer (Abbildung 16a) mit einem etwa 100 nl großen Volumen des Mäanders kann eine effiziente Initialmischung realisiert werden, wodurch GS 1 aktiviert wird. Bei beiden mikrofluidischen Verfahren kann die Verweilzeit[u] über die Kanallänge mit Bezug zur Flussrate sehr genau eingestellt werden. Dadurch sind sowohl CF als auch SF frei von subjektiven Einflüssen und zeichnen sich durch hohe Reproduzierbarkeit aus. Dadurch konnte wiederum für den zweiten Wachstumsschritt gezeigt werden, dass es, nachdem GS 2 mit den angereicherten Seeds aus GS 1 okuliert wurde, lediglich eine Initialmischung erfordert um die Goldnanowürfel herzustellen. Entscheidend ist dabei die Gewährleistung der idealen Inkubationszeit von 8 - 10 min. Wie in Abbildung 14 dargestellt ist, konnte die optimale Inkubationszeit aus der Korrelation der Kinetik für GS 2 (alle 35 s Aufnahme eines Spektrums) mit

---

[u] Die Verweilzeit gibt die Dauer eines definierten Flüssigkeitsvolumens in einer Anlage (z.B. Mikromischer, miniaturisierter Kanal) an.

den zugehörigen REM-Bildern ermittelt werden. Um die Qualitätsaussagen hinsichtlich Formausprägung zu vereinfachen, wurde aus den Einzelspektren ein Bewertungsfaktor[v] ermittelt, der eine rein spektroskopische Abschätzung der idealen Würfelform ermöglicht. Anhand der TEM-Aufnahmen ist ersichtlich, dass bei Nichteinhalten der Inkubationszeit die Formausprägung leidet, indem es entweder zu unvollständigen oder überwachsenen Goldnanowürfeln kommt. Der exakte Abbruch der Wachstumsreaktion von GS 2 ist somit essentiell und kann durch Zentrifugieren realisiert werden. Sowohl die Inkubationszeit von mehreren Minuten, was die Verwendung von Mikromischern unrentabel macht, als auch der Fakt der Zentrifugation sprechen an dieser Stelle für ein Batchverfahren. Somit können direkt einige Mikroliter des GS 1-Ansatzes in die mit GS 2 vorbereiteten Zentrifugenröhrchen überführt und die Zentrifuge auf die optimierten Zeiten programmiert werden. Das Gesamtsystem ist beispielhaft für das CF-Verfahren mittels DFM in Abbildung 16 a dargestellt. Mit beiden Kombinationen konnten erfolgreich und reproduzierbar Goldnanowürfel erzeugt werden was in Abbildung 15 für die Kombination SF und Batch sowie in Abbildung 18 für CF und Batch dargestellt ist. Damit konnte anhand von zwei Beispielen (Silberprismen und Goldnanowürfel) belegt werden, dass sich die postulierte Kombination verschiedener Methoden zur optimalen Synthese anisotroper Nanopartikel für deren Herstellung eignet. Im folgenden Kapitel wird näher auf die Vorteile und neuen Möglichkeiten eingegangen, die sich im Besonderen durch das Verwenden von Mikromischern für die Synthese plasmonischer Nanopartikel ergeben.

	I	II	III	IV
V_{Seeds}	100 µl	75 µl	50 µl	25 µl
λ_{max}	558 nm	566 nm	584 nm	608 nm
FWHM	91nm	99 nm	131 nm	181 nm
Stokes Diam.	67 ± 5 nm	77 ± 6 nm	85 ± 8 nm	94 ± 8 nm
Edge Length	54 ± 4 nm	62 ± 5 nm	68 ± 6 nm	76 ± 6 nm
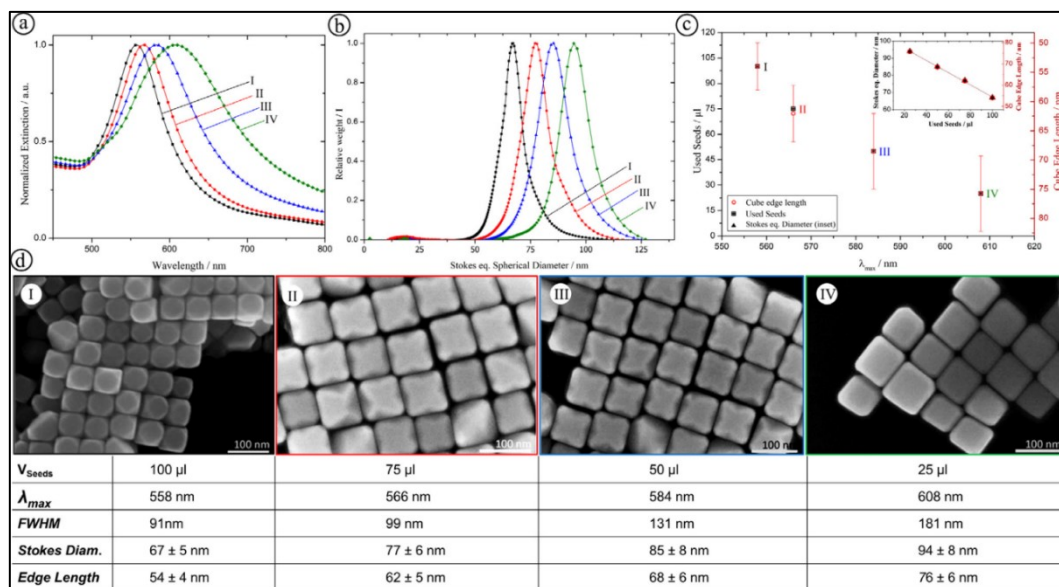
Abbildung 15: *LSPR-Spektrum (a), Größenverteilung basierend auf Dichtegradientenzentrifugation (DCS) (b) und deren Korrelation mit Bezug zu den eingesetzten Volumina der angereicherten Seeds von GS 1 (c) zur Herstellung verschieden großer Goldnanowürfel (d) mittels des Segmentierten Fluss-Verfahrens. [MT3]*

---

[v] Der Bewertungsfaktor (*Figure-Of-Merit, FOM*) ergibt sich aus der Extinktion am Maximum der LSPR-Bande, dividiert durch die Extinktion beim Mittelwert der LSPR-Bande.

3.4. Effizienzsteigerung durch Mikrofluidik [MT3]; [MT4]

Die Verwendung von CTAB bzw. CTAC hat eine entscheidende Rolle bei der mikrofluidischen Prozessierung (siehe Kapitel 3.2). Darüber hinaus ist die Nutzung von Surfaktanten essentiell zur Herstellung von formanisotropen Metallnanopartikeln (siehe Kapitel 3.1 sowie Tabelle 1 in Kapitel 3.5). Weitere Parameter haben jedoch ebenfalls einen entscheidenden Einfluss, sowohl auf die Ausbildung der finalen Nanopartikelmorphologie als auch auf deren Ausbeute und Größe. Aufgrund der hohen Reproduzierbarkeit, der großen Flexibilität und der einfachen Bedienung ist das im Kapitel 3.3 etablierte und in Abbildung 16a dargestellte mikrofluidische System für die-Analyse essentieller Parameter zur anisotropen Nanopartikelherstellung prädestiniert. Zur Verdeutlichung sind die entsprechenden Parameter sowie ihr jeweiliger Einfluss durch grau hinterlegte Textfelder in Abbildung 16 hervorgehoben. Sie beziehen sich auf (I) die Inkubationszeit von GS 1 (Kanallänge), (II) die Konzentration der angereicherten Seeds hinsichtlich der finalen Partikelgröße (Tropfenanzahl) und (III) der Zusätze bezüglich der auszubildenden Partikelmorphologie (insbesondere NaBr). Durch die mikrofluidische Mischung der Edukte im DFM lassen sich
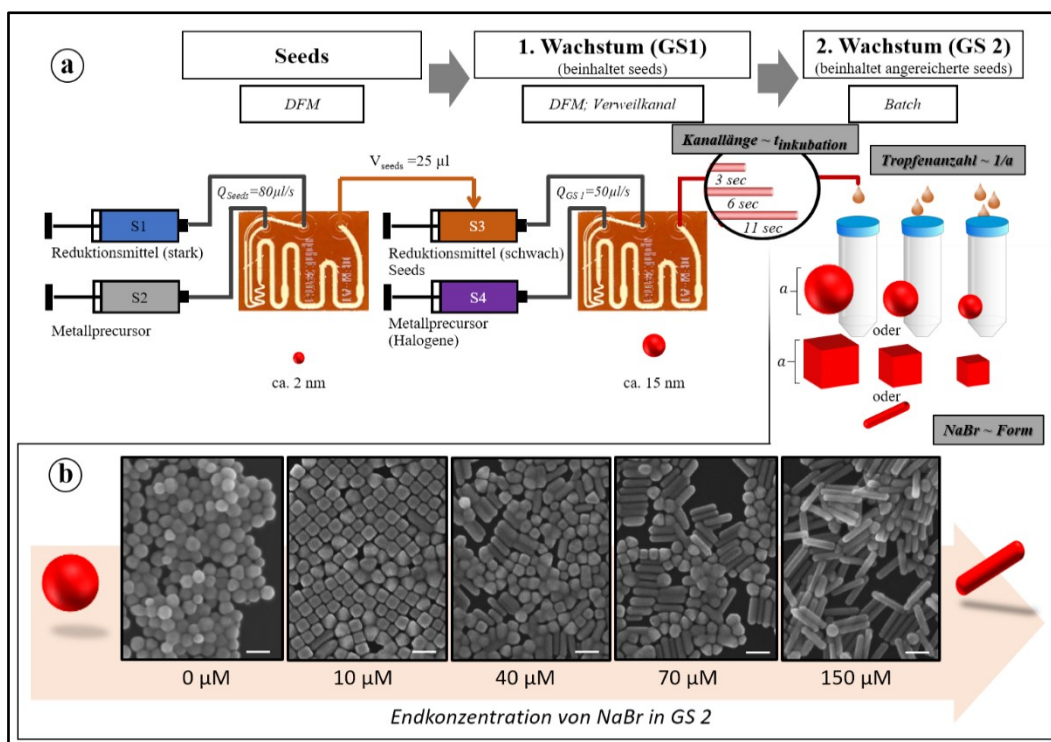

Abbildung 16: *Übersicht des vollständigen Aufbaus zur Synthese anisotroper Goldnanopartikel inklusive der zu untersuchenden Parameter (grau hinterlegte Textfelder). Die Herstellung ist in drei aufeinander aufbauende Stufen untergliedert, wobei die Synthese wie auch der erste Wachstumsschritt effizient mittels DFM realisiert wird. Die Kombination aus DFM und anschließendem Verweilkanal erlaubt für die erste Wachstumsphase ein reproduzierbares Einstellen verschiedener Inkubationszeiten, bevor die angereicherten Seeds in die zweite Wachstumslösung getropft werden. Dabei kann über die Tropfenanzahl die resultierende Größe der Nanopartikel kontinuierlich variiert werden (a). Über die NaBr-Konzentration in der zweiten Wachstumslösung lässt sich weiterhin die Partikelmorphologie (quasisphärisch, Kubus, Stäbchen) einstellen, so dass sich sowohl die Form wie auch die Größe der Nanopartikel parallel durchstimmen lassen. Die Maßstabskala in den REM-Bildern beträgt 100 nm (b).*

gezielt geringe Volumina angereicherter Seeds herstellen (wenige Mikroliter), die, entgegen dem Batchansatz (einige Milliliter), fast vollständig für das weitere Wachsen aufgebraucht werden und darüber hinaus frei von subjektiven Befindlichkeiten direkt in GS 2 getropft werden können. Da es sich um eine optimale Mischung handelt (siehe Kapitel 3.2), ist die Einstellung der Inkubationszeit der angereicherten Seeds einfach, effizient und sehr genau mit Hilfe eines Verweilkanals nach dem eigentlichen Mischelement (Mäander) möglich. Bei konstanter Gesamtflussrate lässt sich somit durch Längenveränderung des Verweilkanals die Durchflusszeit der aktivierten GS 1 und damit auch die Inkubationszeit der angereicherten Seeds systematisch variieren. Der stetige Abbruch der Reaktion wird schließlich durch den Transfer der angereicherten Seeds in den GS 2 Ansatz realisiert. Unter Verwendung mehrerer GS 2 Mastermixansätze wird somit aufgrund der kontinuierlichen Herstellung angereicherter Seeds und der systematisch mikrofluidisch bedingten Einhaltung ihrer Inkubationszeiten eine hohe Effizienz bei maximaler Reproduzierbarkeit erreicht. In Abbildung 17 ist der zeitliche Verlauf und damit die Entwicklung der angereicherten Seeds (aktivierte GS 1) bezüglich der Formausbeute zu Goldnanowürfel dargestellt. Ohne Transfer in GS 2 resultiert dieser Zwischenschritt in 15 nm große GS 1 Nanopartikel, wobei deren Kinetik (gemessen am LSPR-Maximum bei 523 nm) auf einen exponentiellen Verlauf deutet, der nach ca. 60 min in ein Plateau übergeht. Durch die beschriebene Längenänderung des Verweilkanals konnten diskrete Inkubationszeiten realisiert und mittels REM-Bildern bezüglich der resultierenden Würfelform und -ausbeute korreliert werden. Anders als in der Literatur beschrieben [145], stellt sich dabei heraus, dass der optimale Zeitpunkt des Transfers in GS 2 nach ca. 7 Sekunden erfolgen sollte. Kürzere Inkubationen führen zum unvollständigen Wachsen, was sich in Goldnanowürfeln mit abgerundeten Ecken wiederspiegelt. Zu lange Inkubationszeiten resultieren dagegen in ein Überwachsene Goldnanopartikel. Für das Erreichen der optimalen Würfelform mit maximaler Ausbeute muss der Transfer demzufolge genau nach dem exponentiellen Anstieg der Extinktion (Abbildung 17) erfolgen. Reproduzierbar und damit frei von methodischen und subjektiven Einflüssen ist dieses Ziel nur mikrofluidisch zu erreichen und fließt als zentrales Resultat in den mikrofluidische Aufbau ein, indem der Verweilkanal auf 180 cm Länge eingestellt und somit eine Durchlaufzeit von 7,2 Sekunden erreicht wird. Die Effizienz und die Möglichkeiten des optimierten Aufbaus werden demonstriert, indem Goldnanowürfel mit verschiedenen Kantenlängen erzeugt werden. Im ursprünglichen Batchprotokoll mussten dafür beide Transferprozesse (Seeds in GS 1 und von dort erneut in GS 2) gleichermaßen geändert werden [145]. Das hat zur Folge, dass für jede Würfelgröße eine separate GS 1 hergestellt werden muss. Demzufolge müssen laut Protokoll für vier verschiedene Würfelgrößen insgesamt 40 ml GS 1 (4 Ansätze) bereitgestellt werden, wovon aber nur wenige µl gebraucht würden. Somit sind mehr als 99 % des GS 1-Ansatzes Überschuss und können aufgrund unkontrollierter Inkubationszeit nicht weiter verwertet
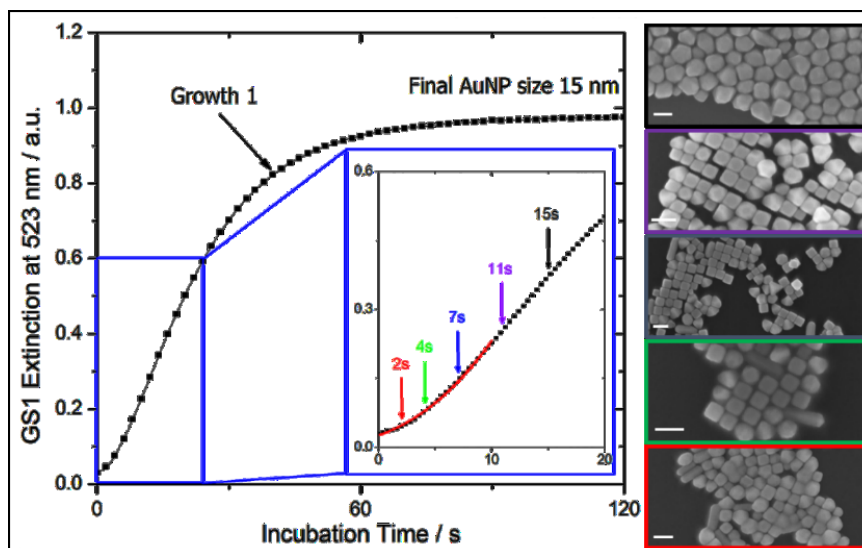
Abbildung 17: *Kinetik des Maximums der LSPR-Bande (523 nm) der ersten Wachstumsphase (GS 1) zur Herstellung von Goldnanowürfeln. Das Insert stellt die ersten 20 s vergrößert dar und markiert einzelne, durch den mikrofluidischen Aufbau exakt und reproduzierbar einstellbare Inkubationszeiten, nach denen die angereicherten Seeds in GS 2 überführt wurden, mit zugehörigen REM-Bildern (Maßstab entspricht 100 nm) nach 15 s, 11 s, 7 s, 4 s, und 2 s Inkubation. [MT4]*

werden. Mithilfe der mikrofluidischen Verfahren ist es jedoch möglich, dass ausschließlich der zweite Transfer variiert werden muss, um die Größe der zu erhaltenden Nanowürfel einzustellen (Abbildung 15 für SF-Verfahren). Es wird immer dieselbe Seedmenge (25 µl im Ansatz) verwendet, um GS 1 zu aktivieren, jedoch das Volumen der entstandenen angereicherten Seeds nach GS 2 verändert, indem die Tropfenanzahl (9 µl pro Tropfen beim CF-Verfahren) variiert wird. Dieses Resultat ist nicht in einen Batchansatz übertragbar, da man zur exakt gleichen Zeit alle vier verschiedenen Volumina aus der einen GS 1 in die vier GS 2 transferieren müsste, um die Inkubationszeit konstant zu halten. Darüber hinaus würde es bei dem beschriebenen hohen Chemikalienausschuss von GS 1 bleiben, wobei insbesondere die Ressource Gold (in Form von HAuCl$_4$) für weitere Prozesse unverwertbar ist. Allein dieser ökonomische wie auch ökologische Aspekt spricht für die Effizienz des in Abbildung 16 beschriebenen mikrofluidischen Aufbaus, bei dem in lediglich einem Prozessdurchlauf die Kantenlängen und damit die LSPR-Position der entstehenden Goldnanowürfel durchgestimmt werden kann (Abbildung 20), ohne das überflüssige GS 1-Ansätze entstehen.

Weiterhin spielen Additive eine entscheidende Rolle bei der Ausprägung anisotroper Formen der Nanopartikel (siehe Tabelle 1 in Kapitel 3.5). So konnte bei dem Versuch, ausschließlich CTAC für die Goldnanowürfelsynthese zu verwenden, ausnahmslos Goldsphären hergestellt werden, die sich bezüglich ihrer Größeneinstellung jedoch exakt so verhielten wie die Nanowürfel. CTAC spielt zwar eine entscheidende Rolle hinsichtlich mikrofluidischer Prozessierung, jedoch scheint es allein nicht auszureichen, um anisotropes Wachstum zu erzeugen. Durch die Herstellung der Goldsphären und der Goldwürfel kann das mikrofluidische System generell als Plattform zur

Herstellung verschiedener plasmonischer Nanopartikel validiert werden. Darüber hinaus eröffnet es jedoch eine effiziente Möglichkeit zur Parameteruntersuchung (*Screening*) bezüglich der Formkontrolle von Nanopartikeln. Die Kombination aus CTA^+ basierter Nanopartikelsynthese und der mikrofluidischen Plattform stellt ein ideales Modelsystem für die gezielte Analyse verschiedener Gegenionen hinsichtlich Partikelmorphologie dar. Bei sonst identischen Prozessbedingungen wurden dafür vier verschiedene Halogenide (NaF; NaCl; NaBr; NaI) der zweiten Wachstumslösung (GS 2) zugegeben. Die Ergebnisse in Abbildung 18a verdeutlichen, dass weder Fluorid noch Chlorid oder Iodid anisotropes Wachstum induzieren können, selbst wenn die Konzentration erhöht wird. Iodid adsorbiert unspezifisch, Chlorid bindet zu schwach und Iodid wiederum zu stark auf der Goldoberfläche. Ausschließlich durch Bromid als Gegenion konnte dadurch die Würfelform erreicht werden. Durch zu hohe NaBr-Konzentration kommt es jedoch zu weiteren, teilweise undefinierten Partikelpopulationen. Um den Effekt von Br^- auf die Formanisotropie weiter zu untersuchen, wurden sowohl der ersten Wachstumslösung (GS 1) wie auch der zweiten Wachstumslösung (GS 2) verschiedene NaBr-Konzentrationen zugeführt und die Ergebnisse in Abbildung 18b gegeneinander aufgetragen. Wie zu erwarten war, kommt es ganz ohne NaBr ausschließlich zu sphärischen Goldnanopartikeln. Doch entgegen der Inkubationszeit von GS 1 spielt die NaBr Konzentration hier für die Ausbildung von Goldnanowürfeln eine untergeordnete Rolle. Deutlich wird das daran, dass sich selbst bei höheren NaBr-Konzentrationen keine Würfel erzeugen lassen, sofern nicht wenigstens geringe Bromidmengen in GS 2 vorhanden sind. Andersherum lassen sich jedoch auch Goldnanowürfel erzeugen, wenn NaBr ausschließlich in GS 2 vorhanden ist. Dadurch ist NaBr in GS 1 scheinbar überflüssig, wodurch wiederum die gesamte Synthese vereinfacht wird. Darüber hinaus lässt sich durch die NaBr-Konzentration in der zweiten Wachstumslösung (GS 2) die Kantenschärfe der Goldnanowürfel sehr fein einstellen. Bei zu hoher Konzentrationen (50 µM) treten jedoch neue, undefinierte Partikelpopulationen auf. Durch die sukzessive weitere Steigerung von NaBr bis 150 µM in GS 2 kommt es schließlich zur Ausbildung von Goldnanostäbchen. Ähnliches konnten bereits Garg und Kollegen 2010 für Nanostäbchen zeigen, als sie den Zusammenhang zwischen dem Aspektverhältnis der Stäbchen und der NaBr-Konzentration untersuchten. In ihrer Studie, die sich auf lediglich einen Wachstumsschritt bezieht, waren jedoch Bromidkonzentrationen von mindestens 20 mM und geringe Konzentrationen von Sibernitrat erforderlich um überhaupt Nanostäbchen zu erzeugen [146]. Anders als bei Garg und in der weiteren Literatur beschrieben, erfolgt die Stäbchenbildung in der vorliegenden Arbeit, ganz ohne die als essentiell bezeichnete, aber bis dato unklare Bedeutung von Silberionen [147]. Damit ist gezeigt, dass NaBr nicht nur das Aspektverhältnis von Nanostäbchen, sondern generell die Partikelmorphologie effizient steuert und dass durch dessen Variation präzise zwischen der sphärischen, der kubischen und der Stäbchenform gewechselt wer-

den kann. Voraussetzung ist jedoch die stabile und reproduzierbare Prozessführung, die durch die mikrofluidische Plattform realisiert wird. Mit einem Prozessdurchlauf können somit drei verschiedene Partikelspezies innerhalb weniger Minuten erzeugt werden (Zusammengefasst in Abbildung 16b), ohne dass überschüssige und unbrauchbare Goldlösung entsteht. Dabei ist die Verwendung von CTAC anstelle von CTAB entscheidend. CTA$^+$ ist zur Kanalpassivierung hinsichtlich mikrofluidischer Prozessierung essentiell und Chlorid als dessen Gegenion hat keinen Einfluss auf die Formausprägung. Nur dadurch kann die Bromidkonzentration in GS 2 sehr fein eingestellt und damit die entstehende Nanopartikelmorphologie sensibel justiert werden. Damit profitieren sowohl die Herstellung der Gold- wie auch der Silbernanopartikel durch die sinnvolle Kombination der Verfahren. Deutlich wird das an der wesentlich erhöhten Ausbeute an Silberprismen sowie an der vereinfachten und parallelen Synthese verschiedener Goldnanopartikel mittels der mikrofluidischen Plattform. Beides kann mit rein klassischen Batchverfahren nicht erreicht werden. Besonders jene Prozessschritte, die in ein mikrofluidisches Verfahren überführt wurden, oder direkt davon abhängen, konnten auf die Vorteile der Mikrofluidik aufbauen und somit die gesamte Nanopartikelherstellung verbessern. Die Parallelversuche ausschließlich im Batch zeigen dabei die Limitationen des klassischen Verfahrens, wobei der direkte Vergleich wiederum die Leistungsfähigkeit der mikrofluidischen, bzw. kombinatorischen Ansätze verdeutlicht. Im folgenden Kapitel wird schließlich auf die optischen Eigenschaften der plasmonischen Nanopartikel, deren Modifikation und das Potenzial in der Sensorik eingegangen.
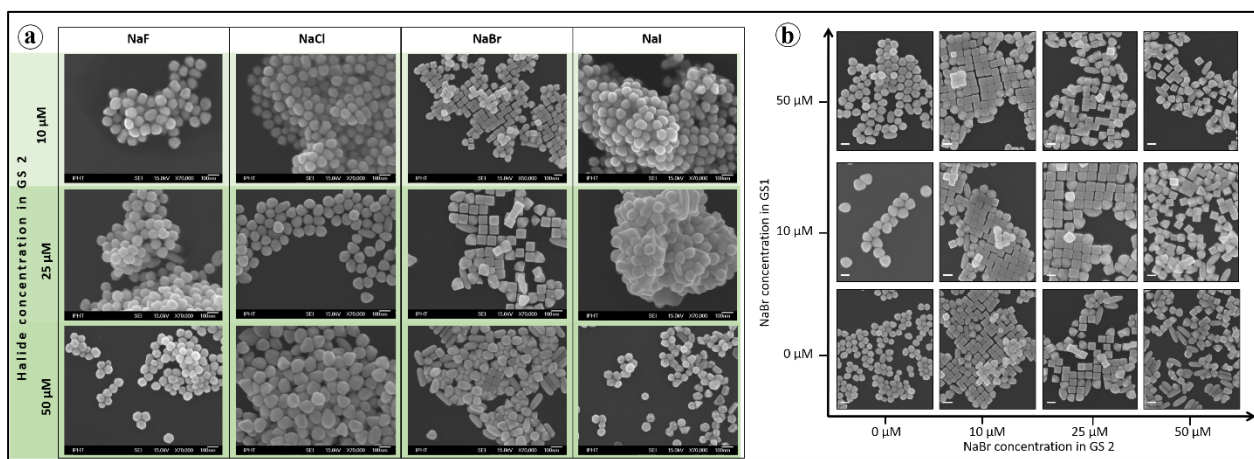

Abbildung 18: *Übersicht von REM-Aufnahmen zum Einfluss von Halogeniden in GS 2 bezüglich der resultierenden Form von Goldnanopartikeln (a). Gegenüberstellung verschiedener NaBr-Konzentrationen in GS 1 sowie GS 2. Der Maßstab entspricht 100 nm (b). [MT4]*

3.5. Postsynthetische Stabilisierung und Anwendung formanisotroper meNP hinsichtlich sensorischer Applikationen [MT1 - MT7]

Neben dem Einfluss der Liganden auf die Partikelmorphologie wirken sich diese und weitere Zusätze auch auf die Stabilität der Partikelsuspensionen und besonders auf die optischen Eigenschaften der Nanopartikel aus. In Tabelle 1 sind die Effekte verschiedener Liganden auf die intrinsischen Faktoren sowie auf die Zusammenhänge bezüglich optischer Resonanz (LSPR) und Stabilität zusammengefasst. Die postsynthetische Prozessierung der entstandenen Nanopartikel ist dabei abhängig vom jeweiligen Einsatzgebiet und kann vom galvanischen Ätzen bis zur gezielten Oberflächenmodifizierung reichen. Unter anderem konnten in dieser Arbeit die in Tabelle 1 grün markierten Verfahren und Chemikalien für postsynthetische Prozesse verwendet werden. Vor allem der Ligandenaustausch spielt bei anisotropen Nanopartikeln eine entscheidende und kritische Rolle. Die Partikeloberfläche muss frei von Surfaktanten sein, damit die Nanopartikel auf Oberflächen immobilisiert und chemische Ereignisse oder Moleküle detektiert werden können. Dabei können Liganden oder Moleküle, die das optische Verhalten der plasmonischen Nanopartikel verändern, umgekehrt durch eben diesen Prozess auch detektiert werden. Solange es zur Verschiebung des LSPR-Signals kommt, ist es dabei egal, ob die Liganden die Nanopartikel lediglich umgeben (S_S) oder sich direkt an deren Oberfläche anlagern bzw. anbinden (S_B). Für biosensorische Anwendungen steht dabei die Funktionalisierung der Nanopartikel mit biologischen Molekülen (z.B. DNA, RNA, Proteine, Aptamere) im Vordergrund, wobei verschiedene Strategien angewendet wurden (siehe Tabelle 1 und 2 in [MT1]). Dadurch können unter anderem einfache Vor-Ort-Analysen (*Point-of-Care, POC*) etabliert werden, die das chemisches Event (z.B. eine Nachweisreaktion) aufgrund der Farbänderung der Partikelsuspension (Kolorimetrie) detektieren. Die plasmonischen Nanopartikel fungieren dabei generell als optischer Transducer, indem sie extrem sensibel auf Brechungsindexänderungen in der Partikelumgebung durch Verschieben des LSPR-Signals reagieren. Neben kolorimetrischen Sensoren in Wellplatten und anderen Reaktionsgefäßen, konnte dieses Sensorprinzip erfolgreich in Lichtwellenleiter überführt werden. Dafür wurden die plasmonischen Nanopartikel an *getaperten* (verjüngten) optischen Fasern (Abbildung 19a) sowie auf die Kerne von *suspended-core-fibers* (SCF, kernfreihängende optische Faser, Abbildung 19b) immobilisiert. Durch die kernumgebenden freien Kanäle der SCF können, wie in Abbildung 19b skizziert, Fluide entlang des lichtleitenden Kerns gepumpt werden, so dass eine integrierte neuartige optofluidische Sensorplattform entsteht. Generell entscheidend für das sensorische Potenzial ist dabei die Sensitivität S der jeweiligen Nanopartikel (siehe Kapitel 2.1). Goldsphären mit einem Durchmesser von 80 nm haben eine Bulk-sensitivität (S_B) von 104 nm/RIU. Dagegen weisen Goldnanowürfel mit einer Kantenlänge von ebenfalls etwa 80 nm eine S_B von ca. 200 nm/RIU auf (siehe Abbildung 8 in [MT3]).

Tabelle 1: Übersicht zu Stabilisierungs- und Beschichtungsmaterialien für plasmonische Nanopartikel und deren Effekte. In Grün die in der Promotion verwendeten Materialien

Beschichtungs-/ Ligandenmaterial	Effekt auf die Nanopartikel bzw. die Suspension:	
	Form, Größe & Zusammensetzung	*Optisch & Stabilisierung*
ORGANISCH		
Monomer		
Kleine geladene Moleküle		
• Natriumcitrat	Größe sehr gut, Form bedingt einstellbar	Ladungsstabilisierung
• Penicillamin	geringer Größeneinfluss	Interpartikelabstand pH-Wert abhängig reversibel
Surfactant		
• CTAB; CTAC; MTAB	Formausprägung; Größe; Aspektverhältnis	Stabilisierung; Monolayerbildung; Orientierung (bei Immobilisation)
• DDT	Größe	
• SDS	Formausprägung	
• Oleyamine	Formausprägung, Aspektverhältnis	
• Gemini surfactant	Formausprägung	Orientierung, Assemblierung
Polymere		
nicht Ionisch		
• PEG; PVA; PE	-	Stabilisierung; Ligandenaustausch
• PVP	Formausprägung	
• PNIPAM; POEGMA	-	Interpartikelabstand Temperatur-/ pH-abhängig reversibel
ionisch		
• Polyelektrolyte, PSSS	Formausprägung	LBL-Sensorik, Interpartikelabstand ist pH-Wert abhängig
• PDDA (Polyolmethode)	Formausprägung	Stabilisierung
• Proteine und Peptide	-	Interpartikelabstand pH-Wert abhängig reversibel, Erkennungselement für LSPR-Sensorik
• DNA & Oligonukleotide	-	Interpartikelabstand, Erkennungselement für LSPR-Sensorik
ANORGANISCH		
Dielektrisch	-	
• SiO$_2$	-	Stabilisierung und Änderung des RI → Verschiebung und Dämpfung von LSPR
• Halbleiter	-	
Metalle		
• Silber*	Legierung, Kern-Hülle Strukturen	LSPR-Verstärkung, hypsochrome Verschiebung, multiple LSPR-Banden
• Gold*	Galvanischer Austausch → neue Form, Legierung	Stabilisierung, bathochrome Verschiebung
• Ni/NiO	Legierung → magnetische Eigenschaften	LSPR-Dämpfung
• Pd; Pt	Legierung→ neue katalytische Effekte	LSPR-Dämpfung
Metalloxide; -halide und -sulfide	Änderung der chemischen Zusammensetzung	LSPR-Dämpfung und Bandenverschiebung

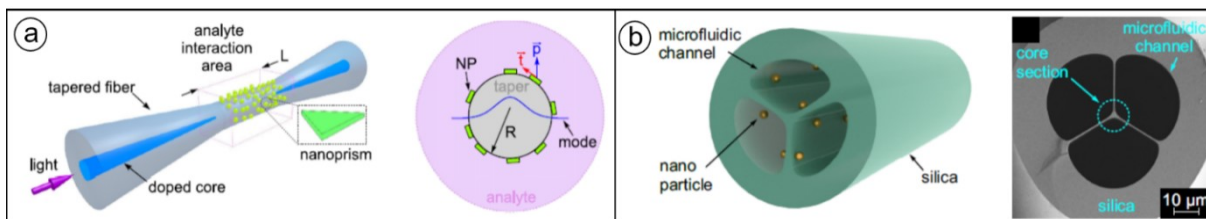*für Nanopartikel des jeweiligen anderen Metalls

Abbildung 19: *Plasmonische Nanopartikel als optische Sensoren in Lichtwellenleitern. Bei getaperten (verjüng-ten) optischen Fasern wurden goldstabilisierte Sibernanoprismen immobilisiert (a). In SCF wurden entlang der freien Kanäle des lichtleitenden Faserkerns Goldnanopartikeln immobilisiert. Durch Spülen der freien Kanäle mit Fluiden konnte somit eine optofluidische Plattform realisiert werden (b). [MT6; MT7]*

Daran wird deutlich, dass die Nanopartikelform einen entscheidenden Einfluss auf die Sensitivi-tät hat. Insbesondere anisotrope plasmonische Nanopartikel zeichnen sich an ihren Spitzen, Ecken und Kanten durch eine starke Fokussierung der Plasmonen aus, wodurch es zu einer hohen Feldverstärkung kommt, was zu einer großen Sensitivität führt. So ist selbst die Sensitivi-tät von volumen- und flächenmäßig kleineren Goldnanowürfeln mit der Kantenlänge von 53 nm, mit 126 nm/RIU größer als die der sphärischen 80 nm Goldpartikel. Die Abbildung 20 zeigt dar-über hinaus die Sensitivitäten verschieden großer, mikrofluidisch hergestellter Goldnanowürfel (siehe Kapitel 3.4). Je größer die Goldnanowürfel sind, desto höher ist auch ihre Sensitivität. Gleiches gilt auch für Silbernanopartikel, die aufgrund des geringeren materialspezifischen Dämpfungsfaktors jedoch ohnehin eine höhere Sensitivität aufweisen als Nanopartikel aus Gold.
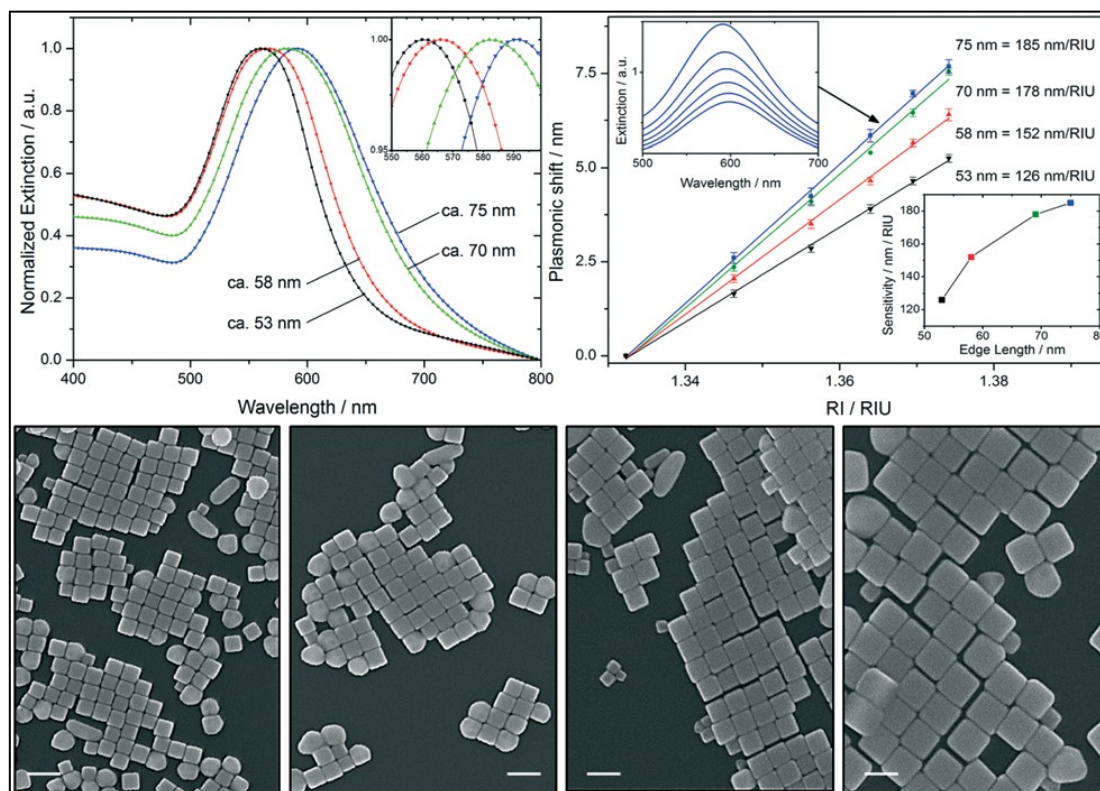

Abbildung 20: *Mittels mikrofluidischer Plattform (CF-Verfahren) hergestellte Goldnanowürfel verschie-dener Kantenlängen (REM-Aufnahmen von links nach rechts: 53 nm, 58 nm, 70 nm und 75 nm). und deren Spektrale Charakterisierung sowie zugehörige Bulksensitivität (S_B). Der Maßstab entspricht 100 nm. [MT4]*

Die Abbildung 21b zeigt, dass sphärische Silbernanopartikel mit einem Durchmesser von 8 nm eine Sensitivität von 90 nm/RIU erreichen. Dagegen zeigen anisotrope Silberpartikel, wie die in Kapitel 3.3 synthetisierten Silberprismen mit Kantenlängen von 12 nm bis 70 nm, Bulksensitivitäten (S_B) von 160 nm/RIU bis zu 475 nm/RIU. Silbernanopartikel und speziell ihr anisotropes Pendant sind somit ideale Kandidaten für die Verwendung als optische Transducer. Entgegen dem chemisch inerten Gold ist Silber jedoch sehr reaktiv, wodurch es besonders an Luft zur Alterung (z.B. Korrosion) von Nanopartikeln kommt. Vor allem anisotrope Silberpartikeln sind von unkontrollierten Umformeffekten (*reshaping Effect,* [MT5]) betroffen, die signifikante chemische sowie strukturelle und damit auch optische Eigenschaftsänderungen hervorrufen. Das Ziel der postsynthetischen Prozessierung ist daher die Stabilisierung der Silbernanopartikel, ohne dass dabei die optischen Eigenschaften verloren gehen. Durch gezielte Oberflächenpassivierung konnten Silbernanopartikel in eine Silikatschicht eingekapselt werden (Abbildung 6o in Kapitel 3.1). Gleiches konnte mit den forminstabilen Silberprismen durchgeführt werden, die daraufhin eine höhere Beständigkeit bei vergleichbaren optischen Eigenschaften aufwiesen. Wie in Abbildung 21b dargestellt ist, verringert sich zwar die Bulksensitivität von 555 nm/RIU auf ca. 280 nm/RIU bei einer Silikathülle mit einem Durchmesser von etwa 83 nm, jedoch ist die Sensitivität noch erheblich höher als für sphärische Gold- und Silbernanopartikel. Darüber hinaus können Standartanbindungsprotokolle aus der Glas- und Silikatchemie angewandt werden. Dennoch geht durch die Abschottung der Silberoberfläche die Möglichkeit der Molekülanbindung und der Detektion an den Spitzen, dem Ort mit der maximalen Feldverstärkung, verloren. Um jedoch auch dieses Kriterium zu erfüllen, wurden die Silberprismen durch epitaktisches Aufwachsen einer dünnen (< 2 nm) Goldschicht stabilisiert. Dabei handelt es sich um einen chemischen Wachstumsschritt in Lösung, bei dem es zur katalytischen Abscheidung von Gold ausschließlich auf den Kanten der Silberprismen kommt. Da der Prozess sehr sensibel ist, entsteht bei zu hohen Goldkonzentrationen *galvanic replacement* (galvanischer Austausch) Reaktionen [148], bei
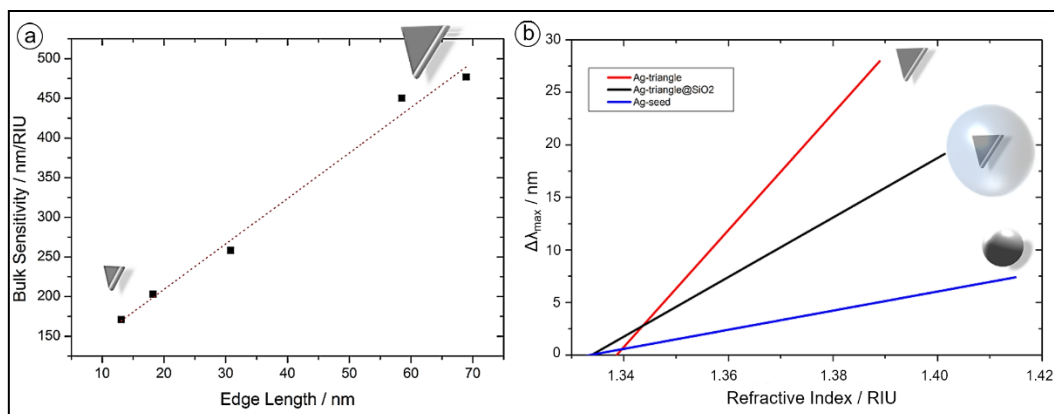

Abbildung 21: *Bulksensitivitäten (S_B) von Silbernanoprismen in Lösung mit unterschiedlicher Kantenlänge (a). Vergleich der Sensitivitäten von sphärischen, silikatumhüllten sowie nativen prismenförmigen Silbernanopartikeln [MT5]*

denen dem jeweiligen Nanopartikel das Silber entzogen wird, so dass ausschließlich ein Gold-rahmen übrigbleibt (Abbildung 6f in Kapitel 3.1). Die goldstabilisierten Silbernanoprismen haben im Vergleich zu den nativen Nanoprismen aus Silber eine geringfügig rotverschobene LSPR-Bande. Das große sensorische Potenzial dieser Nanopartikel kann anhand des in Abbildung 19a dargestellten Aufbaus der getaperten optischen Faser demonstriert werden. Auf den Faserkern immobilisiert erreichen die goldstabilisierten Sibernanoprismen bei einer Belegungsdichte von ca. 210 NP/µm^2 eine Sensitivität von nahezu 900 nm/RIU. Daran wird deutlich, dass vor allem anisotrope Nanopartikel bei gezielter postsynthetischer Prozessierung ein großes Leistungsver-mögen bezüglich sensorischer Anwendungen besitzen. Dabei können sie insbesondere in Kom-bination mit anderen Technologien, wie optischen Lichtwellenleitern, neue Einsatzgebiete er-schließen.

4. Zusammenfassung und Ausblick /Summary and Outlook

In der vorliegenden Arbeit wurde das Potenzial mikrofluidischer Verfahren untersucht, um definierte plasmonische Nanopartikel mit exakt spezifischen optischen Eigenschaften herzustellen. Beginnend mit den Herausforderungen bezüglich der generellen Nanopartikelsynthese und im Speziellen mit der Keimbildung sowie dem anisotropen Wachstum konnten Ansatzpunkte zur Optimierung definiert werden. Mit dem Vergleich verschiedener mikrofluidischer Verfahren wurden schließlich die Optimierungsstrategien untersucht.

Im ersten Abschnitt konnte die mikrofluidische Synthese von kleinen Gold- und Silberseedpartikeln mit schmalen Partikelgrößenverteilungen realisiert werden. Die Keimbildung konnte somit von einem schrittweisen Prozess in einen kontinuierlichen Prozess überführt werden. Vor allem Synthesen mit starken Reduktionsmitteln, wie $NaBH_4$, profitieren von den Verfahren, da der verwendete Mikromischer (DFM) die schnellen Reaktionskinetiken durch eine sehr kurze und effiziente Mischzeit von 4 ms bedienen kann, so dass kleinere Seedpartikel mit geringerer Größenverteilung erzeugt werden konnten. In diesem Zusammenhang zeigte auch die Synthese von Goldseeds im segmenierten Fluss (SF) großes Potenzial, da es hier nicht zum Reaktorfouling kam. Dagegen kam es beim kontinuierlichen Verfahren (CF) zum Materialverlust als Folge der Ablagerungen von Gold und Silber an den Kanalwänden, die jedoch durch Verwendung von Säure wieder regeneriert werden konnten. Indem die amphiphilen Moleküle die Kanaloberfläche passivieren, konnte durch Verwendung von Tensiden (CTAB und CTAC) als Additive das Reaktorfouling schließlich auch beim CF-Verfahren ganz unterbunden werden.

In diesem Zusammenhang wurden auch Additive zum anisotropen Wachsen der Seedpartikel genutzt. Es konnte gezeigt werden, dass die optimale Kombination verschiedener Synthesemethoden sinnvoll ist, um von den jeweiligen Vorteilen zu profitieren, die Nachteile jedoch zu minimieren. Für Silberprismen konnte ein zweistufiges System etabliert werden, dass aus Seedsynthese und Seedwachstum besteht. Die Seedsynthese basiert auf einem kontinuierlichen mikrofluidischen Verfahren, bestehend aus verschiedenen, an die jeweiligen Reaktionsgeschwindigkeiten und -bedürfnisse adaptierten Mikromischern. Dadurch wurden ein Vormischprozess und der eigentliche Syntheseprozess realisiert. Im anschließenden Batchverfahren konnten die mikrofluidisch erzeugten Seeds mit hoher Ausbeute in Silberprismen wachsen und die geometrischen und optischen Eigenschaften gezielt eingestellt werden. Gleiches wurde bei der dreistufigen Herstellung von Goldnanowürfeln realisiert. Nachdem die optimalen Parameter der kritischen Reaktionskinetiken identifiziert wurden, konnten die Methoden an die jeweiligen zeitkritischen Prozesse angepasst werden. Seedsynthese und erster Wachstumsschritt (GS1) wurden mikrofluidisch (sowohl SF als auch CF) realisiert und der zweite Wachstumsschritt (GS2) erfolgte

im Batchverfahren. Die somit erzeugten Goldnanowürfel zeichnen sich durch eine hohe Reproduzierbarkeit sowie Formausbeute aus und ließen sich in ihrer Größe und damit auch ihrer LSPR-Bande kontrolliert einstellen.

Darauf aufbauend konnte eine mikrofluidische Plattform etabliert werden, die ein effizientes Modellsystem für Parameterstudien hinsichtlich anisotropen Nanopartikelwachstums darstellt, da sie frei von subjektiven Einschätzungen und Einflüssen ist. Es wurden Screeningverfahren bezüglich des Inkubationsverhaltens der angereicherten Seeds, deren ausschließlicher Konzentration hinsichtlich Partikelgröße und des Einflusses von Additiven (F^-, Cl^-, Br^-, I^-) auf die Nanopartikelmorphologie durchgeführt. Im Ergebnis konnte das mikrofluidische Verfahren reproduzierbare Inkubationen und dadurch hohe Partikelausbeuten sowie die Möglichkeit der Feineinstellung der Nanopartikelgröße ermöglichen. Hinsichtlich der Additive zeigte sich, dass ausschließlich Bromid die Partikelmorphologie stark beeinflussen kann und sich somit durch dessen Manipulation explizit im zweiten Wachstumsschritt parallel sphärische, kubische und stäbchenförmige Goldnanopartikel herstellen lassen. Damit konnte gezeigt werden, dass die mikrofluidische Plattform eine kostengünstige (ökonomisch und ökologisch) und vielseitige Nanopartikelsynthese ermöglicht, die sich durch ihr hohes Maß an Prozesskontrolle auszeichnet und auf diese Weise nicht im herkömmlichen Batchverfahren realisiert werden kann.

Darüber hinaus zeigten die synthetisierten plasmonischen Nanopartikel ein großes Potenzial für biosensorische Applikationen. Als optischer Transducer konnten sie in ein neuartiges, optofluidisches Fasersystem integriert werden und zeichnen sich durch hohe Sensitivitäten aus. Vor allem anisotrope Nanopartikel, wie Goldwürfel und Silberprismen, überzeugten dabei durch ihre hohe Sensitivität. Um Alterungseffekten vorzubeugen konnten die Silberprismen erfolgreich mit einer Silikathülle oder einem dünnen Goldrahmen auf den Kanten stabilisiert werden, wobei für beide Verfahren weiterhin eine hohe Sensitivität gewährleistet werden konnte. Dadurch wurde für getaperte optische Fasern ermöglicht, goldstabilisierte Silberprismen mit extrem hohen Sensitivitäten als Transducer zu verwendet.

Zusammenfassend lass sich schlussfolgern, dass anisotrope plasmonische Nanopartikel für neuartige sensorische Applikationen gut geeignet sind und durch den dadurch entstehenden hohen Bedarf an diesen Nanopartikeln wiederum mikrofluidische Verfahren gefragt sind. Diesen eröffnet es dadurch die Möglichkeit, ihre Vorteile hinsichtlich Partikelausbeute, Prozesskontrolle und Reproduzierbarkeit konsequent auszuspielen. Darüber hinaus erlauben die mikrofluidischen Strategien völlig neue Ansätze der Partikelherstellung und könnten daher die Realisierung neuer oder bis dato ungenutzter Reaktionsparameter und -räume zur Erzeugung neuartiger und unkonventioneller plasmonsicher Nanopartikel ermöglichen. Es ist daher gut möglich, dass sie somit die nächste Generation der Nanopartikelherstellung einläuten.

The presented work investigated the potential of microfluidic methods to produce well defined plasmonic nanoparticles with accurate optical properties. Starting with the challenge of the general synthesis of nanoparticles especially with the nucleation as well as the anisotropic growth, starting points for their optimization were specified. By comparing different microfluidic methods, optimization strategies were analyzed.

In the first part of the study, a microfluidic synthesis of small gold and silver seeds with narrow particle size distribution could be realized. The nucleation was therefore transferred from a stepwise process into a continuous process. Most of all, the synthesis reactions with strong reducing agents like $NaBH_4$ benefit from these methods, since the used micromixer (DFM) can handle the fast reaction kinetics with short and efficient mixing times in the millisecond range and therefore produce smaller seed particles with decreased size distributions. In this context, also the synthesis of gold seeds with the segmented flow (SF) approach depicted a high potential, since it precludes reactor fouling. In contrast, the continuous flow (CF) method suffered from a loss of material as the consequence of unwanted deposition of gold and silver at the channel walls. However, the channel walls could be regenerated with acid afterwards. By passivating the channel surfaces with amphiphilic molecules, the as additive utilized tensides (CTAB and CTAC) were able to entirely prohibit the reactor fouling also for the CF-method.

Within this relation, additives were further used to initiate an anisotropic growth of the seed particles. It could be demonstrated that an ideal combination of different synthesis strategies is reasonable to benefit from the advantages of the methods but also minimize the disadvantages. In order to produce silver prisms, a two-step system could be arranged that consists of seed synthesis and the later growth of them. The synthesis of the seeds is based on a continuous microfluidic process containing different micromixers which were adopted to the velocity and requirements for the reaction. Thus, a premixing part and a real synthesis part were realized. In the subsequent batch process, the microfluidically synthesized seeds could be grown to highly yielded silver prisms with adjustable geometric and optical properties. The same was done for the three-step production of gold nanocubes. After identifying the optimal parameters for the critical reaction kinetics, the methods could be adopted to the respective time critical processes. Seed synthesis and the first growth step (GS1) could be realized with microfluidic methods (both SF and CF) and the second growth step (GS2) was done in a batch approach. The gold nanocbues produced with this protocol benefit from the high reproducibility as well as the high yield in shape. It was also possible to tune and control their edge lengths and hence the LSPR-peak position.

Based on these results, a microfluidic platform could be established, which represents an efficient model system for parameter studies concerning anisotropic nanoparticle growth and is free

of subjective influences and evaluations. Thus, screening processes regarding the incubation behavior of the reinforced seeds, their used concentration with respect to the final nanoparticle size and the influence of additives on the morphology of nanoparticles were done. The results showed that microfluidic methods enable reproducible incubation and therefore high particle yields concerning the desired shape, as well as the possibility of fine tuning the nanoparticle sizes. In terms of the additives, it was shown that solely bromid can strongly influence the morphology of the nanoparticles. By modifying bromid only in the second growth step, spherical, cubed- and rod-shaped nanoparticles can be produced in a parallel manner. Therefore, it could be demonstrated that the microfluidic platform allows a cost-efficient (economically and ecologically) and versatile nanoparticle synthesis, which enables a high mass of process control that cannot be reached in conventional batch approaches.

Furthermore, the synthesized plasmonic nanoparticles offer a great potential for biosensorics applications. By acting as optical transducers, they could be integrated into an innovative opto-fluidic fiber system and displayed high sensitivities. Notably, anisotropic nanoparticles like gold cubes and silver prisms persuaded with their high sensitivities. In order to prevent aging effects, silver prisms could be successfully stabilized with a silica shell or a thin gold frame only at the particle edges, by maintaining for both methods still a high sensitivity. Thus, gold stabilized silver prisms could be used for tapered optical fibers.

The results clearly depict the suitability of anisotropic plasmonic nanoparticles for innovative sensor applications, whereby based on the need of these nanoparticles, microfluidic methods are demanded. In turn, this allows microfluidic methods consistently utilize their advantages concerning nanoparticle yield, process control and reproducibility. In addition, microfluidic strategies enable entire new concepts of nanoparticle synthesis and could therefore realize new or until now unused reaction parameters and spaces for the creation of novel plasmonic nanoparticles. Thus, it is possible that they herald the next generation of nanoparticle production.

5. Veröffentlichte Arbeiten

Im Folgenden sind die Nachdrucke der Publikationen, die für die vorliegende Dissertation berücksichtigt wurden, zusammengefasst. Weiterhin ist jeder Publikation eine Erklärung zu den Eigenanteilen sowie zu weiteren Doktoranden/ Doktorandinnen als Koautoren an den Publikationen und Zweitpublikationsrechten bei der vorliegenden kumulativen Dissertation angehangen[w].

5.1. Plasmonic nanoparticle synthesis and bioconjugation for bioanalytical sensing [MT1]

Autorenschaft der Publikation:

Andrea Csáki[w]	Konzeptentwicklung
	Verfassen des Manuskripts
	Datenanalyse und -Interpretation
Matthias Thiele[w]	Konzeptentwicklung
	Datenanalyse und – Interpretation
	Diskussion und Korrektur des Manuskripts
Jacqueline Jatschka	Diskussion und Korrektur des Manuskripts
André Dathe	Diskussion und Korrektur des Manuskripts
David Zopf	Diskussion und Korrektur des Manuskripts
Ondrej Stranik	Diskussion und Korrektur des Manuskripts
Wolfgang Fritzsche	Korrektur des Manuskripts
	Projektleitung

Vorschlag zur Anrechnung der Publikationsäquivalente: **0,5 (Übersichtsartikel)**

Eng. Life Sci. 2015, 15, 266–275

Der Nachdruck der folgenden Publikation erscheint mit freundlicher Genehmigung von *WILEY-VCH.* Reprinted with kind permission from *WILEY-VCH*

---

[w] Geteilte Autorenschaft

Andrea Csáki

Matthias Thiele

Jacqueline Jatschka

André Dathe

David Zopf

Ondrej Stranik

Wolfgang Fritzsche

Leibniz Institute of Photonic
Technology, Jena, Germany

Review

Plasmonic nanoparticle synthesis and bioconjugation for bioanalytical sensing

Plasmonic nanoparticles, e.g. nanoscale particles consisting of noble metals, show high potential as transducer elements in novel optical sensors. Their optical properties are based on collective and coherent oscillation of the conduction electrons by irradiating electromagnetic waves. The resulting resonance band (localized surface plasmon resonance [LSPR]) is adjustable in the UV- to near-infrared spectral range and can be defined by the chemical synthesis. The synthesis conditions can determine dimension, material and particle shape, and these parameters represent the main factors for the position of the LSPR and the bulk sensitivity. Therefore, a reproducible synthesis of nanoparticles with defined LSPR is of importance. The sensing principle is based on the strong influence of the surrounding medium's refractive index. Especially, anisotropically shaped particles are especially sensitive to small changes in the medium; therefore, their defined synthesis is in the focus of current developments. In this review, we give an overview of the different synthesis techniques for nanoparticles, including miniaturized fluid devices. For sensoric applications, the conjugation of nanoparticles with biomolecules represents a key step; thus, typical functionalization approaches are considered. In the following sections, different LSPR sensing strategies are introduced, and possible applications, especially in DNA analytics, are demonstrated.

1 Introduction

Plasmonic nanoparticles—nanoparticles consisting of noble metals such as gold, silver, platinum and palladium—exhibit a large potential as optical labels. The optical signal, the scattered light, of a single particle is five orders of magnitude higher compared to the optical response generated by a typical fluorescence dye molecule [1,2]. These extraordinary optical properties allow versatile sensor applications for future (bio)analytics. The origin of this optical potential is based on the collective oscillation of free conduction electrons in the nanoscale particles [3,4]. This oscillation leads to the occurrence of localized surface plasmon resonance (LSPR) that depends on intrinsic factors such as material composition, size and shape of the particles (Fig. 1). In addition, the refractive index of the surrounding medium influences the LSPR position. This is the base for the sensoric potential

of plasmonic nanoparticles. The intrinsic factors determine the main sensitivity of the particles [5]. Because these factors can be adjusted during the synthesis, it represents a critical step for the development of sensitive optical transducers. In this review, general strategies of nanoparticle synthesis are presented in relation to the proposed sensing techniques. For this purpose, different functionalization methods of the particles with biomolecules will be shown. Different LSPR sensing concepts will be introduced, and their sensoric potential is demonstrated.

2 Synthesis of metal nanoparticles

2.1 General strategies

Metal nanoparticles and clusters can be formed by assembly of atoms as a kind of bottom-up approach [5,6], or top-down by dispersion of bulk materials [4]. The main strategy for nanoparticle synthesis is based on the chemical reduction in liquids. By this so-called colloidal synthesis, metal ions in solution are reduced by using an electron donor molecule. Here we can distinguish between a direct reduction with a reducing agent and the reduction

Correspondence: Dr. Andrea Csáki (csaki@ipht-jena.de), Leibniz Institute of Photonic Technology, A.-Einstein-Str. 9, 07745 Jena, Germany

Abbreviations: eLSPR, LSPR on ensemble; **LSPR,** localized surface plasmon resonance; **snpLSPR,** single-particle LSPR
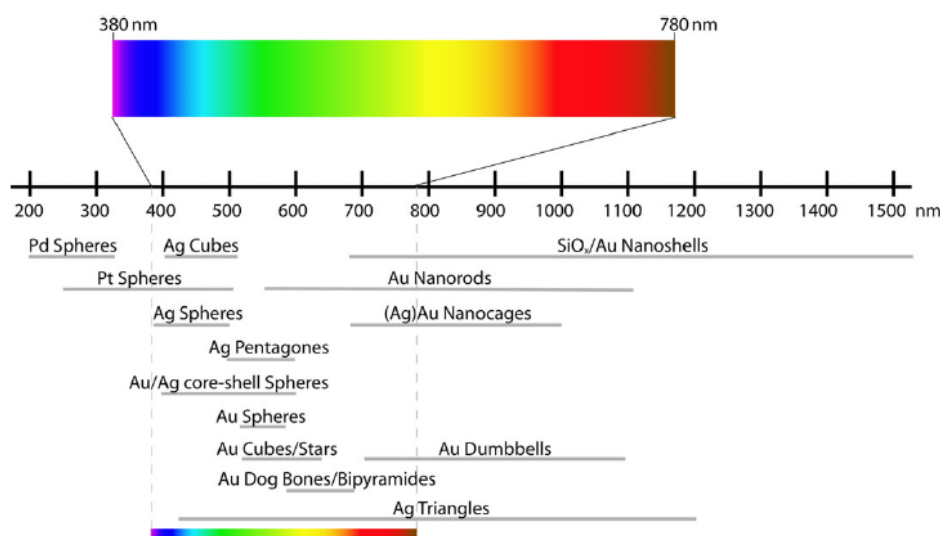
Figure 1. Overview over the spectral range of localized surface resonances for various plasmonic nanoparticles between the UV- and the near-infrared spectral ranges.

in presence of organic ligands. The latter particles represent the so-called monolayer protected clusters or particles, also Brust-particles [7–10]. Possible reducing agents are phosphor [11, 12], formaldehyde [13], acetone [14], citrate [10, 15, 16], ascorbic acid [17], tannic acid [18–20], salicylic acid [20], oxalic acid [15], ethyl alcohol [21], hydroxylamine [22, 23] or sodium borohydride. In general, the strength and the amount of the used reducing agent have a key effect to the resulting particle size.

An alternative for the large-scale synthesis of plasmonic nanoparticles is the nature-analogous bioreduction, where the metal salt reduction occurs in organisms or uses organic material as reducing agent. Different kind of microorganisms, like bacteria [24], fungi [25, 26] and marine algae [27] can act as direct producer for intra- or extracellular synthesis supporter. Also lichen or their metabolites can mediate nanoparticle synthesis [28].

Another possibility to prepare plasmonic nanoparticles is based on the dispersion of atoms from the bulk materials. These methods often require a high-energy source, and do additionally waste large part of the often precious materials. High voltage [29], laser beam [30], microwave or sonochemical forces [31, 32] allow the generation of plasmonic nanoparticles in high amount. Unfortunately, without additional and cumbersome structuring steps (like electron beam lithography); these methods usually result in only spherical-shaped nanoparticles. A shape-defining synthesis including exact particle dimension is best realized using the colloidal synthesis. An overview from current theories for mechanisms of the synthesis is described in Subsection 2.2.

2.2 Mechanisms of colloidal synthesis

The classical model for colloidal synthesis of nanoparticles (Fig. 2A) distinguishes between two subsequent reaction steps, a fast nucleation and a slower growing step [15, 16, 33]. Initiation of the reaction is the reduction of metal ions to atoms. The increasing amount of atoms leads to a crossing of the nucleation concentration threshold, and first nuclei are formed. Then, the nuclei will grow until the metal ions are consumed. The final size and the size distribution of the nanoparticles depend on the nucleation function. According to this, the number of the nuclei should be the same as that of the nanoparticles at the end of the synthesis reaction. This is not the case in practice [34]; therefore, new theoretical models were developed recently, proposing a novel view on the particle formation: Multiple nucleation and growth steps occur successively or with overlaps [35, 36]. The earlier nuclei may aggregate and thereby form new nuclei for the growth (Fig. 2B). This so-called "aggregative synthesis process" is divided in four steps. A first nucleation process depends on the used reducing agent: in the case of Au nanoparticles, citrate reduction yields a nucleation time of ~60 s, by sodium borohydrate <200 ms. After this fast nucleation, a coalescence of the nuclei follows (Au/citrate ~20 min; Au/$NaBH_4$ > 200 ms). Subsequently, slow and fast growth steps occur. In the case of silver nanoparticles, the reaction kinetic is more complex [36, 37]. The nucleation function for the aggregative nucleation process depends on the used solvent, the concentration of the precursors and the reaction temperature. These three factors determine the density of the primary nuclei. The kind and the concentration of the reducing agents, the ionic strength, polymer stabilizers, ligands and surfactants represent additional factors for the nanoparticle-forming kinetics and the resulting particle sizes. Especially, anisotropically shaped nanoparticles exhibit excellent optical properties. Their synthesis is divided in several steps and requires surface detergents [38, 39]. Therefore, for a better process control, exact parameters and homogeneous fast local mixing are required. All this is ideally realized in microfluidic reactors.
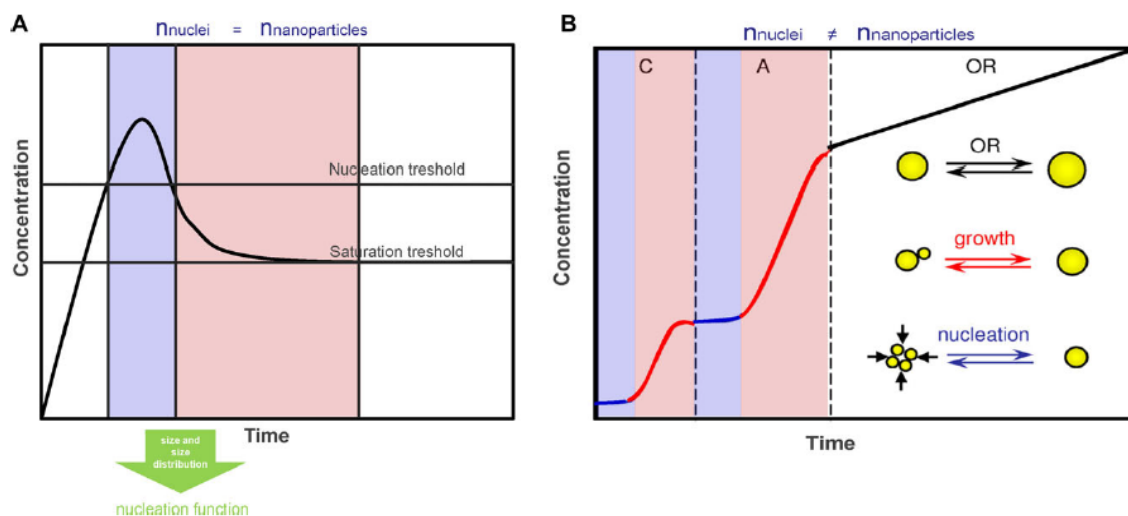
Figure 2. (A) LaMer diagram of the nucleation step in classical kinetics (adapted from [109]) versus (B) aggregative kinetics of the nanoparticle building (adapted from [36]).
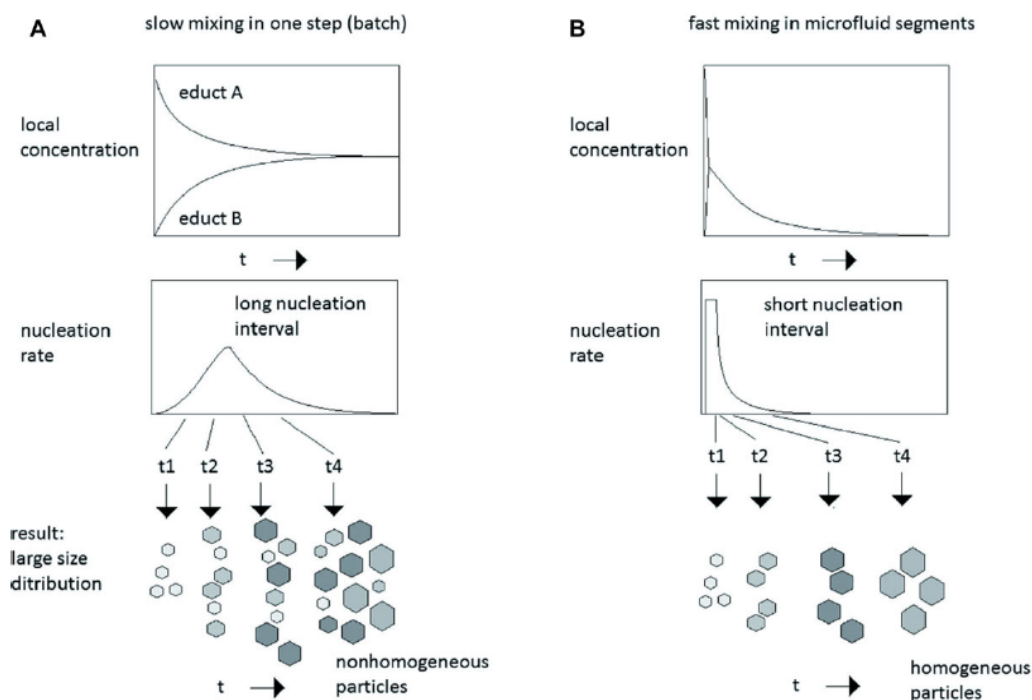

Figure 3. Comparison of nanoparticle synthesis in batch with the microfluidics approach. Reprinted with permission from [46]. Copyright 2012 American Chemical Society.

2.3 Microfluidic synthesis of nanoparticles

The synthesis of plasmonic nanoparticles can be realized on different scales. The main used technology is the batch synthesis, usually on mL scale. Here, an exact control of the mixing process is hard. This need motivated the development of novel microfluidic technologies [40, 41] (Fig. 3). The microfluidic synthesis of nanoparticles can be realized in segmented- or in continuous flow [42, 43]. In both cases, material requirements are low and the diffusion distances are very short. This allows a fast

mixing of the reactants and an optimal temperature distribution in the reactor. In addition, microfluidic channels also allow online monitoring and therefore a better reaction control. The exact control over particle size and distribution allows a better adjustment of the desired optical properties. Especially for the synthesis of anisotropic nanoparticles, an exact process control is of utmost importance [44]. In this two-step synthesis, the first step can generate well-defined and extremely small, monocrystalline seed particles, whereas the second step allows adjustment of the final dimension, shaped and size distribution. Silver triangles, in particular, can be synthesized only, if the first step guarantees all criteria [45]. The use of segmented flow allows the high-yield synthesis of such seed particles. Therefore, the LSPR position can be controlled exactly by adjusting the dimension of the triangles in the second step of this synthesis [46].

As an extension of this continuous-flow technique, another method combines different microreactor units for synthesis control. In the case of silver seeds, three steps for the mixing of reactants by different flow rates are needed. For a slow reaction (reaction half-life: T_{50} = several seconds) with low flow rates, LASAR or ROSAR (multilamination) micromixers are suitable [47, 48], whereas slow reactions (T_{50} = several seconds) with high flow rates, T-shaped micromixer [49] are suitable; for an ultrafast reaction ($T_{50} < 1$ ms) with a high flow rate for at least one component, a Dean-flow mixer is adequate [50–52]. Using combinations of these three mixers, the quality of the seeds can be optimized. Consequently, the synthesis yield can be increased from <70 up to ~90% for triangles, accompanied by a better tuning of the optical properties.

3 Biofunctionalization of plasmonic nanoparticles

Bioanalytical applications of metal nanoparticles have been established in the early 1980s [53], especially for electron microscopic techniques. Later they were also used as optical label in biochip techniques [54], and for light-induced manipulation of small biomolecules [55, 56], chromosomes [57] and cells [58]. Current developments are focused on the use of these particles for drug delivery [59] and modern sensing approaches [60, 61]. For all these techniques, a specific functionalization of the nanoparticles with biomolecules is necessary. The main problem is the stability of the colloidal nanoparticles. Most particles are only charge-stabilized after the synthesis. The particles are usually negatively charged by the presence of reducing ligands. In-between the particles, an electrostatic repulsion stabilize against aggregation. Small changes in the pH of the solvent or ionic conditions can partially deprotect the surface charges and decrease the repulsion. This can induce an irreversible coalescence (aggregation), rendering the colloidal solution unusable for applications. Most biofunctionalization processes are based on a strong interaction of specifically functionalized biomolecules with the metal particle surface in form of self-assembly monolayers.

The biomolecules replace the primary attached, reducing ligands. This ligand exchange reaction can be very hazardous for the particle stability, especially if the salt concentration is increased. The bioconjugation is mostly divided in two steps. First, the charged biomolecules bind electrostatically to the particle surface. In a second step, a self-organization process, the molecules build a statistically ordered layer around the particle. For biosensing, the recognition elements—which are complementary to the desired target—have to be attached at the surface of the nanoparticles. Table 1 lists the main strategies for the bioconjugation of plasmonic nanoparticles. For silver nanoparticles the same principles are adaptable, with some differences in the binding strength or the kinetics [62]. For biofunctionalization of anisotropically shaped nanoparticles, surface-blocking ligands (often detergents) should be removed first. The most used detergents are CTAB/CTAC, PVP, SDS or bis(2-ethylhexyl) sulfosuccinate. They are applied to induce the defined crystalline growth [39, 63, 64]. Their removal is usually quite laborious. On the one hand, the ligands can be exchanged or used as charged starting layer in layer-by-layer assembly [65–67]. For gold nanorods for example, CTAB results in a positively charged layer around the particles. Using a layer-by-layer step, poly(styrenesulfonate) can be utilized as negatively charged layer for the binding of antibodies on nanorods [65, 68]. On the other hand, ligand exchanging with thiol-modified polyethylenglycol is also a successful method for the conjugation of nanorods. This biocompatible layer allows direct in vivo applications [69].

The specific conjugation of metal nanoparticles allows their implementation in biosensoric devices as a transducer. Biorecognition strategies are based on the key-and-lock principle of the biomolecule-biomolecule interaction, which usually is extremely specific. In Table 2 various recognition elements (and their targets) are listed.

4 Application potential of plasmonic nanoparticles—LSPR sensing

Plasmonic nanoparticles are sensitive to changes of the refractive index in the surrounding media. This is the main principle of LSPR sensing (Fig. 4). The position of the resonance peak shifts to longer wavelengths upon binding of molecules onto the particle surface (see Fig. 4C and D). This shift is related to the bulk and surface sensitivity of the nanoparticles (determined by the intrinsic factors and given by the synthesis) as well as to the amount of the bound molecules [70]. In addition to this shift, the plasmonic effect induces a local field-enhancement around the nanoparticles. This is useful for Raman-related techniques and for metal-enhanced fluorescence. A classification of different LSPR sensing types is possible by the dimension and the principle of signal generation [71]. Generally, we can distinguish between refractive index sensing, resonance coupling effects and field-enhancement [72] (Fig. 4A). The main field of the LSPR sensing is the refractive index sensing. This is realizable in 1D, 2D or 3D particle arrangement, as single nanoparticles (snpLSPR), particle-layer ensembles (eLSPR) or article solutions (colorimetry).

The refractive index sensing at the single-particle level, the snpLSPR, was pioneered by the groups of Feldman, Schultz and van Duyne [73–76]. The main principle of this technique is based on the measurement of the single nanoparticle's response

269

Table 1. Bioconjugation strategies for plasmonic nanoparticles

Interaction	Ligand functionality	Examples	References
	Metal nanoparticles		
Covalent interaction	Thiol group (primary, dithiols)	DNA, proteins, peptides	[85, 92–94]
	Thiol group + click-chemistry or NHS/EDC		
	Amino group	DNA, proteins, antibodies, peptides	[62, 94]
Hydrophobic interaction	tryptophan	Proteins/"protein corona"	[95]
Electrostatic interaction	Charge, layer-by-layer assembly (LbL)	DNA, proteins/"protein corona", e.g. enzymes, antibodies, other biopolymers—poly electrolyte layers (PEL)	[66]
	Monolayer protected particles		
Ligand exchange reaction	Thiol group		[96]
	Metal nanoparticles with silica shell		
Covalent interaction	Silane	DNA, antibodies	[97, 98]
	Silane and NHS/EDC-chemistry	DNA, antibodies	[99]
	Silane and click-chemistry	DNA, antibodies, . . .	[100, 101]

Table 2. Biorecognition strategies for bioanalytical sensings.

Recognition element	Interaction	Target	Reference
DNA/RNA	Hybridization (hydrogen bonds)	DNA/RNA	[85]
Peptide nucleic acids	Hybridization (hydrogen bonds)	DNA/RNA	[102, 103]
Aptamers	Lock-key molecule-molecule interaction	Proteins, amino acids, sugars, steroids, pesticides	[104]
Antibodies	Antigen-antibody interaction	Antigens, cells, microorganism, proteins	[12, 105]
Molecularly imprinted polymers	Molecule-molecule interaction	Amino acids, sugars, steroids, pesticides, small biomolecules	[106]
Streptavidin	Biotin-streptavidin interaction	Biotin-modified target, e.g. DNA	[107, 108]

in form of resonance peak shift during the bioanalytical process (Fig. 4C). The optical response is measured as scattering information of only one single nanoparticle. In the experimental setup of snpLSPR, two different main concepts are possible. The scattering signal of the single nanoparticles can be measured using a signal output coupling by a mirror and the use of entrance slits to a grating-based spectrometer [77]. Otherwise, scattering signals of the single particle are selected from the field of view of immobilized and statistically distributed nanoparticles using a pinhole (Fig. 4B) [61, 76, 78]. Both methods allow the measurement of whole scattering information for just one nanoparticle at a time. Compared to near-field techniques such as SNOM, the measurement time here is much lower (few seconds compared to some 10 min) but with a lower topographically resolution [79]. The snpLSPR measurement of only one nanoparticle allows measurement of plasmon resonances before and after analytical sensing steps, or the real-time detection of bioanalytes. In case of DNA analytics, the capture DNA acts as a recognition element [61]. Their binding to the nanoparticle surface induces a first shift in the plasmon resonance (compared to the bare nanoparticle resonance). The binding of the analyte DNA (e.g. PCR fragment), which triggers a second shift, represents the actual sensor response.

Current developments show a detection limit comparable to other sensing concepts. The full width at half maximum of single nanoparticle compared to the peak from a whole population of nanoparticles is much smaller and so simpler to detect. Therefore, the measurement of single-particle spectra results in a narrower peak width compared to the measurements on nanoparticle ensemble, allowing more precise detection of the LSPR shift [77]. One limitation of the single-particle technique is the used rather sophisticated optical system (microspectroscopy) with a signal stability around one nanometer. In addition, this principle is hampered by the high costs of the devices and time-consuming data analysis for a statistical relevant amount of single nanoparticle. An extension of this technique, the imaging spectrometer allows a parallel readout of several nanoparticle signals in one-step and in a much shorter time [80, 81].

Ensemble-based eLSPR utilizes a cost-efficient measurement principle. By this method, the extinction of the whole particle layer is the basis of the optical signal. In its simplest form, the nanoparticles are immobilized as a layer on an optically transparent substrate which will be implemented in microfluidic channels. The optical signal is generated in transmission mode. The optical readout system can be realized using a low-cost spectrometer and it allows a measurement of LSPR shift with a resolution of around 10 pm (depending on the light source and detector). A main drawback of this method is that the signal is generated by the nanoparticle layer and only generic statements about the binding events can be made, whereas with snpLSPR
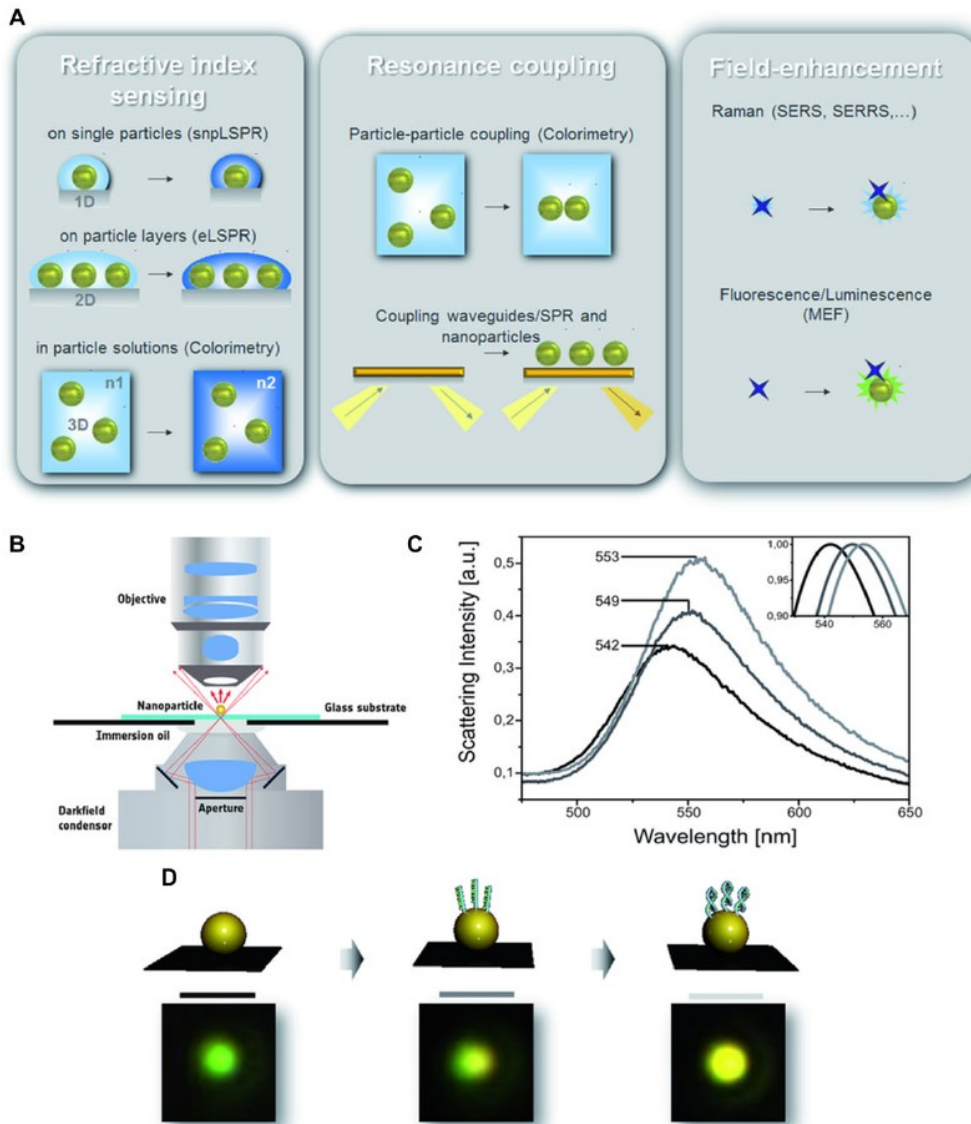
Figure 4. (A) Classification of LSPR sensing types by the transducer dimension and the signal development. (B) Dark-field microscopic device and (C, D) scheme of the snpLSPR for DNA-analytics: A single nanoparticle (D, left) is covered with a layer of single-stranded capture DNA (D, center) that is complementary to the target DNA. If this target DNA is present, their binding leads to another resonance shift (D, right). Dark-field images with a dimension of 5 μm.

distinctive correlation is possible. However, due to the low requirements regarding equipment, this concept is well-suited for the development of devices for point-of-care applications. A special kind of the eLSPR works with plasmonic particle layers inside of optical fibers. Using the nanoparticle layer deposition method, a homogeneous coverage with selected particles inside of microstructured optical fiber (MOF) channels is possible for fibers several meters in length [82]. This method combines for

the immobilization of nanoparticles a self-assembly monolayer techniques with microfluidic coupling of microstructured optical fibers, and allows the exact optical tuning of the fibers, their use for LSPR sensing and for controlled microfluidic management. In addition, it enables multiplexed bioanalytics where the different channels of the fiber provide individual signals [83].

Moreover, the combination of eLSPR sensing with the cavity ring-down readout principle enables a realization of sensitive
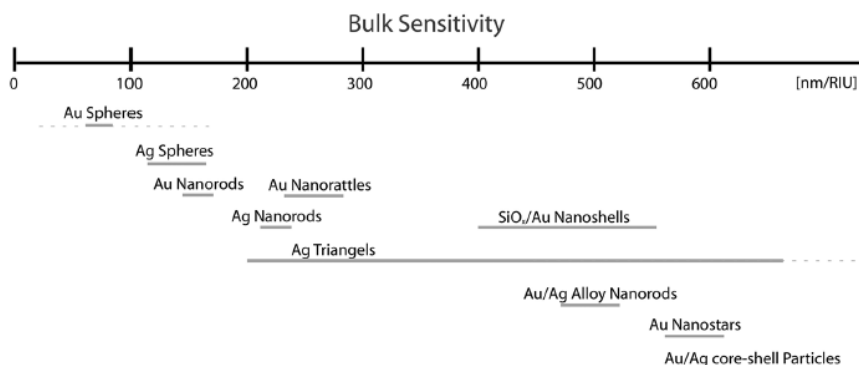
271

Figure 5. Comparison of the bulk sensitivities for different plasmonic nanoparticles.

bioanalytical sensors [84]. In this case, the measurement of the photon lifetime is extremely fast and sensitive. The principle is based on the light-trapping inside of high-quality optical cavity with a signal-enhancement. This powerful tool for low-loss optical spectroscopy represents a 2–3 orders of magnitude increased detection limit compared to the conventional spectrometric measurements.

The typically used concept for LSPR sensing, the colorimetry, is based on the spectral measurement of nanoparticle solutions. In this case, the refractive index changes and/or the optical coupling of the particle resonances induce a shift in the particle LSPR [85, 86]. This method allows simple assays for bioanalytical applications, for example, the detection of pathogens or other contaminants [87–89]. Colorimetry is also usable for an estimation of the sensitivities of different plasmonic nanoparticles. Especially, anisotropically shaped nanoparticles and particles with defined core-shell ratio show high bulk sensitivity (Fig. 5) [90, 91].

5 Concluding remarks

Plasmonic nanoparticles exhibit a high potential for future bioanalytical applications based on their characteristic optical properties. These particles can be prepared using simple chemical reactions based on colloidal chemistry. The reaction kinetic needs well-defined conditions for reproducible synthesis of nanoparticles. Therefore, microfluidic devices are a preferred technique for the synthesis. In a subsequent biofunctionalization step, plasmonic nanoparticles can be modified with various kinds of biomolecules. These conjugated nanoparticles can act as a transducer in optical sensing devices. The binding of analytes on recognition elements (biomolecules on a particle surface) using a specific biomolecule-biomolecule interaction represents the actual sensing step. Plasmonic particles allow different sensing concepts. LSPR sensing in different arrangement of the particles are usable for refractive index sensing. In addition, nanoparticles can induce a high field-enhancement for Raman-related techniques or metal-enhanced fluorescence. In general, plasmonic nanoparticles offer a large potential of future bioanalytical applications.

Practical application

Colloidal synthesis of plasmonic nanoparticles allows the development of novel cost-efficient optical biosensors. The particles act as optical transducers. The readout of the optical signal of the localized surface plasmon resonances—which lies usually in the visible range—can be realized by a simple technology. Different biorecognition strategies are possible by biofunctionalization of plasmonic nanoparticles. Therefore, various classes of molecules can be detected using this technique.

The authors have declared no conflict of interest.

6 References

[1] Yguerabide, J., Yguerabide, E. E., Light-scattering submicroscopic particles as highly fluorescent analogs and their use as tracer labels in clinical and biological applications. I. Theory. *Anal. Biochem.* 1998, *262*, 137–156.

[2] Yguerabide, J., Yguerabide, E. E., Light-scattering submicroscopic particles as highly fluorescent analogs and their use as tracer labels in clinical and biological applications. II. Experimental characterization. *Anal. Biochem.* 1998, *262*, 157–176.

[3] Mie, G., Beiträge zur Optik trüber Medien speziell kolloidaler Metallösungen. *Ann. Phys.* 1908, *25*, 377–445.

[4] Kreibig, U., Vollmer, M., *Optical Properties of Metal Clusters*, Vol. 25, Springer, Berlin 1995.

[5] Steinbrück, A., Csáki, A., Fritzsche, W., Metal nanoparticles for molecular plasmonics, in: Geddes, C. D. (Ed.), *Reviews in Plasmonics* 2010, Vol. *2010*, Springer, New York 2012; pp. 1–37.

[6] Daniel, M. C., Astruc, D., Gold nanoparticles: Assembly, supramolecular chemistry, quantum-size-related properties,

and applications toward biology, catalysis, and nanotechnology. *Chem. Rev.* 2004, *104*, 293–346.

[7] Bartlett, P. A., Bauer, B., Singer, S. J., Synthesis of water-soluble undecagold cluster compounds of potential importance in electron microscopic and other studies of biological systems. *J. Am. Chem. Soc.* 1978, *100*, 5085–5089.

[8] Schmid, G., Pfeil, R., Boese, R., Bandermann, F. et al., Au55[P(C6H5)3]12CI6—ein Goldcluster ungewöhnlicher Größe. *Chem. Ber.* 1981, *114*, 3634–3642.

[9] Brust, M., Walker, M., Bethell, D., Schiffrin, D. J. et al., Synthesis of thiol-derivatized gold nanoparticles in a two-phase liquid-liquid system. *J. Chem. Soc. Chem. Commun.* 1994, 801–802.

[10] Lee, P. C., Meisel, D., Adsorption and surface-enhanced Raman of dyes on silver and gold sols. *J. Phys. Chem.* 1982, *86*, 3391–3395.

[11] Faraday, M., Experimental relations of gold (and other metals) to light. *Philos. Trans. R. Soc. Lond.* 1857, *147*, 145–181.

[12] Faulk, W. P., Taylor, G. M., An immunocolloid method for the electron microscope. *Immunochemistry* 1971, *8*, 1081–1083.

[13] Zsigmondy, R., Über lösliches Gold. *Z. Elektrochem.* 1898, *4*, 546–549.

[14] Davies, A. E., The kinetics of the coagulation of gold sols. An investigation of the "Thermo-Senescence Effect" exhibited at elevated temperatures. *J. Phys. Chem.* 1928, *33*, 274–284.

[15] Turkevich, J., Stevenson, P. L., Hiller, J., Nucleation and growth process in the synthesis of colloidal gold. *Discuss. Faraday Soc.* 1951, *11*, 55–75.

[16] Frens, G., Controlled nucleation for the regulation of the particle size in monodisperse gold suspensions. *Nature* 1973, *241*, 20–22.

[17] Stathis, E. C., Gatos, H. C., Determination of gold with ascorbic acid. *Ind. Eng. Chem. Anal. Ed.* 1946, *18*, 801–801.

[18] Slot, J. W., Geuze, H. J., A new method of preparing gold probes for multiple-labeling cytochemistry. *Eur. J. Cell Biol.* 1985, *38*, 87–93.

[19] Weiser, H. B., Reyerson, L. H., Inorganic colloid chemistry. *J. Phys. Chem.* 1934, *39*, 305–306.

[20] Garbowski, L., Anwendung höherwerthiger Phenole, Phenolsäuren, Aldehyde und Phenolaldehyde zur Herstellung der Hydrosole von Gold, Platin und Silber. *Ber. Dtsch. Chem. Ges.* 1903, *36*, 1215–1220.

[21] Baigent, C. L., Müller, G., A colloidal gold prepared with ultrasonics. *Cell. Mol. Life Sci.* 1980, *36*, 472–473.

[22] Gutbier, A., Beiträge zur Kenntnis anorganischer Kolloide. *Z. Anorg. Chem.* 1902, *32*, 347–356.

[23] Brown, K. R., Lyon, L. A., Fox, A. P., Reiss, B. D. et al., Hydroxylamine seeding of colloidal Au nanoparticles. 3. Controlled formation of conductive Au films. *Chem. Mater.* 2000, *12*, 314–323.

[24] Du, L., Jiang, H., Liu, X., Wang, E., Biosynthesis of gold nanoparticles assisted by *Escherichia coli* DH5α and its application on direct electrochemistry of hemoglobin. *Electrochem. Commun.* 2007, *9*, 1165–1170.

[25] Mukherjee, P., Senapati, S., Mandal, D., Ahmad, A. et al., Extracellular synthesis of gold nanoparticles by the fungus *Fusarium oxysporum. ChemBioChem* 2002, *3*, 461–463.

[26] Ahmad, A., Senapati, S., Khan, M. I., Kumar, R. et al., Extracellular biosynthesis of monodisperse gold nanoparticles by a novel extremophilic actinomycete, *Thermomonospora* sp. *Langmuir* 2003, *19*, 3550–3553.

[27] Singaravelu, G., Arockiamary, J. S., Kumar, V. G., Govindaraju, K., A novel extracellular synthesis of monodisperse gold nanoparticles using marine alga, *Sargassum wightii* Greville. *Colloids Surf B Biointerfaces* 2007, *57*, 97–101.

[28] Shankar, S. S., Ahmad, A., Sastry, M., Geranium leaf assisted biosynthesis of silver nanoparticles. *Biotechnol. Prog.* 2003, *19*, 1627–1631.

[29] Bredig, G., Haber, F., Über Zerstäubung von Metallkathoden bei der Elektrolyse mit Gleichstrom. *Ber. Dtsch. Chem. Ges.* 1898, *31*, 2741–2752.

[30] Barcikowski, S., Hahn, A., Kabashin, A. V., Chichkov, B. N., Properties of nanoparticles generated during femtosecond laser machining in air and water. *Appl. Phys. A Mater. Sci. Process.* 2007, *87*, 47–55.

[31] Chen, W., Cai, W., Zhang, L., Wang, G., Sonochemical processes and formation of gold nanoparticles within pores of mesoporous silica. *J. Colloid Interface Sci.* 2001, *238*, 291–295.

[32] Zhu, Y.-J., Chen, F., Microwave-assisted preparation of inorganic nanostructures in liquid phase. *Chem. Rev.* 2014, *114*, 6462–6555.

[33] LaMer, V. K., Kenyon, A. S., Kinetics of the formation of monodispersed sulfur sols from thiosulfate and acid. *J. Colloid Sci.* 1947, *2*, 257–264.

[34] Kimling, J., Maier, M., Okenve, B., Kotaidis, V. et al., Turkevich method for gold nanoparticle synthesis revisited. *J. Phys. Chem. B* 2006, *110*, 15700–15707.

[35] Polte, J., Ahner, T. T., Delissen, F., Sokolov, S. et al., Mechanism of gold nanoparticle formation in the classical citrate synthesis method derived from coupled in situ XANES and SAXS evaluation. *J. Am. Chem. Soc.* 2010, *132*, 1296–1301.

[36] Wang, F., Richards, V. N., Shields, S. P., Buhro, W. E., Kinetics and mechanisms of aggregative nanocrystal growth. *Chem. Mater.* 2013, *26*, 5–21.

[37] Polte, J., Tuaev, X., Wuithschick, M., Fischer, A. et al., Formation mechanism of colloidal silver nanoparticles: Analogies and differences to the growth of gold nanoparticles. *ACS Nano* 2012, *6*, 5791–5802.

[38] Xiong, Y., Xia, Y., Shape-controlled synthesis of metal nanostructures: The case of palladium. *Adv. Mater.* 2007, *19*, 3385–3391.

[39] Xia, Y. N., Xiong, Y. J., Lim, B., Skrabalak, S. E., Shape-controlled synthesis of metal nanocrystals: Simple chemistry meets complex physics? *Angew. Chem. Int. Ed.* 2009, *48*, 60–103.

[40] Song, Y., Hormes, J., Kumar, C. S. S. R., Microfluidic synthesis of nanomaterials. *Small* 2008, *4*, 698–711.

[41] Zhao, C.-X., He, L., Qiao, S. Z., Middelberg, A. P. J., Nanoparticle synthesis in microreactors. *Chem. Eng. Sci.* 2011, *66*, 1463–1479.

[42] Wagner, J., Kohler, J. M., Continuous synthesis of gold nanoparticles in a microreactor. *Nano Lett.* 2005, *5*, 685–691.

[43] Lazarus, L. L., Riche, C. T., Marin, B. C., Gupta, M. et al., Two-phase microfluidic droplet flows of ionic liquids for the synthesis of gold and silver nanoparticles. *ACS Appl. Mater. Interfaces* 2012, *4*, 3077–3083.

[44] Boleininger, J., Kurz, A., Reuss, V., Sonnichsen, C., Microfluidic continuous flow synthesis of rod-shaped gold and silver nanocrystals. *Phys. Chem. Chem. Phys.* 2006, *8*, 3824–3827.

[45] Aherne, D., Ledwith, D. M., Gara, M., Kelly, J. M., Optical properties and growth aspects of silver nanoprisms produced by a highly reproducible and rapid synthesis at room temperature. *Adv. Funct. Materials* 2008, *18*, 2005–2016.

[46] Knauer, A., Csáki, A., Möller, F., Huhn, C. et al., Microsegmented flow-through synthesis of silver nanoprisms with exact tunable optical properties. *J. Phys. Chem. C* 2012, *116*, 9251–9258.

[47] Nguyen, N.-T., Wu, Z., Micromixers—A review. *J. Micromech. Microeng.* 2005, *15*, R1–R16.

[48] Hessel, V., Löwe, H., Schönfeld, F., Micromixers—A review on passive and active mixing principles. *Chem. Eng. Sci.* 2005, *60*, 2479–2501.

[49] Hoffmann, M., Schlüter, M., Räbiger, N., Experimental investigation of liquid–liquid mixing in T-shaped micro-mixers using -LIF and -PIV. *Chem. Eng. Sci.* 2006, *61*, 2968–2976.

[50] Dean, W., XVI. Note on the motion of fluid in a curved pipe. *Lond. Edinb. Dubl. Philos. Mag. J. Sci.* 1927, *4*, 208–223.

[51] Castelain, C., Mokrani, A., Le Guer, Y., Peerhossaini, H., Experimental study of chaotic advection regime in a twisted duct flow. *Eur. J. Mech. B Fluids* 2001, *20*, 205–232.

[52] Sudarsan, A. P., Ugaz, V. M., Multivortex micromixing. *Proc. Natl. Acad. Sci.* 2006, *103*, 7228–7233.

[53] Horisberger, M., Colloidal gold: A cytochemical marker for light and fluorescent microscopy and for transmission and scanning light microscopy. *Scan. Electron Microsc.* 1981, *II*, 9–31.

[54] Reichert, J., Csaki, A., Kohler, J. M., Fritzsche, W., Chip-based optical detection of DNA hybridization by means of nanobead labeling. *Anal. Chem.* 2000, *72*, 6025–6029.

[55] Wirth, J., Garwe, F., Hahnel, G., Csaki, A. et al., Plasmonic nanofabrication by long-range excitation transfer via DNA nanowire. *Nano Lett.* 2011, *11*, 1505–1511.

[56] Hüttmann, G., Radt, B., Serbin, J., Lange, B. I. et al., High precision cell surgery with nanoparticles? *Med. Laser Appl.* 2002, *17*, 9–14.

[57] Csáki, A., Garwe, F., Steinbruck, A., Maubach, G. et al., A parallel approach for subwavelength molecular surgery using gene-specific positioned metal nanoparticles as laser light antennas. *Nano Lett.* 2007, *7*, 247–253.

[58] Hirsch, L. R., Stafford, R. J., Bankson, J. A., Sershen, S. R. et al., Nanoshell-mediated near-infrared thermal therapy of tumors under magnetic resonance guidance. *Proc. Natl. Acad. Sci. USA* 2003, *100*, 13549–13554.

[59] Cai, W., Gao, T., Hong, H., Sun, J., Applications of gold nanoparticles in cancer nanotechnology. *Nanotechnol. Sci. Appl.* 2008, *1*, 17–32

[60] Camara, A. R., Gouvêa, P. M. P., Dias, A. C. M. S., Braga, A. M. B. et al., Dengue immunoassay with an LSPR fiber optic sensor. *Opt. Express* 2013, *21*, 27023–27031.

[61] Schneider, T., Jahr, N., Jatschka, J., Csaki, A. et al., Localized surface plasmon resonance (LSPR) study of DNA hybridization at single nanoparticle transducers. *J. Nanopart. Res.* 2013, *15*, 1–10.

[62] Steinbrück, A., Csáki, A., Ritter, K., Leich, M. et al., Gold-silver and silver-silver nanoparticle constructs based on DNA

[63] Jana, N. R., Gram-scale synthesis of soluble, near-monodisperse gold nanorods and other anisotropic nanoparticles. *Small* 2005, *1*, 875–882.

[64] Tao, A. R., Habas, S., Yang, P., Shape control of colloidal metal nanocrystals. *Small* 2008, *4*, 310–325.

[65] Huang, X., El-Sayed, I. H., Qian, W., El-Sayed, M. A., Cancer cell imaging and photothermal therapy in the near-infrared region by using gold nanorods. *J. Am. Chem. Soc.* 2006, *128*, 2115–2120.

[66] Gittins, D. I., Caruso, F., Tailoring the polyelectrolyte coating of metal nanoparticles. *J. Phys. Chem B* 2001, *105*, 6846–6852.

[67] Schönhoff, M., Self-assembled polyelectrolyte multilayers. *Curr. Opin. Colloid Interface Sci.* 2003, *8*, 86–95.

[68] Sokolov, K., Follen, M., Aaron, J., Pavlova, I. et al., Real-time vital optical imaging of precancer using anti-epidermal growth factor receptor antibodies conjugated to gold nanoparticles. *Cancer Res.* 2003, *63*, 1999–2004.

[69] Niidome, T., Yamagata, M., Okamoto, Y., Akiyama, Y. et al., PEG-modified gold nanorods with a stealth character for in vivo applications. *J. Control. Release* 2006, *114*, 343–347.

[70] Kvasnicka, P., Homola, J., Optical sensors based on spectroscopy of localized surface plasmons on metallic nanoparticles: Sensitivity considerations. *Biointerphases* 2008, *3*, FD4–FD11.

[71] Csáki, A., Berg, S., Jahr, N., Leiterer, C. et al., Plasmonic nanoparticles—Noble material for sensoric applications, in: Chow, P. E. (Ed.), *Gold Nanoparticles: Properties, Characterization and Fabrication*, Nova Science Publishers, Hauppauge, NY, 2010, pp. 245–261.

[72] Csáki, A., Schröder, K., Willsch, R., Bartelt, H. et al., *Plasmonic nanoparticles for optical biosensing*, SPIE Photonics, Prague 2011.

[73] Raschke, G., Kowarik, S., Franzl, T., Sonnichsen, K. et al., Biomolecular recognition based on single gold nanoparticle light scattering. *Nano Lett.* 2003, *3*, 935–938.

[74] Haes, A. J., Van Duyne, R. P., A nanoscale optical biosensor: Sensitivity and selectivity of an approach based on the localized surface plasmon resonance spectroscopy of triangular silver nanoparticles. *J. Am. Chem. Soc.* 2002, *124*, 10596–10604.

[75] Mock, J. J., Smith, D. R., Schultz, S., Local refractive index dependence of plasmon resonance spectra from individual nanoparticles. *Nano Lett.* 2003, *3*, 485–491.

[76] Schultz, S., Smith, D. R., Mock, J. J., Schultz, D. A., Single-target molecule detection with nonbleaching multicolor optical immunolabels. *Proc. Natl. Acad. Sci. USA* 2000, *97*, 996–1001.

[77] Sönnichsen, C., Geier, S., Hecker, N. E., von Plessen, G. et al., Spectroscopy of single metallic nanoparticles using total internal reflection microscopy. *Appl. Phys. Lett.* 2000, *77*, 2949–2951.

[78] Mock, J. J., Barbic, M., Smith, D. R., Schultz, D. A. et al., Shape effects in plasmon resonance of individual colloidal silver nanoparticles. *J. Chem. Phys.* 2002, *116*, 6755–6759.

[79] Sönnichsen, C., *Plasmons in Metal Nanostructures.* Cuvillier Verlag, Göttingen 2001, p. 134.

[80] Bingham, J. M., Willets, K. A., Shah, N. C., Andrews, D. Q. et al., Localized surface plasmon resonance imaging:

hybridization of thiol- and amino-functionalized oligonucleotides. *J. Biophotonics* 2008, *1*, 104–113.

Simultaneous single nanoparticle spectroscopy and diffusional dynamics. *J. Phys. Chem. C* 2009, *113*, 16839–16842.

[81] Ruemmele, J. A., Hall, W. P., Ruvuna, L. K., Van Duyne, R. P., A localized surface plasmon resonance imaging instrument for multiplexed biosensing. *Anal. Chem.* 2013, *85*, 4560–4566.

[82] Csáki, A., Jahn, F., Latka, I., Henkel, T. et al., Nanoparticle layer deposition for plasmonic tuning of microstructured optical fibers. *Small* 2010, *6*, 2584–2589.

[83] Schwuchow, A., Zobel, M., Csáki, A., Schröder, K. et al., Monolayers of different metal nanoparticles in microstructured optical fibers with multiplex plasmonic properties. *Opt. Mater. Express* 2012, *2*, 1050–1055.

[84] Zeuner, T., Paa, W., Schmidl, G., Zopf, D. et al., Optical readout of a nanoparticle based sensor by cavity ring-down spectroscopy. *Sens. Actuators B Chem* 2014, *195*, 352–358.

[85] Mirkin, C. A., Letsinger, R. L., Mucic, R. C., Storhoff, J. J., A DNA-based method for rationally assembling nanoparticles into macroscopic materials. *Nature* 1996, *382*, 607–609.

[86] Nath, N., Chilkoti, A., Label free colorimetric biosensing using nanoparticles. *J. Fluoresc.* 2004, *14*, 377–389.

[87] Li, H., Rothberg, L., Colorimetric detection of DNA sequences based on electrostatic interactions with unmodified gold nanoparticles. *Proc. Natl. Acad. Sci. USA* 2004, *101*, 14036–14039.

[88] Liu, D., Qu, W., Chen, W., Zhang, W. et al., Highly sensitive, colorimetric detection of mercury(II) in aqueous media by quaternary ammonium group-capped gold nanoparticles at room temperature. *Anal. Chem.* 2010, *82*, 9606–9610.

[89] Xue, X., Wang, F., Liu, X., One-step, room temperature, colorimetric detection of mercury (Hg2+) using DNA/nanoparticle conjugates. *J. Am. Chem. Soc.* 2008, *130*, 3244–3245.

[90] Steinbrück, A., Stranik, O., Csáki, A., Fritzsche, W., Sensoric potential of gold–silver core–shell nanoparticles. *Anal. Bioanal. Chem.* 2011, *401*, 1241–1249.

[91] Pustovalov, V., Astafyeva, L., Fritzsche, W., Optical properties of core–shell gold–silver and silver–gold nanoparticles for near UV and visible radiation wavelengths. *Plasmonics* 2012, *7*, 469–474.

[92] Dubois, L. H., Nuzzo, R. G., Synthesis, structure and properties of model organic surfaces. *Annu. Rev. Phys. Chem.* 1992, *43*, 437–463.

[93] Zhang, X., Servos, M. R., Liu, J., Instantaneous and quantitative functionalization of gold nanoparticles with thiolated DNA using a pH-assisted and surfactant-free route. *J. Am. Chem. Soc.* 2012, *134*, 7266–7269.

[94] Lévy, R., Thanh, N. T. K., Doty, R. C., Hussain, I. et al., Rational and combinatorial design of peptide capping ligands for gold nanoparticles. *J. Am. Chem. Soc.* 2004, *126*, 10076–10084.

[95] Dominguez-Medina, S., Blankenburg, J., Olson, J. et al., Adsorption of a protein monolayer via hydrophobic interactions prevents nanoparticle aggregation under harsh environmental conditions. *ACS Sustain. Chem. Eng.* 2013, *1*, 833–842.

[96] Templeton, A. C., Wuelfing, W. P., Murray, R. W., Monolayer-protected cluster molecules. *Acc. Chem. Res.* 2000, *33*, 27–36.

[97] Lamture, J. B., Beattie, K. L., Burke, B. E., Eggers, M. D. et al., Direct detection of nucleic acid hybridization on the surface of a charge coupled device. *Nucleic Acids Res.* 1994, *22*, 2121–2125.

[98] Möller, R., Csaki, A., Köhler, J. M., Fritzsche, W., DNA probes on chip surfaces studied by scanning force microscopy using specific binding of colloidal gold. *Nucleic Acids Res.* 2000, *28*, e91.

[99] Grabarek, Z., Gergely, J., Zero-length crosslinking procedure with the use of active esters. *Anal. Biochem.* 1990, *185*, 131–135.

[100] Kolb, H. C., Finn, M. G., Sharpless, K. B., Click chemistry: Diverse chemical function from a few good reactions. *Angew. Chem. Int. Ed.* 2001, *40*, 2004–2021.

[101] Haensch, C., Hoeppener, S., Schubert, U. S., Chemical modification of self-assembled silane based monolayers by surface reactions. *Chem. Soc. Rev.* 2010, *39*, 2323–2334.

[102] Egholm, M., Buchardt, O., Nielsen, P. E., Berg, R. H., Peptide nucleic acids (PNA). Oligonucleotide analogs with an achiral peptide backbone. *J. Am. Chem. Soc.* 1992, *114*, 1895–1897.

[103] Su, X., Kanjanawarut, R., Control of metal nanoparticles aggregation and dispersion by PNA and PNA-DNA complexes, and its application for colorimetric DNA detection. *ACS Nano* 2009, *3*, 2751–2759.

[104] Kim, D., Jeong, Y. Y., Jon, S., A drug-loaded aptamer—Gold nanoparticle bioconjugate for combined CT imaging and therapy of prostate cancer. *ACS Nano* 2010, *4*, 3689–3696.

[105] Tanaka, K., Mitsushima, A., Yamagata, N., Kashima, Y. et al., Direct visualization of colloidal gold-bound molecules and a cell-surface receptor by ultrahigh-resolution scanning electron microscopy. *J. Microsc.* 1991, *161*, 455–461.

[106] Wulff, G., Molecular imprinting in cross-linked materials with the aid of molecular templates—A way towards artificial antibodies. *Angew. Chem. Int. Ed. Engl.* 1995, *34*, 1812–1832.

[107] Chaiet, L., Wolf, F. J., The properties of streptavidin, a biotin-binding protein produced by streptomycetes. *Arch. Biochem. Biophys.* 1964, *106*, 1–5.

[108] Hiriyanna, K., Varkey, J., Beer, M., Benbow, R., Electron microscopic visualization of sites of nascent DNA synthesis by streptavidin-gold binding to biotinylated nucleotides incorporated in vivo. *J. Cell Biol.* 1988, *107*, 33–44.

[109] Beattie, K. L., Monodisperse colloids of transition metal and lanthanide compounds. *Pure Appl. Chem.* 1989, *61*, 937–941.

5.2. High-Throughput Synthesis of Uniform Silver Seed Particles by a Continuous Microfluidic Synthesis Platform [MT2]

Autorenschaft der Publikation:

Matthias Thiele	Konzeptentwicklung und Verfassen des Manuskripts (inkl. Abbildungen)
	Diskussion und Korrektur des Manuskripts
	Kalkulation der Fluidparameter und Etablierung der Plattform
	Adaption der Synthese auf mikrofluidische Verfahren
	Erhebung und Evaluieren der Daten
Andrea Knauer	Diskussion des Konzepts und der Ergebnisse
	Diskussion und Korrektur des Manuskripts
Andrea Csáki	Diskussion und Korrektur des Manuskripts
	Diskussion des Konzepts und der Ergebnisse
Daniéll Malsch	Entwerfen und Anfertigen der Mikromischer
	Einführen in mikrofluidische Druckmessungen
Thomas Henkel	Entwerfen und Anfertigen der Mikromischer
	Diskussion des Konzepts und der Ergebnisse
J. Michael Köhler	Korrektur des Manuskripts
Wolfgang Fritzsche	Diskussion und Korrektur des Manuskripts
	Projektleitung

Vorschlag zur Anrechnung der Publikationsäquivalente: **1**

Chem. Eng. Technol. 2015, 38, No. 7, 1131–1137

Der Nachdruck der folgenden Publikation erscheint mit freundlicher Genehmigung von *Chemical WILEY-VCH.* Reprinted with kind permission from *WILEY-VCH*

Matthias Thiele[1]

Andrea Knauer[2]

Andrea Csáki[1]

Daniell Mallsch[1]

Thomas Henkel[1]

Johann Michael Köhler[2]

Wolfgang Fritzsche[1]

[1]Leibniz Institute of Photonic Technology, Jena, Germany.

[2]Ilmenau University of Technology, Institute for Physics, Dept. of Physical Chemistry and Micro Reaction Technology, Ilmenau, Germany.

High-Throughput Synthesis of Uniform Silver Seed Particles by a Continuous Microfluidic Synthesis Platform

Controlled silver particle geometries require at least a synthesis in two steps which strongly differ in their reaction kinetics. For the first step, the very fast seed formation, chaotic advection-based micromixers are tested in combination with a batch reactor for the growth step. Nanoparticles with narrow size distribution and excellent shape uniformity can be prepared in large batches. To achieve a highly reproducible and homogeneous particle solution, a microfluidic system containing three different micromixers for optimal mixing of the chemical precursors is established, allowing stringent control of every synthesis step. The produced silver particles can be used as seeds for forming anisotropic particles. Their further potential is demonstrated by preparation of anisotropic silver triangles. The thus generated seed particles are better suited for growing to triangles than those from conventional batch synthesis.

1 Introduction

Metal nanoparticles are becoming favorite objects in current plasmonics [1]. Their extraordinary optical properties in form of sharp optical resonances, i.e., localized surface plasmon resonances (LSPR), are based on coherent oscillations of free conductive electrons upon irradiating electromagnetic waves [2]. The position of the LSPR and, therefore, the potential application strongly depends on the material, size, and shape of the nanoparticles [3]. These factors can be adjusted by the chemical synthesis. Different applications as biochip- or cell-label [4, 5], as optical antenna for manipulation of biomolecules [6, 7], or as sensor transducer [8] are based on this potential.

The application of gold spheres (LSPR by 520 nm) in bioanalytics is widely spread [8–10]. These particles are chemically relative stable, their synthesis and biofunctionalization is well-established, and they are well biocompatible. Unfortunately, these particles are limited by their LSPR wavelength range above 520 nm. Triangular-shaped silver nanoparticles offer much higher scattering and absorption efficiency and additionally a spectral range tunable over the whole visible and infrared spectral range from 400 to 1200 nm [11] but the chemical synthesis of silver triangles is more complex compared to spheres

[12–14]. In classical batch synthesis, the resulting nanoparticles are often polydisperse and their plasmonic properties, based on their geometry, are difficult to control. The critical part in the two-step synthesis is the first step, i.e., generation of small crystalline seed nanoparticles. In general, miniaturization in the synthesis can be helpful to optimize this step [15].

Different strategies of microfluidics starting from a small capillary up to a complex network of different fluid units have been proposed [16, 17]. The main advantage of microfluidic systems is the small dimension of the channels and structures which results in shorter diffusion lengths and a higher surface-to-volume-ratio. Consequently, microsystems allow for a fast exchange of material and energy [5, 13, 18, 19]. For an optimal synthesis, the mixing parameters are of key importance. Changes in mixing conditions can result in uncontrollable colloid morphologies and/or various sizes. Therefore, with increasing complexity of the particle shape, more control during the synthesis is needed. Direct control of the synthesis parameters allows the immediate control during the synthesis to reach a homogeneous composition of the mixture [14]. This is the basis for the synthesis of nanoparticles with homogeneous particle size distribution and well-defined particle geometry.

A novel system is described with a combination of different microfluidic units to create small and monodisperse silver seed particles utilizing a rather fast reducing agent ($NaBH_4$). Three different micromixers allow optimal mixing conditions of the reaction adducts and overcome diffusion limitations of classical methods and, therefore, variations in particle size and crystallinity. The resulting defined seed particles enable a defined

Correspondence: Dr. Andrea Csáki (csaki@ipht-jena.de), Leibniz Institute of Photonic Technology, Albert-Einstein-Straße 9, 07745 Jena, Germany.

synthesis of silver triangles in the subsequent growing step. The exact tuning of the optical properties of the resulting silver triangles is the basis of enhanced future bioanalytical applications.

2 Experimental

2.1 Experimental Setup

All mixers and units were prepared under cleanroom conditions by photolithography and subsequent wet-chemical etch processes. The Dean flow mixer (DFM, Fig. 1 c) and T-mixer (Fig. 1 a) were prepared with two glass (borofloat) layers with a half-channel in each layer. The T-mixer served as a single T-mixer (2× in, 1× out, 1× closed). Therefore, one channel was blocked with paraffin. The split-and-recombine-mixer (SAR mixer, Fig. 1 b) consists of three layers (glass-silicon-glass). All layers of the individual mixer were connected by an anodic bonding process.

The geometrical and channel parameters of the mixers are summarized in Tab. 1. All mixers were aligned in special mounts which were also prepared at the IPHT, enabling a precise connection of the chip-integrated fluid ports by polytetra-fluoroethylene (PTFE) tubes with an inner diameter of 0.5 mm (Jasco Germany GmbH, Gross-Umstadt, Germany). For carrying the fluids, the pump Cedosis (cetoni GmbH, Korbußen Germany) was employed which allows the parallel use of four individual channels.

2.2 Experimental Procedure

The preparation of silver nanotriangles is a modified method based on the work of Aherne et al. [13]. It is split in a two-step synthesis part. First, the silver seed particles are prepared. In a second, the growing step, the prepared seeds are used to start a 2D growth that results in silver triangles.

2.2.1 Batch Synthesis of Silver Seed Particles (bSEED)

The standard protocol for the synthesis of small silver seed particles is a discontinuous batch approach at room temperature as illustrated in Fig. 2. Under vigorous stirring, 250 μL poly(sodium 4-sty-renesulfonate (PSSS; 0.5 g L^{-1}; Sigma-Aldrich Chemie GmbH Munich, Germany) as a facet blocking reagent and 300 μL of ice-cooled NaBH$_4$ (10 mM; Carl Roth GmbH & Co. KG, Karlsruhe, Germany) as reducing agent were added to 5 mL of a sodium citrate solution (2.5 mM; Carl Roth). Following the drop-wise addition of silver nitrate (0.5 mM, Merck KgaA, Darmstadt, Germany), a color change from transparent to bright yellow was observed pointing out the formation of small silver nanoparticles.

2.2.2 Continuous Microfluidic Synthesis of Silver Seed Particles (μSEED)

In order to allow a better comparison, the chemicals and concentrations utilized for the continuous synthesis in the microfluidic setup and the batch approach were the same. An exception is NaBH$_4$, which was used in the same concentration but diluted in 10 mM NaOH (Carl Roth) instead of water. This small change results in a higher stability of the species at room temperature that minimizes the need for cooling the NaBH$_4$ solution [20]. Instead of adding the chemical into the flask, glass syringes (ILS GmbH, Stützerbach, Germany) were taken, arranged in the syringe pump and connected with the micro-mixers (Fig. 3).

2.2.3 Selective Growth of Silver Seed Particles to Silver Nanoprisms

The possibility for an anisotropic growth of the as-prepared seeds is used as a proof of their quality and for a direct comparison of microfluidic- and batch-prepared seeds. Before growing silver seeds to prisms, [BH$_4$]$^-$ has to be fully consumed. To prevent any influence of borohydride to the growing step, the seeds were incubated for at least 15 h at room temperature (23 °C) prior to further use. Under strict stirring, 75 μL of a
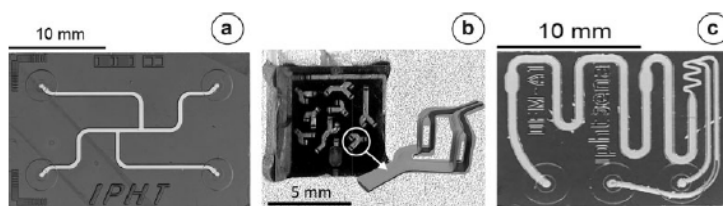

Figure 1. Microreactors used in the synthesis device. (a) Glass/glass double T-mixer (one channel is closed for use as single T-mixer), (b) glass/Si/glass split-and-recombine (SAR) mixer, (c) glass/glass Dean flow mixer.
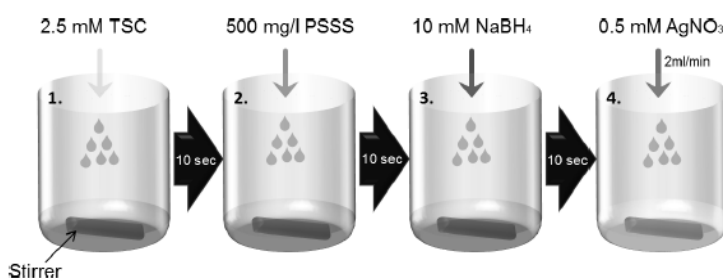

Figure 2. Steps of the batch seed synthesis. The sequence of the chemical steps is crucial.

Table 1. Comparison of the parameters for the different micromixers.

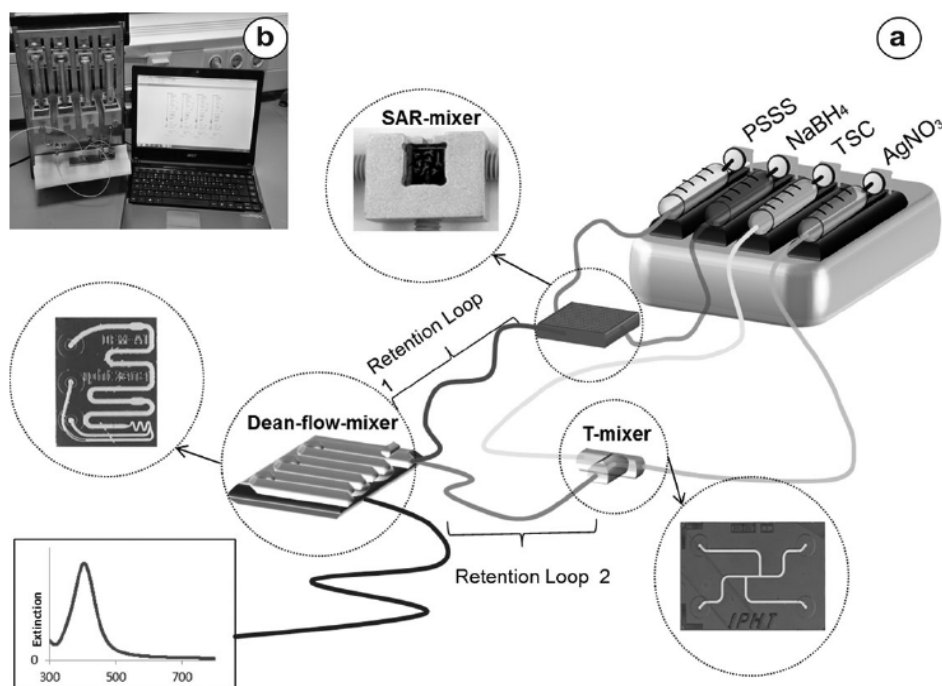|	T-mixer	SAR mixer	DFM
Mask width [mm]	0.3	0.075	0.05
Etch depth [mm]	0.13	0.075	0.13
Material	Glass	Glass/silica/glass	Glass

Figure 3. Continuous-flow synthesis of silver seed particles: scheme (a) and image (b) of the complete synthesis setup.

freshly prepared ascorbic acid solution (10 mM; Carl Roth) was added to 5 mL ultrapure water. Next, a varying amount (10–650 µL) of seed particles was added. The concentration, or in this case the volume, of the used seeds in the growing solution correlates with the final prisms size, i.e., edge length, and therefore also with the position of the LSPR peak and the color of the particle solution [13].

A higher concentration of seeds gives smaller prisms and shorter wavelengths for the LSPR peak positions, whereas a lower concentration results in larger edge lengths and higher plasmon wavelengths. The next step was the drop-wise addition of 3 mL AgNO$_3$ (0.5 mM) under permanent stirring. By adding the silver ions, the growing is initiated and becomes visible by a change in the solution color depending on the used amount of seeds as mentioned above. For charge stabilizing the prisms, 500 µL of sodium citrate (25 mM) was added to the suspension after ~ 2 min of finishing the AgNO$_3$ addition.

2.3 Characterization of Nanoparticles

The prepared particles were stored in the dark at 8 °C until they were characterized by transmission electron microscopy (TEM; Zeiss DSM 960, Jena, Germany), high-resolution TEM (HR-TEM; JEM-3010, Jeol, Tokyo, Japan), scanning electron microscopy (SEM; JSM 6700F, Jeol, Tokyo, Japan), and scanning force microscopy (AFM; Nanoscope IIIa, Bruker Corp., Billerica, MA, USA). The synthesis yield for the triangle-shaped particles was quantified by AFM. The resulting plasmon peaks were measured with a UV-VIS spectrometer Jasco V-630 (JASCO Germany GmbH, Gross-Umstadt, Germany).

3 Results and Discussion

3.1 Synthesis of Silver Seed Particles Using a Batch Reactor and the Continuous Microfluidic Device

The steps of a classical batch synthesis are presented in Fig. 2. In this stepwise method, one reactant after another is added into the flask, while the chemicals have to be well stirred. It is highly important to keep the order of chemicals, but it is obviously problematical to do it in a perfectly reproducible way since the time between adding of several chemicals as well as the exact mixing state are difficult to control. Due to differences between each run, the resulting silver seed particles are slightly different each time.

This problem can be solved using micromixers by which an efficient mixing can be realized without any actuator or other active mixing parts (passive mixing). Since there is no active mixing in the microreactor, there has to be an applied flow that generates the mixing. This fact can be seen as an advantage since it predestines the microfluidic synthesis approach for a continuous process. However, since four different fluids with various velocities have to be matched, a special arrangement of three different micromixers and a syringe pump are needed to create a microfluidic setup that allows an efficient mixing of all fluids in adequate manner. The complete device is presented in Fig. 3. This setup is an arrangement of a synchronized system of mixers with different fluid behaviors and mixing characteristics to handle the several flow regimes in one complex device.

In general, the system can be divided into two parts, the premixing part and the silver seed synthesis part. In the first one, all four fluids have to be merged to create two active intermedi-

ates which will be mixed in the second part to start the nucleation. An overview of the different fluid regimes in the several micromixers is presented in Tab. 2.

However, to characterize and understand the need for different mixers, some fluid and mixing parameters have to be introduced. The Reynolds number (Re) has no dimension and describes the ratio of inertial forces and viscous forces. It is used to characterize whether a flow regime is either laminar or turbulent, and on this basis causes either an enhanced or worse mixing of the fluids in the channel. The Dean number ($De = Re\,(Dh/Rc)^{1/2}$) is also a dimensionless quantity that is associated with the magnitude of the secondary flow field which can be utilized for improving fluid mixing. The De-number depends on the Re-number, the characteristic dimension of the microchannel (Dh), and the radius of curvature (Rc) of the channel bend. Around $De > 150$, secondary vortices appear, with even more complex flow fields for increasing De-number.

By transferring the synthesis process into microfluidics, the volumes of the batch approach were also transmitted into flow rates while keeping the several concentrations. This results in completely different flow rates of the single fluids and, therefore, requires different mixers. For mixing NaBH$_4$ with PSSS, a SAR mixer is employed since it creates optimal mixing by slow flow rates and small Re [21, 22]. The advantage of an SAR mixer is the cascade structure of basis elements to reach a multilamination flow in order to realize a larger surface for material exchange and to shorten the diffusion ways. The used SAR mixer consists of eight basis units that generate 256 parallel laminations, whereby one element includes splitting, reshaping, and a recombination process (Fig. 1 b) [21].

The application of different micromixers like T-mixers for this approach did not produce convincing results, e.g., seed particles with low quality or no functionality of a later anisotropic growing since the blocking agent PSSS was not efficiently mixed, and implicates the necessity for an SAR mixer. For mixing of sodium citrate and silver nitrate, a standard T-shaped mixer was used since both fluids were transported with high flow rates close to the working point of the T-mixer at a Re of 188 [23].

As indicated in Fig. 2, the two mixers represent the first steps of the synthesis part, whereas there will be no synthesis at that point. This premixing creates active intermediates and provides the required chemicals for the continuous process. Therefore, the reaction in this step is slow and in the time range of seconds. The real synthesis starts in the next step of merging the two active intermediates in which the silver ion donator and the reducing agent NaBH$_4$ come together. This is the critical step since the two intermediates have totally different flow rates, but still have to be mixed in a high-efficiency order since the reaction of nucleation and synthesis is an ultrafast reaction in the lower millisecond regime. For this purpose, a Dean flow mixer (DMF) was employed which can handle two dissimilar flow rates by utilizing the so-called Dean effect [24, 25]. The Dean effect is based on a rotation movement of the fluids caused by the curved channels (meander) and results in a swirling/turbulence that supports the convection of molecules. In each meander, the fast core-fluid replaces the slow outer-wall fluid by centrifugal force [26]. The mixer consists of five meanders and needs at least one high working flow rate. In particular, one flow rate can be slow while the other one has to be high. This is the case in the utilized setup, as seen in Tab. 2.

In contrast to the conventional batch approach where mixing is hard to control, the DFM eliminates local differences in concentrations and achieves optimal mixing conditions. Both the T-mixer and the DFM depend on secondary flow fields for efficient fluid mixing [26] but only by using the glass DFM it is possible to handle fast reaction (< milliseconds [27]) and therefore control the synthesis of uniform silver seed particles by applying the strong reducing agent NaBH$_4$.

Borohydride is often taken for the synthesis of gold and silver nanoparticles since it is a strong reducing agent and can lead to different nanoparticle sizes. The size variation of gold nanoparticles can be contributed to the fact that NaBH$_4$ is generally used in ice-cooled water to slow down the reaction rate of water molecules and borohydride and thereby increases the reproducibility [15]. It was shown that it is difficult to control the temperature and cooling of one chemical by performing the synthesis at room temperature. So the method of NaBH$_4$ dissolved in the same concentration of NaOH was introduced that guarantees a stability/reactivity over several hours at room temperature [20]. However, since this is of high interest for a continuous synthesis over hours, another main advantage was figured out by using it generally in microreaction technique processes. During normal use of NaBH$_4$ in water, hydrogen gases out after some minutes. The hydrogen in the fluid system hinders an optimal control of flow rates and velocities since the system is now compressible and uncontrolled energy dissipation can occur. By using NaBH$_4$ diluted in NaOH, the borohydride is stabilized and no gas hinders the fluid control. This observation is crucial since it predestinates the general use of NaBH$_4$ for microfluidic applications.

Table 2. Fluidic parameters for the microfluidic setup for continuous silver seed (μSEED) particle synthesis.

Micromixer	Chemical	Flow rate [μL s^{-1}]	Flow velocity in each mixing unit [m s^{-1}]	Re	De
SAR mixer	NaBH$_4$	2	0.253	27	65
	PSSS	1.67			
T-mixer	TSC	33	0.509	188	216
	AgNO$_3$	33			
DFM	Intermediate 1	3.67	1.698	457	671
	Intermediate 2	66			

During the synthesis process, some kind of reactor fouling by deposition of silver at the channel walls can be observed (Fig. 4) starting after some minutes. The fouling in microfluidic reactors represents a well-known problem in microfluidics [28]. The fluid behavior of the mixers was characterized before and after a synthesis with the result that the influence of the reactor fouling on the fluidic behavior is limited. As depicted in Fig. 4, the channel shrinking was recalculated by measuring the pressure. After 12 min with 50 mL of prepared µSEED solution, the radius decreases only by 10 %. Additionally, a cleaning process with concentrated nitric acid regenerates the mixer structure completely (Fig. 4).

3.2 Comparison of Batch and Microfluidic Synthesis of Silver Seeds

For a direct comparison of the two methods, all chemicals were freshly prepared and used immediately. Moreover, exactly the same chemicals were employed and the synthesis was done at exactly the same time. Since the batch approach is a stepwise method, a maximal volume of around 10 mL can be prepared per batch. In contrast, the microfluidic approach allows a continuous synthesis theoretically without limitation except that given by the syringes. By means of 25-mL syringes, a volume of 50 mL of µSEEDs was prepared. The main differences of the resulting seed particles are obvious in the particle dimension and size distribution as indicated in Fig. 5.

While the resulting seeds in batch show a diameter of 6.1 ± 2.5 nm, the µSEEDs are much smaller with 4.7 ± 0.6 nm. With the sizes of the prepared seed particles, a theoretical concentration of around 8×10^{-8} mol L^{-1} for the microfluidic seeds and 3.2×10^{-8} mol L^{-1} for the batch seeds will be prepared. Even if the differences in the spectra and by the full width at half maximum (FWHM) firstly are not clearly visible, the µSEEDs are qualitatively better as demonstrated in the subsequent growing step. Smaller seed particles are a basic requirement for the synthesis of anisotropic nanoparticles. The comparison of
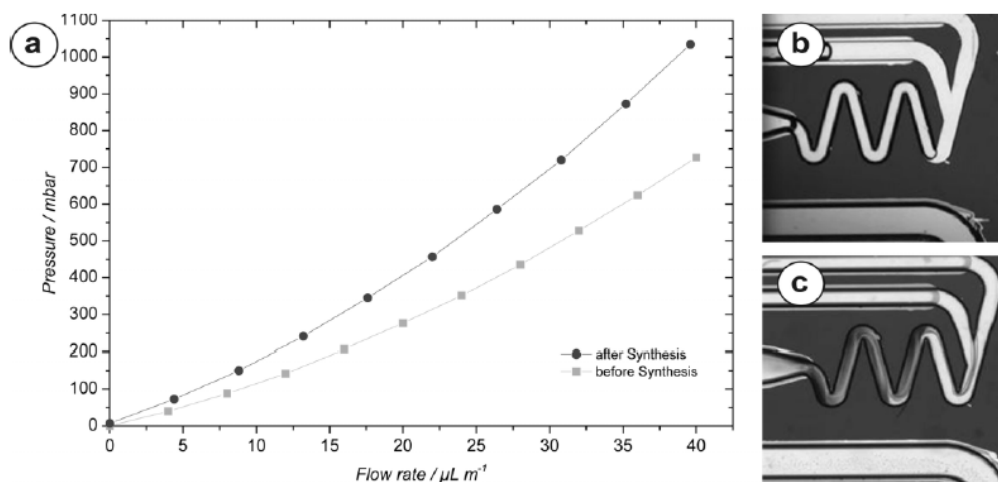

Figure 4. Fluidic behavior (a) and image of the DFM device before (b) and after (c) the synthesis, showing the influence of reactor fouling.
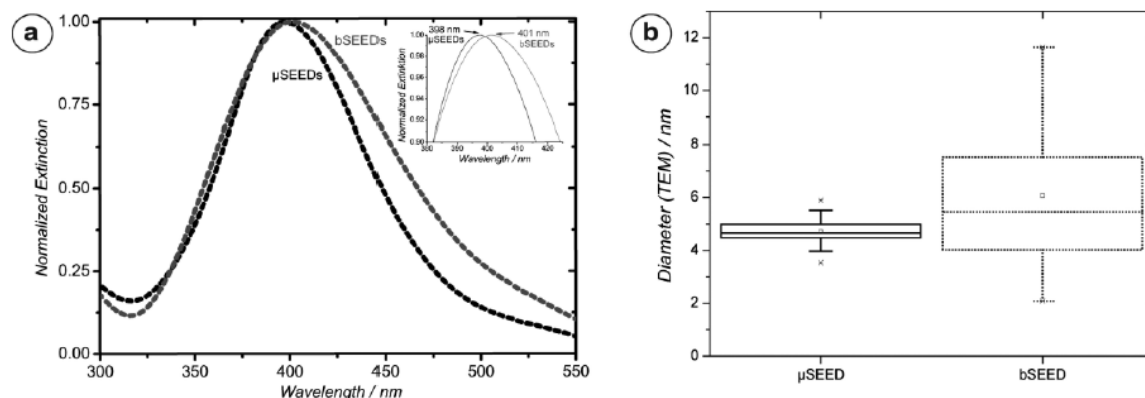

Figure 5. Direct comparison of the UV-VIS spectrum (a) and the particle diameter distribution from TEM as boxplot diagram (b). The LSPR band of the batch seeds is broader (FWHM = 112 nm) than the fluidic prepared ones (FWHM = 90 nm). (b) The fluidic ones exhibit a much narrower size distribution (6.1 ± 2.5 nm vs. 4.7 ± 0.6 nm).

the particle size distribution is shown in Fig. 5 b. The main consequence of the higher-quality seeds can be explained by an improved yield of the silver triangles compared to spherical ones in the second synthesis step from less than 70 % with bSEEDs up to 93 % using μSEEDs. The resulting triangles exhibit nearly the same dimensions and are crystalline as displayed in Fig. 6.

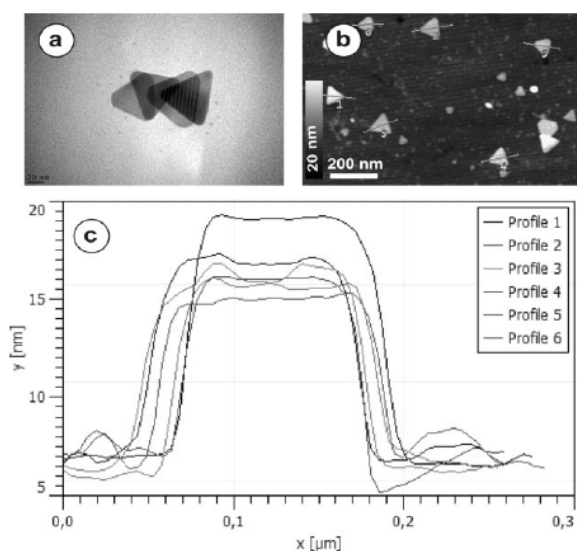

Figure 6. Silver nanoprisms (triangular-shaped nanoparticles) based on μSEEDS. (a) TEM image, (b) AFM image of silver nanoprisms, (c) corresponding high profile of different prisms in (b).

With both, the bSEEDs and the μSEEDs, it is possible to prepare silver nanoprisms. But using μSEEDs, a rather exact adjustment of the particle dimension, here edge length and thickness, and therefore the position of the plasmon band is possible (Fig. 7). Compared to triangle synthesis with bSEEDs, the edge length by μSEEDs is much smaller: $75\,\mu L \rightarrow 81\,nm$ (batch) and $60\,nm$ (fluidic); $200\,\mu L \rightarrow 46\,nm$ (batch) and $44\,nm$ (fluidic); $400\,\mu L \rightarrow 31\,nm$ (batch) and $27\,nm$ (fluidic), at a thickness of $11\,nm$. The resulting silver triangles are excellent optical transducers for LSPR sensing with exactly adjustable spectral properties for future life science applications.

4   Summary and Conclusions

A novel microfluidic device is presented for the defined synthesis of silver triangular-shaped nanoparticles with a high-throughput continuous seed particle synthesis in the first step. Instead of $\sim 10\,mL$ seed particles solution for the batch approach, the microfluidic setup allows a continued synthesis of tens of milliliters and a seed particle concentration of $\sim 8 \times 10^{-8}\,mol\,L^{-1}$. The device combines three different micromixers, namely, a split-and-recombine-mixer, a T-shaped mixer, and a Dean-flow-mixer, in one platform for a defined fluid manipulation. This is necessary for the synthesis of silver seed particles in a two-step synthesis process. The chemical adducts were optimally mixed, and the resulting seed particles are well-defined and sufficiently small for the subsequent synthesis step, i.e., the growth in triangular-shaped geometry in batch. Future work will be focused on the complete automation of the synthesis with real-time reaction control and testing of the resulting plasmonic nanoparticles for biosensing applications.
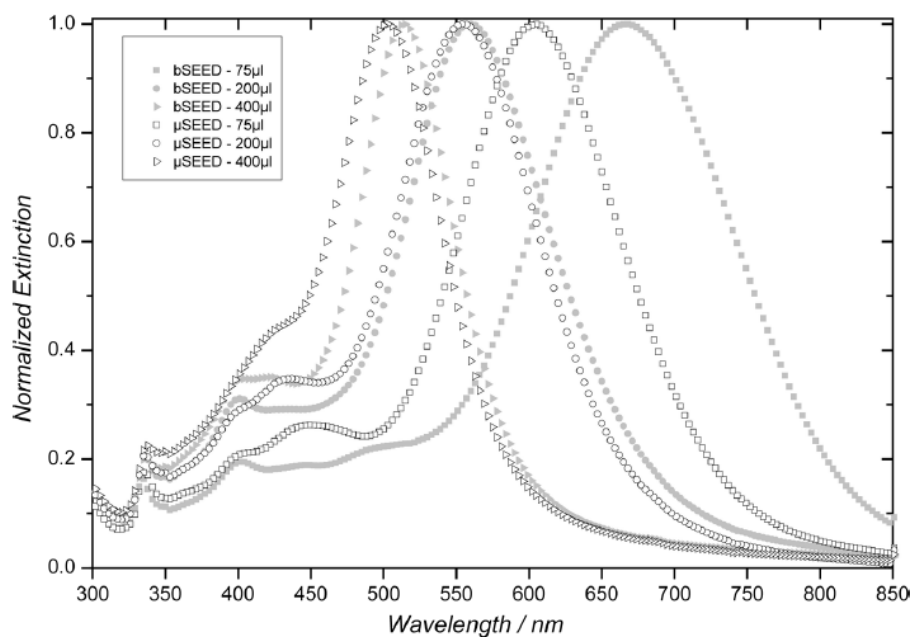

Figure 7. Spectral comparison of grown silver prisms from bSEEDs and μSEEDs.

Chemical Engineering & Technology Research Article

Abbreviations

μSEED	microfluidic device-generated silver seed particles
AFM	scanning force microscopy (atomic force microscopy)
bSEED	batch reactor-generated silver seed particles
De	Dean-number
DFM	Dean flow mixer
FWHM	full width at half maximum
HR-TEM	high-resolution TEM
LSPR	localized surface plasmon resonances
PSSS	poly(sodium 4-styrenesulfonate)
PTFE	polytetrafluoroethylene
Re	Reynolds-number
SAR	split-and-recombine(-mixer)
SEM	scanning electron microscopy
TEM	transmission electron microscopy
TSC	trisodium citrate
UV-VIS	ultraviolet and visible

References

[1] A. Csáki et al., *Philos. Trans. R. Soc. London, Ser. A* **2011**, *369 (1950)*, 3483–3496. DOI: 10.1098/rsta.2011.0145

[2] U. Kreibig, M. Vollmer, *Optical Properties of Metal Clusters*, Series in Materials Science, Springer, Berlin **1995**.

[3] A. Csáki et al., in *Gold Nanoparticles: Properties, Characterization and Fabrication* (Ed: P. E. Chow), Nova Science Publishers, Hauppauge, NY **2010**.

[4] J. Reichert, A. Csáki, J. M. Kohler, W. Fritzsche, *Anal. Chem.* **2000**, *72 (24)*, 6025–6029. DOI: 10.1021/Ac000567y

[5] W. Fritzsche, T. A. Taton, *Nanotechnology* **2003**, *14 (12)*, R63.

[6] J. Wirth et al., *Nano Lett.* **2011**, *11 (4)*, 1505–1511. DOI: 10.1021/Nl104269x

[7] A. Csáki et al., *Nano Lett.* **2007**, *7 (2)*, 247–253.

[8] T. Schneider et al., *J. Nanopart. Res.* **2013**, *15 (4)*, 1–10. DOI: 10.1007/s11051-013-1531-7

[9] C. A. Mirkin, R. L. Letsinger, R. C. Mucic, J. J. Storhoff, *Nature* **1996**, *382 (6592)*, 607–609.

[10] A. Csáki, R. Möller, W. Fritzsche, *Expert Rev. Mol. Diagn.* **2002**, *2 (2)*, 187–193.

[11] M. Rycenga et al., *Chem. Rev.* **2011**, *111 (6)*, 3669–3712. DOI: 10.1021/cr100275d

[12] R. Jin et al., *Science* **2001**, *294 (5548)*, 1901–1903.

[13] D. Aherne, D. M. Ledwith, M. Gara, J. M. Kelly, *Adv. Funct. Mater.* **2008**, *18 (14)*, 2005–2016.

[14] A. Knauer et al., *Chem. Eng. J.* **2012**, *227*, 80–89. DOI: 10.1016/j.cej.2012.10.008

[15] J. M. Köhler, S. Li, A. Knauer, *Chem. Eng. Technol.* **2013**, *36 (6)*, 887–899. DOI: 10.1002/ceat.201200695

[16] A. Knauer et al., *J. Phys. Chem. C* **2012**, *116 (16)*, 9251–9258. DOI: 10.1021/Jp210842g

[17] A. Knauer et al., *Chem. Eng. J.* **2013**, *227*, 191–197. DOI: 10.1016/j.cej.2012.07.041

[18] C.-X. Zhao, L. He, S. Z. Qiao, A. P. J. Middelberg, *Chem. Eng. Sci.* **2011**, *66 (7)*, 1463–1479. DOI: 10.1016/j.ces.2010.08.039

[19] Y. Song, J. Hormes, C. S. S. R. Kumar, *Small* **2008**, *4 (6)*, 698–711. DOI: 10.1002/smll.200701029

[20] M. N. Martin, J. I. Basham, P. Chando, S.-K. Eah, *Langmuir* **2010**, *26 (10)*, 7410–7417. DOI: 10.1021/la100591h

[21] W. Ehrfeld, V. Hessel, V. Haverkamp, *Microreactors*, Wiley Online Library, **2000**.

[22] V. Hessel, H. Löwe, F. Schönfeld, *Chem. Eng. Sci.* **2005**, *60 (8–9)*, 2479–2501. DOI: 10.1016/j.ces.2004.11.033

[23] S. Dreher, N. Kockmann, P. Woias, *Heat Transfer Eng.* **2009**, *30 (1–2)*, 91–100. DOI: 10.1080/01457630802293480

[24] W. R. Dean, *The London, Edinburgh, and Dublin Philos. Mag. J. Sci.* **1927**, *4 (20)*, 208–223.

[25] W. R. Dean, *Philos. Mag. Ser. 7* **1928**, *5 (30)*, 673–695. DOI: 10.1080/14786440408564513

[26] A. P. Sudarsan, V. M. Ugaz, *Proc. Natl. Acad. Sci. U.S.A.* **2006**, *103 (19)*, 7228–7233. DOI: 10.1073/pnas.0507976103

[27] P. Jörg et al., *J. Phys. Conf. Ser.* **2010**, *247 (1)*, 012051.

[28] J. Wagner, J. M. Kohler, *Nano Lett.* **2005**, *5 (4)*, 685–691. DOI: 10.1021/nl050097t

5.3. Gold nanocubes – Direct comparison of synthesis approaches reveals the need for a microfluidic synthesis setup for a high reproducibility [MT3]

Autorenschaft der Publikation:

Matthias Thiele	Konzeptentwicklung und Verfassen des Manuskripts (inkl. Abbildungen)
	Aufbau und Etablierung des CF mikrofluidischen Systems
	Erhebung und Evaluieren der Daten
	Charakterisierung der Nanopartikel
Joanne Zi En Soh	Erhebung und Evaluieren der Daten bezüglich SF-Verfahren
Andrea Knauer	Charakterisierung der Nanopartikel
	Diskussion des Konzepts und der Ergebnisse
	Diskussion und Korrektur des Manuskripts
Daniéll Malsch	Entwerfen und Anfertigen der Mikromischer
	Simulation der Mischparameter
Ondrej Stranik	Diskussion und Korrektur der Datenauswertung
	Erarbeiten der FOM
Robert Müller	Diskussion des Konzepts und der Ergebnisse
Andrea Csáki	Diskussion des Konzepts und der Ergebnisse
	Korrektur des Manuskripts
Thomas Henkel	Simulation der Mischparameter
J. Michael Köhler	Diskussion und Korrektur des Manuskripts
Wolfgang Fritzsche	Diskussion und Korrektur des Manuskripts
	Projektleitung

Vorschlag zur Anrechnung der Publikationsäquivalente: 1

Gold nanocubes – Direct comparison of synthesis approaches reveals the need for a microfluidic synthesis setup for a high reproducibility

CrossMark

Matthias Thiele [a,*], Joanne Zi En Soh [b], Andrea Knauer [c], Daniell Malsch [a], Ondrej Stranik [a], Robert Müller [a], Andrea Csáki [a], Thomas Henkel [a], J. Michael Köhler [c], Wolfgang Fritzsche [a]

[a] Leibniz Institute of Photonic Technology (IPHT), Dept. of Nano Biophotonics, Albert-Einstein-Straße 9, 07745 Jena, Germany
[b] Universiti Teknologi Malaysia, Advanced Diagnostics and Progressive Human Care Research, Skudai, 81310 Johor, Malaysia
[c] Technische Universität Ilmenau, Institute for Chemistry and Biotechnology, Dept. of Physical Chemistry and Micro Reaction Technology, Gustav-Kirchhoff-Str. 1, D-98693 Ilmenau, Germany

HIGHLIGHTS

- Pointing out the need of four steps-synthesis (different incubation times) of Au-cubes.
- Investigates kinetic study and highlights the variations for different growth steps.
- We create a FOM (TEM, UV–VIS) for easy quantifications of the critical parameters.
- Discusses the need of reactor types (batch, microfluidics) for different parameters.
- Show automation ways, raise in yield/shape & reduced material usage by microfluidics.

GRAPHICAL ABSTRACT
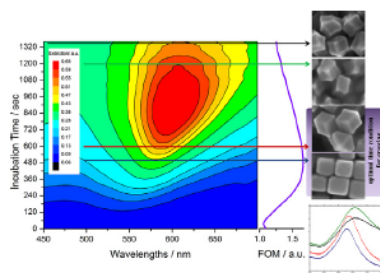
ARTICLE INFO

ABSTRACT

The production of non-spherical gold nanoparticles is a rather complex process and requires a multistep synthesis including surface blocking detergents such as CTAC and CTAB (cetyltrimethylammonium chloride; -bromide). Especially gold nanocubes are difficult to realize since they have six close packed 100-planes and they need at least three separate, highly controlled production steps: the synthesis step, where the seed particles will be formed, followed by two independent growing steps. One main challenge is to find the optimal conditions for the different steps, since the incubation times differs in several magnitudes for each step (seeds: ms, growing solution 1: sec, growing solution 2: min). Based on this discrepancy we present a study and comparison of different synthetic methods for each step. Starting with a classical batch approach we also transferred the synthesis into microfluidics and therefore compare continuous (one-phase) as well as segmented flow techniques, and discusses the benefits of each method. We present the additional advantage of CTAC in microfluidics since it passivates the channel surfaces and thereby inhibits clogging. A further detailed kinetic study of the two growing steps identifies the incubation time as critical parameter for a defined (cubed-like) geometry and facilitates the use of microfluidic methods for the first growing step, since it eliminates subjective decisions. Due to the kinetic study in combination with electron-microscopic characterization we propose a Figure Of Merit (FOM) for the second growth step that simplifies the evaluation of the point in time when to terminate the reaction to obtain perfectly shaped Au nanocubes. We also demonstrate the sensitivity (comparison of Au

433

nanocube and Au nanosphere) and the possibility of tuning the cube edge length (and so the plasmon peak position) and highlight their correlation as a fundament for an automated microfluidic synthesis and versatile applications, like biosensing.

1. Introduction

Noble metal – such as gold (Au) and silver (Ag) – nanoparticles (meNP) exhibit unique physical and chemical properties attributed to their intermediate sizes between bulk and molecular compounds. Especially the optical behavior is characteristic, since the conductive electrons of nano scaled noble metals behave like an oscillate dipole while exciting with coherent light and resulting in a surface plasmon. In the case of planar metal (layers) this process is known as surface plasmon resonances (SPR), for meNP it is termed localized surface plasmon resonance (LSPR). The plasmon resonance is the base for different kinds of optical labels and sensors in biology, chemistry and medicine [1–5]. Changes in the surrounding medium – in detail the change of the refractive index (RI) around the particle – such as induced by the binding of molecular layers result in a shift of the LSPR signal and can be measured without any previous labeling [6]. Indeed the meNP acts as a mediator, known as optical transducer [3]. Based on this principle, it is possible to realize different arrangements of LSPR-sensors like meNP solutions or immobilized meNP (ensembles or single particles) [7] to detect various kinds of analytes like small molecules, DNA, proteins, or even whole cells [2,8–14]. Depending on composition, size, and shape, different resonance regimes and sensitivities can be realized [15,16]. Furthermore, the use of anisotropic meNPs like cubes, prisms, bipyramids and rods enables amplified signals based on the local field enhancement at tips and corners [16,17]. Especially surface enhanced Raman spectroscopy (SERS) benefits from these features. However, based on the different aim and the need of defined meNP, a lot of effort was done in new NP-designs [18–21], whereas for many applications a fine tuning is still needed regarding yield, quality, reproducibility and simplicity. One example is the synthesis of gold nanocubes [17,22,23] which is widely considered as difficult since the cubes are confined by six closed 100-planes, requiring for their formation exact growth conditions. Xia et al. [24] also described how small changes in temperature, mixing conditions, precursor composition, impurity and reaction-time can lead to different results and further discusses microfluidic platforms as a strategy to fulfill these requirements [25]. In this work we describe a reproducible protocol that is based on the micro fluid technique and leads to the generation of homogeneous gold nanocubes with adjustable geometrical dimensions, high yields of the desired shape, and narrow particle size distributions.

The synthesis method is based on a protocol published in 2010 by Wu et al. [26] in conventional flask based laboratory batch-type (discontinuous, Fig. 1a) reaction. The synthesis consists of three steps (depicted in Fig. 2) and is transferred into microfluidic techniques, whereat continuously (the mixed fluid streams and therefore also the resulting solution have the same phase Fig. 1b) and segmented flow (a fluid stream consisting of two phases, that creates in-line small separated droplets as single reactors Fig. 1c) approaches will be used and compared directly. Compared to the poor mixing qualities of conventional batch methods, we show that with microfluidic approaches a precise control and mass transfer for the nucleation and the grow processes is possible. That allows us to control the different requirements for the several synthesis steps (Fig. 2) and yields ideal homogeneity of Au seed particles based on the good mixing opportunities. We will further show that the success of the protocol depends on a strict schedule of time-critical process steps. This again will be supported by using microfluidics with well-defined residence times that enables a significantly increased reproducibility of optimal shaped Au nanocubes and a simple tuning of particle sizes, since the micro flow-through based protocol is much less prone to random errors during the synthesis. The segmented flow technique also realizes a decreased reactor volume down to segment volumes of some pl and nl by keeping the mixing conditions and therefore minimizes material consumption [27]. Regarding this, we will discuss the benefit of microfluidics at each step. At the end we will shortly compare the sensitivity (shift of the plasmon peak by changing the RI) of classical spherical and cubed Au nanoparticles, to highlight the potential of Au nanocubes for sensor applications.

2. Experiments

The synthesis of Au cubes is based on the procedure of Wu et al. [26] that includes three steps. Fig. 2 provides the chronology of the three synthetic steps and lists the appropriate method, that is used for this step. At the beginning of synthesis, Au seeds are produced by reduction of gold ions with sodium borohydride in the presence of CTAC. The formation of gold cubes is achieved by growing the Au seeds through a metal-catalyzed deposition of gold atoms upon the reduction of gold salt solution with ascorbic acid. For all steps, the conventional synthesis procedure (batch) is done by following
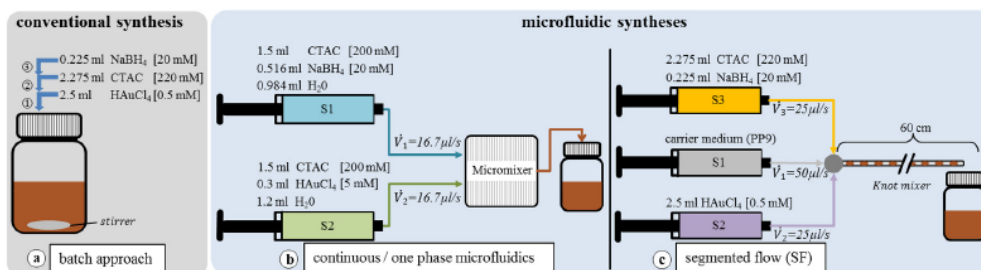

Fig. 1. Comparison of different synthesis methods for Au seed particles and experimental arrangement, including the used chemical and fluidic parameters. For the conventional synthesis a discontinuous batch approach (a) is used whereas two microfluidic approaches based on continuous (b) and segmented flow (c) technique are used.
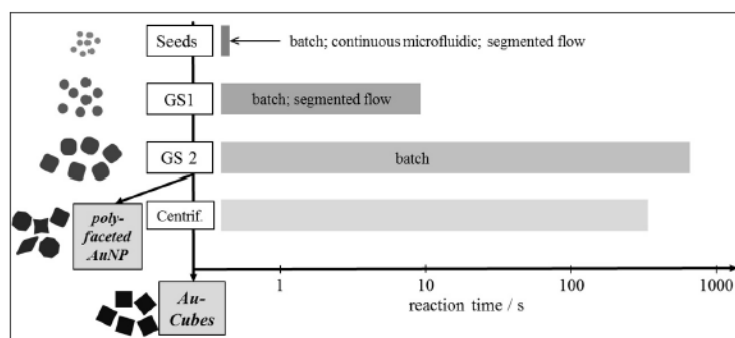
Fig. 2. Hierarchical order of the three-step synthesis for Au cubes with the corresponding reaction time on logarithmic scale and the realized experimental method for each step. (GS – grow solution; Centrif – centrifugation).

the published protocol as a reference to compare the results obtained by microfluidic synthesis. As described in Fig. 2 the seeds where synthesized using batch, segmented flow and continuous microfluidics procedures, whereat for the first growth step (GS 1) segmented flow and batch methods were used. The final second growth (GS 2) was realized by using the batch approach respectively. Fig. 1 gives an overview of all synthetic methods (batch, continuous microfluidics and segmented flow) that are used for this work.

2.1. Chemicals and materials

All chemicals were used as received from the suppliers without further purification. For the synthesis of seed particles, the chemicals were hydrogen tetrachloroaurate trihydrate ($HAuCl_4 \cdot 3H_2O$, 99.9%, Carl Roth GmbH, Karlsruhe, Germany), cetyltrimethylammonium chloride (CTAC, 98%, Merck KgaA, Darmstadt, Germany) and sodium borohydride ($NaBH_4$, 98%, Merck KGaA, Darmstadt, Germany). For growth of nanocubes, in addition to chemicals previously stated, ascorbic acid (AA, 99.7%, Merck KGaA, Darmstadt, Germany) and sodium bromide (NaBr, >99%, Sigma Aldrich Chemie GmbH, Munich. Germany) were used. Ultrapure water was used for preparation of all solutions and D-glucose (Sigma Aldrich Chemie GmbH, Munich. Germany) was used for sensitivity measurements. Perfluoromethyldecalin (PP9, F2 Chemicals Ltd., Lea Town, UK) was used as the carrier medium to implement segmented flow. For the microfluidic experiments, syringes (2.5 ml ILS, ILS Innovative Laborsysteme GmbH, Stützerbach, Germany) mounted on a multiaxial, electronically controlled syringe pump system (Cetoni NeMESYS and Cetoni Cedosis, Cetoni GmbH, Korbussen, Germany) with independently controllable axes were used. The syringes and the manifold were connected to standard available PEEK fluid connectors using PTFE tubing (Jasco Germany GmbH, Gross-Umstadt, Germany) with an inner diameter of 0.5 mm. The Dean-Flow-Mixer (DFM) and corresponding mount were fabricated in-house at the IPHT and connected via PTFE tubing as well.

2.2. Experimental procedure and setup

2.2.1. Synthesis of Au seed particles

Following to the standard protocol for the conventional synthesis of Au seeds (Fig. 1a), 2.5 ml of $HAuCl_4$ [0.5 mM] were continuously stirred (at 700 RPM; stir bar 12 mm long and 6 mm in diameter) in a 15 ml glass vial (neoLab Migge GmbH, Heidelberg, Germany) while 2.275 ml CTAC [220 mM] and 0.225 ml $NaBH_4$ [20 mM] is added. The solution turns brown after a few seconds, thereby indicating the formation of Au seed particles. For the continuous microfluidic (one phase-) synthesis of Au seeds (Fig. 1b) a

Dean-Flow-Mixer (DFM) made of glass is used [28]. The mixer has two inlets, which will merge at the mixing structure (meander with 5 bends) and a single outlet (Fig. 4). Each inlet is connected with a 2.5 ml syringe, whereby the first syringe (S1) is filled with 1.5 ml CTAC [200 mM], 0.516 ml $NaBH_4$ [20 mM] and 0.984 ml H_2O. The second syringe (S2) contains 1.5 ml CTAC [200 mM], 0.3 ml $HAuCl_4$ [5 mM] and 1.2 ml H_2O. On each syringe channel a flow of 16.7 $\mu l\,s^{-1}$ is applied, resulting in a flow of around 33 $\mu l\,s^{-1}$ at the mixing channel. The Volume of the micro structured meander is around 140 nl. The prepared, brown colored seed solution is collected in a glass vial.

For the segmented flow (SF) synthesis of Au seeds (Fig. 1c), three syringes are needed. The first syringe contains a solution of 2.275 ml CTAC [220 mM] and 0.225 ml $NaBH_4$ [20 mM], a second syringe holds a solution of 2.5 ml $HAuCl_4$ [0.5 mM]. Each channel has a flow of 25 $\mu l\,s^{-1}$. The individual aqueous reactant solutions are continuously injected into a constant stream of 50 $\mu l\,s^{-1}$ of an immiscible carrier medium (PP9) made by a third syringe to generate a segmented flow within the micro channel. All three channels are connected at a four port manifold where the segments will be created. With this setup the segments have a volume of ca. 200 nl and a length of 1 mm. After passing a knot mixer [29] and finally the outlet, both phases separate immediately from each other. The organic phase collects at the bottom of the vessel since it has a higher density, the colloidal solution on top of the carrier fluid can be taken out and processed further without any purification [27].

2.2.2. Growing of seed particles into Au nanocubes

As shown in Fig. 2, there will be a two-step growth process of the as-prepared seed particles, whereby the batch growth solution 1 (GS 1) and growth solution 2 (GS 2) includes in general the same chemicals and were each prepared in 50 ml disposable tubes. 0.25 ml $HAuCL_4$ [10 mM] were added to 9.625 ml CTAC [105 mM] followed by the addition of 0.01 ml NaBr [10 mM] and 0.09 ml of AA [40 mM]. A correct amount of ascorbic acid and Bromide-ions is crucial for the shape of the product [5,19]. At a temperature of 30 °C and under vigorous mixing a certain amount of seed particles (0.025 ml, 0.05 ml 0,75 ml and 0.1 ml) that determines the final cube size was added to the vial and shaken. Next, the resulting intermediate of GS 1 was added into GS 2 after approximately 10 s (see time axis in Fig. 2) when the color of the reaction solution changes from transparent to light pink. However, instead of the seed-particles in the GS 1, includes the GS 2 the same amount of as prepared intermediate GS 1 nanoparticles (0.025 ml, 0.05 ml 0,75 ml and 0.1 ml). As shown in Fig. 2 the GS 2 growing process is relatively long and requires to be left undisturbed for about 8 min after an initial shake. The produced particle solution had

to be centrifuged at 5000 rpm^{-1} for 3 min and re-dispersed in water. The kinetic measurements were done by adding one-third of the volumes of the previous explained grow solutions into a 3 ml glass cuvette while continuous stirring the solution (700 rpm).

For the SF grow process of GS 1 stage, the setup is similar to the one for the seed synthesis in Fig. 1c. Again, three syringes are utilized and the respective reactant concentrations and flow rates are summarized in Table 1. For achieving the optimal growth temperature of 30 °C, the mixer tubing was inserted into a resistive heating plate. After the first growing step, the resulting solution (single droplets) was directly added to GS 2 as described above.

2.2.3. Sensitivity measurements of the particle solutions

For sensitivity measurements, the particle solutions were incubated with various concentrations of glucose to change the refractive index of the solution in a controlled way, and then measure to the respective LSPR-peak position. Different glucose concentration like 0%; 5%; 10% and 20% were mixed in the ratio 1:1 (v/v) with the particular particle solution.

2.3. Characterization of nanoparticles

The prepared particles were visualized using scanning electron microscopy (SEM, Hitachi S-4800 FE-SEM, Hitachi High Technologies America, Inc, Schaumburg, Illinois) to confirm shape and size of the nanoparticles and differential centrifugal sedimentation spectroscopy (DCS, DC 20000, CPS Instruments Inc., Newtown, PA) for determination of the size and size-distribution (in case of DCS the stokes equivalent sedimentation diameter is used). The resulting plasmon peaks were measured using UV–Vis spectrophotometry (V-630, JASCO Germany GmbH, Gross-Umstadt, Germany and Specord 200, Analytik Jena AG, Germany). The crystallographic characterizations were done by diffraction XRD (X'PERT MPD Pro; PANalytical, Almelo, NL) to measure the rocking curves.

3. Results and discussion

3.1. Hierarchical order and seed particles synthesis

The synthesis of anisotropic noble-metal nanoparticles is usually a multiple-step process including the synthesis of small and uniform seed particles. Wu et al. [26] described a well working three step approach for the synthesis of Au nanocubes. In the first step, small gold seed crystals with diameters in the range of 2–3 nm are formed by reducing tetrachloroauric acid by sodium borohydride in the presence of a 0.1 M CTAC (cetyltrimethylammonium chloride) matrix. The seed nanoparticle synthesis is

Table 1
Arrangement of the chemicals in the syringes for the segmented flow growing of GS 1. The colored fields in the column of the syringes belong to the similar colored syringes in the setup in Fig. 1c, since the setup is the same for seeds and GS 1, and just the parameters are changing.

Syringe	Flow rate [µl s^{-1}]	Substance	Concentration [mM]	Volume [ml]
#1	41.7	PP9	–	2.5 (full syringe)
#2	13.3	CTAC	105	4.75
		HAuCl$_4$	10	0.25
#3	13.3	CTAC	105	4.875
		NaBr	10	0.01
		AA	40	0.09
		Au Seeds	–	0.01; 0.025; 0.04

followed by two growth steps. If one looks at the timescale of the entire procedure in Fig. 2, it is obvious, that each stage requires a different duration. Each step duration differs in at least one order of magnitude, starting from the really fast synthesis part, where the nucleation starts within the first 100 ms [30,31]. In contrast, the first growth stage of seed particles in the GS 1 requires much longer time (some seconds), followed by the last growing step of GS 2 in the minute range (for a detailed time discussion of the two growing stages see below). The different optimal reaction times depicted in Fig. 2 are the motivation to look for novel, more appropriate approaches instead of the conventional one. Since the nucleation is hard to control in conventional batch approaches (caused on the fast reaction compared to the insufficient mixing opportunities), two microfluidic approaches (continuously and segmented flow) were developed to manage the fast reaction. The transfer from a beaker method into microfluidics was realized using the experimental arrangement in Fig. 1b and c, where the chemicals where portioned into two syringes. As the seed generating reaction takes place immediately, it is crucial that the reducing agent NaBH$_4$ and the gold ions are each placed in separate syringes. The influence of the final NaBH$_4$ concentration can be found in the supporting information. A high total flow rate is applied to achieve optimal mixing conditions and keep the nucleation time interval low to form homogeneous and small seed nanoparticles. In the one (homogeneous) phase microfluidic setup, the nucleation takes place in the mixing structure ("meander") of the DFM, at the fluid-interface, at which the two streams converge (see Fig. 4). Caused by the "Dean-Effect", a rotational movement of the fluids is introduced by the curved channels and results in a swirling, that supports the convection of molecules and realizes a fast mixing [32].

A comparison of the various size distribution of conventionally and microfluidically processed Au seed nanoparticles as measured by DSC is given in Fig. 3a. Under similar chemical conditions it could be shown that the microfluidic preparation methods lead to the formation of smaller seed particles with narrower size distribution (half widths) compared to the produced particles of the conventional synthesis strategy. The result is a seed particles solution with a mean particle diameter of 2.9 nm and a FWHM (full width at half maximum) of 1.6 nm, whereas the seeds in the batch approach have a size of 3.6 nm and a FWHM of 2.0 nm. This large difference in the seed performance can be attributed to the precise control over the mixing and rapid mass transfer for the nucleation and growth process within a micromixer in contrast to the poor mixing qualities of the conventional batch method. It is also worth to note that the retention time after the continuous microfluidic synthesis has no observable influence on the fabricated seeds, since different channel-lengths after the micro mixer/nucleation spot results in the same quality and homogeneity of particles (Fig. 4 SI). Again this supports the fast mixing conditions of the precursors within 81 µs, which leads to a rapid and complete nucleation process, even suppresses polydispersity and is in good agreement with synthesis-mechanism described in the literature [31]. In contrast to synthesis in batch, in the DFM the reaction takes place after mixing is completed. In Fig. 4c the mixing characteristics of the DFM have been assessed using the instantaneous formation of a dark red ferric rhodanide complex from the two nearly colorless aqueous solutions containing FeCl$_3$ and NH$_4$SCN. Mixing is completed, if no lamination pattern between the two phases remains visible and the color intensity becomes constant. However, by using the DFM with the total internal flow rate (Q) of 33 µl s^{-1}, a sufficient mixing occurs, that is further supported by the high Reynolds (Re) and Dean (De) number of 214 and 223 and prevents concentration discrepancies of classical batch reactors [32]. In a beaker, a local high concentration of gold ions cannot be well distributed at this timescale and results in more heterogeneous particle sizes and a broader size distribution compared to
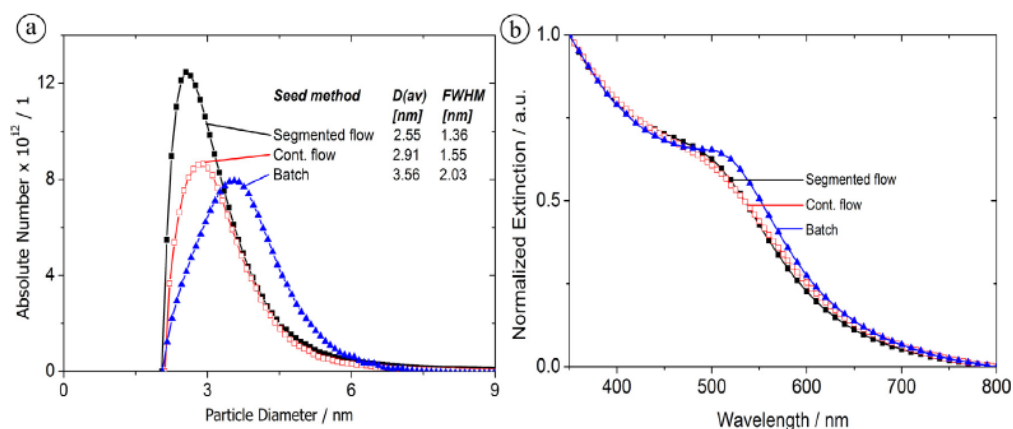
Fig. 3. Comparison of the different methods for seed particle synthesis characterized by (a) differential centrifugal sedimentation spectroscopy (DCS) and (b) UV–VIS based data.
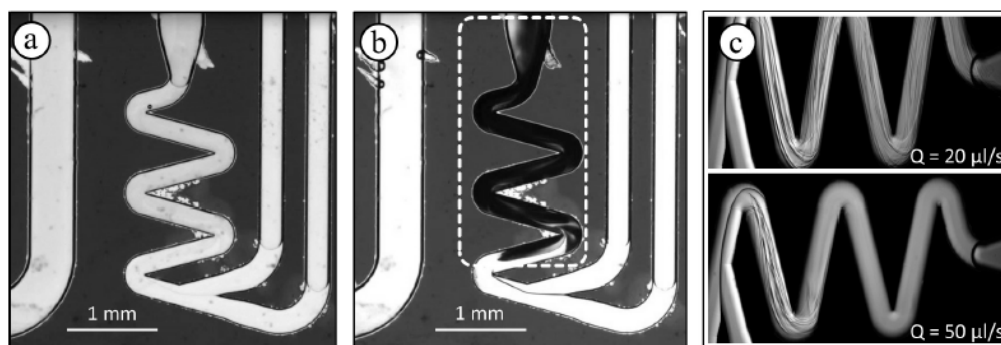

Fig. 4. Microfluidic DFM-reactor after the synthesis of Au seeds with (a) and without 100 mM CTAC (b). CTAC as detergent apparently passivates the channel walls and suppresses thereby any channel clogging (region implied by the dotted area) due to gold deposition (dark regions in b). An efficient tracer mixing for total internal flow rates Q higher than 20 μl s^{-1} is implied by stationary Dean flow pattern induced at the bends of the reactor (c).

synthesis in the microfluidic approach. However, as it also can be seen in Fig. 3, the seed particles in the SF are with 2.51 nm in diameter and a FWHM at 1.36 nm even smaller than the ones prepared in the continuous flow process. In the SF the nucleation takes part in the aqueous segments and März et al. [33] already showed, that very fast reactions (T_{50} < ms) similar to the nucleation can be handled. In contrast to the one-phase microfluidic system, the segments will be generated by using an immiscible organic fluid (PP9) in a third syringe (Fig. 1c), to separates the aqueous segments from each other. Thereby each segment serves as a single, separate reactor for the synthesis. The mixing characteristic in the segments is determined by the segment velocity (flow rates and -ratio of each channel) and the channel arrangement (in detail: linear or winding channels). In our setup, the knot mixer and a velocity of more than 60 mm s^{-1} results in efficient mixing, with an even better complex internal flow (due to the higher velocity) than demonstrated previously [34]. Since the micro reactors control reactions more precisely than classical batch reactors, both microfluidic approaches for the synthesis of seed particles are better suited than the conventional method. In Fig. 3b the extinction spectra of seed particles from the conventional and the microfluidic synthesis approaches are compared. All spectra show a shoulder instead of a significant peak at around 500 nm. The average particle diameter

is too small for the formation of a plasmon mode. Only for sizes larger than 4 nm, the collective oscillation of the free electron gas in the conductive band of the nanoparticles leads to clearly observable plasmon resonance bands in optical spectroscopy [35]. The shoulders at 500 nm are therefore attributed to seed particle, that have sizes above the average particle diameter, which again indicates smaller Au seed particles for the microfluidic approaches, since they have no or a much less distinct shoulder. A typical problem often observed in micro reactor synthesis of metal nanoparticles is the adsorption and accumulation of particles at the channel walls. This can finally end up with a clogging of the channels (reactor fouling) [36,37], that makes the reactor unusable. In the case of the studied synthesis, this effect could be avoided. This important result can be explained by the presence of CTAC in the solution. Fig. 4 shows the microfluidic reactor after the synthesis of Au seed particles with and without CTAC in a direct comparison (instead of CTAC the same volumes of water was used, to keep the process- and chemical conditions comparable). As a detergent, the hydrophilic heads of CTAC blocks the glass surface of the channel walls and prevents reactor fouling, so that there is no need for any prior channel passivation or reactor regeneration. A simple cleaning with water is sufficient to allow further synthesis. That effect could have a big impact on micro reactor NP synthesis, since it simplifies

the use of microfluidics and predestinates micromixers in general for a CTAC and CTAB associated particle synthesis.

3.2. First grow step (GS 1): seed to intermediates

After the seed synthesis, a subsequent growing step is needed (see Fig. 2). Different as described by Wu et al. [26], we used the as prepared seed particles directly after the synthesis without any aging or purification process, since the used volume of seed solution is negligible in contrast to the total volume of the GS 1 (as the ratio is 1:400). For the preparation of gold nanocubes with edge lengths of about 80 nm, 25 µl of the previously synthesized gold seed NPs were added to the reactant premixture of the first growth solution. The empirically found synthesis protocol of Wu and co-workers [26] predicts that the reinforced seed nanoparticles are picked up at an early stage of development and added quickly to the second growth solution (GS 2). At this point, the protocol asks for a subjective decision at which time the removal of grown seed particles should take place. With the addition of the gold seed particles into the growing solution, the reaction of the gold deposition is initiated. After about 15 s the initially colorless clear GS 1 turns pale pink due to the progress of the gold particle growth. The slightly reinforced gold seeds should be added into the second growth solution immediately after the first manifestation of the plasmon absorption. The remaining sample volume of the first growth step turns finally red and cannot be used for further syntheses after completion of particle growth, as SEM images show irregular particle geometries (Fig. 5 SI). While the small gold seed particles are stable for hours and aliquots can be taken continuously for subsequent syntheses, the first growth step has to be repeated for each single experiment (in detail for each nanocube population). The conventional method requires a total volume of 10 ml for both growth solutions (GS 1 and GS 2). For the synthesis of gold nanocubes, only 25 µl of GS1 are transferred to GS 2. For economic reasons alone, it is advisable to convert the first growth step in a microfluidic method, since the volume of product solution to be produced can be precisely regulated by the microfluidic synthesis. In the case of the segmented flow approach each droplet behaves as a single reactor and enables thereby a parallelization of the Au cube growth. The reinforcement of the Au seed nanoparticles was carried out under the chemical and fluidic conditions that are given in Table 1. Respective reactant premixing helps to reduce the complexity of the SF reactor. A Stokes equivalent average sphere diameter of the microfluidically produced GS1 NP of 14.3 nm was determined by DCS analysis (Fig. 5c). UV–vis analysis showed a narrow plasmon absorption mode at 522 nm and is similar to the batch approach given in Fig. 5b.

3.3. Second growth step (GS2): intermediates to Au nanocubes

For further growth into nanocubes, the GS1 product was collected in an Eppendorf®-tube and 25 µl of the reinforced seed particles were immediately transferred into the second growth solution. For this growth step, which leads to the formation of nanocubes, the reaction solution should remain motionless after a short turning over. Therefore a realization of the third synthesis step in a micro flow-through system is not useful. In all experiments, the second growth step was carried out in batch. The addition of 25 µl particle solution produced in the previous experimental step leads for both synthesis methods of GS 1 (batch and SF) to the formation of gold nanocubes with edge lengths of about 80 nm. As also described in the literature, the sizes of multi-step growing particles depend strongly on the number of seeds in the several growth solutions. Less seeds results in bigger particles by an equal metal salt concentration. If one in contrast increases the volume of seeds, the particle sizes will decrease [26,27,38]. However, with the SF method of growth step one (GS 1), the edge length of the nanocubes could be easier and faster tuned compared to a classical batch method, since each segment acts as a single batch. Therefore a continuous production of GS 1 segments with the SF is possible, whereby the consumed material could be reduced. It is further possible to change the cube edge lengths by using only ones 25 µl of seeds into the segmented flow GS 1 and add afterwards different volumes (25 µl; 50 µl; 75 µl and 100 µl) of the as prepared segmented flow GS 1 into GS 2. The cube sizes where tuned therefor in a range between 55 and 80 nm with a corresponding plasmon peak between 556 and 608 nm (Fig. 6).

The transfer of the necessary amount of seed particles at the third experimental step remained as described above. In Fig. 6b, the average Stokes equivalent sphere diameters of the nanocube samples with different edge lengths are shown. As expected, a higher volume of seed nanoparticles leads to the formation of smaller Au nanocubes. The DCS data in Fig. 6b specify the Stokes equivalent spherical diameter of the cubes. From these values, the edge lengths x can be estimated according Eq. (1), by using the radius r

$$x = \sqrt[3]{\frac{4}{3} * \pi * r^3} \tag{1}$$

The inset in Fig. 6c shows the correlation between used amounts of seed particles and the corresponding stokes equivalent diameter as well as the edge length of the resulting cubes. We found almost linear correlation of $-0.287\ nm\ \mu l^{-1}$ for the cube edges regarding the used seed volume. For a tailored fabrication of uniform seeds, the correlation between seed amounts and edge length concerning the plasmon maxima are plotted by using the SF
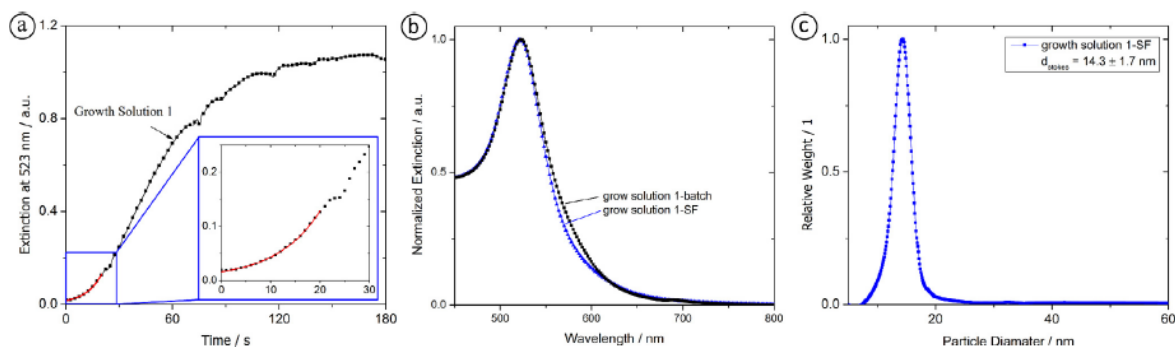

Fig. 5. Results of the intermediate state of GS1. (a) The kinetics of GS1 induces a sigmoidal grow of the GS1-particles and was measured for 3 min at a fix wavelength of 523 nm, since (b) the spectra of the resulting GS1 solutions (batch & SF) have their peak around 523 nm. The resulting particles have a diameter of 14.7 ± 1.7 nm (c).

438   *M. Thiele et al. / Chemical Engineering Journal 288 (2016) 432–440*

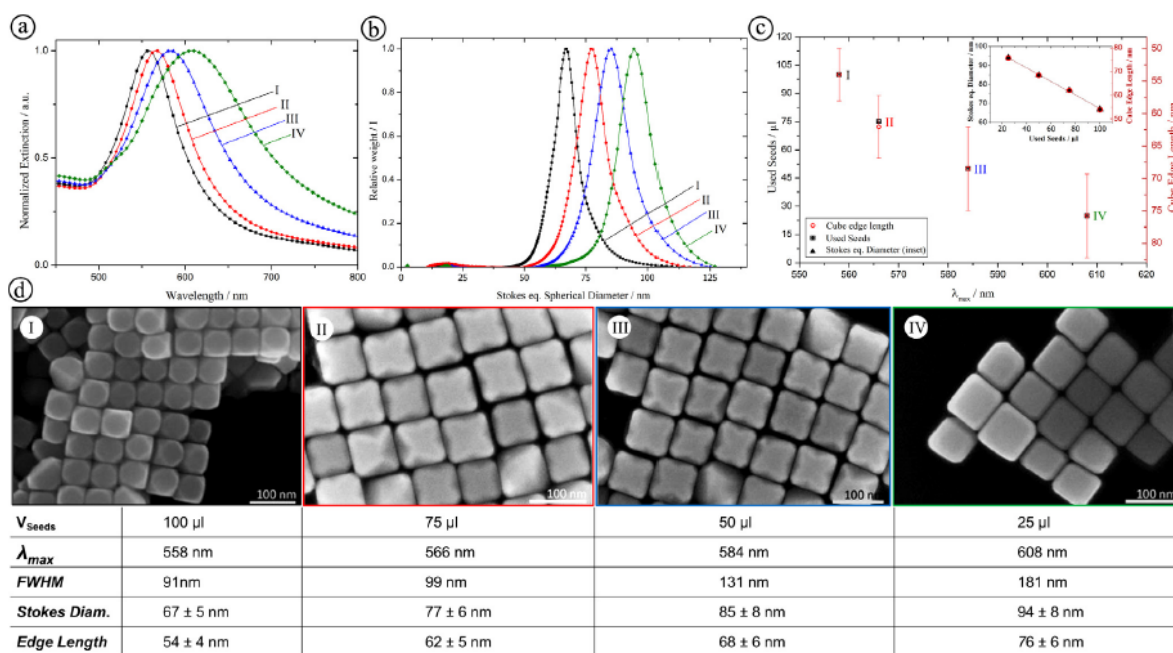| V_{Seeds}	100 µl	75 µl	50 µl	25 µl
λ_{max}	558 nm	566 nm	584 nm	608 nm
FWHM	91 nm	99 nm	131 nm	181 nm
Stokes Diam.	67 ± 5 nm	77 ± 6 nm	85 ± 8 nm	94 ± 8 nm
Edge Length	54 ± 4 nm	62 ± 5 nm	68 ± 6 nm	76 ± 6 nm

Fig. 6. UV–vis spectra (a), DCS spectra (b), their correlation including the amount of reinforced Au seeds taken from GS 1 (by using only ones 25 µl of seeds into GS 2) (c) and SEM images (d) of Au nanocubes prepared with the SF approach.

approach for the GS 1. With respect to the data in Fig. 6 and regarding to the microfluidic method, an automated and customized synthesis of Au nanocubes seems possible. However, as implied in Fig. 2, timescales and kinetics of the diverse steps are truly different from each other. By disregarding this feature, it is impossible to reach a perfect cube, since an overgrowing of the cubes will appear and result in uncontrolled shapes of dodecahedrons, trisoctahedrons, bipyramides and so on.

3.4. Kinetic control of the particle grow to form precisely shaped Au nanocubes

The process of overgrowing can arise at two points during the Au cube fabrication: during the grow process 1 (GS 1) and 2 (GS 2). As described above and by Wu et al. [26] the intermediates (reinforced seeds) from GS1 had to be transferred into GS2 when the color of GS 1 becomes pale pink. To determine the effective reaction time, we measured the kinetics of GS 1 by recording the intensity change at the peak maximum of 522 nm for 3 min. As can be seen in Fig. 5a, the resulting plot has a sigmoidal trend that indicates 3 phases, namely an exponential increase, a turning point and a stationery phase. The inlet in Fig. 5a gives a further magnification of the first 30 s in which the transfer should be completed. As can be seen further in Fig. 2 of the SI, the GS 1-particles are uniform in size, but differ in shape, since no regular geometries can be observed. However, the best results for the transfer were reached after exact 10 s, which again could be reached reproducible only with the SF-approach, since a transfer by using a pipette allows not really sub-second precision. Thus, the flow rate of GS 1 was accurate adjusted so that the reinforced particles were collected after exact 10 s of incubating by directly adding them to the second grow solution. Although the timescale for the second growth stage is more than one order of magnitude longer compared to the first one, the illustration in Fig. 7 highlights also for this step the crucial time dependency. Equal to the data for the GS 1 solution, the kinetic for the GS 2 solution was measured at a time interval of

35 s for 22 min. Since the plasmon peak for 80 nm sized cubes was expected around 600 nm (Fig. 6a), the interval for wavelength was set between 450 and 700 nm. As can be seen in Fig. 7b, after a slight increase of the extinction for the whole range at the beginning, a peak appears after 8 min at about 580 nm and red shifts slightly, whereat the extinction is continuous increasing until it starts to fall after about 20 min. The inset in Fig. 7a shows some discrete spectra and highlights the changes in the form of the curves over the time. In addition to the indicated plasmon band shift and intensity increase, a broadening of the peak appears, that makes it hard to identify optimal growth conditions. However, to overcome these problems and classify the results of the time resolved spectral characterization, a Figure of Merit (FOM) was determined for each single time interval (Fig. 7a). The FOM is defined as the intensity at the peak maximum divided by the intensity of the peak average and depicts the best conditions for growing. For example, if there would be no change during the time, the FOM would show just a line at 1. If there is a change, different values arise, whereas the maximum gives the best relation between intensity and peak wide compared to all curves of the dataset. The maximum value in Fig. 7a is at 1.66 and occurs after 490 s, although one would expect it later, since the corresponding spectra in Fig. 7b has not reached the maximum of intensity of the plasmon peak. The result denotes that the incubation of GS 2 should be finished after about 490 s. To further prove the conclusion, different GS 2 were stopped after different times of incubation by centrifugation, and SEM images of the particular samples were made to compare the spectral behavior and the corresponding shapes (Fig. 7c). The GS 2 was stopped after (I) 490 s; (II) 595 s; (III) 1190 s and (IV) 1368 s, these times are also highlighted in the graphs in Fig. 7a and b for a better understanding. The SEM images in Fig. 7c shows for all Au cube populations a good homogeneity, that indicates in general the high quality of the synthesis method (seeds and GS 1 in SF), but to reach also a high shape quality, the GS 2 has to be stopped after 8–10 min. Shorter incubation results in not yet finished cubes, as indicated by rounded corners,
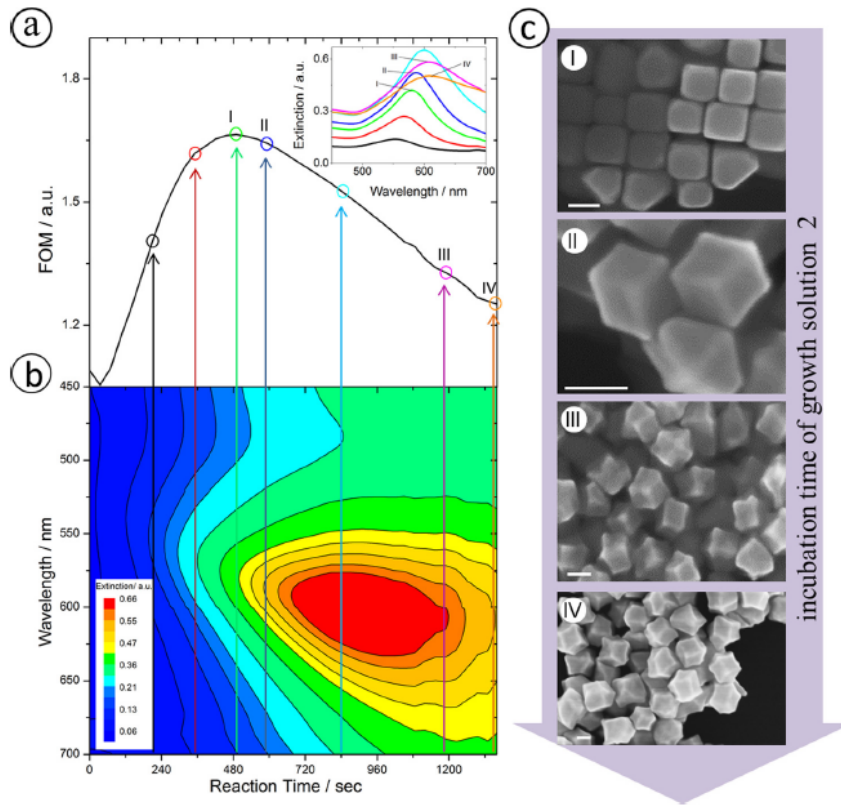
Fig. 7. Since the kinetics of GS 2 (b) is hard to quantify, a FOM was calculated and plotted (a). Spectra at some discrete reaction times are highlighted in the inset. For particles with (λ_{max} = 600 nm and a = 80 nm edge lengths were used. Four typical SEM images (c) at different reaction times (I–IV) show the corresponding evolution and overgrow of Au nanocubes (scale bar is 50 nm) and indicates an optimal reaction time between 8 and 10 min.
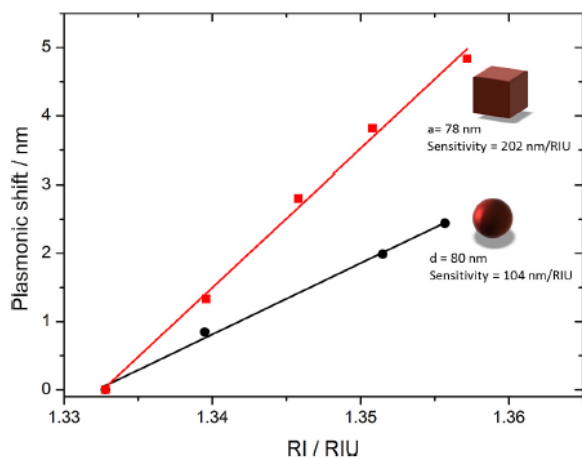

Fig. 8. Direct comparison of bulk sensitivities of Au cubes and Au spheres of comparable dimensions.

whereat longer incubation results in an overgrowing. A further detailed discussion concerning the crystal structure can be found in the SI. The results are in good agreement with the FOM in Fig. 7a and with this confirm the theory for the need for an interruption during the second growth process to Au nanocubes. Since the growing time to Au cubes in Fig. 7c includes the centrifugation of 3 min, the initially discussion of different steps of the synthesis

can be extended to a fourth phase, namely a centrifugation step as introduced in Fig. 2. This is due to the fact, that the grow solution contains residual gold ions and reducing agent that supports the further growing if it will not be removed.

3.5. Sensoric potential of Au nanocubes

Since the shape of the nanocrystal strongly affects the RI-sensitivity [15], sharp edges, corners and tips enhance furthermore the local electrical field and should have a significant impact on the sensitivity of the nanoparticles. Fig. 8 shows a comparison for the bulk sensitivities of Au nanocubes and Au spheres. For a better contrast equal dimensions where used, with 80 nm spheres (Fig. 7 SI) and 78 nm cubes (Fig. 8 SI). The Au spheres have with 104 nm/ RIU only about half of the sensitivity of the Au nanocubes with 202 nm/ RIU, although the lateral dimensions are similar. This result demonstrates firstly the high impact of edges and corners and secondly the high potential of Au cubes for sensing applications. It further points out the Au cubes as a suitable model for calculation of theoretical sensitivities as one class of anisotropic particles with a simple geometry and homogeneous size distribution as depicted in the SEM images of the paper.

4. Conclusion

In summary, we demonstrated that the synthesis of Au nanocubes is a rather complex process that contains four single steps: synthesis of small seeds, short growing process (GS 1), long grow-

ing process (GS 2) and finally a centrifugation step to stop the growing and therefore prevent an overgrowing. While compared directly with a batch approach, we highlighted that with a microfluidic set up (single-phase or segmented flow) smaller and more homogenous Au seed particles will be created. Attributed to the CTAC, we showed that no channel clogging occurs. While around 12 min are needed for the whole synthesis of Au nanocubes, the detailed study of the kinetics for the two growing steps showed different time scales and conditions for each step. By transferring the first growth step into a microfluidic segmented flow process, the critical incubation time of 10 s could be reproducible realized avoiding any subjective influence. For the second growth step, we correlated the kinetic measurements with SEM images to establish a FOM that enables an easy quantification of the critical incubation time. While the second incubation time is between 8 and 10 min and doesn't require further mixing, there is no need for a microfluidic setup. By using these parameters we demonstrated that a size tuning of the Au cubes is easily possible by changing the volume/concentration of seeds to GS 1, and GS 1-intermediates to the GS 2-solution, what again could be simple and reproducible realized by the segmented flow approach.

Funding sources

Acknowledgement

Appendix A. Supplementary material

TEM and SEM images of microfluidic synthesized cubes with different retention times, the influence of NaBH4 concentration, as well as rocking curves and detailed graphs of the sensitivity of the nanoparticles can be found, in the online version, at http://dx.doi.org/10.1016/j.cej.2015.12.020.

References

[1] O. Stranik, J. Jatschka, A. Csáki, W. Fritzsche, Development of new classes of plasmon active nano-structures and their application in bio-sensing and energy guiding, Front. Phys. 9 (5) (2014) 652–664.
[2] K.M. Mayer, F. Hao, S. Lee, P. Nordlander, J.H. Hafner, A single molecule immunoassay by localized surface plasmon resonance, Nanotechnology 21 (25) (2010) 255503.
[3] K.M. Mayer, J.H. Hafner, Localized surface plasmon resonance sensors, Chem. Rev. 111 (6) (2011) 3828–3857.
[4] D. Bartczak, O.L. Muskens, S. Nitti, T. Sanchez-Elsner, T.M. Millar, A.G. Kanaras, Interactions of human endothelial cells with gold nanoparticles of different morphologies, Small 8 (1) (2012) 122–130.
[5] M.L. Personick, C.A. Mirkin, Making sense of the mayhem behind shape control in the synthesis of gold nanoparticles, J. Am. Chem. Soc. 135 (49) (2013) 18238–18247.
[6] S.K. Dondapati, T.K. Sau, C. Hrelescu, T.A. Klar, F.D. Stefani, J. Feldmann, Label-free biosensing based on single gold nanostars as plasmonic transducers, ACS Nano 4 (11) (2010) 6318–6322.
[7] A. Csáki, M. Thiele, J. Jatschka, A. Dathe, D. Zopf, O. Stranik, W. Fritzsche, Plasmonic nanoparticle synthesis and bioconjugation for bioanalytical sensing, Eng. Life Sci. 15 (3) (2015) 266–275.
[8] F.J. Hernandez, S.K. Dondapati, V.C. Ozalp, A. Pinto, C.K. O'Sullivan, T.A. Klar, I. Katakis, Label free optical sensor for Avidin based on single gold nanoparticles functionalized with aptamers, J. Biophotonics 2 (4) (2009) 227–231.
[9] J.D. Driskell, C.A. Jones, S.M. Tompkins, R.A. Tripp, One-step assay for detecting influenza virus using dynamic light scattering and gold nanoparticles, The Analyst 136 (15) (2011) 3083–3090.
[10] T. Schneider, N. Jahr, J. Jatschka, A. Csaki, O. Stranik, W. Fritzsche, Localized surface plasmon resonance (LSPR) study of DNA hybridization at single nanoparticle transducers, J. Nanoparticle Res. 15 (4) (2013).
[11] N. Enkin, E. Sharon, E. Golub, I. Willner, Ag nanocluster/DNA hybrids: functional modules for the detection of nitroaromatic and RDX explosives, Nano Lett. 14 (8) (2014) 4918–4922.
[12] G.K. Joshi, K.N. Blodgett, B.B. Muhoberac, M.A. Johnson, K.A. Smith, R. Sardar, Ultrasensitive photoreversible molecular sensors of azobenzene-functionalized plasmonic nanoantennas, Nano Lett. 14 (2) (2014) 532–540.
[13] A. Niazov-Elkan, E. Golub, E. Sharon, D. Balogh, I. Willner, DNA sensors and aptasensors based on the hemin/G-quadruplex-controlled aggregation of Au NPs in the presence of L-cysteine, Small 10 (14) (2014) 2883–2891.
[14] L. Soares, A. Csaki, J. Jatschka, W. Fritzsche, O. Flores, R. Franco, E. Pereira, Localized surface plasmon resonance (LSPR) biosensing using gold nanotriangles: detection of DNA hybridization events at room temperature, Analyst 139 (19) (2014) 4964–4973.
[15] H. Chen, L. Shao, K.C. Woo, T. Ming, H.-Q. Lin, J. Wang, Shape-dependent refractive index sensitivities of gold nanocrystals with the same plasmon resonance wavelength, J. Phys. Chem. C 113 (41) (2009) 17691–17697.
[16] M. Thiele, I. Götz, S. Trautmann, R. Müller, A. Csáki, T. Henkel, W. Fritzsche, Wet-chemical passivation of anisotropic plasmonic nanoparticles for LSPR-sensing by a silica shell, Mater. Today: Proc. 2 (1) (2015) 33–40.
[17] Q. Zhang, N. Large, H. Wang, Gold nanoparticles with tipped surface structures as substrates for single-particle surface-enhanced Raman spectroscopy: concave nanocubes, nanotrisoctahedra, and nanostars, ACS Appl. Mater. Interfaces 6 (19) (2014) 17255–17267.
[18] Y. Jin, Engineering plasmonic gold nanostructures and metamaterials for biosensing and nanomedicine, Adv. Mater. 24 (38) (2012) 5153–5165.
[19] M.R. Langille, M.L. Personick, J. Zhang, C.A. Mirkin, Defining rules for the shape evolution of gold nanoparticles, J. Am. Chem. Soc. 134 (35) (2012) 14542–14554.
[20] W. Niu, L. Zhang, G. Xu, Seed-mediated growth of noble metal nanocrystals: crystal growth and shape control, Nanoscale 5 (8) (2013) 3172–3181.
[21] A.R. Tao, S. Habas, P. Yang, Shape control of colloidal metal nanocrystals, Small 4 (3) (2008) 310–325.
[22] J. Zhang, M.R. Langille, M.L. Personick, K. Zhang, S. Li, C.A. Mirkin, Concave cubic gold nanocrystals with high-index facets, J. Am. Chem. Soc. 132 (40) (2010) 14012–14014.
[23] S.J. Hsu, P.Y. Su, L.Y. Jian, A.H. Chang, I.J. Lin, Vertex and edge truncated octahedron gold crystals. N-alkylimidazole and silver(I) ion controlled morphology transformation, Inorg. Chem. 49 (9) (2010) 4149–4155.
[24] Y. Xia, Y. Xiong, B. Lim, S.E. Skrabalak, Shape-controlled synthesis of metal nanocrystals: simple chemistry meets complex physics?, Angew Chem. Int. Ed. Engl. 48 (1) (2009) 60–103.
[25] L. Zhang, Y. Xia, Scaling up the production of colloidal nanocrystals: should we increase or decrease the reaction volume?, Adv Mater. 26 (16) (2014) 2600–2606.
[26] H.L. Wu, C.H. Kuo, M.H. Huang, Seed-mediated synthesis of gold nanocrystals with systematic shape evolution from cubic to trisoctahedral and rhombic dodecahedral structures, Langmuir 26 (14) (2010) 12307–12320.
[27] A. Knauer, A. Csáki, F. Möller, C. Hühn, W. Fritzsche, J.M. Köhler, Microsegmented flow-through synthesis of silver nanoprisms with exact tunable optical properties, J. Phys. Chem. C 116 (16) (2012) 9251–9258.
[28] M. Thiele, A. Knauer, A. Csáki, D. Mallsch, T. Henkel, J.M. Köhler, W. Fritzsche, High-throughput synthesis of uniform silver seed particles by a continuous microfluidic synthesis platform, Chem. Eng. Technol. 38 (7) (2015) 1131–1137.
[29] A. Knauer, J.M. Köhler, Screening of multiparameter spaces for silver nanoprism synthesis by microsegmented flow technique, Chem. Ing. Tech. 85 (4) (2013) 467–475.
[30] B. Abécassis, F. Testard, O. Spalla, P. Barboux, Probing in situ the nucleation and growth of gold nanoparticles by small-angle X-ray scattering, Nano Lett. 7 (6) (2007) 1723–1727.
[31] J. Polte, R. Erler, A.F. Thünemann, S. Sokolov, T.T. Ahner, K. Rademann, F. Emmerling, R. Kraehnert, Nucleation and growth of gold nanoparticles studied via in situ small angle X-ray scattering at millisecond time resolution, ACS Nano 4 (2) (2010) 1076–1082.
[32] A.P. Sudarsan, V.M. Ugaz, Multivortex micromixing, Proc. Nat. Acad. Sci. USA 103 (19) (2006) 7228–7233.
[33] A. Marz, K.R. Ackermann, D. Malsch, T. Bocklitz, T. Henkel, J. Popp, Towards a quantitative SERS approach–online monitoring of analytes in a microfluidic system with isotope-edited internal standards, J. Biophotonics 2 (4) (2009) 232–242.
[34] D. Malsch, M. Kielpinski, R. Merthan, J. Albert, G. Mayer, J.M. Köhler, H. Süße, M. Stahl, T. Henkel, μPIV-Analysis of Taylor flow in micro channels, Chemical Engineering Journal 135 (2008) S166–S172 (Supplement 1 (0)).
[35] U. Kreibig, Electronic properties of small silver particles: the optical constants and their temperature dependence, J. Phys. F: Met. Phys. 4 (7) (1974) 999.
[36] J. Wagner, T. Kirner, G. Mayer, J. Albert, J.M. Köhler, Generation of metal nanoparticles in a microchannel reactor, Chem. Eng. J. 101 (1–3) (2004) 251–260.
[37] J. Wagner, T. Tshikhudo, J. Kohler, Microfluidic generation of metal nanoparticles by borohydride reduction, Chem. Eng. J. 135 (2008) S104–S109.
[38] H.-L. Wu, C.-H. Chen, M.H. Huang, Seed-mediated synthesis of branched gold nanocrystals derived from the side growth of pentagonal bipyramids and the formation of gold nanostars, Chem. Mater. 21 (1) (2009) 110–114.

5.4. Combination of microfluidic high-throughput production and parameter screening for an efficient shaping of gold nanocubes using *Dean-Flow* mixing [MT4]

Autorenschaft der Publikation:

Matthias Thiele	Konzeptentwicklung und Verfassen des Manuskripts (inkl. Abbildungen)
	Aufbau und Etablierung der mikrofluidischen Plattform
	Erhebung und Evaluieren der Daten
	Charakterisierung der Nanopartikel
	Gezielte Parameterstudien
Andrea Knauer	Diskussion des Konzepts und der Ergebnisse
	Diskussion und Korrektur des Manuskripts
Daniéll Malsch	Entwerfen und Anfertigen der Mikromischer
	Simulation der Mischparameter
Andrea Csáki	Diskussion des Konzepts und der Ergebnisse
	Korrektur des Manuskripts
Thomas Henkel	Simulation der Mischparameter
	Diskussion und Korrektur des Manuskripts
J. Michael Köhler	Diskussion und Korrektur des Manuskripts
Wolfgang Fritzsche	Diskussion und Korrektur des Manuskripts
	Projektleitung

Vorschlag zur Anrechnung der Publikationsäquivalente: 1

Lab Chip, 2017,17, 1487-1495

Check for updates

Combination of microfluidic high-throughput production and parameter screening for efficient shaping of gold nanocubes using Dean-flow mixing†

Matthias Thiele,[a] Andrea Knauer,[b] Daniéll Malsch, [iD][a] Andrea Csáki,*[a] Thomas Henkel,[a] J. Michael Köhler[b] and Wolfgang Fritzsche[a]

Metal nanoparticles and their special optical properties, the so-called localized surface plasmon resonance (LSPR), facilitate many applications in various fields. Due to the strong dependency of the LSPR on particle geometry, their synthesis is a challenging and time-consuming procedure especially for non-spherical shapes. In contrast, micromixers offer new experimental approaches and therefore enable the simplification of several processes. By using a zigzag micromixer (Dean-Flow-Mixer, DFM) that induces Dean-flow secondary flow patterns, we theoretically and experimentally show the mixing efficiency. Thus, we highlight the advantages of using it in the multistep synthesis of Au nanoparticles. Based on a narrow size distribution of Au nanocubes and an increased yield in combination with higher reproducibility, we depict the need for and advantage of the DFM to control the incubation times during the growth process. We further show that, by using the DFM, easy and very fast Au nanocube edge length tuning (53 nm, 58 nm, 70 nm and 75 nm) is possible by simultaneously reducing the consumption of the materials by up to 95%. We finally demonstrate the versatile abilities by using the DFM for parameter screening on examples of different halides and accessible bromide in the growth solutions. Therefore, we highlight the optimal concentration for the different growth regimes and the influences on the Au nanoparticle morphology (spheres, cubes and rods) and their defined shaping.

Introduction

Metallic nanoparticles (meNPs) are known for their attractive optical behaviour known as Localized Surface Plasmon Resonance (LSPR)[1] that makes them perfect candidates for optical labels or transducers in biology,[2–5] medicine[6,7] and nanotechnology.[8–10] Different publications therefore deal with theoretical explanation and practical simulation of the LSPR activity[11,12] still with focus on new and deeper insights[13–15] into its mechanism. However, the main parameters that influence the LSPR are the meNPs' composition, size, shape and surroundings. The surroundings (Refractive Index, RI) can be easily modified and is therefore often used for sensing appli-

cations,[1,16] whereas the composition as well as the shape and size cannot simply be changed once the synthesis is completed. In particular, a balance between the shape and size is needed for tailored meNPs and LSPR responses. Therefore, for spherical gold nanoparticles (AuNPs), the size is the most challenging parameter since the sphere is an energetically and thus thermodynamically convenient structure.[17] In contrast, shape-anisotropic structures like prisms, stars, cubes, rods and wires need high control of their size and shape to achieve a high yield of the desired meNP structure and therefore enable higher sensing performance and the possibility of engineering extraordinary nano-constructs. For example, Ag nanoprisms exhibit the highest LSPR-bulk sensitivity published,[18] and nanorods are of high interest concerning polarization studies[19] and localized field-enhancement,[20] whereas Au nanocubes are perfectly suited building blocks for the assembly of advanced plasmonic devices.[21,22] Various publications exist for preparing shape-anisotropic meNPs, based on either (I) a one-pot synthesis or (II) a seeded growth method. Even if both methods require a facet blocking agent (like CTAC and CTAB) for directed growth, the one-pot synthesis yields less meNPs with the desired shape, since efficient

[a] Dept. of Nano Biophotonics, Leibniz Institute of Photonic Technology (IPHT), Albert-Einstein-Straße 9, 07745 Jena, Germany. E-mail: andrea.csaki(at)ipht-jena.de
[b] Dept. of Physical Chemistry and Micro Reaction Technology, Institute for Chemistry and Biotechnology, Technische Universität Ilmenau, Gustav-Kirchhoff-Str. 1, D-98693 Ilmenau, Germany

control of nucleation and particle growth is almost impossible. For the seeded growth method, this is much easier since its purpose is the separation of the two competing processes. Therefore, the seeded growth method is the most efficient procedure for synthesis of monodisperse meNPs and has become the most commonly used chemical synthetic approach for generating anisotropic meNPs. Recently, a lot of effort has been made to summarize and understand the seed-mediated growth process since Jana *et al.* demonstrated the first Au nanorods based on this method in 2001.[23] A general discussion and explanation of the details is part of various good reviews.[24–27] But all of them have in common that the morphology of the final product is influenced by many different factors, emphasizing the importance of splitting the nucleation and growth steps temporally as well as physically to have at least two main steps. In particular, a plethora of parameters (the capping agent, the role of halides and additives, the seed concentration and the reducing agent), their role during the synthesis and their effect on each other are hard to examine which makes the synthesis challenging. Although the synthesis of the shape-favoured spherical AuNPs benefits from the classical flask-based synthetic approach (in the context of narrow size distribution and better shape regularity),[28,29] this method – the so-called batch method – is limited or even partially inappropriate for the desired needs. However, the advantages of microfluidics facilitate the meNP synthesis and allow a parallel screening of different parameters.[30] Starting with the synthesis and growth of spherical AuNPs in micromixers,[31,32] the production of more complex meNP structures was transferred fully or partly into microfluidics.[33–36] Particularly, the segmented flow (SF) approach was utilized for the synthesis of various shape-anisotropic meNPs such as rods,[30,37] prisms[38,39] and cubes,[30,40] whereas continuous phase (CS) microfluidics is poorly investigated. Micromixers as part of continuous microfluidics allow – in contrast to batch methods – efficient mixing and therefore precise parameter control during the synthesis. In particular, seed formation by reductive nucleation of noble metal ions in the presence of strong reducing agents where the precursors are reduced completely is known to be a very fast chemical process. Thus, the time requirements for a 50% turnover of the reaction can be estimated from published information to be below 100 ms (ref. 41 and 42) which represents the key information for the micromixer selection. But even slow reactions with weak reducing agents (such as ascorbic acid in the growth step) have to be well mixed and controlled since metal reduction takes place only on existing nuclei that act as catalysts. Since the incubation time strongly affects their growth, time-critical processes are crucial for shape-anisotropic meNPs and further influence their shape and yield. In previous work, improved synthesis of Ag nanoprisms has already been demonstrated by using a microfluidic platform containing different appropriate micromixers for each set of reaction conditions.[43] The benefit of combining batch and microfluidic methods to realize highly efficient fabrication of Au nanocubes was further shown.[35]

Therefore, the several production steps and the advantages of SF and CS syntheses especially for the seeding process were highlighted. The use of SF for a first growth step and a flask-based second growth step could further be emphasized by also introducing a FOM to quantify the incubation time. Based on this work, we want to extend the study to seeded growth synthesis of AuNPs and highlight the usage of a simple microfluidic set-up containing just one micromixer for the two main steps to overcome the above discussed issues. To perform the reactions without diffusion limitation, mixing should be completed before any significant conversion occurs during the chemical reaction.

Hence, mixing should be completed within less than 1 ms. The most common multi-lamination principle is implemented in split-and-recombine micromixers, which reliably perform at low flow rates (Q) and Reynolds numbers (Re)[44] even for highly viscous fluids. However, due to the low fluid velocity, mixing is fairly slow to some seconds, which conflicts with the target reaction characteristics.[45] Alternative principles are based on chaotic advection, which can be induced at high Re at edges or bends in microchannels, where the formation of secondary flow patterns due to inertial effects results in highly efficient multi-lamination. Thus, we will depict the high mixing efficiency for the zigzag micromixer used, the Dean-Flow-Mixer (DFM), by comparing simulations and experimental results and further show the advantages of using the DFM for the multi-step synthesis of AuNPs depicted in Fig. 1. We will discuss the suitability of the DFM especially for the three time-critical steps (seed formation, first growth step and second growth step) of Au nanocube synthesis displayed in Fig. 2. Therefore, we describe the advantages of and need for the easily adjustable residence channel after the mixing part and emphasise its importance in successfully and reproducibly fabricating Au nanocubes with high shape homogeneity and yield. Based on this, we will focus on the simplified and efficient parameter screening using the DFM to adjust the favoured nanostructures (spheres, cubes or rods) and their size. Hence, we demonstrate the influence of different halides (chiefly NaBr) on the particle shape and show the feasibility of parallel Au nanocube size tuning by simultaneously lowering the amount of consumed material and the required total time.

Materials and methods

Chemicals and materials

Ultrapure water was used for the preparation of solutions, and all chemicals were used as-received from suppliers without further purification unless mentioned otherwise in the text. For the synthesis of seed particles, the chemicals were tetrachloroaurate trihydrate ($HAuCl_4 \cdot 3H_2O$, 99.9%, Carl Roth GmbH, Karlsruhe, Germany), cetyltrimethylammonium chloride (CTAC, 98%, Merck KGaA, Darmstadt, Germany) and sodium borohydride ($NaBH_4$, 98%, Merck
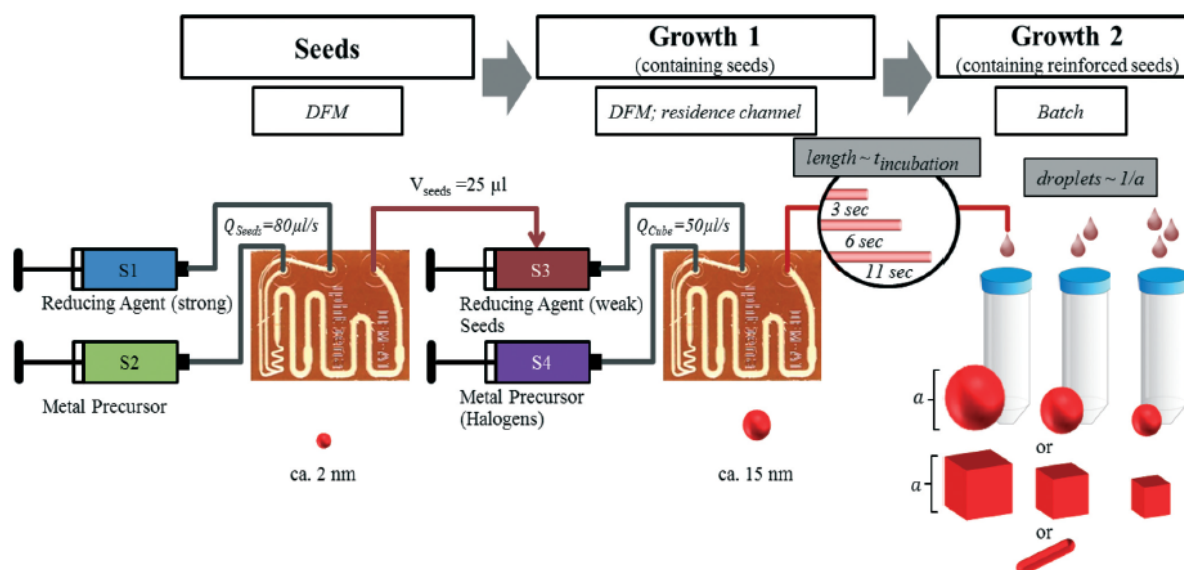
Lab on a Chip

Fig. 1 Illustration of the complete set-up for the microfluidic synthesis of Au nanoparticles. Particle growth is divided into three main parts, namely seed synthesis in the DFM, followed by a first growth step also realized within the DFM in combination with different channel lengths (residence channels) for realizing different incubation times followed by a second growth step in batch. Depending on the contents of the growth solutions, parallel production of spheres, cubes and rods can be realized. The detailed contents of the syringes and tubes are explained in the text.

KGaA, Darmstadt, Germany). For the growth step and investigations of halide influences, ascorbic acid (AA, 99.7%, Merck KGaA, Darmstadt, Germany), sodium bromide (NaBr), sodium chloride (NaCl), sodium iodide (NaI) and sodium fluoride (NaF, >99%, Sigma Aldrich Chemie GmbH, Munich, Germany) were further used. The sensitivity was measured by changing the concentration of D-glucose (Sigma Aldrich Chemie GmbH, Munich, Germany). Ferric chloride ($FeCl_3$, Carl Roth GmbH, Karlsruhe,

Fig. 2 Time-critical processes for the different steps with corresponding mixing and growth times for the synthesis of Au nanocubes and -rods. Since the mixing times for the seed synthesis as well as the first growth step are in the ms range, a DFM micromixer is applicable. A further adjusted incubation time of the first growth step of a few seconds supports the usage of the DFM with a regulated residence channel since too long or short incubation (by using NaBr) leads to randomly shaped particles (dotted arrow). The same situation occurs in the second growth step, but on a timescale of minutes that is efficiently realized in flasks. By not using NaBr, Au nanospheres will be obtained.

Germany) and ammonium thiocyanate (NH_4SCN, Sigma Aldrich Chemie GmbH, Munich, Germany) were used for demonstrating the mixing characteristics, whereas the software OpenFOAM was used for the CFD simulations and ParaView/paraFOAM for the postprocessing. For the microfluidic experiments, syringes (2.5 ml ILS, ILS Innovative Laborsysteme GmbH, Stützerbach, Germany) mounted on a multiaxial, electronically controlled syringe pump system (Cetoni NeMESYS and Cetoni Cedosis, Cetoni GmbH, Korbussen, Germany) with independently controllable axes were used. The Dean-Flow-Mixer (DFM) in Fig. 3 and the corresponding mount were fabricated in-house at the IPHT and connected *via* PTFE tubing (inner diameter of 0.5 mm, Jasco Germany GmbH, Gross-Umstadt, Germany) with the syringes.
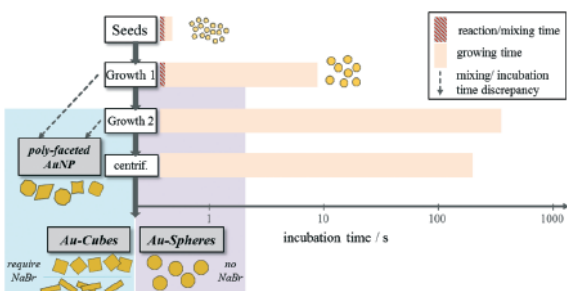
Au nanoparticle preparation and measurements

The AuNP formation is a three-step process at room temperature (strictly at 21 °C) as depicted in Fig. 1 and 2. The synthesis of small Au seeds was started by merging the two solutions S1 (1.5 ml CTAC [200 mM], 0.516 ml $NaBH_4$ [20 mM], 0.984 ml H_2O) and S2 (1.5 ml CTAC [200 mM], 0.3 ml $HAuCl_4$ [5 mM], 1.2 ml H_2O) with a total flow rate of 80 μl s^{-1} in the micromixer. The prepared Au seeds were used in the subsequent growth step (GS1 solution). The two solutions S3 (2442.5 μl CTAC [100 mM], 12.5 μl seeds, 45 μl AA [40 mM]) and S4 (2370 μl CTAC [100 mM], 125 μl $HAuCl_4$ [10 mM]) were also mixed in the micromixer with a total flow rate of 50 μl s^{-1}. The resulting AuNP suspension (reinforced seeds) was directly dropped into the second growth step (GS2) solution
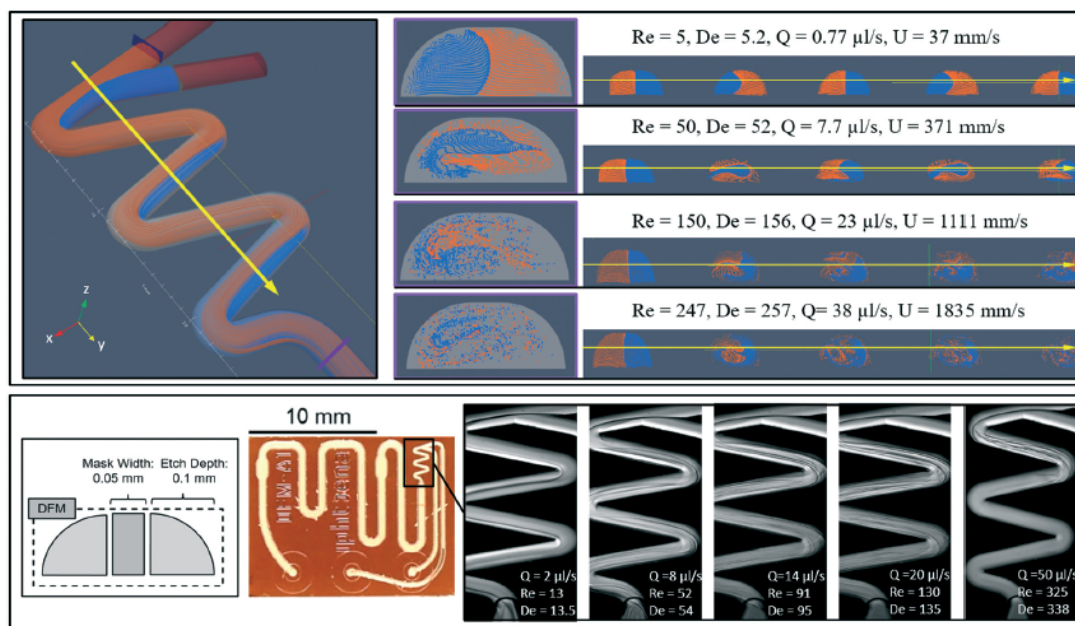
Paper

Fig. 3 Characterization of the Dean-Flow-Micromixer (DFM). The top part shows the CFD simulations with the domain model on the left, the containing outlet monitor face (middle column), and the lamination progress (along the yellow arrow) as monitor faces (right column) for different flow regimes. The bottom part demonstrates the experimental results starting with the geometrical parameters, the DFM glass chip and images of the lamination pattern at increasing flow rates (from left to right).

containing 9625 µl CTAC [100 mM], 250 µl $HAuCl_4$ [10 mM] and 90 µl AA [40 mM]. This solution was initially vortexed, left undisturbed for around 16 minutes and then washed (centrifugation at 5000 rpm for at least 3 min and resuspension of the red pellet in H_2O). In the case of the Au nanocubes, 5 µl of a 10 mM NaBr stock solution was added to S4 and 10 µl to GS2 solution unless mentioned differently in the text. To end up with Au nanorods, the volume of NaBr solution added to the GS2 solution was further increased as described in the text. Afterwards, the AuNPs were characterized using scanning electron microscopy (SEM, Hitachi S-4800 FE-SEM, Hitachi High Technologies America, Inc., Schaumburg, Illinois) and the resulting plasmon peaks as well as bulk sensitivity were measured using UV-vis spectrophotometry (V-630, JASCO Germany GmbH, Gross-Umstadt, Germany). For bulk sensitivity measurements, 100 µl of D-glucose (50% w/w) were added five times to 500 µl of the corresponding Au nanocube suspension. After each addition, mixing and short incubation, the spectra and the RI were measured.

DFM implementation

The micromixer was realized by anisotropic wet etching of half channels into glass followed by anodic or thermal bonding. The channel cross-section is given in Fig. 3. The feed lines were realized as full channels with an integrated optical detection window in the outlet channel for optional spectroscopic monitoring of the reaction progress. The mixer structure was implemented as a half channel of 5 bends with a bend angle of beta = 150 degrees and inflow and outflow sections. The inner bend was realized as an acute angle. The system was prepared as a glass microfluidic device with two inlets and one outlet. The etch depth was 0.1 mm, the mask width was 0.05 mm and the mixer length was 6.112 mm.

Experimental mixing characteristics. Experimental assessment of the mixing characteristics was performed by the formation of a dark-red colored ferric rhodanide complex from $FeCl_3$ and NH_4SCN. The reaction can be considered as instantaneous; the reagents are solvated metal ions and small anions as in the target reaction. Hence, the system can be expected to be an appropriate model for the target reaction. The nearly colorless aqueous ferric chloride solution and the aqueous ammonium thiocyanate solution were fed into the two inlets. The reaction proceeds at the interface between the two fluids and the reaction front becomes visible as can be seen on a gray-level scale in Fig. 3. Mixing is completed as soon as the overall color depth in the channel is steady and remains constant along the fluid transport path.

Mixing characteristics simulations. The experimental results are complemented with data, obtained by CFD simulations. The stationary flow fields were calculated for the experimentally investigated parameters. Multi-lamination patterns and residence time distributions were derived from the fluid trajectories obtained by streamline calculation during postprocessing of the CFD data.

Lab on a Chip

Results and discussion

Mixing processes in a zigzag microchannel with finite element simulations and optical studies

Here, Dean-flow secondary flow patterns[46,47] are induced at the bends at high Reynolds and Dean numbers (De). Mixing efficiency is nearly independent from the inflow configuration – hence, more than two reagent flows can be combined and fed into the system at arbitrary flow rates without disturbing the mixing efficiency. The efficiency of the Dean-flow formation increases with the bend angle – therefore, the zigzag mixer with high bend angles (beta $\gg$ 90°) can be assessed as the most convenient type. Efficient mixing in zigzag mixers is expected for Re > 80.[48] However, Fig. 3 compares CFD simulations with experimental mixing data of the DFM. At lower Re, the system switches to laminar co-flow without mixing. At moderate flow rates with Re = 40–50, minor Dean-flow patterns cause a lateral elongation of the interface between the two reactants. However, the geometric transformation produced at a bend is reversed by the next one. Even at Re = 150 and De = 156, no homogeneous interlacing of the fluid trajectories was observed in the simulation. This confirms the experimental data and indicates that the critical Re for mixing in the developed system significantly exceeds the values of Re = 80, given by Mengeaud.[48] A switch to perfect mixing was experimentally determined at Re > 250 which was confirmed by the CFD simulations.

Au nanocube synthesis using DFM

The complete setup and single steps for the synthesis of AuNPs are summarized respectively in Fig. 1 and 2. To achieve the simultaneous production of all nuclei, the metal precursor and reducing agent have to be stored in separate syringes and then instantaneously mixed and homogeneously distributed in the entire solution volume. To fulfil these requirements, the DFM was used for the seed synthesis with a total flow rate (Q) of 80 µl s^{-1} ($Q_1 = Q_2$). The collected Au seeds are of high quality as we have already discussed in our previous publication.[35] Here, we wanted to further highlight the usage of the DFM in the first growth step. Therefore, the seeds – together with the reducing agent – are merged with the metal precursor in the micromixer using a total flow rate of Q = 50 µl s^{-1}. After passing the residence channel, the reinforced seeds were released dropwise (9 µl) directly into the second growth solution. After an initial vortex, the GS2 solution should remain untouched for around 16 min.[35] With this procedure, a high yield of regulated Au nanospheres can be produced (Fig. S2, ESI†). At this point, it should be mentioned that – based on the passivation through CTA$^+$ – no clogging or fouling of the DFM occurs and simple cleaning with water regenerates it. However, just by introducing small amounts of NaBr into the growth solutions, it is possible to produce with the same set-up and parameters a high yield of Au nanocubes (Fig. 5 and 6). By a
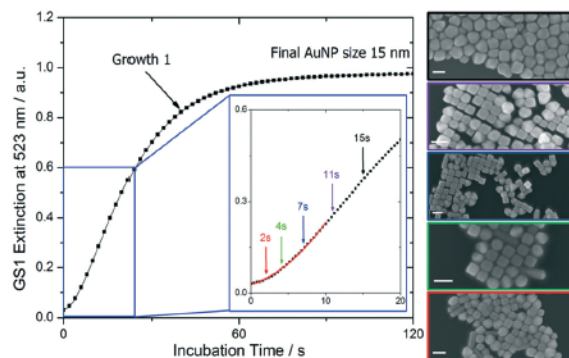

Fig. 4 Kinetics of GS1 solution measured at the LSPR of 523 nm for 2 h for the fabrication of Au nanocubes. The inset shows magnification of the first 20 s and depicts several incubation times for GS1 solution with the corresponding SEM images of 15 s, 11 s, 7 s, 4 s, and 2 s (from top to bottom). Scale bar = 100 nm.

further increase of the NaBr amount, it is also possible to generate Au nanorods. Hence, a detailed study of the influence of bromide and other halides on the fabrication of Au nanostructures can be found below. Since in the published batch method[49] for Au nanocube synthesis, a small amount (25 µl) of seeds has to be mixed with 10 ml of GS1 solution, and after a certain incubation time, 25 µl from the 10 ml GS1 solution has to be mixed again with 10 ml of GS2 solution, three negative aspects are observed: (I) the incubation time and transfer time from GS1 solution to GS2 solution are subjective and therefore hardly reproducible; (II) the rest of the GS1 solution cannot be used anymore since the optimal incubation time has now been passed. Therefore, the rest of the GS1 solution is wasted; (III) it will be even worse if one wants to tune the cube
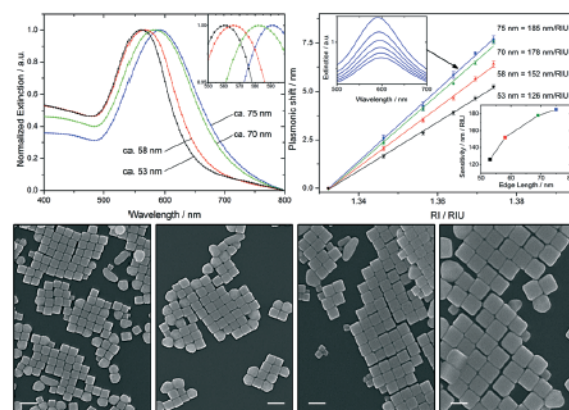

Fig. 5 Spectral characterization (inset: magnification of the LSPR peaks) and corresponding bulk sensitivity (inset: (top) raw graphs at different RIs for 90 nm Au nanocubes and (bottom) sensitivity dependency on Au nanocube sizes) of varied Au nanocube dimensions with corresponding SEM images (left to right: 53 nm; 58 nm; 70 nm; 75 nm). Scale bar = 100 nm.
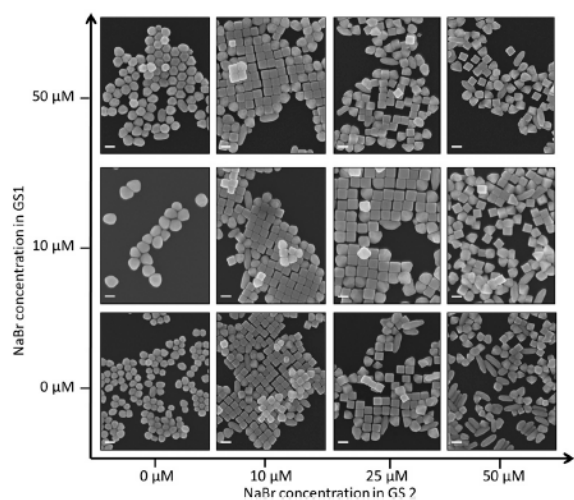
Paper

Fig. 6 Parameter screening for the influence of NaBr. It is crucial that GS2 solution contains NaBr, otherwise no Au nanocubes form even with high NaBr concentration in GS1 solution. On the other hand, it is possible to synthesize Au nanocubes even without NaBr in GS1 solution. An increasing NaBr amount in GS2 solution sharpens the cubes and introduces a second nanoparticle population of Au nanorods. Scale bar = 100 nm.

edge lengths. Normally by increasing the volume of the seed solution for the transfer and using this volume again to transport the reinforced seeds into the GS2 solution, the Au nanocubes' edge lengths can be decreased due to the higher number of seeds but the same amount of gold precursor in the solution. However, for each Au nanocube size population, a freshly prepared 10 ml GS1 solution has to be provided, but only a few microliters will be consumed. The following sections explain how to address and solve the mentioned problems for Au nanocube synthesis by using the DFM.

Fine-tuning of incubation time for GS1 solution by defining the residence channel length

Each period of the three-step Au nanocube synthesis needs an optimal time domain, as depicted in Fig. 2. For the first and second growth steps (GS1 solution and GS2 solution), fast and good initial mixing of the reactants is crucial to start the reaction (mixing time) followed by growth time. Both can be summarized as incubation time that largely differs for each of the two steps. Fig. 4 indicates that especially for GS1 solution the incubation time is crucial and has a big impact on Au nanocube yield. To quantify this effect, the kinetics of GS1 solution were measured by online tracking of the extinction at 523 nm (LSPR maximum) for 2 h. The resulting sigmoid function rises exponentially within the first 30 s, increases linearly afterwards and finally flattens after around two minutes. The resulting GS1 solution AuNPs are in all cases spherical with a diameter of around 15 nm (Fig. S1, ESI†). However, in the case of the Au nanocubes, the result indicates that the GS1 solution AuNPs change fast within the first 30 s which is in good

agreement with the publication of Wu *et al.* which postulates a transfer of the GS1 solution AuNPs into the GS2 solution after a few seconds when the solution turns light pink.[49] Since this information is highly subjective and therefore difficult to reproduce in batch, a microfluidic setup is required. By using the DFM, the growth of Au seeds starts as soon as the seeds and metal precursor merge in the meander (see Fig. 2, Growth 1), where exactly at this point also the incubation time starts. The applied total flow (Q = 50 µl s^{-1}) introduces efficient mixing (Fig. 3) and thus a change in the channel length after the mixing area (residence channel) easily realizes different incubation times with high accuracy. The combination of controllable mixing and residence channel lengths or rather incubation time is highly reproducible since, in contrast to batch synthesis, identical and non-subjective parameters are applied. However, to identify the predominant influence of GS1 solution alteration and therefore its optimal incubation time, different residence channel lengths were realized. Thus, after various incubation times, the GS1 solution AuNPs were transferred directly into the GS2 solution and checked using the corresponding SEM images (Fig. 4). The GS1 solution incubation was stopped after 2 s, 4 s, 7 s, 11 s and 15 s. By comparing the SEM images, the best shaped Au nanocubes can be found at an incubation time of 7 s. Both too long and too short incubation times will result in less well-shaped Au nanocubes which indicates the need for controlling the GS1 solution and therefore the usage of the DFM.

Lowering material consumption and online tuning of Au nanocube edge lengths and sensitivity

For the three-step synthesis of Au nanocubes, the seeds will be 160 000 times diluted in the final GS2 solution. It is based on the transfer of 25 µl seeds into the GS1 solution and – after their incubation for 7 s – again 25 µl of the reinforced seeds into the GS2 solution (Fig. 1). Therefore, in the batch approach, 10 ml of GS1 solution has to be prepared but only 25 µl of the solution is further used for transfer into the GS2 solution. The rest of the GS1 solution cannot be used at all, since the incubation time of 7 s is exceeded and the cubes would not be well shaped (see Fig. 4). By using the DFM for generating the GS1 solution, the partial growth of the seeds can be controlled and thus, only the needed amount of the GS1 solution can be activated by merging the metal precursor and seeds/reducing agent. Therefore, significantly less waste (95%) of the GS1 solution occurs and constant mixing and incubation time enable reproducible continuous production of Au nanocubes. The result is less consumption of gold by lowering the synthesis time in parallel. This further allows the fast production of different Au nanocube sizes as depicted in Fig. 5. Originally by changing the volume of seeds added into the GS1 solution and also of reinforced seeds added into the GS2 solution, the Au nanocube edge lengths can be varied.[49] The disadvantage is the need for an always freshly prepared GS1 solution (containing different seed concentrations) for each edge length and the already discussed accompanying

Lab on a Chip

over-production of GS1 solution. By using the appropriate NaBr concentration (see the next chapter) in the growth solutions, there is no need for altering the seed concentration in the GS1 solution to change the cubes' edge lengths. Therefore, the GS1 solution can be produced continuously in the DFM as described above and only the amount of GS1 solution (reinforced seeds) transferred into the GS2 solution has to be altered to tune the edge lengths. This enables continuous parallel production of differently sized Au nanocubes as can be seen in Fig. 5 by using less material and time compared to the classical batch method. One droplet of GS1 solution added to the GS2 solution equals 9 μl and generates Au nanocubes with an edge length of 75 ± 6 nm and a LSPR maximum at 592 nm. By increasing the number of GS1 solution drops added to the GS2 solution, the cubes' edge lengths decrease. Two, three and four droplets equal to 18 μl, 27 μl and 36 μl of GS1 solution and create 70 ± 5 nm, 58 ± 5 nm and 53 ± 4 nm Au nanocubes (calculation in Fig. S3, ESI†) with a LSPR maximum at 582 nm, 566 nm and 560 nm, respectively. Based on the sharp corners and tips, the prepared Au nanocubes are perfectly suited for sensing with the largest ones also having the highest sensitivity of 185 nm RIU^{-1} (Fig. 5 and S4, ESI†).

Parameter screening and influence of counter ions on morphology and shaping

The synthesis of shape-anisotropic meNPs is a rather complex process which is influenced by a number of parameters. To analyze the influence of several parameters, one needs a synthesis procedure that is on the one hand highly reproducible and on the other hand simple and fast (highly parallelized). The DFM fulfils these requirements. Therefore, we used the above described microfluidic and CTA$^+$-mediated AuNP growth in the DFM as a model procedure to analyse the influence of different counter ions. With the parameters for the Au nanocube synthesis maintained, we introduced four different halides (NaF, NaCl, NaBr and NaI) into GS2 solution and varied their final concentration from 10 μM to 25 μM and finally to 50 μM. Except for NaBr, all halide additives result in almost spherical shaped AuNPs as summarized in Fig. S5, ESI† which is in good agreement with the literature.[50] However, in the case of Br$^-$ as the counter ion, the particles are expectedly cube-shaped. Hence, to get deeper insight into the mechanisms and influence of NaBr, we screened its effect on the two different growth stages by including it into GS1 solution and GS2 solution. Even if GS1 solution needs exact control of incubation time, Fig. 6 depicts that the influence of NaBr on Au nanocube yield and shape is negligible. Even without NaBr in GS1 solution, it is possible to yield Au nanocubes with high performance. The main influence of NaBr is apparent in GS2 solution. Since there will be no Au nanocubes if GS2 solution is free of NaBr although the concentration in GS1 solution is high, it is strongly required at this point. As soon as one introduces small amounts (10 μM) of NaBr in GS2 solution, high yields of Au nanocubes can be obtained
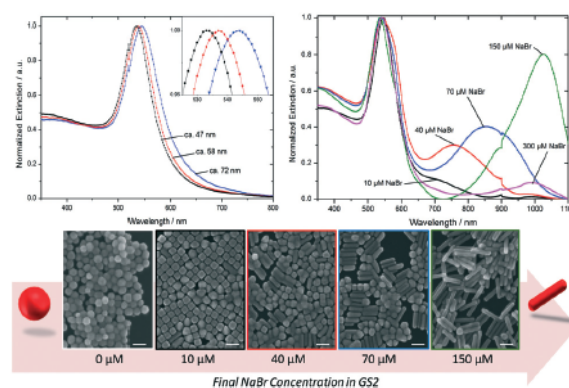

Fig. 7 Tuning of nanoparticle morphologies using the DFM. The left spectra show the size tuning for spherical Au nanoparticles by totally not using NaBr. Meanwhile, the right spectra and SEM images (scale is 100 nm) below indicate the evolution of Au nanospheres to nanocubes and finally to nanorods with dependency on the accessible bromide concentration only in GS2 solution (the break at 900 nm is attributed to the grating substitution of the spectrometer).

(Fig. 6 and S5, ESI†). By increasing the concentration of NaBr in GS2 solution, the sharpness of Au nanocubes can be boosted until a point where a second population of Au nanorods appears. This transition point may lie between 25 μM and 50 μM NaBr.

Parallelized high-throughput production of Au nanospheres, Au nanocubes and Au nanorods

It seems that Br$^-$ is appropriate to delicately control the Au nanoparticle morphology where even tiny amounts strongly influence particle growth. Therefore, Fig. 7 displays the evolution from spheres to cubes up to rods just by changing the NaBr concentration in GS2 solution. Since the DFM allows reproducible and parallel screening and production of AuNPs, the results in Fig. 7 are realized within less than 30 minutes in a one-shot experiment. However, without NaBr, only spherical AuNPs appear. Similar to the Au nanocube edge length tuning described beforehand, it is possible to further adjust their size and therefore the spectral position (Fig. 7) just by altering the volume of the seeds from the GS1 solution introduced into the GS2 solution (Fig. S2, ESI†). By increasing the NaBr concentration to 10 μM, the expected Au nanocubes are the main result. As one further increases the concentration of NaBr, one yields Au nanorods rather than cubes. This can be also estimated from the spectra in Fig. 7 in which with increasing NaBr concentration, a second band arises which is attributed to the longitudinal mode of the Au nanorods. By increasing the NaBr amount to 150 μM, the highest yield of Au nanorods can be found. In turn, too high concentration (300 μM) decreases the yield which indicates the sensitivity to the Br$^-$ concentration of Au nanoparticle growth. Nevertheless, it is remarkable that expectedly, Au nanorods form, although there are no silver ions present in any of the growth solutions. Further, the bromide concentration is below the reported minimum concentration for the production of Au

Paper

nanorods.[51] However, both factors could have an influence on the size tuning (aspect ratio) of the Au nanorods, since it is not just adaptable on the method that was used for tuning the sizes of Au spheres and Au nanocubes.

Conclusions

By taking all the discussed parameters into account, the DFM is perfectly suited for the synthesis of AuNPs. Based on the high mixing efficiency and speed, a homogeneous distribution of the chemical species can be reproducibly realized. The DFM in combination with an adjustable residence channel allows perfect control of the incubation time after the fast mixing. The resulting high reproducibility, fluid control options, fast synthesis and reduced material consumption that are introduced by using the DFM further enable efficient size and parameter screening. Therefore, we were able to show that GS1 solution is crucial for the synthesis of Au nanocubes. In particular, the incubation time has a big impact on the yield and shape, whereas NaBr is not needed at this point of the synthesis protocol. In contrast, NaBr is crucial for GS2 solution, since other halides or its absence leads solely to spherical shaped AuNPs. Whereas low NaBr concentrations are required to guide the growth to Au nanocubes, higher bromide concentrations are needed to end up with Au nanorods. Therefore, we demonstrated with one simple setup containing the DFM a possibility to tune in a parallel manner different Au nanoparticle morphologies with an opportunity for further size and corresponding spectral tuning.

Acknowledgements

Notes and references

1   K. M. Mayer and J. H. Hafner, *Chem. Rev.*, 2011, 111, 3828–3857.
2   M. H. Jazayeri, H. Amani, A. A. Pourfatollah, H. Pazoki-Toroudi and B. Sedighimoghaddam, *Sens. Biosensing Res.*, 2016, 9, 17–22.
3   R. Ahijado-Guzman, J. Prasad, C. Rosman, A. Henkel, L. Tome, D. Schneider, G. Rivas and C. Sonnichsen, *Nano Lett.*, 2014, 14, 5528–5532.
4   K. Saha, S. S. Agasti, C. Kim, X. Li and V. M. Rotello, *Chem. Rev.*, 2012, 112, 2739–2779.
5   B. Pelaz, G. Charron, C. Pfeiffer, Y. Zhao, J. M. de la Fuente, X. J. Liang, W. J. Parak and P. Del Pino, *Small*, 2013, 9, 1573–1584.
6   D. Bartczak, O. L. Muskens, S. Nitti, T. Sanchez-Elsner, T. M. Millar and A. G. Kanaras, *Small*, 2012, 8, 122–130.
7   Y. T. Tung, C. C. Chang, Y. L. Lin, S. L. Hsieh and G. J. Wang, *Biosens. Bioelectron.*, 2016, 77, 90–98.
8   T. Kraus, L. Malaquin, H. Schmid, W. Riess, N. D. Spencer and H. Wolf, *Nat. Nanotechnol.*, 2007, 2, 570–576.
9   G. Chen, I. Roy, C. Yang and P. N. Prasad, *Chem. Rev.*, 2016, 116, 2826–2885.
10 M. Fedoruk, M. Meixner, S. Carretero-Palacios, T. Lohmüller and J. Feldmann, *ACS Nano*, 2013, 7, 7648–7653.
11 J. Jatschka, A. Dathe, A. Csáki, W. Fritzsche and O. Stranik, *Sens. Biosensing Res.*, 2016, 7, 62–70.
12 A.-I. Henry, J. M. Bingham, E. Ringe, L. D. Marks, G. C. Schatz and R. P. Van Duyne, *J. Phys. Chem. C*, 2011, 115, 9291–9305.
13 W. Liu, R. F. Oulton and Y. S. Kivshar, *Sci. Rep.*, 2015, 5, 12148.
14 A. Knauer and J. M. Koehler, *Phys. Chem. Chem. Phys.*, 2016, 18, 15943–15949.
15 H. Nishi, S. Hiroya and T. Tatsuma, *ACS Nano*, 2015, 9, 6214–6221.
16 O. Kedem, A. Vaskevich and I. Rubinstein, *J. Phys. Chem. C*, 2014, 118, 8227–8244.
17 Y. Wang, J. He, C. Liu, W. H. Chong and H. Chen, *Angew. Chem., Int. Ed.*, 2015, 54, 2022–2051.
18 D. E. Charles, D. Aherne, M. Gara, D. M. Ledwith, Y. K. Gun'ko, J. M. Kelly, W. J. Blau and M. E. Brennan-Fournet, *ACS Nano*, 2010, 4, 55–64.
19 C. Sönnichsen and A. P. Alivisatos, *Nano Lett.*, 2005, 5, 301–304.
20 A. Lukach, K. Liu, H. Therien-Aubin and E. Kumacheva, *J. Am. Chem. Soc.*, 2012, 134, 18853–18859.
21 B. Goris, G. Guzzinati, C. Fernandez-Lopez, J. Perez-Juste, L. M. Liz-Marzan, A. Trugler, U. Hohenester, J. Verbeeck, S. Bals and G. Van Tendeloo, *J Phys Chem C Nanomater Interfaces*, 2014, 118, 15356–15362.
22 D. Lee and S. Yoon, *J. Phys. Chem. C*, 2015, 119, 7873–7882.
23 N. R. Jana, L. Gearheart and C. J. Murphy, *Adv. Mater.*, 2001, 13, 1389–1393.
24 S. E. Lohse, N. D. Burrows, L. Scarabelli, L. M. Liz-Marzán and C. J. Murphy, *Chem. Mater.*, 2014, 26, 34–43.
25 S. E. Lohse and C. J. Murphy, *Chem. Mater.*, 2013, 25, 1250–1261.
26 M. L. Personick and C. A. Mirkin, *J. Am. Chem. Soc.*, 2013, 135, 18238–18247.
27 Y. Xia, Y. Xiong, B. Lim and S. E. Skrabalak, *Angew. Chem., Int. Ed.*, 2009, 48, 60–103.
28 C. Hanske, G. González-Rubio, C. Hamon, P. Formentin, E. Modin, A. Chuvilin, A. Guerrero-Martínez, L. F. Marsal and L. M. Liz-Marzán, *J. Phys. Chem. C*, 2017.
29 J. Rodríguez-Fernández, J. Pérez-Juste, F. J. García de Abajo and L. M. Liz-Marzán, *Langmuir*, 2006, 22, 7007–7010.
30 L. Zhang and Y. Xia, *Adv. Mater.*, 2014, 26, 2600–2606.
31 J. Wagner, T. Kirner, G. Mayer, J. Albert and J. M. Köhler, *Chem. Eng. J.*, 2004, 101, 251–260.
32 J. Wagner and J. M. Köhler, *Nano Lett.*, 2005, 5, 685–691.

78

Lab on a Chip

33 J. Boleininger, A. Kurz, V. Reuss and C. Sönnichsen, *Phys. Chem. Chem. Phys.*, 2006, 8, 3824.
34 J. M. Köhler, H. Romanus, U. Hübner and J. Wagner, *J. Nanomater.*, 2007, 2007, 7.
35 M. Thiele, J. Z. E. Soh, A. Knauer, D. Malsch, O. Stranik, R. Müller, A. Csáki, T. Henkel, J. M. Köhler and W. Fritzsche, *Chem. Eng. J.*, 2016, 288, 432–440.
36 S. E. Lohse, J. R. Eller, S. T. Sivapalan, M. R. Plews and C. J. Murphy, *ACS Nano*, 2013, 7, 4135–4150.
37 S. Duraiswamy and S. A. Khan, *Small*, 2009, 5, 2828–2834.
38 A. Knauer, A. Csáki, F. Möller, C. Hühn, W. Fritzsche and J. M. Köhler, *J. Phys. Chem. C*, 2012, 116, 9251–9258.
39 A. Knauer and J. M. Köhler, *Chem. Ing. Tech.*, 2013, 85, 467–475.
40 H. Mehenni, L. Sinatra, R. Mahfouz, K. Katsiev and O. M. Bakr, *RSC Adv.*, 2013, 3, 22397.
41 J. Polte, R. Erler, A. F. Thünemann, S. Sokolov, T. T. Ahner, K. Rademann, F. Emmerling and R. Kraehnert, *ACS Nano*, 2010, 4, 1076–1082.
42 M. Wuithschick, S. Witte, F. Kettemann, K. Rademann and J. Polte, *Phys. Chem. Chem. Phys.*, 2015, 17, 19895–19900.
43 M. Thiele, A. Knauer, A. Csáki, D. Mallsch, T. Henkel, J. M. Köhler and W. Fritzsche, *Chem. Eng. Technol.*, 2015, 38, 1131–1137.
44 L. Capretto, W. Cheng, M. Hill and X. Zhang, *Top. Curr. Chem.*, 2011, 304, 27–68.
45 V. Hessel, H. Löwe and F. Schönfeld, *Chem. Eng. Sci.*, 2005, 60, 2479–2501.
46 W. R. Dean, *Philos. Mag.*, 1927, 4, 208–223.
47 W. R. Dean, *Philos. Mag.*, 1928, 5, 673–695.
48 V. Mengeaud, J. Josserand and H. H. Girault, *Anal. Chem.*, 2002, 74, 4279–4286.
49 H. L. Wu, C. H. Kuo and M. H. Huang, *Langmuir*, 2010, 26, 12307–12313.
50 N. Almora-Barrios, G. Novell-Leruth, P. Whiting, L. M. Liz-Marzán and N. López, *Nano Lett.*, 2014, 14, 871–875.
51 L. Scarabelli, A. Sanchez-Iglesias, J. Perez-Juste and L. M. Liz-Marzan, *J. Phys. Chem. Lett.*, 2015, 6, 4270–4279.

5.5. Wet-chemical passivation of anisotropic plasmonic nanoparticles for LSPR-sensing by a silica shell [MT5]

Autorenschaft der Publikation:

Matthias Thiele[w]	Konzeptentwicklung und Verfassen des Manuskripts (inkl. Abbildungen)
	Erhebung und Evaluieren der Daten
	Planung und Durchführung der Experimente
	Charakterisierung der Nanopartikel
Isabell Götz[w]	Charakterisierung der Nanopartikel
	Planung und Durchführung der Experimente
	Erhebung und Evaluieren der Daten
	Diskussion und Korrektur des Manuskripts
Steffen Trautmann	Charakterisierung der Nanopartikel
	Diskussion des Konzepts und der Ergebnisse
Robert Müller	Diskussion der Ergebnisse
	Korrektur des Manuskripts
Andrea Csáki	Diskussion der Ergebnisse
	Konzeptentwicklung und Korrektur des Manuskripts
Thomas Henkel	Diskussion und Korrektur des Manuskripts
Wolfgang Fritzsche	Diskussion und Korrektur des Manuskripts
	Projektleitung
Vorschlag zur Anrechnung der Publikationsäquivalente:	**1**

5th International conference on Advanced Nano Materials

Wet-chemical passivation of anisotropic plasmonic nanoparticles for LSPR-sensing by a silica shell

Matthias Thiele*, Isabell Götz, Steffen Trautmann, Robert Müller, Andrea Csáki, Thomas Henkel and Wolfgang Fritzsche

Leibniz Institute of Photonic Technology (IPHT), Dept. Nanobiophotonics, Albert-Einstein-Straße 9, 07745 Jena, Germany

Abstract

Metal nanoparticles showing the effect of localized surface plasmon resonance (LSPR), a collective oscillation of the conduction electrons upon interaction with light, represent an interesting tool for bioanalytics. This resonance is influenced by changes in the environment, and can be therefore used for the detection of molecular layers. The sensitivity, this means the extent of wavelength resonance shift per change in refractive index in the environment, represents an important performance parameter. It is higher for silver compared to gold particles, and is also increased for anisotropic particles. So silver triangles show a high potential for highly sensitive plasmonic nanoparticles. However, the stability under ambient conditions is rather poor.

The paper demonstrates the passivation of silver triangles by silica coating using a wet-chemical approach. It compares the sensitivity for particles with and without passivation, and visualizes the passivation effect in a high resolution, single particle TEM study.

1. Introduction

Metal nanoparticles (meNP) allow new applications in medicine, optical imaging and sensing, since their optical behavior is strongly related to the localized surface plasmon resonance (LSPR) [12, 20, 27, 26]. This effect exists only for meNP that are smaller than the wavelength of the incident light, whereby the conductive electrons behave like an oscillating dipole which is excited by the resonance frequency [12]. Influenced by the material, shape, size and surrounding medium [8], the LSPR-peak position can be tuned over the whole optical spectra and beyond, to reach a large spectral variability (Fig. 1), which makes them suitable for a wide scope of applications [4, 18].

* Corresponding author. Tel.: 0049-3641-206-360
E-mail address: matthias.thiele@ipht-jena.de

MeNP could have a big impact especially as optical transducers for biological sensing, since they show a high signal, no bleaching and the possibility of a label-free sensing [2, 19] combined with a high sensitivity [5, 7]. An established sensing method is the variation of the particle surrounding, by changing the refractive index (RI) [14]. For example, for a DNA-biosensor, the meNP surface can be conjugated with DNA (capture DNA) [9, 11], that is complementary to the studied analyte DNA. In the presence of analyte DNA, it will bind (hybridize), resulting in a red-shift of the LSPR-signal [16, 22]. However, the meNP acts as a transducer of LSPR-sensor and has to be well chosen. One main issue is the sensitivity of a meNP, the ratio of the shift of the plasmon peak related to the RI-unit. It is know that form-anisotropic meNP can show a higher sensitivity compared to isotropic (spherical) ones, due to the strong, geometrically determined LSPR-field [15, 23]. So there is a stronger accumulation of the field at tips (like stars), corners (like rods) and edges compared to spherical ones [15, 17, 28]. A comparison of sensitivities of different meNP-shapes in solution clearly shows a high sensitivity for core/shell and alloy meNPs [20], but the highest sensitivity is shown by silver nanotriangles, which makes them ideal candidates for LSPR-sensing [13]. With respect to the size (edge length) it is furthermore possible to tune the LSPR-peak from UV-vis-range to near infrared (Fig. 1). Unfortunately, the stability of such silver-nanotriangles is rather poor, since they have a high surface energy and will be reshaped to spherical silver nanoparticles [6, 24]. Moreover, they are chemically reactive in ambient conditions. To overcome this problem they can be stabilized by using silica, to form a protective silica layer around the nanotriangles. A usual method for coating nanoparticles is the Stöber-method [21], where the meNP are used as seeds followed by subsequently growing of silica on their surface by a catalyzed condensation of TEOS (tetraethyl-orthosilicate) using ammonia [3]. However, since silver nanoparticles in general are known for their chemical instability against ammonia, it is even harder to encapsulate silver triangles without losing their shape [25]. To overcome this problem, we took advantage of other alkaline compounds and study their influence. We investigated the aging process of nanotriangles and will present the direct protective influence of the silica layer to the triangles. Finally we will show that the silica shell will have a high influence of the sensing behavior of the nanotriangles, but also that the protected triangles will still have good sensing qualities.
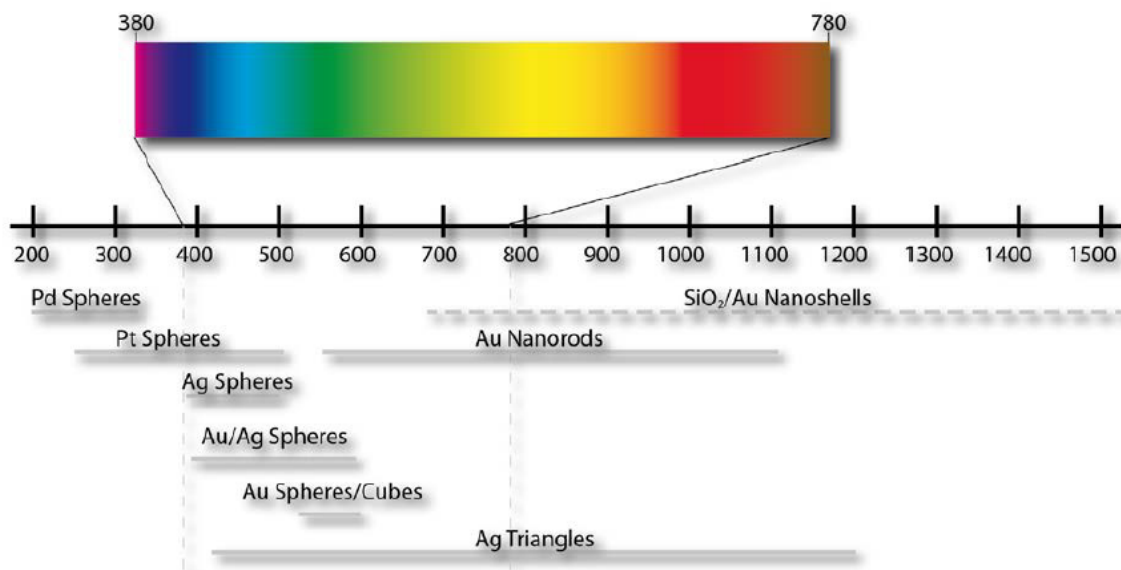
Fig. 1. Overview about the spectral ranges of plasmonic nanoparticles made by different materials and forms

2. Methods and Materials

2.1. Synthesis of silver nanotriangles

The production of silver nanotriangles is a modified method based on the work of Aherne et al [1]. This two-step synthesis is split in a synthesis part; in which silver seed particles with dimensions of about 14-150 nm are prepared. The second, the growing part uses the prepared seeds to start a two dimensional growth that results in silver triangles. For the seed synthesis, 5 ml sodium citrate (2.5 mM, Carl Roth GmbH + CO. KG, Karlsruhe, Germany) is used in a 15 ml PMMA centrifuge tube on a vortex mixer (Vortex-Genie 2; USA Scientific, Ocala FL). Under permanent shaking 250 µl Poly(sodium 4-styrenesulfonate) (0.5 g/l; 70 kDa, Sigma-Aldrich Chemie GmbH Munich, Germany) and 300 µl of a fresh, in ice water prepared $NaBH_4$ solution (10 mM, Carl Roth GmbH + CO. KG, Karlsruhe, Germany) are added. In the next step, 5 ml of $AgNO_3$ (0,5 mM; Merck KGaA Darmstadt, Germany) at a constant rate of 1 ml/min are added. After a few minutes of adding silver ions, the colorless solution turns from bright green/yellow to yellow (Figure 3 left tube).

After the synthesis is completed, the prepared seed particles are used to grow them to nanotriangles. For this purpose 5 ml ultrapure water in a 15 ml centrifuge tube is again used on a vortex mixer. Under strict shaking, 75 µl of a freshly prepared ascorbic acid solution (10 mM; Carl Roth GmbH + CO. KG, Karlsruhe, Germany) is added, followed by various amounts of the as-prepared seeds. The amount of seeds varies between 10 µl and 650 µl, the amount determining the edge length of the later triangles, that also correlates with the color of the solution and the LSPR-peak position as one can see in Fig 3. A high amount of seeds in the solution yields smaller triangles, whereby a low amount of seeds results in larger ones. After adding the seeds, 3 ml of $AgNO_3$ (0.5 mM) are added at a rate of 1 ml/min. Within a few seconds a color change is observed, starting from yellow to the appropriate color for the used amount of seeds. After the reaction is completed, it is necessary to add 500 µl of sodium citrate (25 mM) to achieve a charge stabilization of the triangles.

2.2. Silica-shell around the silver nanotriangles

The prepared triangles will be stabilized by adding a silica shell. For the preparation, 1 ml of the nano triangle solution was added to 7.51 ml ethanol containing the described concentration (1 mM, 2 mM and 4 mM) of TEOS (Sigma-Aldrich Chemie GmbH Munich, Germany) in a glass flask under rigorous stirring. To initialize the hydrolysis, 1.01 ml of an 8.8 M dimethylamine solution (DMA, Merck KGaA Darmstadt, Germany) was added and stirred for 2 days in the dark at 8°C. After the reaction is completed, the solution was washed two times by centrifugation, redispersed first in ethanol and finally in water.

2.3. Characterization

The prepared particles were stored in the dark at 8°C until they were characterized using transmission electron microscopy (TEM, Zeiss DSM 960, Jena, Germany), high resolution TEM (Jeol JEM_3010, Japan) and scanning force microscopy (Nanoscope III, Bruker Corporation Billerica, MA, USA). For the sensitivity measurements, refractive index series were prepared from different concentrations of D-glucose (Sigma-Aldrich Chemie GmbH Munich, Germany) in water from 0 to 60 m/V%. After mixing with the nanoparticles, the resulting plasmon peaks were measured using Jasco V-630 (JASCO Germany GmbH, Gross-Umstadt, Germany)

3. Results and Discussions

Silver triangles in various sizes were prepared as described. A wide range of colors of the various solutions is observed (Fig. 2a). Apparently it is the result of the different sizes, which lead to variations in the localized surface plasmon resonance (LSPR) bands. When comparing the color and the size of each particle preparation, the correlation between size and color of its resonance band become apparent (Fig. 2a). As already stated, the sensitivity
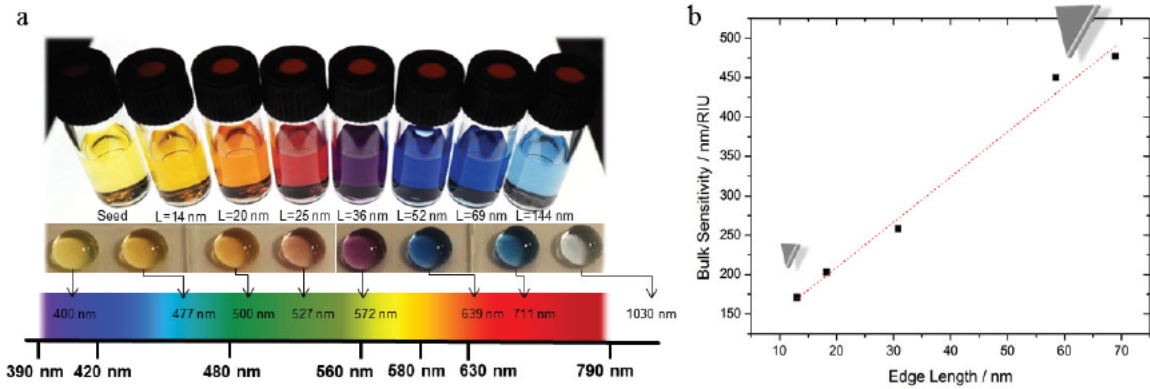
Fig. 2. (a) Solution of silver nanotriangles tuned from VIS to NIR with corresponding edge length (L) and LSPR-peak position.(b) Corresponding sensitivity in dependency on their dimension. In both cases are edge lengths calculated by setting the thickness to 8 nm (mean thickness from AFM) [1].

is of highest concern for possible sensing applications. Therefore, silver triangles of different sizes (edge lengths, L) were tested for their sensing properties using refractive index standards in solution (bulk sensitivity). A range of bulk-sensitivities between 200 and 600 nm/RIU were determined (Fig. 2b). A linear correlation between the size and the sensitivity was observed, whereas the bulk sensitivity can be calculated by equation one.

$$Bulk\ Sensitivity = 5.73 \cdot L + 94.40 \quad [nm/RIU] \tag{1}$$

In general, larger particles exhibit better sensitivity. However, at the same time, increasing size shifts the position of the LSPR band towards the infrared, moving out of the visible range. In conclusion, the particles show a convincing sensitivity in a suitable spectral range. When working with silver nanoparticles, a rather fast aging is observed [6, 28]. Thereby the surface seems to react with components of the atmosphere, resulting in an irreversible change. This process was studied on the ultramicroscopic scale at a single particle. While the particle scanned directly after synthesis shows the expected triangular shape (Fig. 3a), AFM imaging of the same particle after 12 hours in air shows significant structural changes: At all three corners, a significant growth of material is observed. This clearly results in a changed LSPR band, so that these particles have no defined and fixed LSPR band. This effect hinders a simple bioassay (measuring the same particle before and after analyte binding), but also the design of particles of a certain fixed LSPR band.
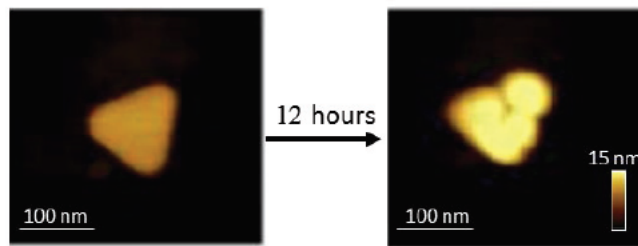
Fig. 3. AFM images of the same single triangle without a stabilizing silica layer/shell before (left) and after (right) aging for 12 hours in air.

A passivating layer as protection of the silver particle against the environment represents one approach to solve this problem. A silica coating of spherical silver particles was demonstrated using dimethylamine (DMA) [10] as source for the ammonia needed in the silica synthesis. In order to protect the more sensible silver nanotriangles, an additional protection layer of mercaptohexadecanoic acid (MHA) was introduced. We studied the stability of silver

nanotriangles in DMA and found that the particles only slowly decay (less than 10% loss in LSPR band amplitude in 10 min), so that for a fast and immediate starting reaction, the effect should be negligible. Therefore, the silica shells for the silver nanotriangles were synthesized using DMA.

Table 1. Used concentration of TEOS and corresponding LSPR-peak maxima, thickness of the generated silica shell and the radius of the tip as a marker for etching by using DMA as a basic catalyzer for the modified Stöber-method.

	Amount of precursor			
	no TEOS	1 mM TEOS	2 mM TEOS	4 mM TEOS
λ_{max}	666 nm	692 nm	689 nm	696 nm
Shell thickness	-	1.5 ± 0.8 nm	60 ± 5 nm	83 ± 6 nm
Tip radius	6.2 ± 1.8 nm	8.5 ± 0.8 nm	7.1 ± 1.4 nm	7.7 ± 1 nm

Varying the starting concentration of the silica-source TEOS, the thickness of the silica shell around the silver nanotriangles can be tuned between a very few and hundred nanometers (Tab. 1 and Fig. 4). Using this parameter, both thin layers (preserving the original nano triangle geometry) as well as large spherical shells are possible.
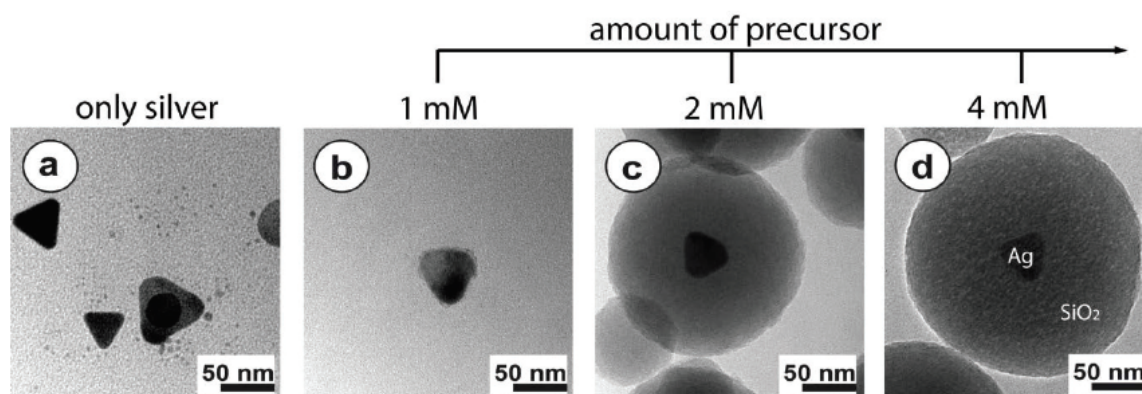
Fig. 4: Corresponding TEM-images to Table 1 of core-shell triangles with different silica shell thicknesses prepared with various concentrations of TEOS, starting from (a) 0 mM, (b) 1 mM to (c) 2 mM and finally (d) 4 mM.

For bioanalytical applications, the response of the LSPR signal of the particles to refractive index changes of the surrounding represents the key parameter. When the particles are covered by a passivating layer, is this response still observed? And to what extent? In order to clarify this issue, the sensitivity of particles of 56 nm side lengths was studied with and without a silica layer of 83 nm thickness. Therefore, the refractive index of the surrounding was changed, and the resulting wavelength shift in resonance measured and plotted as nm shift per refractive index unit (RIU). Nanotriangles without layer exhibited a sensitivity of about 555 nm/RIU (Fig. 5), which is in agreement with the plot shown in Fig. 2b. When a silica layer of about 83 nm was applied, a sensitivity of 283 nm/RIU was found. Compared to typical sensitivity values below 100 nm/RIU (Au spheres), 170 nm/RIU (Ag spheres) or 180 nm/RIU (Au nanorods), this value represents still a significant gain in sensitivity, now in combination with a stabilized nanoparticle and a surface which allows for standard attachment chemistry as utilized in the case of glass or silicon for DNA or protein microarray technologies.
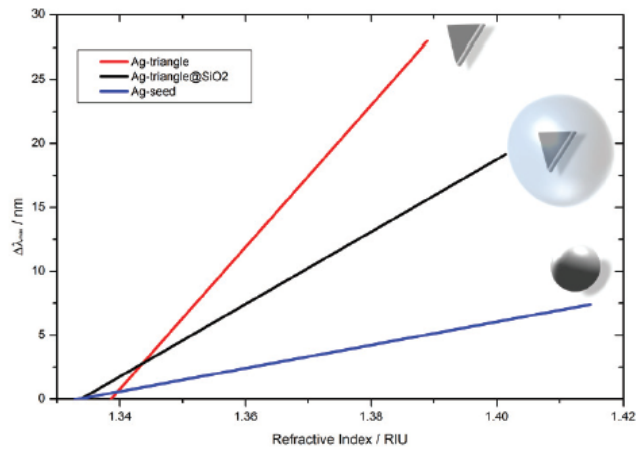
Fig. 5.Sensitivity of silver triangles with an edge length of around 56 nm with silica shell of 83 nm thickness (black line, 283nm/RIU) and without (black line, 555 nm/RIU). For comparison (the thickness of the triangles is 8 nm), the blue line represents a silver sphere of 8 nm diameter (91 nm/RIU).

For this quite thin protecting layer, a characterization of the protecting ability is quite challenging. Best visualization is achieved in a TEM, when the e-beam is absorbed accordingly by the various materials, with metals having a much higher contrast compared to silica as shown in Fig. 4. So single-particle studies were conducted in high-resolution TEM studying the behavior of the coated particles under the influence of the electron beam (Fig. 6), which is known to have damaging effect. In order to demonstrate the effect of the electron beam on protected as well as unprotected particles, a particle with an incomplete silica shell was chosen. Here, the silica cover showed two defects, which are marked by the red arrows in Fig. 6a. Following the effect of the electron beam over time, one can clearly see that the destructive processes starts on these sites of the pinholes. This observation demonstrates that the silica layer passivates the underlying silver against damaging effects, even on these small dimensions of just a few nanometers.
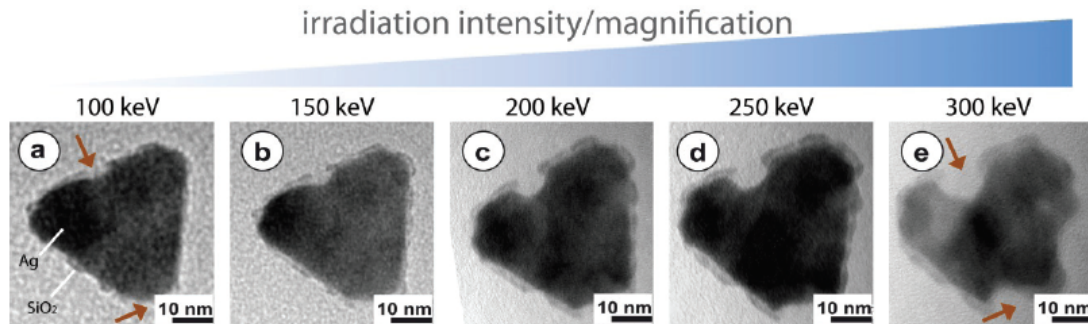
Fig. 6.Time series of a single, silica covered silver triangle in TEM, showing the structural disintegration under the influence of the electron beam. Silica thickness is less than 2 nm. This process clearly starts at the points where the silica cover is not complete (red arrows in a).

4. Conclusion

Passivation of silver nanotriangles allows an efficient protection of these otherwise often instable particles in combination with a preserved sensitivity. The utilization of a wet chemical approach for silica coating allows to control the thickness by variations of the synthesis parameters. The beneficial high sensitivity of the particles

towards refractive index change sensing is sufficiently preserved by this step, in combination with a strong protection. A high-resolution TEM study allowed to demonstrate this protection with a sub-particle resolution.

Acknowledgements

References

[1]   Aherne D, Ledwith D M, Gara M and Kelly J M 2008 Optical Properties and Growth Aspects of Silver Nanoprisms Produced by a Highly Reproducible and Rapid Synthesis at Room Temperature *Advanced Functional Materials* **18** 2005-16

[2]   Dondapati S K, Sau T K, Hrelescu C, Klar T A, Stefani F D and Feldmann J 2010 Label-free Biosensing Based on Single Gold Nanostars as Plasmonic Transducers *ACS Nano* **4** 6318-22

[3]   Guerrero-Martinez A, Perez-Juste J and Liz-Marzan L M 2010 Recent progress on silica coating of nanoparticles and related nanomaterials *Adv Mater* **22** 1182-95

[4]   Huang T and Nancy Xu X H 2010 Synthesis and Characterization of Tunable Rainbow Colored Colloidal Silver Nanoparticles Using Single-Nanoparticle Plasmonic Microscopy and Spectroscopy *Journal of materials chemistry* **20** 9867-76

[5]   Jakab A, Rosman C, Khalavka Y, Becker J, Trügler A, Hohenester U and Sönnichsen C 2011 Highly Sensitive Plasmonic Silver Nanorods *ACS Nano* **5** 6880-5

[6]   Jiang, Zeng and Yu 2007 Thiol-Frozen Shape Evolution of Triangular Silver Nanoplates *Langmuir* **23** 2218-23

[7]   Joshi G K, McClory P J, Dolai S and Sardar R 2012 Improved localized surface plasmon resonance biosensing sensitivity based on chemically-synthesized gold nanoprisms as plasmonic transducers *Journal of Materials Chemistry* **22** 923

[8]   Kelly K L, Coronado E, Zhao L L and Schatz G C 2002 The Optical Properties of Metal Nanoparticles: The Influence of Size, Shape, and Dielectric Environment *The Journal of Physical Chemistry B* **107** 668-77

[9]   Kim J-Y and Lee J-S 2010 Synthesis and Thermodynamically Controlled Anisotropic Assembly of DNA−Silver Nanoprism Conjugates for Diagnostic Applications *Chemistry of Materials* **22** 6684-91

[10]   Kobayashi Y, Katakami H, Mine E, Nagao D, Konno M and Liz-Marzan L M 2005 Silica coating of silver nanoparticles using a modified Stober method *J Colloid Interface Sci* **283** 392-6

[11]   Liu M, Wang Z, Zong S, Zhang R, Zhu D, Xu S, Wang C and Cui Y 2013 SERS-based DNA detection in aqueous solutions using oligonucleotide-modified Ag nanoprisms and gold nanoparticles *Anal Bioanal Chem* **405** 6131-6

[12]   Mayer K M and Hafner J H 2011 Localized surface plasmon resonance sensors *Chem Rev* **111** 3828-57

[13]   Millstone J E, Hurst S J, Metraux G S, Cutler J I and Mirkin C A 2009 Colloidal gold and silver triangular nanoprisms *Small* **5** 646-64

[14]   Mock J J, Smith D R and Schultz S 2003 Local Refractive Index Dependence of Plasmon Resonance Spectra from Individual Nanoparticles *Nano Letters* **3** 485-91

[15]   Nelayah J, Kociak M, Stephan O, Geuquet N, Henrard L, Garcia de Abajo F J, Pastoriza-Santos I, Liz-Marzan L M and Colliex C 2010 Two-dimensional quasistatic stationary short range surface plasmons in flat nanoprisms *Nano Letters* **10** 902-7

[16]   Schneider T, Jahr N, Jatschka J, Csaki A, Stranik O and Fritzsche W 2013 Localized surface plasmon resonance (LSPR) study of DNA hybridization at single nanoparticle transducers *J Nanopart Res* **15** 1-10

[17]   Senthil Kumar P, Pastoriza-Santos I, Rodriguez-Gonzalez B, Javier Garcia de Abajo F and Liz-Marzan L M 2008 High-yield synthesis and optical response of gold nanostars *Nanotechnology* **19** 015606

40   *Matthias Thiele et al. / Materials Today: Proceedings 2 (2015) 33 – 40*

[18]   Si G, Ma Z, Li K and Shi W 2011 Triangular Au–Ag Nanoframes with Tunable Surface Plasmon Resonance Signal from Visible to Near-Infrared Region *Plasmonics* **6** 241-4

[19]   Sönnichsen C and Alivisatos A P 2004 Gold Nanorods as Novel Nonbleaching Plasmon-Based Orientation Sensors for Polarized Single-Particle Microscopy *Nano Letters* **5** 301-4

[20]   Steinbruck A, Stranik O, Csaki A and Fritzsche W 2011 Sensoric potential of gold-silver core-shell nanoparticles *Anal Bioanal Chem* **401** 1241-9

[21]   Stöber W, Fink A and Bohn E 1968 Controlled growth of monodisperse silica spheres in the micron size range *J Colloid Interface Sci* **26** 62-9

[22]   Stranik O, Jatschka J, Csáki A and Fritzsche W 2014 Development of new classes of plasmon active nano-structures and their application in bio-sensing and energy guiding *Front. Phys.* 1-13

[23]   Xia Y, Xiong Y, Lim B and Skrabalak S E 2009 Shape-controlled synthesis of metal nanocrystals: simple chemistry meets complex physics? *Angew Chem Int Ed Engl* **48** 60-103

[24]   Xiong Y 2011 Morphological changes in Ag nanocrystals triggered by citrate photoreduction and governed by oxidative etching *Chem Commun (Camb)* **47** 1580-2

[25]   Xue C, Chen X, Hurst S J and Mirkin C A 2007 Self-Assembled Monolayer Mediated Silica Coating of Silver Triangular Nanoprisms *Adv Mater* **19** 4071-4

[26]   Yguerabide J and Yguerabide E E 1998 Light-Scattering Submicroscopic Particles as Highly Fluorescent Analogs and Their Use as Tracer Labels in Clinical and Biological Applications: I. Theory *Analytical Biochemistry* **262** 137-56

[27]   Yguerabide J and Yguerabide E E 1998 Light-Scattering Submicroscopic Particles as Highly Fluorescent Analogs and Their Use as Tracer Labels in Clinical and Biological Applications: II. Experimental Characterization *Analytical Biochemistry* **262** 157-76

[28]   Zijlstra P, Paulo P M, Yu K, Xu Q H and Orrit M 2012 Chemical interface damping in single gold nanorods and its near elimination by tip-specific functionalization *Angew Chem Int Ed Engl* **51** 8352-5

5.6. Gold-reinforced silver nanoprisms on optical fiber tapers – A new base for high precision sensing [MT6]

Autorenschaft der Publikation:

Torsten Wieduwilt	Konzeptentwicklung und Verfassen des Manuskripts (inkl. Abbildungen)
	Erhebung und Evaluieren der Daten
	Planung und Durchführung der Experimente
Matthias Zeisberger	Simulationen des optischen Verhaltens der Nanopartikel
	Diskussion der Ergebnisse
Matthias Thiele	Herstellung und Stabilisierung der Silberprismen
	Protokoll zur Nanopartikelimmobilisierung
	Charakterisierung der Nanopartikel
	Diskussion der Ergebnisse und Korrektur des Manuskripts
Brenda Doherty	Diskussion der Ergebnisse
Mario Chemnitz	Diskussion der Ergebnisse
Andrea Csáki	Diskussion und Korrektur des Manuskripts
Wolfgang Fritzsche	Korrektur des Manuskripts
Markus A. Schmidt	Diskussion und Korrektur des Manuskripts
	Projektleitungung

Vorschlag zur Anrechnung der Publikationsäquivalente: 0,75

APL PHOTONICS 1, 066102 (2016)

Der Nachdruck der folgenden Publikation erscheint mit freundlicher Genehmigung von *AIP Publishing.* Reprinted with kind permission from *AIP Publishing.*

Gold-reinforced silver nanoprisms on optical fiber tapers—A new base for high precision sensing

T. Wieduwilt,[1,a] M. Zeisberger,[1] M. Thiele,[1] B. Doherty,[1,2] M. Chemnitz,[1,2] A. Csaki,[1] W. Fritzsche,[1,2] and M. A. Schmidt[1,2,3]

[1]*Leibniz Institute of Photonic Technology e.V., Albert-Einstein-Str.9, 07745 Jena, Germany*
[2]*Abbe Center of Photonics, Friedrich-Schiller-University, Max-Wien-Platz 1, 07743 Jena, Germany*
[3]*Otto Schott Institute of Material Research, Friedrich-Schiller-University, Fraunhoferstr.6, 07743 Jena, Germany*

Due to their unique optical properties, metallic nanoparticles offer a great potential for important applications such as disease diagnostics, demanding highly integrated device solutions with large refractive index sensitivity. Here we introduce a new type of monolithic localized surface plasmon resonance (LSPR) waveguide sensor based on the combination of an adiabatic optical fiber taper and a high-density ensemble of immobilized gold-reinforced silver nanoprisms, showing sensitivities up to 900 nm/RIU. This result represents the highest value reported so far for a fiber optic sensor using the LSPR effect and exceeds the corresponding value of the bulk solution by a factor of two. The plasmonic resonance is efficiently excited via the evanescent field of the propagating taper mode, leading to pronounced transmission dips (-20 dB). The particle density is so high (approx. 210 particle/μm^2) that neighboring particles are able to interact, boosting the sensitivity, as confirmed by qualitative infinite element simulations. We additionally introduce a qualitative model explaining the interaction of plasmon resonance and taper mode on the basis of light extinction, allowing extracting key parameters of the plasmonic taper (e.g., modal attenuation). Due to the monolithic design and the extremely high sensitivity we expect our finding to be relevant in fields such as biomedicine, disease diagnostics, and molecular sensing. © 2016 Author(s). All article content, except where otherwise noted, is licensed under a Creative Commons Attribution (CC BY) license (*http://creativecommons.org/licenses/by/4.0/*). [http://dx.doi.org/10.1063/1.4953671]

I. INTRODUCTION

Metallic nanoparticles (meNPs) can show a very distinct optical response in the visible and near infrared part of the spectrum in case their diameters fall into the nanoscale domain. Here, an incident electromagnetic wave can excite the electrons inside the metal, which leads to a plasma-type oscillation of the electron ensemble, i.e., to the so-called localized surface plasmon resonance (LSPR). Particular for deep subwavelength meNP diameters, the optical response resembles that of a point dipole with a precisely defined phase retardation and orientation of the dipole axis. In comparison to their propagating counterparts in planar and cylindrical geometries,[1–3] LSPR shows extreme strong field confinements, i.e., their penetration depth into the surrounding dielectric is of the order of tens of nanometers only,[4] which makes them attractive for detecting nanoscale environmental changes which, for instance, are imposed by chemical reactions.

Colloidal meNPs have shown to be extremely useful particularly from the application perspective, since they are fabricated on large scales using chemical synthesis, i.e., a bottom-up approach, giving rise to large sample yields in contrast to, e.g., lithographic fabrication methods. Together

---

[a]Author to whom correspondence should be addressed. Electronic mail: torsten.wieduwilt@ipht-jena.de

1, 066102-1

with the above-mentioned strong field confinement, this particular feature has made them attractive for applications such as biomedicine[5,6] or nanoscale sensing.[7] One important application example of colloidal NPs is the detection of molecular events via an imposed change of the LSPR: The strong field confinement allows detecting small refractive index (RI) changes of the surrounding analyte in a nanoscale environment around the NP via measuring the spectral shift of LSPR. The key parameter characterizing this phenomenon is the sensitivity S, which is defined by the ratio between the spectral shift of the LSPR $\Delta\lambda_R$ and the change of the refractive index in the vicinity of the meNP Δn ($S = \Delta\lambda/\Delta n$).[8] As a result functionalization of plasmonic NPs with receptor (capture) molecules (e.g., proteins, antigens, and ssDNA) allows the identification of selective molecular bindings effect (e.g., antigen-antibody or DNA-DNA binding), which represents a key for, e.g., disease diagnosis.[9–11] Another important application field of colloidal meNPs is cancer therapy, where first results indicate that laser-induced heating of NPs via strong energy dissipation can help to locally destroy pathogenic tissue.[12–14]

Many of the currently employed plasmonic colloidal systems rely on noble metals such as gold or silver due to low intrinsic ohmic damping, which ultimately yields in strong LSPRs in the visible and near infrared.[4] Up to date, the most widely used colloidal NPs are gold nanospheres due to long-term stability and straightforward synthesis pathway. However, these nanospheres reveal comparably low RI sensitivity (of the order of 80 nm/RIU),[8] making them unattractive in case very small amounts of species are to be detected. This problem can be addressed by using NPs with large aspect ratios, which can show up to one order of magnitude larger sensitivity values and can be used for molecular sensing via local molecular binding.[15] With respect to application in biosensing and medicine, meNPs with "pointish"-type shapes such as cubes or stars[16] have recently attracted a lot of attention, since they give rise to extraordinary high sensitivities in case the analyte to be detected locally binds at the sharp edges of the NP.

For practical reasons colloidal nanoparticles are typically immobilized on solid surfaces and are investigated using, e.g., dark field microscopy,[17,18] whereas the incident light excites the LSPR and the scattered light is collected via high numerical aperture objectives. This approach has found wide-spread use but lacks monolithic and straightforward device integration and the possibility of investigating large ensembles of meNPs.

One promising scheme to address this issue is to integrate colloidal meNPs into photonic waveguiding system, which for instance can be realized by placing the NPs into the evanescent fields of an optical mode. Here, the LSPRs are excited via the tails of the propagating modes and the spectral properties of the plasmonic resonance can be measured via examining the waveguide transmission. This hybrid scheme has been successfully implemented within the scope of planar photonics, as for instance it was shown that LSPRs can be coupled to the modes of slab waveguides; in this case the meNPs were deposited on top of the waveguide, leading to a substantial transmission modification.[19,20]

However, planar waveguides reveal intrinsic problematic features such as high optical loss due to, e.g., surface roughness or surface state absorption, the prerequisite of complex fabrication technology and incompatibility to fiber optical technology. One attractive solution to the mentioned problems is to combine meNP and optical fibers on the basis of fiber-optical tapers: These highly integrated photonic elements consist of down-tapered optical fibers to diameters so small that the evanescent field of the optical mode penetrates the surrounding material, i.e., the analyte. Tapers have been successfully employed for exciting both propagating surface plasmon-polaritons[21–25] and localized plasmonic modes, whereas in the latter case only NPs with comparably low sensitivity have been employed (e.g., gold nanospheres (diameter 24 nm) sensitivity of ~51 nm/RIU)[26] mostly using single mode fibers. Besides the mentioned tapers, the evanescent field can be also accessed using techniques such as mechanical stripping of the cladding, which was used for plastic-clad multimode fibers[27–31] and chemical removal of the cladding via etching used for silica clad multimode[32] and single mode fibers, respectively.[33] Other types of fiber-optic sensors not using plasmonic excitations rely on effects such as long-period gratings (1500 nm/RIU),[34] coupling to modes beyond modal cut-off (301 000 nm/RIU),[35] directional mode coupling (3200 nm/RIU),[36] multimodal interference (667 nm/RIU),[37] focused ion-beam
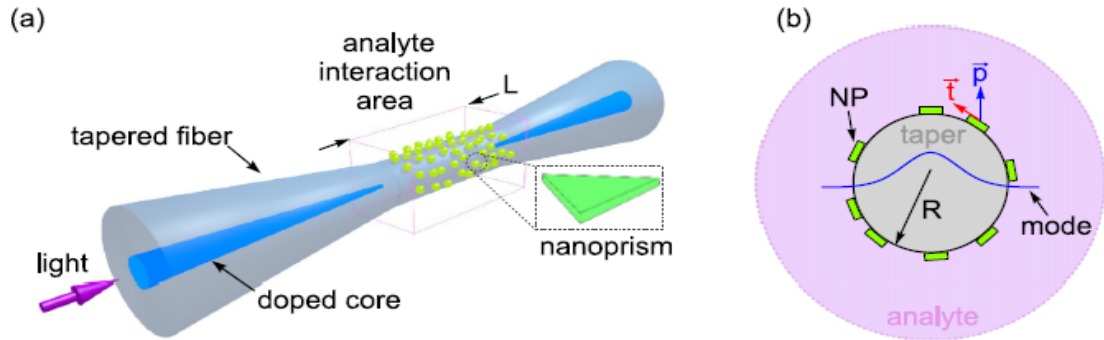
FIG. 1. (a) Schematic of the plasmonic fiber optical taper coated with highly sensitive silver-gold nanoprisms in the region of the taper waist. The magenta box indicates the domain the analyte is applied. (b) Cross section of the plasmonic taper in the domain the nanoprisms are deposited. The small green structures indicate the nanoprisms on the surface of the taper and the purple curve represents the propagating of fundamental optical taper mode. The two vectors indicate the local orientations of the polarization vector of the guided mode $\vec{p}$ and the vector parallel to the film surface of the NP $\vec{t}$.

machined Fabry-Perot cavities (1130 nm/RIU, 1150 nm/RIU),[38,39] and laser-written Bragg gratings (10 nm/RIU).[40]

Here we show that silver nanoprisms immobilized on an adiabatic optical fiber taper Fig. 1(a) result in a novel hybrid plasmonic-photonic system with extraordinary high sensitivity values of about 900 nm/RIU, which exceeds that of the corresponding bulk solution by a factor of two. This key feature of our system results from the fact that the taper allows precise engineering of the interaction between LSPR and taper mode. In fact the fraction of evanescent field outside the taper has been adjusted such that meNP densities sufficiently high for interaction of the LSPRs of neighboring meNPs can be established on the taper surface, which results in substantially higher sensitivities than compared to the case of meNPs dispersed in solution.

Moreover, strong transmission dips with extinction ratios of up to 20 dB are observed, making the taper approach particular attractive for index sensing. Since the LSPRs are detected via analyzing the change of the transmission through the taper, our system represents a highly integrated and straightforward-to-use approach, which has the potential to give rise to a full monolithic sensor being compatible with fiber circuitry. The taper and the meNP immobilization are straightforward to conduct and due to mm-long interaction length our sensor is of macroscopic scale, making it attractive from the handling perspective.

In addition to all relevant experimental details, we present a fitting model which allows explaining the interaction of LSPR and taper mode on the basis of light extinction and extracting key characteristics of the plasmonic taper such as the modal attenuation. We also present simulations from a qualitative scattering model, showing that interparticle interaction leads to a substantial increase in RI sensitivity in the case of high particle densities.

II. THEORETICAL BACKGROUND

The working principle of the meNP-enhanced fiber taper presented here relies on the interaction of the LSPR with the propagating mode inside the taper. Within the taper waist, the evanescent field of the guided wave penetrates the analyte and excites the LSPRs of the meNPs on the surface of the taper. The corresponding fraction of electromagnetic energy is in fact removed from that of the optical mode (via scattering and absorption of the nanoparticle) and as a result strong transmission dips are observed. A key feature of the taper concept is that the fraction of field in the analyte, i.e., the fraction exciting the LSPR, can be precisely adjusted via the taper diameter, ultimately allowing for investigating meNP ensembles with extremely high coverage. For the structure discussed here the fraction of evanescent field in the analyte is only 0.1% in case water is surrounding the taper (at 700 nm), allowing to examine meNP ensemble with a density so high that neighboring meNPs interact.

The attenuation coefficient of the mode propagating inside the taper γ (i.e., LSPR-induced extinction coefficient) can be described by a line integral along the circumference of the taper, leading to

$$\gamma = \oint_{r=R} \frac{N\sigma(\phi,\Delta\lambda)}{A_{\text{eff}}(r,\phi,\Delta\lambda)} dl, \tag{1}$$

with the density of the nanoprisms N (number of meNPs per unit area), the relative wavelength $\Delta\lambda = \lambda - \lambda_R$ (λ: vacuum wavelength, λ_R: LSPR resonance wavelength), the azimuthal angle dependent extinction cross section $\sigma(\phi)$, and the taper radius R. In case of an anisotropic meNP (which holds for the nanoprisms considered here), the excitation of the LSPR depends on the relative orientation of meNP (defined here as the unity vector parallel to the meNP surface $\vec{t}$) and unity polarization vector of the guided mode $\vec{p}$ at the location of the meNP (Fig. 1(b)). Since the extinction cross section is generally defined with respect to intensity,[41] we define $\sigma(\phi) = \sigma_0(\vec{t}\cdot\vec{p})^2$ including the bulk extinction cross section σ_0, which can either be determined from simulating the scattering properties of a single meNP or from measuring the particle extinction. Here we determined σ_0 from bulk solution (subsequently denoted as σ_s), which is to some extent a different situation compared to plasmonic taper case. In solution the particles are randomly orientated along all three spatial directions, whereas in the taper case the particles lie on the taper surface, i.e., are preferentially oriented normal to the taper axis. This orientation imposes a reduced dimensionality in the taper situation ($3 \rightarrow 2$) leading to a larger cross section (i.e., more particles contribute to the overall extinction), which can be accounted for by the following substitution: $\sigma_t = \sigma_s \cdot 3/2$. This ansatz assumes that the maximum LSPR excitation is achieved for parallel orientation of $\vec{p}$ and $\vec{t}$, whereas there is negligible contribution of the LSPR excitation in the perpendicular direction. This leads to $\sigma_t(\phi) = \sigma_t \cos^2\phi$ (ϕ: angle between $\vec{t}$ and $\vec{p}$) and is in correspondence with the qualitative planar waveguide simulations shown later, which shows that the strongest LSPR excitation is achieved for TE-polarization, i.e., $\phi = 0$. The parameter $A_{\text{eff}}(r,\phi,\Delta\lambda)$ refers to the area of the mode on the surface of the taper[42,43] and is associated with the Poynting vector distribution of the mode under investigation S_z,

$$A_{\text{eff}}(R,\Delta\lambda) = \frac{\int_{A=\infty} S_z(r,\phi,\Delta\lambda)dA}{S_z(r=R,\phi,\Delta\lambda)}. \tag{2}$$

The effective mode area depends on the azimuthal coordinate, suggesting that γ depends on the azimuthal position of meNP on the taper surface. In the situation investigated here, however, the taper diameters are comparably large, and hence the guided HE_{11} mode has a Gaussian type mode distribution with only a small azimuthal dependence, allowing to define an average and constant effective area $\overline{A}_{\text{eff}} = 2\int S_z dA/(S_z(r=R,\phi=0°,\Delta\lambda) + S_z(r=R,\phi=90°,\Delta\lambda))$. Due to the high symmetry of the cylindrical geometry, $\overline{A}_{\text{eff}}$ has a full analytic form since S_z can be expressed by a single analytic function.[44,45] As a result of independence of A_{eff} on azimuthal angle and the simple mathematical form of $\sigma_t(\phi)$, the line integral Eq. (1) can be equated analytically, leading to

$$\gamma(\Delta\lambda) = \frac{N\sigma_t(\Delta\lambda)}{\overline{A}_{\text{eff}}(\Delta\lambda)} \pi R. \tag{3}$$

This allows expressing the transmitted power P_T through the plasmonic taper of the length L via the following equation:

$$P_T(\Delta\lambda) = P_0 \exp\left(-\frac{N\sigma_t(\Delta\lambda)}{\overline{A}_{\text{eff}}(\Delta\lambda)} \pi R L\right), \tag{4}$$

with the input power P_0.

It is interesting to note that Eq. (4) clearly shows that the modal attenuation is in fact determined by the ratio of the two areas involved, i.e., σ_t/A_{eff}, which emphasizes that tuning the optical mode properties allows the engineering of the transmission properties (inset of Fig. 2).

This tunability feature appears even more pronounced when investigating the ratio R/A_{eff} (Fig. 2) including all geometric parameters determined by the taper and showing that argument
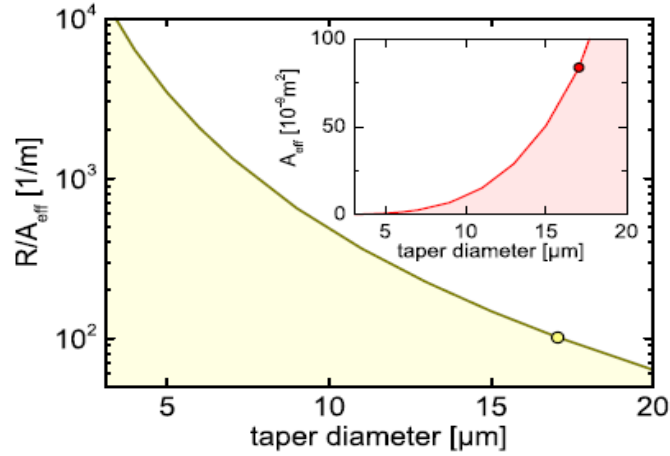
FIG. 2. Dependence of R/A$_{eff}$ ratio on taper diameter at a fixed wavelength of 740 nm (taper material: silica, surrounding analyte: water). The inset shows the effective mode cross section as a function of taper diameter. The points in both plots indicate the configuration used in the experiment (taper diameter 17 μm).

of the exponential function of P_T (Eq. (4)) can be tuned over two orders of magnitude only by changing the taper diameter, which in fact allows studying a broad range of NP densities.

III. FABRICATION AND MEASUREMENT METHOD

For the investigation presented here, we used gold-reinforced silver nanoprisms with approximate dimensions of 40 ± 20 nm and a thickness of 9 ± 2 nm, being chemically fabricated using a combination of seed particle synthesis and subsequent nanoprism growth (inset of Fig. 3(a), see supplementary material, Sec. I[51]). To avoid catalytic oxidation (etching) of the silver in particular at the edges of the nanoprisms,[46,47] we overgrow the nanoprism edges with a thin gold layer, which is a well-known approach to stabilize silver NPs,[48,49] for instance, by using them in physiological conditions[50] (see supplementary material,[51] Sec. I, preparation of mNPs). This step is essential for the temporal stability of our hybrid system, as otherwise the oxidation would impose a morphology
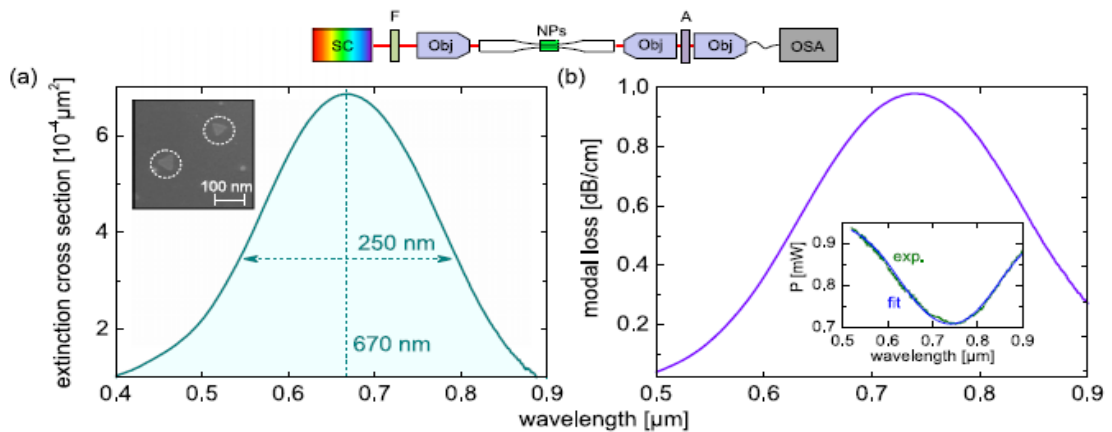
FIG. 3. (a) Spectral distribution of the extinction cross section of the localized plasmonic resonance of the nanoprisms, measured in aqueous solution. The inset exemplarily shows a scanning electron micrograph (SEM) of two silver nanoprisms (highlighted by the dashed circles) deposited onto a planar glass surface. The vertical (horizontal) dashed line represents the center resonance wavelength (FWHM peak width). (b) Spectral distribution of the modal attenuation calculated using the plasmonic taper transmission function defined in Eq. (3). The inset shows the experimentally obtained data (green) and the fit (blue) in case water is used as analyte. The sketch above both plots shows the experimental transmission setup used to determine the transmission properties of the plasmonic tapers (SC: supercontinuum source, F: water filter, Obj: objective, Nikon CF Plan 50×/0.55WD 8.7).

change of the nanoprisms (from triangular to disk shape) resulting in a substantially reduced RI sensitivity. We observe that the nanoprisms have triangular as well as hexagonal shapes.

The fiber tapers have been fabricated from silica-based step-index fibers (Nufern HP780, cut-off wavelength 730 nm) and were tapered down over length of ~84 mm (using a Vytran GPX 3200, total fiber length: 25 cm). The waist had a length of ~14 mm (constant diameter section) and a radius of $R = 8.5 \, \mu$m. The two transition zones had lengths of 35 mm to provide adiabaticity, i.e., avoid higher-order mode excitation, giving rise to a clean fundamental mode in the waist section. Within that section, the influence of the doped core on the propagating modes is so small that it can be neglected. The mode inside the waist can thus be represented by the fundamental (HE_{11}) mode of cylindrical silica strand in either air or the analyte. The nanoprisms were attached to the taper using an aminosilane linker (see supplementary material,[51] Sec. III, preparation of fiber probes).

The nanoprisms were deposited over the entire length of the waist ($L = 14$ mm), whereas the density of the nanoprisms N was coarsely controlled via changing the immobilization time. Due to the comparably broad size distribution of the nanoprisms, it turned out to be difficult to quantify the exact value of N for one fixed deposition time. For instance, in the case of 17 min immobilization time (in the following referred as "long" immobilization time), the particle density was in the order of $(210 \pm 30) \, \text{NPs}/\mu\text{m}^2$, whereas a 90 s deposition ("short" immobilization time) yields $N \approx (50 \pm 30) \, \text{NPs}/\mu\text{m}^2$.

To determine the transmission of the plasmonic fiber taper we used the following experimental setup (top image of Fig. 3(a)): Light from a supercontinuum source SC (SuperK Compact, bandwidth 400 nm–1.8 μm) was coupled into the fiber using a microscope objective (Nikon CF Plan, 50×), and the spectral distribution of the transmitted light was measured by an OSA (Ando, AQ6315A, resolution 2 nm). To prevent sample heating and thus an undesired change of the analyte RI, a 1-cm cuvette filled with water acting as IR blocking filter was inserted just after the output of the light source to avoid absorption via infrared light. The spectra were normalized to corresponding spectra of tapers without meNPs in air, whereas control measurements show no difference in transmission between uncoated tapers in air and water.

The RI sensitivity was determined by measuring the LSPR resonance wavelength (transmission dips) in case the meNP-enhanced taper is immersed in different RI environments. Here we used as analyte a series of D-glucose-water solutions with RI in the range between 1.34 and 1.38 (see supplementary material,[51] Sec. II, optical characterization). The wavelength of the LSPR (transmission dips, for instance Fig. 4) was taken from the transmission curves and plotted as a function of analyte index (at λ_R), allowing the determination of the corresponding slope, i.e., sensitivity (see, for instance, Fig. 5). The sensitivity of the nanoprisms in bulk solution was measured in an analogous
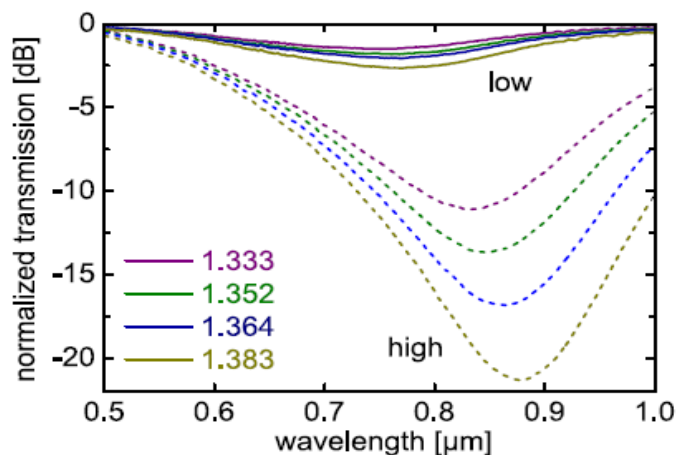
FIG. 4. Wavelength dependence of the measured normalized transmission through the plasmonic taper coated with the nanoprisms. The transmission of tapers with either high (indicated by the dashed lines) or low (indicated by the solid lines) nanoparticle densities has been investigated for four different values of analyte refractive index (numbers refer to the bulk refractive index of the respective analyte at 589 nm. Purple: 1.333, green: 1.352, blue: 1.364, dark yellow: 1.383).
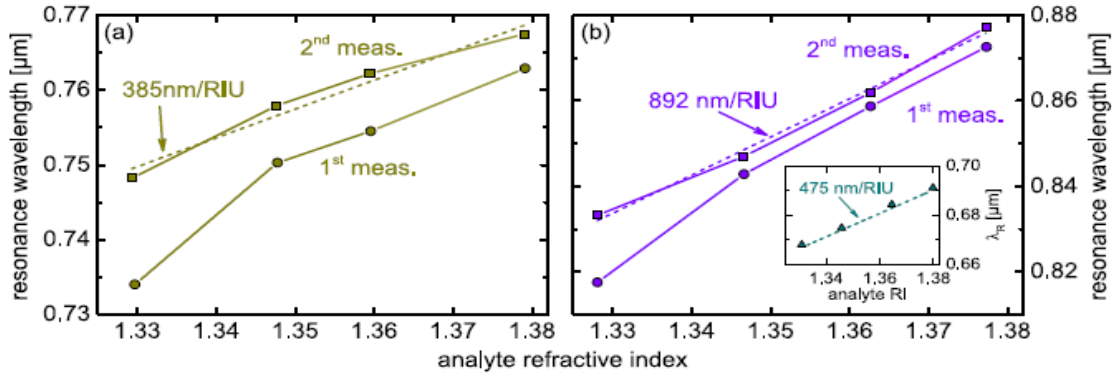
FIG. 5. Resonance wavelength (spectral position of transmission dip) as a function of analyte refractive index of the nanoprism enhanced fiber taper. (a) Low particle density, (b) high particle density. In both plots, the circles refer to the very first conducted measurements, the squares to subsequent measurements after stabilization, which were then used to determine the RI sensitivity (dashed lines). The solid lines are guides-to-the-eye, and the inset in (b) shows the dependence of the localized plasmon resonance wavelength on analyte index of the nanoprisms in solution.

way by combining centrifugation and re-dilution and measuring the spectral distribution of the solution extinction (see supplementary material,[51] Sec. II, optical characterization).

IV. EXPERIMENTAL RESULTS

To analyze the properties of our plasmonic taper on the basis of Eq. (3), we determined at first the extinction cross section of the silver nanoprisms ensemble in water (see supplementary material,[51] Sec. II, optical characterization). We found that the nanoprism ensemble has a rather broadband distribution of σ with a peak resonance wavelength of 670 nm and a maximum cross section of $\sigma_{max,lg} = 6.9 \times 10^{-4} \ \mu m^2$ (Fig. 3(a)), referring to the natural logarithm as defined in Eq. (4), $\sigma_{max,ln} = 15.8 \times 10^{-4} \ \mu m^2$. Compared to typical gold nanosphere systems, the spectral broadness of the investigated ensemble here is comparably large (about 250 nm (FWHM)), which can be attributed to the size distribution of the nanoprisms, leading to a distribution of LSPR wavelength and hence to a spectral broadening of the linewidth. This size distribution is also the reason why the evolution of the extinction coefficient cannot be approximated by a single Lorentzian oscillator function.

To understand the transmission properties of our plasmonic taper, we used Eq. (4) to fit the measured transmission curve in the case of a water analyte using and λ_R, P_0, and N as fitting parameters. It is important to note that in the case of the plasmonic taper the nanoprisms are in fact immobilized on glass and thus a spectral shift of the LSPR is expected compared to the measured resonance of the NPs in solution, i.e., justifies using λ_R as fit parameter ($\sigma = \sigma_t(\lambda_R - \Delta\lambda)$). We observe that the experimentally measured transmission curve is accurately represented by Eq. (4) when using $P_0 = 0.97$ mW, $N = 73.7$ NP/μm^2, and $\lambda_R = 739.1$ nm (inset of Fig. 3(b), determination includes the above mentioned reduced dimensionality of the plasmonic taper), which is within the experimental error margins of the NP density. It needs to be pointed out that we only obtain a good agreement of model and experimental data if we take into account the spectral distribution of the effective mode, whereas a constant value of A_{eff} leads to an insufficient description particularly at the red side of the LSPR.

Using these fit parameters we calculated the modal extinction coefficient using Eq. (3), revealing that our meNP-enhanced taper has a peak resonance loss of the order of 0.98 dB/cm (Fig. 3(b)), lying within the expected attenuation range. Therefore our transmission model allows determining the modal attenuation of meNP-taper system, which is the key parameter of any waveguide system, under measurement conditions and without destroying the sample (as it would be the case if the cut back method is employed).

In a next step we investigated the behavior of the taper transmission for different analyte RIs in the cases of high and low nanoprism density (Fig. 4). We measure in both cases that higher analyte

RIs lead to a shift of the transmission dips to longer wavelength, which results from the red-shifting LSPRs. Moreover we observe substantially deeper transmission dips for larger nanoprism densities compared to low particle coverage. For instance, in the case of $n_{analyte} = 1.383$, a depth of ≈ 2.5 dB is measured for the low coverage, whereas the high nanoprism density results in a transmission dip of ≈ 20 dB. This clearly shows that the plasmonic taper concept is capable of investigating various meNP densities using the same waveguide.

The RI sensitivity of the nanoprisms in solution was determined to 475 nm/RIU (inset of Fig. 5(b), for experimental details see supplementary material,[51] Sec. II, optical characterization), which is significantly higher than that of many used NP-systems such as gold nanospheres (~50 nm/RIU) or gold nanocubes (~80 nm/RIU).

For the plasmonic taper, the evaluation of the measured data showed that the system undergoes a change after the first measurement series, i.e., after the first contact to the glucose solution, imposing a red-shift of the LSPR (Fig. 5). After the first series the plasmonic taper stabilizes and no further changes in λ_R were observed. The reason for the first initial change remains unclear to us and will be targeted in future studies. In the case of a high particle concentration ("long" immobilization time, Fig. 5(b)) we obtain a sensitivity of 892 nm/RIU, which represents the highest value reported for plasmonic optical taper so far and is substantially higher than the sensitivity of the bulk solution (475 nm/RIU, inset of Fig. 5(b)). This clearly shows that tapers provide a unique pathway for achieving highly sensitive devices on a monolithic waveguide platform. As we will discuss in a qualitative example in Sec. V (Fig. 6(b)), these high values are associated with neighboring NPs in the case of high particle density. In case the interparticle distance is larger (means a lower particle density), Fig. 5(a), we measure a lower sensitivity of 385 nm/RIU, which is comparable to that of the bulk solution.

V. QUALITATIVE SIMULATIONS

To gain a qualitative understanding of the high sensitivity values observed in the experiments, we simulate a simplified geometry consisting of a single silver nanodisk (diameter $d = 60$ nm, thickness 10 nm) on a planar slab waveguide (core silica of thickness 17 μm, cladding water) using a combination of analytic mode field expressions and finite-element based scattering, in which the LSPR is excited by the guided waveguide mode (inset of Fig. 6, dielectric functions from Refs. 52 and 53). Simulating the realistic structure would require considering all particle orientations that are
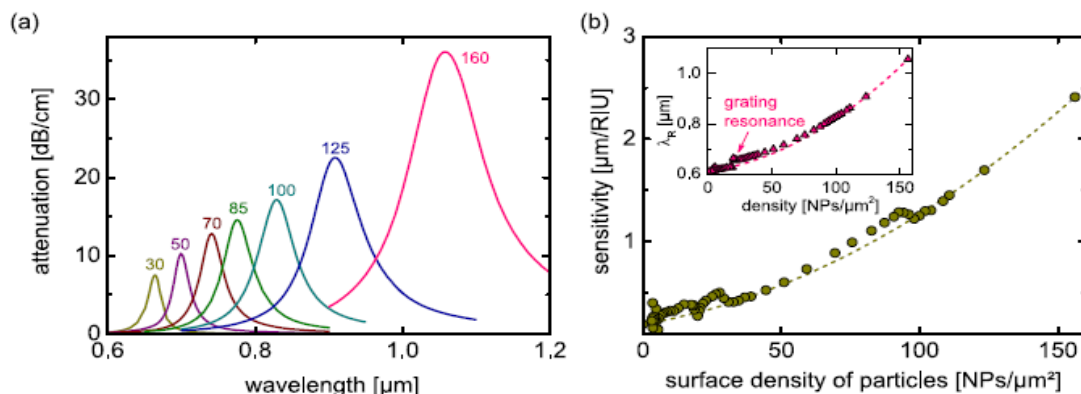
FIG. 6. Simulations of the optical properties of the plasmonic fiber taper calculated using the FEM model (TE-polarization). To reveal the qualitative behavior of the nanoparticle enhanced taper, spherical silver nanoparticles with a diameter of 60 nm are assumed. A constant analyte index of 1.33 is assumed here. (a) Spectral distribution of the modal attenuation for various nanoparticle densities (respective density values are indicated by the numbers on the top of the respective curve). (b) Corresponding refractive index sensitivity (determined at the resonance position (inset), i.e., point of highest attenuation) as a function of nanoparticle surface density. The dashed curve refers to a fitting curve with a square dependence on particle density. The non-trivial curve evolution particularly at small densities can be attributed to grating resonances.

experimentally possible and shapes, which requires a full statistical analysis and is out of the scope of this contribution.

Due to the large taper diameter (17 μm), the taper curvature at the location of the NP can be neglected and the lowest taper mode (HE_{11}-mode) then corresponds to the lowest TE or TM mode of the planar waveguide or a superposition of both depending on the azimuthal position of the particle, i.e., the relative orientation angle ϕ. Various NP densities are considered by assuming periodic boundary conditions (imposing interparticle interaction) and different gap sizes between two neighboring NPs g. The size of the simulation volume is $d + g$ in both directions, leading to $N = 1/(d + g)^2$. We have calculated the electric field distributions of the TE and TM modes analytically[54] and used them as background field distributions in the mentioned simulation volume for obtaining the scattered fields (in Comsol scattered field mode). The FEM simulations yield the scattered and total fields, and by integrating the corresponding Poynting vectors we obtain the scattered and absorbed power from which we can calculate the corresponding modal attenuation induced by one single particle γ_s. The RI sensitivity has been obtained by two identical sets of simulations assuming an analyte RI of 1.33 in one set and 1.34 in the other set. The simulations show that the LSPR excitation in TM polarization ($\vec{E}_{trans} \parallel z$)$\gamma_s$ is much smaller (by a factor >2) compared to the TE case ($\vec{E}_{trans} \perp z$) and the spectral peak loss position is always <700 nm. Therefore, the TE-attenuation is the dominating contribution and is analyzed in more detail.

The attenuation spectra (Fig. 6(a)) show maxima that shift to longer wavelengths (Fig. 6(b)) with increasing amplitude when the particle density increases—a behavior that was also observed in structures such as nanoparticle chains and layers of gold nanospheres.[1,55] As suggested by Fig. 6(b) the RI sensitivity significantly increases (more than a factor of 10) for higher particle density, which overall is a result of increasing interparticle interaction. This effect can be qualitatively understood by the following toy-model: We can approximate our particles as flat ellipsoids with a polarizability in the quasistatic limit given by Ref. 41 $\alpha_P = V(\varepsilon_m - \varepsilon_d)/(\varepsilon_m + L(\varepsilon_m - \varepsilon_d))$ with the metal and surrounding dielectric permittivities ε_m and ε_d, the particle volume V, and the depolarization factor L. Plasmon resonances appear for vanishing real parts of the denominator. Assuming a Drude ansatz for ε_m and the condition $L \ll 1$, we obtain $\lambda_R \approx \lambda_p n_d/\sqrt{L}$ and $S \approx \lambda_P/\sqrt{L}$ (plasma wavelength of silver $\lambda_p = 137$ nm, dielectric refractive index n_d), showing that the sensitivity strongly depends on depolarization. Here, L accounts for the depolarization field that is oriented antiparallel to the polarization vector inside the particle. For a single isolated particle, the depolarization field is entirely caused by the surface charges induced by the incident wave. In case of arrays of particles, neighboring particles impose an additional contribution to the depolarization field resulting from the stray fields of the other particles. The strongest effects on the depolarization field result from the next neighbors in the direction of the polarization of the exciting field. Therefore, the effect of interaction, i.e., the increasing sensitivity for denser ensembles, can be qualitatively interpreted as a reduced depolarization factor (i.e., increasing depolarization field).

This is in correspondence with the experimental observation and explains that we observe higher sensitivity values for higher NP coverages (Fig. 6(b)). The simulated data points scatter around a quadratic polynomial curve. The latter can be related to the quasistatic model which is a good approximation for small ($\ll \lambda$) particle distances (i.e., large particle densities) as well as for single particles (zero density).

In the intermediate domain the periodic particle arrangement can act as a grating with additional resonances that cause deviations from the smooth quadratic dependence. However, these grating effects are not relevant for our experimental situation as there is no periodic arrangement, i.e., the distribution of NPs is entirely statistic.

VI. CONCLUSION AND OUTLOOK

Here we have introduced a new type of monolithic LSPR waveguide sensor based on the combination of an adiabatic optical fiber taper and immobilized gold-reinforced silver nanoprisms, showing refractive index sensitivities up to 900 nm/RIU. This result represents the highest value reported so far for a fiber optic sensor using the LSPRs of metallic nanoparticles and exceeds that of the corresponding bulk solution by a factor of two. The overall idea relies on the LSPR of the

interacting nanoparticles being excited by the evanescent field of the propagating mode, leading to a change of the transmission through the taper. This key feature of our system is that it allows accessing nanoparticle density so high that the particle interacts significantly, which substantially increases the sensitivity. This situation of interacting nanoparticles is typically difficult to achieve, whereas the taper allows precise tuning of the fraction of evanescent field outside the taper. As a result, we are able to access extremely high NP densities allowing LSPRs of neighboring NPs to interact imposing the observed high sensitivity values.

To understand the physics of our system we conducted qualitative scattering simulations revealing that the high sensitivity values are associated with interparticle interactions in case the nanoparticle density on the taper surface is high. In addition, we introduce a fitting model which explains the interaction of LSPR and taper mode on the basis of light extinction and extracting key characteristics of the plasmonic taper such as the modal attenuation. This model also shows that changing the taper geometry principally allows accessing two orders of magnitude of particle concentrations.

Since the LSPRs are detected via measuring the transmission, our system represents a highly integrated and straightforward-to-use approach, which has the potential to give rise to a full monolithic sensor for wavelength interrogation being compatible with fiber circuitry. The taper and the NP immobilization are straightforward to conduct and, due to mm-long interaction length, our sensor is of macroscopic scale, making it highly attractive within areas such as biophotonics, environmental science, or medicine. Next steps will include applying our sensor to a biologically relevant system to specifically detect chemical processes such as DNA binding events for disease diagnostics.

The application range of the extinction model introduced here (e.g., Eq. (1)) is rather general and is not restricted to cylindrical tapers. Therefore we believe that our findings will be important for all kinds of sensors relying on a coupling of a waveguide mode and LSPR, which is particularly important for systems using microstructured or even photonic crystal fibers.

ACKNOWLEDGMENTS

[1] S. A. Maier, M. L. Brongersma, P. G. Kik, and H. A. Atwater, Phys. Rev. B **65**(19), 193408 (2002).

[2] R. Spittel, P. Uebel, H. Bartelt, and M. A. Schmidt, Opt. Express **23**, 12174–12188 (2015).

[3] P. Uebel, M. A. Schmidt, H. W. Lee, and P. S. J. Russell, Opt. Express **20**, 28409–28417 (2012).

[4] S. A. Maier and H. A. Atwater, J. Appl. Phys. **98**(1), 011101 (2005).

[5] W. J. Cho, A. Jung, S. Han, S. M. Lee, T. Kang, K. H. Lee, K. C. Choi, and J. K. Kim, NPG Asia Mater. **7**, e167 (2015).

[6] G. Y. Chen, I. Roy, C. H. Yang, and P. N. Prasad, Chem. Rev. **116**(5), 2826–2885 (2016).

[7] M. A. Schmidt, D. Y. Lei, L. Wondraczek, V. Nazabal, and S. A. Maier, Nat. Commun. **3**, 1108 (2012).

[8] P. Kvasnicka and J. Homola, Biointerphases **3**(3), FD4–FD11 (2008).

[9] A. Csaki, M. Thiele, J. Jatschka, A. Dathe, D. Zopf, O. Stranik, and W. Fritzsche, Eng. Life Sci. **15**(3), 266–275 (2015).

[10] T. J. Wang, C. W. Tu, and F. K. Liu, IEEE J. Sel. Top. Quantum Electron. **11**(2), 493–499 (2005).

[11] L. He, M. D. Musick, S. R. Nicewarner, F. G. Salinas, S. J. Benkovic, M. J. Natan, and C. D. Keating, J. Am. Chem. Soc. **122**(38), 9071–9077 (2000).

[12] X. H. Huang, S. Neretina, and M. A. El-Sayed, Adv. Mater. **21**(48), 4880–4910 (2009).

[13] A. M. Gobin, M. H. Lee, N. J. Halas, W. D. James, R. A. Drezek, and J. L. West, Nano Lett. **7**(7), 1929–1934 (2007).

[14] C. R. Patra, R. Bhattacharya, D. Mukhopadhyay, and P. Mukherjee, J. Biomed. Nanotechnol. **4**(2), 508–514 (2008).

[15] K. M. Mayer and J. H. Hafner, Chem. Rev. **111**(6), 3828–3857 (2011).

[16] H. J. Chen, X. S. Kou, Z. Yang, W. H. Ni, and J. F. Wang, Langmuir **24**(10), 5233–5237 (2008).

[17] D. Y. Lei, A. I. Fernandez-Dominguez, Y. Sonnefraud, K. Appavoo, R. F. Haglund, J. B. Pendry, and S. A. Maier, ACS Nano **6**(2), 1380–1386 (2012).

[18] T. Schneider, N. Jahr, J. Jatschka, A. Csaki, O. Stranik, and W. Fritzsche, J. Nanopart. Res. **15**(4), 1531 (2013).

[19] S. Linden, A. Christ, J. Kuhl, and H. Giessen, Appl. Phys. B: Lasers Opt. **73**(4), 311–316 (2001).

[20] S. Linden, J. Kuhl, and H. Giessen, Phys. Rev. Lett. **86**(20), 4688–4691 (2001).

[21] T. Wieduwilt, K. Kirsch, J. Dellith, R. Willsch, and H. Bartelt, Plasmonics **8**(2), 545–554 (2013).

[22] J. Villatoro, D. Monzon-Hernandez, and E. Mejia, Appl. Opt. **42**(13), 2278–2283 (2003).

[23] D. Monzon-Hernandez and J. Villatoro, Sens. Actuators, B **115**(1), 227–231 (2006).

[24] N. Diaz-Herrera, A. Gonzalez-Cano, D. Viegas, J. L. Santos, and M. C. Navarrete, Sens. Actuators, B **146**(1), 195–198 (2010).

[25] T. Wieduwilt, A. Tuniz, S. Linzen, S. Goerke, J. Dellith, U. Hubner, and M. A. Schmidt, Sci. Rep. **5**, 17060 (2015).

[26] H. Y. Lin, C. H. Huang, G. L. Cheng, N. K. Chen, and H. C. Chui, Opt. Express **20**(19), 21693–21701 (2012).

[27] S. K. Srivastava, V. Arora, S. Sapra, and B. D. Gupta, Plasmonics **7**(2), 261–268 (2012).

[28] W. T. Hsu, W. H. Hsieh, S. F. Cheng, C. P. Jen, C. C. Wu, C. H. Li, C. Y. Lee, W. Y. Li, L. K. Chau, C. Y. Chiang, and S. R. Lyu, Anal. Chim. Acta **697**(1-2), 75–82 (2011).

[29] S. F. Cheng and L. K. Chau, Anal. Chem. **75**(1), 16–21 (2003).

[30] L. K. Chau, Y. F. Lin, S. F. Cheng, and T. J. Lin, Sens. Actuators, B **113**(1), 100–105 (2006).

[31] J. S. Crosby, D. Lucas, and C. P. Koshland, Sens. Actuators, B **81**, 938–942 (2013).

[32] Y. L. Shao, S. P. Xu, X. L. Zheng, Y. Wang, and W. Q. Xu, Sensors **10**(4), 3585–3596 (2010).

[33] J. Luo, J. Yao, Y. G. Lu, W. Y. Ma, and X. Y. Zhuang, Sensors **13**(3), 3986–3997 (2013).

[34] L. Rindorf and O. Bang, Opt. Lett. **33**(6), 563–565 (2008).

[35] D. K. C. Wu, B. T. Kuhlmey, and B. J. Eggleton, Opt. Lett. **34**(3), 322–324 (2009).

[36] H. W. Lee, M. A. Schmidt, P. Uebel, H. Tyagi, N. Y. Joly, M. Scharrer, and P. S. Russell, Opt. Express **19**(9), 8200–8207 (2011).

[37] L. V. Nguyen, K. Hill, S. Warren-Smith, and T. Monro, Sens. Actuators, B **221**, 320–327 (2015).

[38] Z. L. Ran, Y. J. Rao, J. Zhang, Z. W. Liu, and B. Xu, J. Lightwave Technol. **27**(23), 5426–5429 (2009).

[39] T. Wieduwilt, J. Dellith, F. Talkenberg, H. Bartelt, and M. A. Schmidt, Opt. Express **22**(21), 25333–25346 (2014).

[40] S. C. Warren-Smith, R. Kostecki, L. V. Nguyen, and T. M. Monro, Opt. Express **22**(24), 29493–29504 (2014).

[41] C. F. Bohren and D. R. Huffman, *Absorption and Scattering of Light by Small Particles* (Wiley-VCH Verlag GmbH, Weinheim, 1998).

[42] F. Warken, E. Vetsch, D. Meschede, M. Sokolowski, and A. Rauschenbeutel, Opt. Express **15**(19), 11952–11958 (2007).

[43] X. C. Yu, B. B. Li, P. Wang, L. M. Tong, X. F. Jiang, Y. Li, Q. H. Gong, and Y. F. Xiao, Adv. Mater. **26**(44), 7462–7467 (2014).

[44] J. A. Snyder and J. D. Love, *Optical Waveguide Theory* (Chapman and Hall, London, New York, 1983).

[45] F. Le Kien, J. Q. Liang, K. Hakuta, and V. I. Balykin, Opt. Commun. **242**(4-6), 445–455 (2004).

[46] P. Mulvaney, T. Linnert, and A. Henglein, J. Phys. Chem. **95**(20), 7843–7846 (1991).

[47] T. Pal, T. K. Sau, and N. R. Jana, Langmuir **13**(6), 1481–1485 (1997).

[48] D. Aherne, D. E. Charles, M. E. Brennan-Fournet, J. M. Kelly, and Y. K. Gun'ko, Langmuir **25**(17), 10165–10173 (2009).

[49] M. M. Shahjamali, M. Salvador, M. Bosman, D. S. Ginger, and C. Xue, J. Phys. Chem. C **118**(23), 12459–12468 (2014).

[50] K. E. Lee, A. V. Hesketh, and T. L. Kelly, Phys. Chem. Chem. Phys. **16**(24), 12407–12414 (2014).

[51] See supplementary material at http://dx.doi.org/10.1063/1.4953671 for preparation and characterization of the silver nanoprisms as well as the preparation of the nanoparticles-covered optical fiber probe.

[52] P. B. Johnson and R. W. Christy, Phys. Rev. B **6**(12), 4370–4379 (1972).

[53] E. D. Palik, *Handbook of Optical Constants of Solids* (Academic Press, London, 1998).

[54] T. Tamir, G. Griffel, and H. L. Bertoni, *Guided-Wave Optoelectronics: Device Characterization, Analysis, and Design* (Springer, 1995).

[55] E. Martinsson, B. Sepulveda, P. Chen, A. Elfwing, B. Liedberg, and D. Aili, Plasmonics **9**(4), 773–780 (2014).

5.7. Nanoparticle functionalised small-core suspended-core fibre – a novel platform for efficient sensing [MT7]

Autorenschaft der Publikation:

Brenda Doherty	Verfassen des Manuskripts (inkl. Abbildungen) Erhebung und Evaluieren der Daten Planung und Durchführung der Experimente
Andrea Csáki	Konzeptentwicklung Diskussion und Korrektur des Manuskripts Projektleitung
Matthias Thiele	Herstellen der Nanopartikel Charakterisierung der Nanopartikel Diskussion der Ergebnisse und Korrektur des Manuskripts
Matthias Zeisberger	Simulationen des optischen Verhaltens der Nanopartikel Erarbeiten der Theoretische Grundlagen
Anka Schwuchow	Diskussion der Ergebnisse Charakterisierung der Faser
Jens Kobelke	Diskussion der Ergebnisse
Wolfgang Fritzsche	Korrektur des Manuskripts
Markus A. Schmidt	Diskussion und Korrektur des Manuskripts Projektleitung
Vorschlag zur Anrechnung der Publikationsäquivalente:	**0,75**

Nanoparticle functionalised small-core suspended-core fibre – a novel platform for efficient sensing

BRENDA DOHERTY,[1,2,*] ANDREA CSÁKI,[1] MATTHIAS THIELE,[1] MATTHIAS ZEISBERGER,[1] ANKA SCHWUCHOW,[1] JENS KOBELKE,[1] WOLFGANG FRITZSCHE,[1] AND MARKUS A. SCHMIDT[1,2,3]

[1]*Leibniz Institute of Photonic Technology e.V., Albert-Einstein-Str. 9, 07745 Jena, Germany*
[2]*Abbe Center of Photonics, Friedrich-Schiller-University, Max-Wien-Platz, 1, 07743 Jena, Germany*
[3]*Otto Schott Institute of Material Research, Fraunhoferstr.6, Friedrich-Schiller-University, 07743 Jena, Germany*
[*]*brenda.doherty@leibniz-ipht.de*

Abstract: Detecting small quantities of specific target molecules is of major importance within bioanalytics for efficient disease diagnostics. One promising sensing approach relies on combining plasmonically-active waveguides with microfluidics yielding an easy-to-use sensing platform. Here we introduce suspended-core fibres containing immobilised plasmonic nanoparticles surrounding the guiding core as a concept for an entirely integrated optofluidic platform for efficient refractive index sensing. Due to the extremely small optical core and the large adjacent microfluidic channels, over two orders of magnitude of nanoparticle coverage densities have been accessed with millimetre-long sample lengths showing refractive index sensitivities of 170 nm/RIU for aqueous analytes where the fibre interior is functionalised by gold nanospheres. Our concept represents a fully integrated optofluidic sensing system demanding small sample volumes and allowing for real-time analyte monitoring, both of which are highly relevant within invasive bioanalytics, particularly within molecular disease diagnostics and environmental science.

References and links

1. O. Lazcka, F. J. Del Campo, and F. X. Muñoz, "Pathogen detection: A perspective of traditional methods and biosensors," Biosens. Bioelectron. **22**(7), 1205–1217 (2007).
2. P. D'Orazio, "Biosensors in clinical chemistry - 2011 update," Clin. Chim. Acta **412**(19-20), 1749–1761 (2011).
3. S. M. Yoo and S. Y. Lee, "Optical Biosensors for the Detection of Pathogenic Microorganisms," Trends Biotechnol. **34**(1), 7–25 (2016).
4. A. G. Brolo, "Plasmonics for future biosensors," Nat. Photonics **6**(11), 709–713 (2012).
5. S. A. Maier and H. A. Atwater, "Plasmonics: Localization and guiding of electromagnetic energy in metal/dielectric structures," J. Appl. Phys. **98**(1), 011101 (2005).
6. J. Zhao, X. Zhang, C. R. Yonzon, A. J. Haes, and R. P. Van Duyne, "Localized surface plasmon resonance biosensors," Nanomedicine (Lond.) **1**(2), 219–228 (2006).
7. J. Cao, T. Sun, and K. T. V. Grattan, "Gold nanorod-based localized surface plasmon resonance biosensors: A review," Sens. Actuators B Chem. **195**, 332–351 (2014).
8. K. A. Willets and R. P. Van Duyne, "Localized surface plasmon resonance spectroscopy and sensing," Annu. Rev. Phys. Chem. **58**(1), 267–297 (2007).
9. M. Chamanzar, Z. Xia, S. Yeganarayanan, and A. Adibi, "Hybrid integrated plasmonic-photonic waveguides for on-chip localized surface plasmon resonance (LSPR) sensing and spectroscopy," Opt. Express **21**(26), 32086–32098 (2013).
10. J. Homola, S. S. Yee, and G. Gauglitz, "Surface plasmon resonance sensors: review," Sens. Actuators B Chem. **54**(1-2), 3–15 (1999).
11. J. C. Yang, J. Ji, J. M. Hogle, and D. N. Larson, "Metallic nanohole arrays on fluoropolymer substrates as small label-free real-time bioprobes," Nano Lett. **8**(9), 2718–2724 (2008).
12. F. Eftekhari, C. Escobedo, J. Ferreira, X. Duan, E. M. Girotto, A. G. Brolo, R. Gordon, and D. Sinton, "Nanoholes As Nanochannels: Flow-through Plasmonic Sensing," Anal. Chem. **81**(11), 4308–4311 (2009).

13. M. Barth, S. Schietinger, S. Fischer, J. Becker, N. Nüsse, T. Aichele, B. Löchel, C. Sönnichsen, and O. Benson, "Nanoassembled Plasmonic-Photonic Hybrid Cavity for Tailored Light-Matter Coupling," Nano Lett. **10**(3), 891–895 (2010).

14. A. Urrutia, J. Goicoechea, and F. J. Arregui, "Optical Fiber Sensors Based on Nanoparticle-Embedded Coatings," J. Sens. **2015**, 1–18 (2015).

15. J. Luo, J. Yao, Y. Lu, W. Ma, and X. Zhuang, "A Silver Nanoparticle-Modified Evanescent Field Optical Fiber Sensor for Methylene Blue Detection," Sensors (Basel) **13**(3), 3986–3997 (2013).

16. A. M. Aravanis, L. P. Wang, F. Zhang, L. A. Meltzer, M. Z. Mogri, M. B. Schneider, and K. Deisseroth, "An optical neural interface: in vivo control of rodent motor cortex with integrated fiberoptic and optogenetic technology," J. Neural Eng. **4**(3), S143–S156 (2007).

17. S. Faez, Y. Lahini, S. Weidlich, R. F. Garmann, K. Wondraczek, M. Zeisberger, M. A. Schmidt, M. Orrit, and V. N. Manoharan, "Fast, label-free tracking of single viruses and weakly scattering nanoparticles in a nano-fluidic optical fiber," ACS Nano **9**(12), 12349–12357 (2015).

18. M. A. Schmidt, A. Argyros, and F. Sorin, "Hybrid Optical Fibers – an innovative platform for in-fiber photonic devices," Adv. Opt. Mater. **4**(1), 13–36 (2016).

19. T. Wieduwilt, A. Tuniz, S. Linzen, S. Goerke, J. Dellith, U. Hubner, and M. A. Schmidt, "Ultrathin niobium nanofilms on fiber optical tapers - a new route towards low-loss hybrid plasmonic modes," Sci. Rep. **5**, 17060 (2015).

20. T. Wieduwilt, K. Kirsch, J. Dellith, R. Willsch, and H. Bartelt, "Optical Fiber Micro-Taper with Circular Symmetric Gold Coating for Sensor Applications Based on Surface Plasmon Resonance," Plasmonics **8**(2), 545–554 (2013).

21. T. Wieduwilt, M. Zeisberger, M. Thiele, B. Doherty, M. Chemnitz, A. Csaki, W. Fritzsche, and M. A. Schmidt, "Gold-reinforced silver nanoprisms on optical fiber tapers—A new base for high precision sensing," APL Photonics **1**(6), 066102 (2016).

22. J. Cao, E. K. Galbraith, T. Sun, and K. T. V. Grattan, "Cross-Comparison of Surface Plasmon Resonance-Based Optical Fiber Sensors With Different Coating Structures," IEEE Sens. J. **12**(7), 2355–2361 (2012).

23. H. Y. Lin, C. H. Huang, G. L. Cheng, N. K. Chen, and H. C. Chui, "Tapered optical fiber sensor based on localized surface plasmon resonance," Opt. Express **20**(19), 21693–21701 (2012).

24. T. G. Euser, J. S. Y. Chen, M. Scharrer, P. S. J. Russell, N. J. Farrer, and P. J. Sadler, "Quantitative broadband chemical sensing in air-suspended solid-core fibers," J. Appl. Phys. **103**(10), 103108 (2008).

25. S. C. Warren-Smith, J. Wie, M. Chemnitz, R. Kostecki, H. Ebendorff-Heidepriem, T. M. Monro, and M. A. Schmidt, "Third harmonic generation in exposed-core microstructured optical fibers," Opt. Express **24**(16), 17860–17867 (2016).

26. A. M. Cubillas, S. Unterkofler, T. G. Euser, B. J. M. Etzold, A. C. Jones, P. J. Sadler, P. Wasserscheid, and P. S. Russell, "Photonic crystal fibres for chemical sensing and photochemistry," Chem. Soc. Rev. **42**(22), 8629–8648 (2013).

27. G. O. S. Williams, J. S. Y. Chen, T. G. Euser, P. S. Russell, and A. C. Jones, "Photonic crystal fibre as an optofluidic reactor for the measurement of photochemical kinetics with sub-picomole sensitivity," Lab Chip **12**(18), 3356–3361 (2012).

28. A. Csáki, F. Jahn, I. Latka, T. Henkel, D. Malsch, T. Schneider, K. Schröder, K. Schuster, A. Schwuchow, R. Spittel, D. Zopf, and W. Fritzsche, "Nanoparticle Layer Deposition for Plasmonic Tuning of Microstructured Optical Fibers," Small **6**(22), 2584–2589 (2010).

29. K. Schroder, A. Csaki, A. Schwuchow, F. Jahn, K. Strelau, I. Latka, T. Henkel, D. Malsch, K. Schuster, K. Weber, T. Schneider, R. Moller, and W. Fritzsche, "Functionalization of Microstructured Optical Fibers by Internal Nanoparticle Mono-Layers for Plasmonic Biosensor Applications," IEEE Sens. J. **12**(1), 218–224 (2012).

30. A. Schwuchow, M. Zobel, A. Csáki, K. Schröder, J. Kobelke, W. Fritzsche, and K. Schuster, "Monolayers of different metal nanoparticles in microstructured optical fibers with multiplex plasmonic properties," Opt. Mater. Express **2**(8), 1050–1055 (2012).

31. K. M. Mayer and J. H. Hafner, "Localized Surface Plasmon Resonance Sensors," Chem. Rev. **111**(6), 3828–3857 (2011).

32. F. Warken, E. Vetsch, D. Meschede, M. Sokolowski, and A. Rauschenbeutel, "Ultra-sensitive surface absorption spectroscopy using sub-wavelength diameter optical fibers," Opt. Express **15**(19), 11952–11958 (2007).

33. H. Ebendorff-Heidepriem, S. C. Warren-Smith, and T. M. Monro, "Suspended nanowires: Fabrication, design and characterization of fibers with nanoscale cores," Opt. Express **17**(4), 2646–2657 (2009).

34. X. C. Yu, B. B. Li, P. Wang, L. Tong, X. F. Jiang, Y. Li, Q. Gong, and Y. F. Xiao, "Single Nanoparticle Detection and Sizing Using a Nanofiber Pair in an Aqueous Environment," Adv. Mater. **26**(44), 7462–7467 (2014).

35. G. M. Whitesides, "The origins and the future of microfluidics," Nature **442**(7101), 368–373 (2006).

36. J. Turkevich, P. C. Stevenson, and J. Hillier, "A Study of the Nucleation and Growth Processes in the Synthesis of Colloidal Gold," Discuss Faraday Soc, 55 (1951).

37. G. Frens, "Controlled Nucleation for Regulation of Particle-Size in Monodisperse Gold Suspensions," Nature-Phys Sci **241**(105), 20–22 (1973).

103

38. A. M. Cubillas, M. Schmidt, T. G. Euser, N. Taccardi, S. Unterkofler, P. St. J. Russell, P. Wasserscheid, and B. J. M. Etzold, "In Situ Heterogeneous Catalysis Monitoring in a Hollow-Core Photonic Crystal Fiber Microflow Reactor," Adv. Mater. Interfaces **1**(5), 1300093 (2014).
39. S. A. Maier, M. L. Brongersma, P. G. Kik, and H. A. Atwater, "Observation of near-field coupling in metal nanoparticle chains using far-field polarization spectroscopy," Phys. Rev. B **65**(19), 193408 (2002).
40. A. Csáki, M. Thiele, J. Jatschka, A. Dathe, D. Zopf, O. Stranik, and W. Fritzsche, "Plasmonic nanoparticle synthesis and bioconjugation for bioanalytical sensing," Eng. Life Sci. **15**(3), 266–275 (2015).
41. Alexandre Dmitriev, ed., *Nanoplasmonic Sensors* (Springer, 2012).
42. A. Hassani, B. Gauvreau, M. F. Fehri, A. Kabashin, and M. Skorobogatiy, "Photonic crystal fiber and waveguide-based surface plasmon resonance sensors for application in the visible and near-IR," Electromagnetics **28**(3), 198–213 (2008).
43. A. Hassani and M. Skorobogatiy, "Design criteria for microstructured-optical-fiber-based surface plasmon-resonance sensors," J. Opt. Soc. Am. B **24**(6), 1423–1429 (2007).
44. N. J. Florous, K. Saitoh, and M. Koshiba, "Numerical modeling of cryogenic temperature sensors based on plasmonic oscillations in metallic nanoparticles embedded into photonic crystal fibers," IEEE Photonics Technol. Lett. **19**(5), 324–326 (2007).
45. M. Hautakorpi, M. Mattinen, and H. Ludvigsen, "Surface-plasmon-resonance sensor based on three-hole microstructured optical fiber," Opt. Express **16**(12), 8427–8432 (2008).
46. A. Steinbrück, A. Csaki, and W. Fritzsche, "Metal Nanoparticles for Molecular Plasmonics," Reviews in Plasmonics **2010**, 1–37 (2010).

1. Introduction

The non-invasive detection of life-threatening disease is a major challenge in biomedicine, since it requires identifying pathogens of extremely low concentration or even on the single molecular level [1–3]. One promising detection strategy providing such sensitivity and selectivity, without the necessity of molecular labelling, relies on attaching molecular probes to metallic nanoparticles (NPs) [4]. The electron ensemble of such NPs is collectively excited by an external electromagnetic wave at a characteristic wavelength, creating localised surface plasmon resonances (LSPRs) [5]. Functionalising NPs with specific molecular probes then allows detection of molecular binding events via a macroscopic change of the plasmonic resonance [6–9]. Many of the currently used plasmonic devices rely on planar fabrication technology, i.e. planar integrated photonic structures, examples of which include nanohole arrays, nanochannel flow-through sensing, and hybrid optical cavities [10–13]. Despite their success, these devices can show limited device performance due to short light-matter interaction lengths, complex and inefficient launching schemes, and intrinsically high optical loss.

An alternative approach places plasmonic NPs into the evanescent fields of the modes of optical fibres [14,15]. Fibre platforms in general offer profound advantages particularly with respect to bioanalytical application such as: spectral and spatial multiplexing, flexible handling, precise control of modal properties, and the potential for in-vivo applications [16–18]. So far almost all fibre-integrated plasmonic sensors involve multi- or single-mode optical tapers which have been coated either with continuous metallic nanofilms [19,20] or plasmonic NPs [21–23]. Although these systems have displayed refractive index (RI) sensing capabilities, the NPs are located on the outer surface of the taper, yielding non-integrated and delicate-to-handle devices with further disadvantages including the requirement for large analyte volumes with only a fraction used for the actual sensing.

An important class of novel optical fibres, possessing great potential within the field of bioanalytics, are suspended-core fibres (SCFs) (Fig. 1) [24,25]. These microstructured fibres contain axial air channels which extend along the entire fibre length and have diameters of several tens of micrometres. Typically three or four of these channels are arranged such to form a central micrometre-size glass core resembling the geometry of a step index fibre, with the propagating mode deeply penetrating into the channel via its evanescent field. These fibres are particularly attractive from the bioanalytical perspective, as they allow real-time probing of liquid analytes flowing through the channel regions by using the light propagating inside the fibre core. Promising experiments indicate successful application of analytics in SCFs, examples of which include sensing of ionic liquid [24,26] and dynamic detection of

trans/cis isomerisation processes [27]. First attempts to integrate small metallic NPs into SCFs have been recently conducted [28–30], wherein the LSPRs were probed perpendicular to the fibre axis, which does not exploit the advantage of the fibre geometry.

Here we show that a nanoparticle-functionalised suspended core fibre can act as a highly integrated optofluidic platform for efficient RI sensing. Due to the small core diameter, we obtain strong interaction of plasmon and guided mode, allowing us to access two orders of magnitude of nanoparticle densities at moderate sample lengths. The measured sensitivity is of the same order compared to particles in solution, making this monolithic system highly attractive for applications within bioanalytics [31].
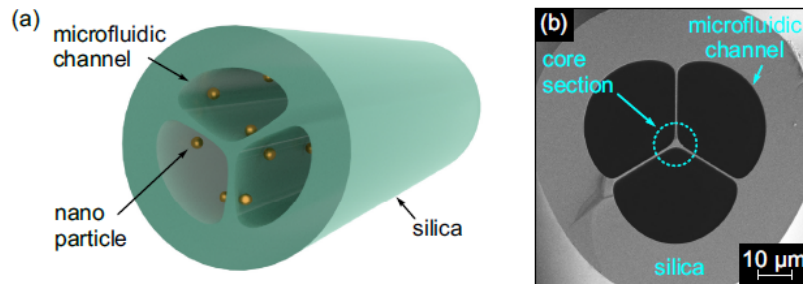

Fig. 1. (a) Schematic of the plasmonic nanoparticle-functionalised suspended-core fibre. (b) Scanning-electron micrograph (SEM) of the microstructured section of the investigated fibre. Grey areas correspond to silica glass, the black regions to air. The dashed cyan circle highlights the core section relevant for the interaction between light and localised surface plasmons.

2. Working principle

The fundamental working principle of NP-enhanced SCFs relies on the interaction of the propagating guided mode with the LSPR of the NPs, whereby the characteristics of the plasmonic resonance are impressed on the spectral distribution of the transmitted light. Therefore a spectral shift of the LSPR imposed by, for instance, a change of the nanoscale RI environment of the NP, will be visible in the modal attenuation spectrum.

The modal attenuation can be calculated by a line integration of the area of the mode along the surface of the SCF core, taking into account the extinction cross section and the density of the NPs [21,32], leading to

$$\gamma = N\sigma \oint A_{eff}^{-1} dl \qquad (1)$$

with the number density of the NPs and the extinction cross section, N and σ, respectively, and the effective modal scattering area on the surface A_{eff}. The latter quantity is defined by

$$A_{eff}(\vec{r}_0) = \frac{\int_{A_\infty} S_z(\vec{r}) dA}{S_z(\vec{r}_0)} \qquad (2)$$

with the axial Poynting vector of the guided mode $S_z(\vec{r})$ and the position of the NP on the surface of the core $(\vec{r}_0)$. This parameter is essential for analysing NP scattering on waveguide systems, with the ratio $f = \sigma/A_{eff}$ referring to the fraction of power removed from the propagating mode by one single NP scattering event. Consequently, detecting objects with small extinction cross sections or investigating systems with low NP densities generally requires small core sizes to obtain sufficiently low values of A_{eff}.

Using finite element simulation we calculated the spectral distribution of A_{eff} for the SCF fibre geometry investigated here (Fig. 1b) and compared it to a cylindrical silica taper in water with a diameter based on the definition given in Ref [24,33]. It is assumed that the NP is located 1 nm above the glass surface in one hole of the SCF (Fig. 2). Smaller values of A_{eff} are

achieved at longer wavelength due to the larger field modal penetration into the analyte (Fig. 2), suggesting that the optimal operating regime of such kind of sensor device is at longer wavelengths.
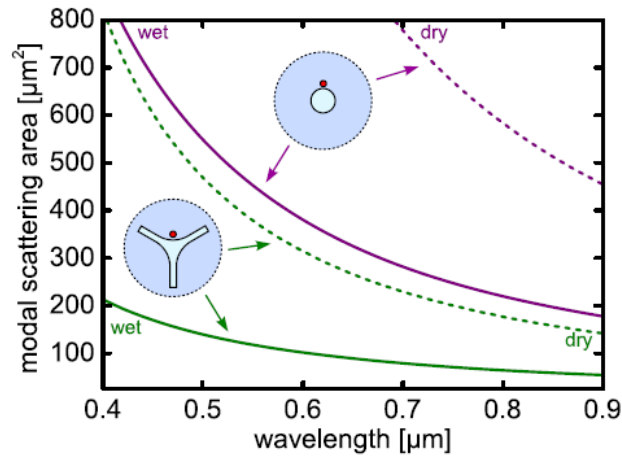

Fig. 2. Comparison of the spectral distributions of the effective modal scattering areas for the 2.8 μm diameter suspended-core fibre investigated here (green curve) and a circular silica taper embedded in water with a diameter of 3.62 μm (purple curve). The dashed and solid lines refer to air or water as analyte medium, respectively. It is assumed that the particle is located 1 nm above the glass surface as indicated by the red dots in the sketches.

Theoretically, a single spherical gold NP of diameter 34 nm at resonance in water (550 nm, $\sigma = 2 \cdot 10^{-3} \mu m^2$) would impose a comparably small reduction of guided power of $f = 1.62 \cdot 10^{-5}$ ($A_{eff} = 120 \ \mu m^2$), whereas for instance a 1μm-diameter polymer bead ($\sigma = 1.5 \ \mu m^2$) reduces the guided power by as much as 1.2%. The latter shows that such small core systems provide a sufficient platform to detect single microparticles [34]. It is interesting to note that the effective modal scattering area of the SCF is almost a factor of three smaller than that of a corresponding taper when using the core diameter definition of Ref [33], emphasising the excellent performance of the SCF platform with regard to sensing.

Equation (1) allows the estimation of the relative change of modal attenuation when exchanging the analyte medium. Simulations of extinction cross section (using the NPs considered here) and modal scattering area reveal an increase of σ upon changing the analyte from air to water, whereas a higher analyte RI imposes a decrease in A_{eff} which is more pronounced at shorter wavelengths (Fig. 2). To obtain a rough estimate of the change of the attenuation, we chose here $\lambda = 700$ nm, which is sufficiently distant from the plasmon resonance. Using the parameters at that wavelength ($\sigma_{air} = 0.012$ NPs/μm^2, $\sigma_{water} = 0.038$ NPs/μm^2, $A_{eff}^{water} = 80 \ \mu m^2$, $A_{eff}^{air} = 230 \ \mu m^2$), a change of modal attenuation of $\Delta \gamma = \gamma_{air} / \gamma_{water} \approx 0.11$ is calculated, implying that the modal attenuation is about a factor 9 higher in case of an aqueous analyte compared to the situation where the cladding medium is air ($\gamma_{water} > \gamma_{air}$).

3. Fibre geometry

The suspended fibre geometry used here consists of three air channels with diameters of several tens of micrometres surrounding a triangular silica core (Figs. 1(a) and 1(b)). The fabrication of this type of fibre relies on stacking three capillaries into a silica jacketing tube and drawing this arrangement into fibre. The diameter of the core section is approximately 2.8 μm (based on the definition given in Ref [24,33].), which is a small value compared to typically used NP functionalised fibre systems (e.g., tapers) [7,23]. The core section is suspended by three struts of approximate thickness 500 nm. The holes adjacent to the core

have shapes close to that of 120° circular section with an area of approximately 1,500 μm^2, which is of the same area as the channels in typical microfluidic devices [35].
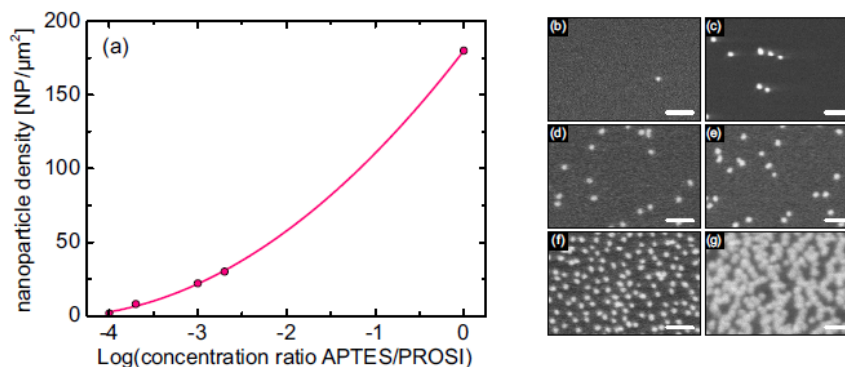

Fig. 3. (a) Density of the nanospheres inside the suspended-core fibre as a function of the concentration ratio of APTES and PROSI (pink points) used. The solid line is a parabolic fitting curve (parameters given in the text). The right-handed images ((b)-(g)) are SEM images of the various achieved densities inside one hole of the respective suspended-core fibre (b: 2 NPs/μm^2; c: 8 NPs/μm^2; d: 22 NPs/μm^2; e: 30 NPs/μm^2; f: 180 NPs/μm^2; g: 500 NPs/μm^2. The scale bars in (b) to (f) correspond to 200 nm and in (g) to 100 nm.

4. Fabrication – NP deposition

The various NP densities (Figs. 3(b)-3(g)) were realised using a nanoparticle layer deposition (NLD) technique as implemented in Refs [28,29]. This is a dynamic low-pressure chemical deposition based on self-assembled monolayers, using amino modification of the interior channel surfaces as adhesive layers for the NPs.

The empty SCF is connected to a peristaltic pump with PVC tubes and microfluidic adaptors for the delivery and exchange of liquids. Following the cleaning and activation of the interior silica surface, the subsequent silane modification involves the perfusion of a ratio of bonding and nonbonding silane volumes, namely (3-Aminopropyl)triethoxysilane (APTES, containing amino group) and n-propyltriethoxysilane (PROSI) respectively (Sigma-Aldrich), whereby the actual volume ratio of APTES and PROSI, Δc, allows control of the NP density inside the channels. The NP solution (Au Nanospheres 34 nm, fabricated by Turkevich-Frens Method [36,37]) is then introduced into the functionalised channels with a low flow rate, allowing the immobilisation of NPs along the entire SCF length.

Up to 6 m coverages of NPs inside the SCF, with homogeneous nanoparticle density (confirmed by taking short sample sections from along the length of the deposited fibre and SEM imaging the pieces' interiors at their end faces), have been achieved independent of the curvature of the channels. The obtained homogeneity compares well with a recently presented deposition approach, over 50cm, relying on directly synthesizing Rh-NPs at the inner walls of a hollow-core optical fibre through reduction of metallic precursor in a gaseous atmosphere [38]. The resulting dependence of NP density on APTES/PROSI ratio yields a curve fit, $N = A + B \log_{10} \Delta c + C(\log_{10} \Delta c)^2$ with the constants $A = 179.95$ NPs/μm^2, $B = 78.00$ NPs/μm^2 and $C = 8.41$ NPs/μm^2, allowing a guideline for tailored density depositions.
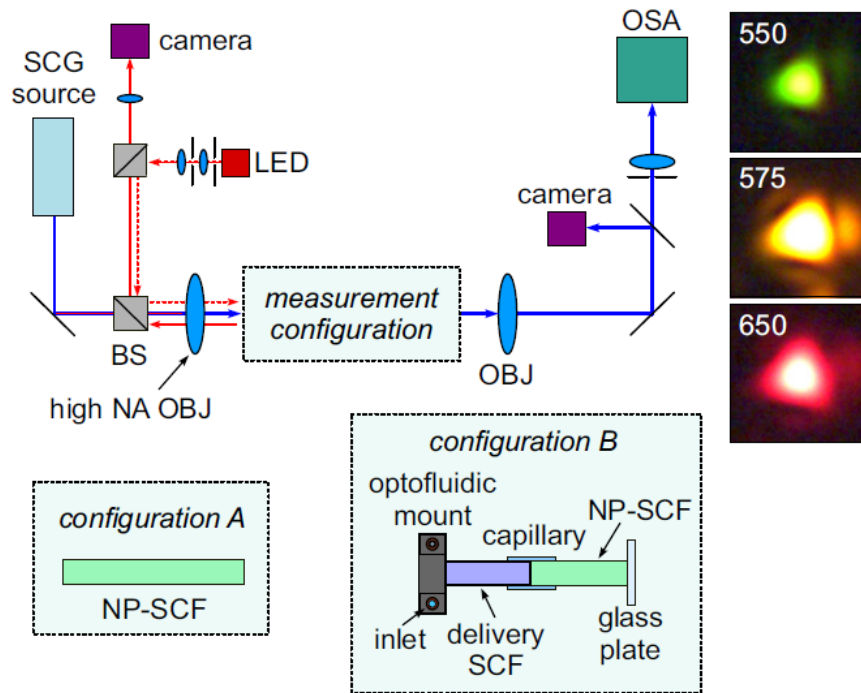
Fig. 4. Schematic of the optofluidic setup used to measure the transmission through the nanoparticle-functionalised suspended-core fibre (SCG: supercontinuum generation; BS: beam splitter; OBJ: objective; OSA: optical spectrum analyzer). The blue arrows refer to the probe light used to determine the transmission characteristics. The red arrows correspond to the light used for imaging the spot of the beam on the input facet of the sample (dashed red lines: illumination light, solid red lines: reflected light). The lower two sketches show the two different measurement configurations used for the quantification of the modal attenuation (configuration A) and for the determination of the refractive index sensitivity (configuration B). The right-handed images show the output mode at selected wavelength for a sample with N = 22 NP/μm^2 (top: 550 nm, middle: 575 nm, bottom: 650 nm) in the case of microchannels filled with air.

5. Experimental

The experimental setup used herein consists of a broadband transmission setup, including an optofluidic sample holder for the simultaneous excitation of the core mode and analyte exchange within the microstructured channels (Fig. 4).

The broadband light (450 nm to 2.4 μm) emitted from a supercontinuum source (SuperK COMPACT, NKT Photonics) passes a beam splitter and the front window of the optofluidic mount and is launched into the fibre core with a high-NA objective (Nikon TU Plan Fluor, 100x objective, NA 0.9). The output mode is either coupled into an optical spectrum analyzer (OSA) or imaged onto a combination of a camera and a narrow bandpass filter to select the wavelength to be imaged. To ensure optimal launching conditions, the spot of the input beam on the fibre front facet is imaged onto a camera using various lenses and a Köhler illumination. This setup ensures excitation of a clean fundamental mode in the SCF for all relevant wavelengths (modal images at selected wavelengths are shown on the right-handed side of Fig. 4).

The modal attenuation has been determined by applying the cutback technique on each of the NP-functionalised fibre samples when the channels are filled with air. Using the aforementioned setup without the optofluidic mount (Fig. 4, configuration A), the fibre end-facet was repeatedly cleaved and the corresponding spectra recorded (typically 4-5 measurements). Due to the high scattering induced by the NPs and the limited dynamic range of the OSA, cutback measurements were performed on short sample lengths, typically starting

at 1 cm and ending 2 mm. Fibre samples with lower densities allowed longer working lengths (up to 9 cm) however the greater plasmonic effect was observed for higher densities.

To determine the RI sensitivity of the deposited SCFs, a sample with a NP density of 22 NPs/μm² was chosen, which represents a compromise between strong plasmon/waveguide mode interaction (i.e., short samples) and an reasonable sample length of about 1-2 cm. Using the abovementioned setup (Fig. 4, configuration B) the SCF was flushed with different RI oils (Oil series AAA, Cargille Laboratories) using a pressurised syringe pump. To avoid difficulties (i.e, sample breakage) involved during mounting and flushing a sample of such short length, an uncoated delivery SCF was butt-coupled to the NP-functionalised sample, with the joining point sealed within a 140 μm capillary while optimising the output mode and transmission. The empty SCF end was then fixed within the input optofluidic mount, ensuring stable and reproducible launching conditions with no significant increase of the overall modal attenuation. The individual RI oil was pumped through the fluidic holder and fibre system until all air bubbles (detectable on camera) were eliminated. A coverslip at the output end of the NP-fibre ensured a flat transmission face, which is essential for efficiently coupling the light into the OSA. Between each spectral series, the system was rinsed (pump and suction) repeatedly with ethanol and air bubbles induced, in order to eliminate remnants of the previous analyte.
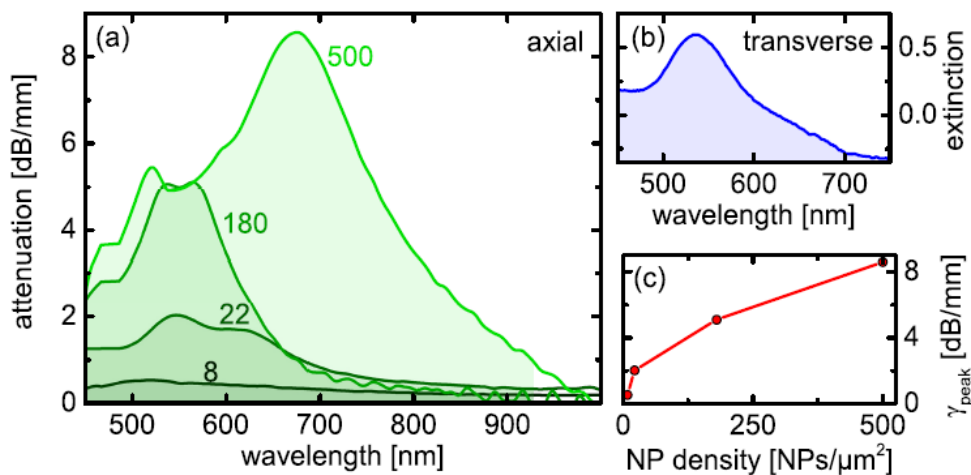
Fig. 5. (a) Measured spectral distribution of the attenuation of the fundamental core mode in the nanoparticle-functionalised suspended-core fibre (microchannels filled with air). The various curves correspond to different nanoparticle densities (most dark green: 8 NPs/μm²; dark green: 22 NPs/μm²; green: 180 NPs/μm²; light green: 500 NPs/μm²). (b) Extinction spectrum of the used nanoparticle ensemble in the case where the nanoparticles are probed transverse to the fibre axis in water (bulk measurement, N = 180 NPs/μm²). (c) Modal attenuation at the most prominent attenuation peak of the individual attenuation curve in (a) as function of nanoparticle density.

6. Result

The spectral distribution of the modal attenuation of the NP-functionalised SCF shows a strong increase in the spectral vicinity of the bulk LSPR (Figs. 5(a) and 5(b)). As suggested by Eq. (1) an increasing NP density leads to increasing modal attenuation (Fig. 5(c)), whereas due to the small core diameter both extremely small NP densities (2 NPs/μm²) as well as very high coverages of up to 500 NPs/μm² can be accessed with our device. Particularly for the two highest coverage densities the average inter-particle edge-to-edge distance (gap size) g is of the order of several tens of nanometres only (180 NPs/μm² − g = 40 nm, 500 NPs/μm² − g = 10 nm, Figs. 3(f) and 3(g)) which allows the LSPRs of neighbouring NPs to interact, overall imposing that the linear dependency between density and attenuation defined in Eq. (1) does not hold (Fig. 5(c)). The samples with the two highest densities show pronounced double peak

features, which presumably arise from both the interaction of neighbouring particles (i.e., plasmonic hybridization) and the polarisation dependence of the scattering process, since the dominant electric field component of the guided mode is different at the various NP locations along the core surface. As shown in [39] the coupling of adjacent particles causes a red shift for in-plane electric fields and a blue shift for out-of-plane fields with closer NPs imposing a stronger shift as confirmed in the experiment presented here.

The RI sensitivity measurements, which have been conducted by pumping various RI oils (series AAA, Cargille Laboratories) into the microchannels of the SCF, show an increase of the wavelength of the transmission dip for higher analyte indices (Fig. 6), which is a result of the shift of the LSPR of the NPs towards longer wavelength (inset of Fig. 6, details of the sensing experiments can be found in the Experimental section (Sec. 5)). Linear fitting of the data points yields a RI sensitivity of 167 nm/RIU, which is within the typically range of sensitivity values of spherical plasmonic NPs [40] and is about 1.5 times higher than the corresponding value when the LSPR are probed transverse to the fibre axis (inset of Fig. 6).
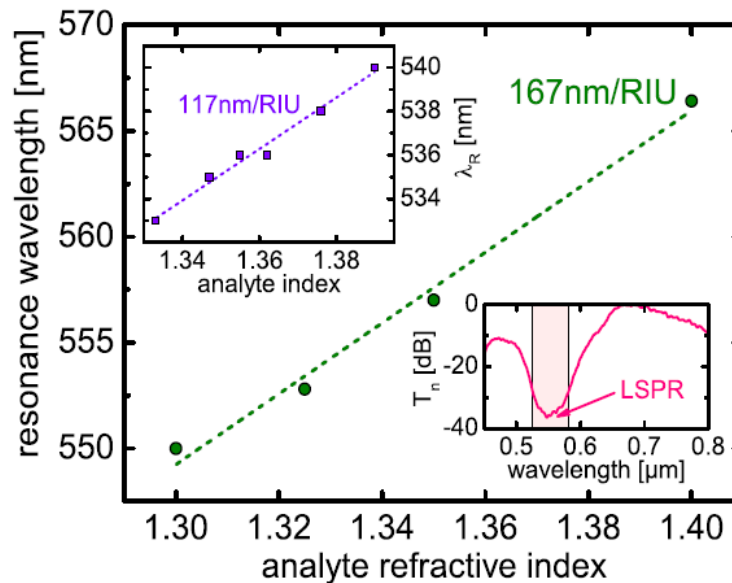
Fig. 6. Measured shift of the resonance wavelength as function of analyte refractive index for a fibre sample with a density of 22 NPs/μm^2 and a length of 4 mm, yielding a sensitivity of 167 nm/RIU. The upper left-hand inset (purple) shows the corresponding plot of nanospheres in aqueous solution when the incident light is perpendicular to the fibre axis (transverse measurement configuration), giving rise to a sensitivity of 117nm/RIU. The lower right-hand inset (pink) shows an example transmission spectrum in the case of a water analyte (normalised to the highest transmission value, light red area indicates the region of the LSPR). Note that this curve includes the spectral characteristics of the various components of the measurement setup (e.g., light source).

7. Conclusion

The specific detection of target species is of major importance within bioanalytics, in particular from the perspective of disease diagnostics. One promising method is to sense molecular binding events via the shift of plasmonic resonances of metallic nanoparticles, which strongly respond to changes in the nanoscale refractive index environment. Ideally this approach combines a monolithic microfluidic platform with an optical waveguide [41–45], where the nanoparticles should be located as close as possible to the guiding core.

Here we introduce the concept of suspended-core fibres with immobilised nanoparticles as an integrated optofluidic platform for efficient refractive index sensing over two orders of magnitude of nanoparticle density. Due to the small guiding core and the microfluidic

channels being in direct contact with that core over a distance of several centimetres, intense interaction of localised plasmons and propagating mode is observed, allowing us to investigate sparse particle ensembles as well as ensembles with extremely high densities. Furthermore, the direct immobilisation of nanoparticles allows for a reusable sensing system.

The core, which to our knowledge has the smallest diameter being used for NPs immobilisation so far, is fully encapsulated inside the fibre and supported by radial strands, leading to superior handling properties compared to freely-suspended waveguide systems such as tapers. The refractive index sensitivity of our sensor when functionalised with gold nanospheres of average diameter 34 nm was measured as 170 nm/RIU for an aqueous analyte, that being 1.5 times higher compared to measurements taken perpendicular to the fibre axis (transverse configuration, upper left-hand inset in Fig. 6) and to sensitivity values of similar NPs dispersed in water [46].

Due to the small core sizes and the integrated arrangement of optical core and microfluidic channels our fibre represents a fully integrated optofluidic sensing system requiring only small sample volumes and allowing for real-time monitoring of the analyte. Therefore we anticipate application of our concept within the area of non-invasive bioanalytics, particular within molecular disease diagnostics and environmental science.

Funding

6. Liste der Publikationen

6.1. Peer-reviewed Publikationen

[1] Csáki A, **Thiele M.,** Jatschka J., et al., (2015), *Plasmonic nanoparticle synthesis and bioconjugation for bioanalytical sensing*, **Engineering in Life Sciences**, Vol.15 No.3, 266-275

[2] **Thiele M.**, Götz I., Trautmann s., et al. (2015), *Wet-chemical Passivation of Anisotropic Plasmonic Nanoparticles for LSPR-sensing by a Silica Shell*, **Materials Today: Proceedings**, Vol.2 No.1, 33-40

[3] **Thiele M.**, Knauer A., Csáki A., et al., (2015), *High-Throughput Synthesis of Uniform Silver Seed Particles by a Continuous Microfluidic Synthesis Platform*, **Chemical Engineering & Technology**, Vol.38 No.7, 1131-1137

[4] **Thiele M.**, Soh J. Z. E., Knauer A., et al., (2016), *Gold nanocubes – Direct comparison of synthesis approaches reveals the need for a microfluidic synthesis setup for high reproducibility*, **Chemical Engineering Journal**, Vol.288, 432-440

[5] Wieduwilt T., Zeisberger M., **Thiele M**, et al., (2017) *Gold-reinforced silver nanoprisms on optical fiber tapers – A new base for high precision sensing*, **APL Photonics**, Vol.1 No.6, 066102

[6] Raie D. S., Mhatre E., **Thiele M**., et al., (2017), *Application of quercetin and its bio-inspired nanoparticles as anti-adhesive agents against Bacillus subtilis attachment to surface*, **Materials Science and Engineering: C**, Vol.70, Part 1, 753-762

[7] **Thiele M**., Knauer A., Malsch D., et al., (2017), *Combination of high-throughput production and parameter screening for efficient shaping of Au nanocubes using Dean-Flow mixing*, **Lab on a Chip,** Vol.17 No.8, 1487-1495

[8] Brenda D., Csáki A., **Thiele M**., et al., (2017), *Nanoparticle functionalised small-core suspended-core fibre – a novel platform for efficient sensing*, **Biomedical Optics Express** , Vol.8 No.2

[9] Brenda D., **Thiele M**., et al., (2017), *Plasmonic Nanoparticle-Functionalized Exposed-Core Fiber – an Optofluidic Refractive Index Sensing Platform*, ***Optics Letters***, Vol.42 No.21

6.2. Konferenzbeiträge

6.2.1. Vorträge und Seminare

[1] Thiele M., *Plasmonic Nanomaterials: From fabrication to application*, NANOTECHNOLOGY Applications in Energy, ENVIRONMENT and HEALTH: benefits and potential risks, 01.-02. November 2017, Rabat, Marokko

[2] Thiele M., Biosensing with plasmonic Nanomaterials - A Workshop -, 17.-18.12.2016; Kairo, Ägypten

[3] Thiele M., *Improved production of plasmonic nanoparticles by using microfluidic device,* 8th Workshop Chemical and Biological Micro Laboratory Technology, 23.-25. Februar. 2016; Ilmenau, Germany

[4] Thiele M., *New strategy of controlled bottom-up synthesis of well-defined plasmonic nanoparticles for biological applications*, 5th International Conference on Advanced Nanomaterials, 02.-04. July 2014, Aveiro, Portugal

[5] Thiele M., *Continuous Microfluidic-based High-Throughput Synthesis of Silver Seed Particles and Silver Triangles for Bioanalytical Applications,* 8th NanoBio-Europe conference, 18.-20. Juni 2012, Varese, Italy

6.2.2. Poster

[1] Thiele M., *Microfluidic high-throughput synthesis of shape-anisotropic plasmonic nanoparticle,* DNA-Nanotechnology 2016, Jena

[2] Thamm S., Thiele M., *Characterization of localized surface plasmon resonance sensing with anisotropic nanoparticles,* DNA-Nanotechnology 2016, Jena

[3] Thiele M., *Continuous production and spectral tuning of highly monodisperse and shape anisotropic nanostructures by using microfluidic synthesis approaches,* Faraday Discussion, Glasgow

[4] Thiele M.; *Microfluidics encounters nanoparticles - reforming the synthesis of plasmonic active nanomaterials,* Molecular Plasmonics 2015, Jena

[5] Garwe F., Thiele M., *Methods to fabricate an Windows Integrated Solar Collector (WISC),* Molecular Plasmonics 2015, Jena

[6] Thiele M., *Synthesis and characterization of plasmonic nanoparticles for bioanalytics, 3rd PhD Retreat of Section D Leibniz Gemeinschaft, Berlin*

[7] Thiele M., *Microfluidic synthesis of silver prisms and subsequently gold-stabilization for a post-synthetic DNA-conjugation as a plasmonic toolbox with DNA-Origamis,* DNA-based functional Materials 2014, Jena

[8] Trautmann S.; Thiele M.*, Investigations of aging effects of immobilized silver nanoprisms,* Molecular Plasmonics 2013, Jena

[9] Thiele M.*, Microfluidic-based continuous synthesis of silver seed particles for subsequent synthesis of anisotropic nanoparticles,* Molecular Plasmonics 2013, Jena

7. Literaturverzeichnis

1. DIN-CEN-ISO/TS27687, *Nanotechnologien – Terminologie und Begriffe für Nanoobjekte – Nanopartikel, Nanofaser und Nanoplättchen.* 2010.

2. Ding, S.-Y., et al., *Nanostructure-based plasmon-enhanced Raman spectroscopy for surface analysis of materials.* Nature Reviews Materials, 2016. **1**(6): p. 16021.

3. Stöckle, R.M., et al., *Nanoscale chemical analysis by tip-enhanced Raman spectroscopy.* Chemical Physics Letters, 2000. **318**(1): p. 131-136.

4. Kneipp, K., et al., *Single Molecule Detection Using Surface-Enhanced Raman Scattering (SERS).* Physical Review Letters, 1997. **78**(9): p. 1667-1670.

5. Pettinger, B., et al., *Tip-enhanced Raman spectroscopy: near-fields acting on a few molecules.* Annual review of physical chemistry, 2012. **63**: p. 379-99.

6. Xia, Y., et al., *Shape-controlled synthesis of metal nanocrystals: simple chemistry meets complex physics?* Angewandte Chemie, 2009. **48**(1): p. 60-103.

7. Faraday, M., *The Bakerian Lecture: Experimental Relations of Gold (and Other Metals) to Light* Philosophical Transactions of the Royal Society, Lonon, 1857: p. 36.

8. Siedentopf, H. and R. Zsigmondy, *Uber Sichtbarmachung und Größenbestimmung ultramikoskopischer Teilchen, mit besonderer Anwendung auf Goldrubingläser.* Annalen der Physik, 1902. **315**(1): p. 1-39.

9. Sharma, V., K. Park, and M. Srinivasarao, *Colloidal dispersion of gold nanorods: Historical background, optical properties, seed-mediated synthesis, shape separation and self-assembly.* Materials Science and Engineering: R: Reports, 2009. **65**(1-3): p. 1-38.

10. Frens, G., *Controlled nucleation for the regulation of the particle size in monodisperse gold suspensions.* Nature Phys Sci, 1973. **241**: p. 20-22.

11. Turkevich, J., P.C. Stevenson, and J. Hillier, *A study of the nucleation and growth processes in the synthesis of colloidal gold.* Discussions of the Faraday Society, 1951. **11**(0): p. 55-75.

12. Mayer, K.M. and J.H. Hafner, *Localized surface plasmon resonance sensors.* Chemical reviews, 2011. **111**(6): p. 3828-57.

13. Kedem, O., A. Vaskevich, and I. Rubinstein, *Critical Issues in Localized Plasmon Sensing.* The Journal of Physical Chemistry C, 2014. **118**(16): p. 8227-8244.

14. Driskell, J.D., et al., *One-step assay for detecting influenza virus using dynamic light scattering and gold nanoparticles.* The Analyst, 2011. **136**(15): p. 3083-90.

15. Bartczak, D., et al., *Interactions of human endothelial cells with gold nanoparticles of different morphologies.* Small, 2012. **8**(1): p. 122-30.

16. Wirth, J., et al., *Plasmonic nanofabrication by long-range excitation transfer via DNA nanowire.* Nano letters, 2011. **11**(4): p. 1505-11.

17. Wirth, J., et al., *Plasmonically enhanced electron escape from gold nanoparticles and their polarization-dependent excitation transfer along DNA nanowires.* Nano letters, 2014. **14**(7): p. 3809-16.

18. Fedoruk, M., et al., *Nanolithography by Plasmonic Heating and Optical Manipulation of Gold Nanoparticles.* ACS Nano, 2013. **7**(9): p. 7648-7653.

19. Deckert-Gaudig, T., et al., *Tip-enhanced Raman spectroscopy - from early developments to recent advances.* Chemical Society Reviews, 2017. **46**(13): p. 4077-4110.

20. Nie, S. and S.R. Emory, *Probing Single Molecules and Single Nanoparticles by Surface-Enhanced Raman Scattering.* Science, 1997. **275**(5303): p. 1102-1106.

21. Darvill, D., A. Centeno, and F. Xie, *Plasmonic fluorescence enhancement by metal nanostructures: shaping the future of bionanotechnology.* Physical chemistry chemical physics : PCCP, 2013. **15**(38): p. 15709-26.

22. Song, Y., J. Hormes, and C.S. Kumar, *Microfluidic synthesis of nanomaterials.* Small, 2008. **4**(6): p. 698-711.

23. Ehrfeld, W., V. Hessel, and H. Löwe, *Microreactors: New Technology for Modern Chemistry*. 2000: Wiley.

24. Hessel, V., et al., *Chemical Micro Process Engineering: Processing and Plants*. 2006: Wiley.

25. Kockmann, N., *Transport Phenomena in Micro Process Engineering*. 2007: Springer Berlin Heidelberg.

26. Polte, J., et al., *SAXS in combination with a free liquid jet for improved time-resolved in situ studies of the nucleation and growth of nanoparticles.* Chemical Communications, 2010. **46**(48): p. 9209-11.

27. Polte, J., et al., *Nucleation and Growth of Gold Nanoparticles Studied via in situ Small Angle X-ray Scattering at Millisecond Time Resolution.* ACS Nano, 2010. **4**(2): p. 1076-1082.

28. Sai Krishna, K., et al., *Millifluidics for time-resolved mapping of the growth of gold nanostructures.* Journal of the American Chemical Society, 2013. **135**(14): p. 5450-6.

29. Kumar, C.S.S.R., *Microfluidic Devices in Nanotechnology: Applications*. 2010: Wiley.

30. Köhler, J.M., S. Li, and A. Knauer, *Why is Micro Segmented Flow Particularly Promising for the Synthesis of Nanomaterials?* Chemical Engineering & Technology, 2013. **36**(6): p. 887-899.

31. Mark, D., et al., *Microfluidic lab-on-a-chip platforms: requirements, characteristics and applications.* Chemical Society Reviews, 2010. **39**(3): p. 1153-82.

32. UnderstandingNano. *Nanoparticle Companies and Products*. [cited 10.07.2017]; Available from: http://www.understandingnano.com/nanoparticle-companies.html.

33. Rycenga, M., et al., *Controlling the synthesis and assembly of silver nanostructures for plasmonic applications.* Chemical reviews, 2011. **111**(6): p. 3669-712.

34. Jatschka, J., et al., *Propagating and localized surface plasmon resonance sensing — A critical comparison based on measurements and theory.* Sensing and Bio-Sensing Research, 2016. **7**: p. 62-70.

35. Chen, H., et al., *Shape-Dependent Refractive Index Sensitivities of Gold Nanocrystals with the Same Plasmon Resonance Wavelength*. The Journal of Physical Chemistry C, 2009. **113**(41): p. 17691-17697.

36. Guo, L., et al., *Strategies for enhancing the sensitivity of plasmonic nanosensors.* Nano Today, 2015. **10**(2): p. 213-239.

37. Martinsson, E., et al., *Local Refractive Index Sensing Based on Edge Gold-Coated Silver Nanoprisms.* The Journal of Physical Chemistry C, 2013. **117**(44): p. 23148-23154.

38. Dondapati, S.K., et al., *Label-free Biosensing Based on Single Gold Nanostars as Plasmonic Transducers.* ACS Nano, 2010. **4**(11): p. 6318-6322.

39. Haes, A.J. and R.P. Van Duyne, *A Nanoscale Optical Biosensor: Sensitivity and Selectivity of an Approach Based on the Localized Surface Plasmon Resonance Spectroscopy of Triangular Silver Nanoparticles.* Journal of the American Chemical Society, 2002. **124**(35): p. 10596-10604.

40. Halas, N.J., et al., *Plasmons in strongly coupled metallic nanostructures.* Chemical reviews, 2011. **111**(6): p. 3913-61.

41. Deng, W., et al., *Metal-enhanced fluorescence in the life sciences: here, now and beyond.* Physical chemistry chemical physics : PCCP, 2013. **15**(38): p. 15695-708.

42. Geddes, C.D. and J.R. Lakowicz, *Editorial: Metal-Enhanced Fluorescence.* Journal of Fluorescence, 2002. **12**(2): p. 121-129.

43. Jeanmaire, D.L. and R.P. Van Duyne, *Surface raman spectroelectrochemistry.* Journal of Electroanalytical Chemistry and Interfacial Electrochemistry, 1977. **84**(1): p. 1-20.

44. Xie, H.N., et al., *Identification of intracellular gold nanoparticles using surface-enhanced Raman scattering.* Nanoscale, 2014. **6**(21): p. 12403-7.

45. Schmid, T., et al., *Nanoscale chemical imaging using tip-enhanced Raman spectroscopy: a critical review.* Angewandte Chemie, 2013. **52**(23): p. 5940-54.

46. Lee, Y.H., et al., *Refractive Index Sensitivities of Noble Metal Nanocrystals: The Effects of Multipolar Plasmon Resonances and the Metal Type.* The Journal of Physical Chemistry C, 2011. **115**(16): p. 7997-8004.

47. Yguerabide, J. and E.E. Yguerabide, *Light-Scattering Submicroscopic Particles as Highly Fluorescent Analogs and Their Use as Tracer Labels in Clinical and Biological Applications: II. Experimental Characterization.* Analytical Biochemistry, 1998. **262**(2): p. 157-176.

48. Yguerabide, J. and E.E. Yguerabide, *Light-Scattering Submicroscopic Particles as Highly Fluorescent Analogs and Their Use as Tracer Labels in Clinical and Biological Applications: I. Theory.* Analytical Biochemistry, 1998. **262**(2): p. 137-156.

49. Csáki, A., et al., *Plasmonic nanoparticle synthesis and bioconjugation for bioanalytical sensing.* Engineering in Life Sciences, 2014: p. n/a-n/a.

50. Nelayah, J., et al., *Mapping surface plasmons on a single metallic nanoparticle.* Nature Physics, 2007. **3**(5): p. 348-353.

51. Goris, B., et al., *Plasmon Mapping in Au@Ag Nanocube Assemblies.* The journal of physical chemistry. C, Nanomaterials and interfaces, 2014. **118**(28): p. 15356-15362.

52. Giannini, V., et al., *Plasmonic nanoantennas: fundamentals and their use in controlling the radiative properties of nanoemitters.* Chemical reviews, 2011. **111**(6): p. 3888-912.

53. Roller, E.-M., et al., *Hotspot-mediated non-dissipative and ultrafast plasmon passage.* Nat Phys, 2017. **advance online publication**.

54. Novotny, L. and N. van Hulst, *Antennas for light.* Nat Photon, 2011. **5**(2): p. 83-90.

55. Heck, C., et al., *Gold Nanolenses Self-Assembled by DNA Origami.* ACS Photonics, 2017. **4**(5): p. 1123-1130.

56. Zhao, P., N. Li, and D. Astruc, *State of the art in gold nanoparticle synthesis.* Coordination Chemistry Reviews, 2013. **257**(3-4): p. 638-665.

57. Polte, J., *Fundamental growth principles of colloidal metal nanoparticles - a new perspective.* CrystEngComm, 2015. **17**(36): p. 6809-6830.

58. Brown, K.R., A.P. Fox, and M.J. Natan, *Morphology-Dependent Electrochemistry of Cytochrome c at Au Colloid-Modified SnO2 Electrodes.* Journal of the American Chemical Society, 1996. **118**(5): p. 1154-1157.

59. Brust, M., et al., *Synthesis of thiol-derivatised gold nanoparticles in a two-phase Liquid-Liquid system.* Journal of the Chemical Society, Chemical Communications, 1994(7): p. 801-802.

60. Brown, K.R. and M.J. Natan, *Hydroxylamine Seeding of Colloidal Au Nanoparticles in Solution and on Surfaces.* Langmuir, 1998. **14**(4): p. 726-728.

61. Stathis, E.C. and H.C. Gatos, *Determination of Gold with Ascorbic Acid.* Industrial & Engineering Chemistry Analytical Edition, 1946. **18**(12): p. 801-801.

62. Li, H., et al., *Simple synthesis of monodisperse, quasi-spherical, citrate-stabilized silver nanocrystals in water.* Langmuir : the ACS journal of surfaces and colloids, 2013. **29**(16): p. 5074-9.

63. Rodríguez-Fernández, J., et al., *Seeded Growth of Submicron Au Colloids with Quadrupole Plasmon Resonance Modes.* Langmuir, 2006. **22**(16): p. 7007-7010.

64. Luty-Błocho, M., et al., *The kinetics of redox reaction of gold(III) chloride complex ions with l-ascorbic acid.* Inorganica Chimica Acta, 2013. **395**: p. 189-196.

65. Ojea-Jiménez, I., N.G. Bastús, and V. Puntes, *Influence of the Sequence of the Reagents Addition in the Citrate-Mediated Synthesis of Gold Nanoparticles.* The Journal of Physical Chemistry C, 2011. **115**(32): p. 15752-15757.

66. Schulz, F., et al., *Little adjustments significantly improve the Turkevich synthesis of gold nanoparticles.* Langmuir : the ACS journal of surfaces and colloids, 2014. **30**(35): p. 10779-84.

67. Baigent, C.L. and G. Müller, *A colloidal gold prepared with ultrasonics.* Experientia, 1980. **36**(4): p. 472-473.

68. Yang, A.-l., et al., *Synthesis of silver nanoparticles and the optical properties.* Optoelectronics Letters, 2013. **9**(1): p. 1-3.

69. Huang, H. and X. Yang, *Synthesis of polysaccharide-stabilized gold and silver nanoparticles: a green method.* Carbohydrate Research, 2004. **339**(15): p. 2627-2631.

70. Doty, R.C., et al., *Extremely Stable Water-Soluble Ag Nanoparticles.* Chemistry of Materials, 2005. **17**(18): p. 4630-4635.

71. Aherne, D., et al., *Optical Properties and Growth Aspects of Silver Nanoprisms Produced by a Highly Reproducible and Rapid Synthesis at Room Temperature.* Advanced Functional Materials, 2008. **18**(14): p. 2005-2016.

72. Polte, J., et al., *Formation Mechanism of Colloidal Silver Nanoparticles: Analogies and Differences to the Growth of Gold Nanoparticles.* ACS Nano, 2012. **6**(7): p. 5791-5802.

73. Skrabalak, S.E., et al., *Facile synthesis of Ag nanocubes and Au nanocages.* Nature protocols, 2007. **2**(9): p. 2182-90.

74. Kim, J.-Y. and J.-S. Lee, *Synthesis and Thermally Reversible Assembly of DNA−Gold Nanoparticle Cluster Conjugates.* Nano letters, 2009. **9**(12): p. 4564-4569.

75. Wang, Z., et al., *Discovery of the DNA "Genetic Code" for Abiological Gold Nanoparticle Morphologies.* Angewandte Chemie International Edition, 2012. **51**(36): p. 9078-9082.

76. Wu, H.-L., C.-H. Chen, and M.H. Huang, *Seed-Mediated Synthesis of Branched Gold Nanocrystals Derived from the Side Growth of Pentagonal Bipyramids and the Formation of Gold Nanostars.* Chemistry of Materials, 2009. **21**(1): p. 110-114.

77. Vivek, J.P. and I.J. Burgess, *Quaternary ammonium bromide surfactant adsorption on low-index surfaces of gold. 2. Au(100) and the role of crystallographic-dependent adsorption in the formation of anisotropic nanoparticles.* Langmuir : the ACS journal of surfaces and colloids, 2012. **28**(11): p. 5040-7.

78. Vivek, J.P. and I.J. Burgess, *Quaternary ammonium bromide surfactant adsorption on low-index surfaces of gold. 1. Au(111).* Langmuir : the ACS journal of surfaces and colloids, 2012. **28**(11): p. 5031-9.

79. Martin, M.N., et al., *Charged Gold Nanoparticles in Non-Polar Solvents: 10-min Synthesis and 2D Self-Assembly.* Langmuir, 2010. **26**(10): p. 7410-7417.

80. Leiterer, C., et al., *Fast self-assembly of silver nanoparticle monolayer in hydrophobic environment and its application as SERS substrate.* Journal of Nanoparticle Research, 2014. **16**(9): p. 2467.

81. Daniel, M.-C. and D. Astruc, *Gold Nanoparticles: Assembly, Supramolecular Chemistry, Quantum-Size-Related Properties, and Applications toward Biology, Catalysis, and Nanotechnology.* Chemical reviews, 2004. **104**(1): p. 293-346.

82. Chanana, M. and L.M. Liz-Marzán, *Coating matters: the influence of coating materials on the optical properties of gold nanoparticles.* Nanophotonics, 2012. **1**(3-4).

83. Dominguez-Medina, S., et al., *Adsorption of a Protein Monolayer via Hydrophobic Interactions Prevents Nanoparticle Aggregation under Harsh Environmental Conditions.* ACS sustainable chemistry & engineering, 2013. **1**(7): p. 833-842.

84. Zhang, X., M.R. Servos, and J. Liu, *Instantaneous and quantitative functionalization of gold nanoparticles with thiolated DNA using a pH-assisted and surfactant-free route.* Journal of the American Chemical Society, 2012. **134**(17): p. 7266-9.

85. LaMer, V.K. and R.H. Dinegar, *Theory, Production and Mechanism of Formation of Monodispersed Hydrosols.* Journal of the American Chemical Society, 1950. **72**(11): p. 4847-4854.

86. Wang, F., et al., *Kinetics and Mechanisms of Aggregative Nanocrystal Growth.* Chemistry of Materials, 2014. **26**(1): p. 5-21.

87. Wuithschick, M., et al., *Illustrating the formation of metal nanoparticles with a growth concept based on colloidal stability.* Physical Chemistry Chemical Physics, 2015. **17**(30): p. 19895-19900.

88. Polte, J., et al., *Mechanistic insights into seeded growth processes of gold nanoparticles.* Nanoscale, 2010. **2**(11): p. 2463-9.

89. Polte, J., et al., *Mechanism of Gold Nanoparticle Formation in the Classical Citrate Synthesis Method Derived from Coupled In Situ XANES and SAXS Evaluation.* Journal of the American Chemical Society, 2010. **132**(4): p. 1296-1301.

90. Frens, G., *Controlled nucleation for the regulation of the particle size in monodisperse gold suspensions.* Nature, 1973. **241**: p. 3.

91. Sivaraman, S.K., S. Kumar, and V. Santhanam, *Monodisperse sub-10 nm gold nanoparticles by reversing the order of addition in Turkevich method--the role of chloroauric acid.* Journal of colloid and interface science, 2011. **361**(2): p. 543-7.

92. Bastus, N.G., J. Comenge, and V. Puntes, *Kinetically controlled seeded growth synthesis of citrate-stabilized gold nanoparticles of up to 200 nm: size focusing versus Ostwald ripening.* Langmuir : the ACS journal of surfaces and colloids, 2011. **27**(17): p. 11098-105.

93. Wuithschick, M., et al., *Turkevich in New Robes: Key Questions Answered for the Most Common Gold Nanoparticle Synthesis.* ACS Nano, 2015. **9**(7): p. 7052-7071.

94. Kumar, C.S.S.R., *Microfluidic Devices in Nanotechnology.* 2010: Wiley-VCH Verlag GmbH & Co. KGaA.

95. Zhao, C.-X., et al., *Nanoparticle synthesis in microreactors.* Chemical Engineering Science, 2011. **66**(7): p. 1463-1479.

96. Gleichmann, N., et al., *Toward microfluidic design automation: a new system simulation toolkit for the in silico evaluation of droplet-based lab-on-a-chip systems.* Microfluidics and Nanofluidics, 2015. **18**(5): p. 1095-1105.

97. Budden, M., et al., *Splitting and switching of microfluid segments in closed channels for chemical operations in the segment-on-demand technology.* Chemical Engineering Journal, 2013. **227**(Supplement C): p. 166-173.

98. Nguyen, N.-T., *Micromixers: Fundamentals, Design, and Fabrication.* 1 ed. 2007: William Andrew.

99. Hessel, V., H. Löwe, and F. Schönfeld, *Micromixers—a review on passive and active mixing principles.* Chemical Engineering Science, 2005. **60**(8-9): p. 2479-2501.

100. Nguyen, N.-T. and Z. Wu, *Micromixers—a review.* Journal of Micromechanics and Microengineering, 2005. **15**(2): p. 1-16.

101. Dreher, S., N. Kockmann, and P. Woias, *Characterization of Laminar Transient Flow Regimes and Mixing in T-shaped Micromixers.* Heat Transfer Engineering, 2009. **30**(1-2): p. 91-100.

102. Ait Mouheb, N., et al., *Numerical and experimental investigations of mixing in T-shaped and cross-shaped micromixers.* Chemical Engineering Science, 2012. **68**(1): p. 278-289.

103. Dean, W.R., *Note on the motion of fluid in a curved pipe.* Philosophical Magazine, 1927. **4**(20): p. 208-223.

104. Dean, W.R., *The stream-line motion of fluid in a curved pipe.* Philosophical Magazine, 1928. **5**(30): p. 673-695.

105. Sudarsan, A.P. and V.M. Ugaz, *Multivortex micromixing.* Proceedings of the National Academy of Sciences of the United States of America, 2006. **103**(19): p. 7228-33.

106. Jensen, K.F., *Microreaction engineering - is small better?* Chemical Engineering Science, 2001. **56**(2): p. 293-303.

107. Knauer, A. and J.M. Köhler, *Screening of Multiparameter Spaces for Silver Nanoprism Synthesis by Microsegmented Flow Technique.* Chemie Ingenieur Technik, 2013. **85**(4): p. 467-475.

108. Hu, J., T.W. Odom, and C.M. Lieber, *Chemistry and Physics in One Dimension: Synthesis and Properties of Nanowires and Nanotubes.* Accounts of Chemical Research, 1999. **32**(5): p. 435-445.

109. Link, S. and M.A. El-Sayed, *Spectral Properties and Relaxation Dynamics of Surface Plasmon Electronic Oscillations in Gold and Silver Nanodots and Nanorods.* The Journal of Physical Chemistry B, 1999. **103**(40): p. 8410-8426.

110. Yu, et al., *Gold Nanorods: Electrochemical Synthesis and Optical Properties.* The Journal of Physical Chemistry B, 1997. **101**(34): p. 6661-6664.

111. van der Zande, B.M.I., et al., *Aqueous Gold Sols of Rod-Shaped Particles.* The Journal of Physical Chemistry B, 1997. **101**(6): p. 852-854.

112. Esumi, K., K. Matsuhisa, and K. Torigoe, *Preparation of Rodlike Gold Particles by UV Irradiation Using Cationic Micelles as a Template.* Langmuir, 1995. **11**(9): p. 3285-3287.

113. Jana, N.R., L. Gearheart, and C.J. Murphy, *Seed-Mediated Growth Approach for Shape-Controlled Synthesis of Spheroidal and Rod-like Gold Nanoparticles Using a Surfactant Template.* Advanced Materials, 2001. **13**(18): p. 1389-1393.

114. Jana, N.R., L. Gearheart, and C.J. Murphy, *Wet Chemical Synthesis of High Aspect Ratio Cylindrical Gold Nanorods.* The Journal of Physical Chemistry B, 2001. **105**(19): p. 4065-4067.

115. Langille, M.R., et al., *Defining rules for the shape evolution of gold nanoparticles.* Journal of the American Chemical Society, 2012. **134**(35): p. 14542-54.

116. Lohse, S.E., et al., *Anisotropic Noble Metal Nanocrystal Growth: The Role of Halides.* Chemistry of Materials, 2014. **26**(1): p. 34-43.

117. Grzelczak, M., et al., *Shape control in gold nanoparticle synthesis.* Chemical Society Reviews, 2008. **37**(9): p. 1783-1791.

118. Wagner, J., et al., *Generation of metal nanoparticles in a microchannel reactor.* Chemical Engineering Journal, 2004. **101**(1-3): p. 251-260.

119. Wagner, J. and J.M. Köhler, *Continuous Synthesis of Gold Nanoparticles in a Microreactor.* Nano letters, 2005. **5**(4): p. 685-691.

120. Lin, X.Z., A.D. Terepka, and H. Yang, *Synthesis of Silver Nanoparticles in a Continuous Flow Tubular Microreactor.* Nano letters, 2004. **4**(11): p. 2227-2232.

121. Rahman, M. and E. Rebrov, *Microreactors for Gold Nanoparticles Synthesis: From Faraday to Flow.* Processes, 2014. **2**(2): p. 466-493.

122. Boken, J., D. Kumar, and S. Dalela, *Synthesis of Nanoparticles for Plasmonics Applications: A Microfluidic Approach.* Synthesis and Reactivity in Inorganic, Metal-Organic, and Nano-Metal Chemistry, 2015. **45**(8): p. 1211-1223.

123. Knauer, A., et al., *Micro continuous flow-through synthesis of triangular silver nanoprisms and their incorporation in complexly composed polymer microparticles.* Chemical Engineering Journal, 2012.

124. Knauer, A., et al., *Microsegmented Flow-Through Synthesis of Silver Nanoprisms with Exact Tunable Optical Properties.* The Journal of Physical Chemistry C, 2012. **116**(16): p. 9251-9258.

125. Knauer, A., et al., *Nanometer precise adjustment of the silver shell thickness during automated Au-Ag core-shell nanoparticle synthesis in micro fluid segment sequences.* Nanoscale, 2014. **6**(10): p. 5230-5238.

126. Knauer, A., et al., *Au/Ag/Au double shell nanoparticles with narrow size distribution obtained by continuous micro segmented flow synthesis.* Chemical Engineering Journal, 2011. **166**(3): p. 1164-1169.

127. Knauer, A., N. Visaveliya, and J.M. Koehler, *Spontaneous transformation of polyelectrolyte-stabilized silver nanoprisms by interaction with thiocyanate.* Journal of colloid and interface science, 2013. **394**: p. 78-84.

128. Duraiswamy, S. and S.A. Khan, *Droplet-based microfluidic synthesis of anisotropic metal nanocrystals.* Small, 2009. **5**(24): p. 2828-34.

129. Duraiswamy, S. and S.A. Khan, *Plasmonic nanoshell synthesis in microfluidic composite foams.* Nano letters, 2010. **10**(9): p. 3757-63.

130. Duraiswamy, S. and S.A. Khan, *Dual-Stage Continuous-Flow Seedless Microfluidic Synthesis of Anisotropic Gold Nanocrystals.* Particle & Particle Systems Characterization, 2014. **31**(4): p. 429-432.

131. Khan, S.A. and S. Duraiswamy, *Controlling bubbles using bubbles--microfluidic synthesis of ultra-small gold nanocrystals with gas-evolving reducing agents.* Lab on a Chip, 2012. **12**(10): p. 1807-12.

132. Boleininger, J., et al., *Microfluidic continuous flow synthesis of rod-shaped gold and silver nanocrystals.* Phys. Chem. Chem. Phys., 2006. **8**(33): p. 3824-3827.

133. Ftouni, J., et al., *Highly controlled synthesis of nanometric gold particles by citrate reduction using the short mixing, heating and quenching times achievable in a microfluidic device.* Nanoscale, 2012. **4**(15): p. 4450-4.

134. Jamal, F., et al., *Gold nanoparticle synthesis in microfluidic systems and immobilisation in microreactors designed for the catalysis of fine organic reactions.* Microsystem Technologies, 2011. **18**(2): p. 151-158.

135. Mehenni, H., et al., *Rapid continuous flow synthesis of high-quality silver nanocubes and nanospheres.* RSC Advances, 2013. **3**(44): p. 22397.

136. SIGMA-ALDRICH. *Gold(III) chloride trihydrate* [cited 22.10.2017]; Available from: http://www.sigmaaldrich.com/catalog/product/aldrich/520918?lang=de&region=DE

137. BBI-SOLUTION. *Gold nanoparticles 10nm.* [cited 22.10.2017]; Available from: https://www.bbisolutions.com/eu/gold-nanoparticles-10nm.html.

138. Chu, H.-C., C.-H. Kuo, and M.H. Huang, *Thermal Aqueous Solution Approach for the Synthesis of Triangular and Hexagonal Gold Nanoplates with Three Different Size Ranges.* Inorganic Chemistry, 2006. **45**(2): p. 808-813.

139. Khanal, A., S.-i. Yusa, and K. Nakashima, *Fabrication of Nanoaggregates of a Triple Hydrophilic Block Copolymer by Cetyltrimethylammonium Chloride Binding.* Langmuir, 2007. **23**(21): p. 10511-10517.

140. Rodríguez-Fernández, J., et al., *Spatially-Directed Oxidation of Gold Nanoparticles by Au(III)−CTAB Complexes.* The Journal of Physical Chemistry B, 2005. **109**(30): p. 14257-14261.

141. Gómez-Graña, S., et al., *Au@Ag Nanoparticles: Halides Stabilize {100} Facets.* The Journal of Physical Chemistry Letters, 2013. **4**(13): p. 2209-2216.

142. Almora-Barrios, N., et al., *Theoretical description of the role of halides, silver, and surfactants on the structure of gold nanorods.* Nano letters, 2014. **14**(2): p. 871-5.

143. Schoenitz, M., et al., *Fouling in microstructured devices: a review.* Chemical Communications, 2015. **51**(39): p. 8213-8228.

144. Wagner, J., T.R. Tshikhudo, and J.M. Köhler, *Microfluidic generation of metal nanoparticles by borohydride reduction.* Chemical Engineering Journal, 2008. **135**: p. S104-S109.

145. Wu, H.L., C.H. Kuo, and M.H. Huang, *Seed-mediated synthesis of gold nanocrystals with systematic shape evolution from cubic to trisoctahedral and rhombic dodecahedral structures.* Langmuir : the ACS journal of surfaces and colloids, 2010. **26**(14): p. 12307-13.

146. Garg, N., et al., *The Role of Bromide Ions in Seeding Growth of Au Nanorods.* Langmuir, 2010. **26**(12): p. 10271-10276.

147. Scarabelli, L., et al., *A "Tips and Tricks" Practical Guide to the Synthesis of Gold Nanorods.* The Journal of Physical Chemistry Letters, 2015. **6**(21): p. 4270-4279.

148. Shahjamali, M.M., et al., *Surfactant-Free Sub-2 nm Ultrathin Triangular Gold Nanoframes.* Small, 2013. **9**(17): p. 2880-2886.

Anhang

Tabelle 2: Meilensteine der mikrofluidischen Synthese und Stabilisierung plasmonischer Nanopartikel

Jahr	Erstautor	Methode	Material	Besonderheit	Titel
2004	Jörg Wagner	**CF**; Mikromischer	Au	Wachsen von AuNP im Mikroreaktor	*Generation of metal NP in a michrochannel reactor*
2005	Xue Zhang Lin	**CF**; miniaturisiertes Durchflussrohr (Kapillare)	Ag	thermische Reduzierung bei T > 100°C; silver pentafluoropropionate & TOA	*Synthesis of silver in a continuous Flow Tubular Microreactor*
	Jörg Wagner	**CF**; Mikroreaktor	Au Seeds	Seedsynthese von AuNP mit NaBH₄ im Mikroreaktor	*Continuous Synthesis of Gold NP-in a microreactor*
2006	Johann Boleininger	**CF**; miniaturisiertes Durchflussrohr (Kapillare)	Au & Ag Stäbchen	Seedwachstum zu Au-Stäbchen (nach Jana2001)	*Microfluidic continuous flow synthesis of rod-shaped gold and silver Nanocrystals*
	David Shalom	**CF**; radial verflochtener Mikromischer	Au	Thiolmodifizierte Synthese von AuNP im Mikroreaktor	*Synthesis of thiol functionalized gold nanoparticles using a continuous flow microfluidic reactor*
2007	Jörg Wagner	**CF**; Mikromischer	Au@Ag	Kern/ Hülle Strukturen	*Formation of Au/Ag NP in a two step micro flow-through Process*
	Jörg Wagner	**CF**; SAR-Mikromischer	Au@Ag	Kern/ Hülle Strukturen von sternförmigen Nanopartikeln mit SAR-Mixer	*Formation of star-like and core-shell AuAg-NP during two-and three-step preparation in batch and in microfluidic system*
	Chen-Hsun Weng	**CF**; Ringreaktor	Au	PDMS basierter Ringreaktor zur AuNP Synthese	*Synthesis of hexagonal Au-NP using a microfluidic reaction system*
2008	Hironori Tsunoyama	**CF**; Laminationsmischer	Au	PVP stabilisierte kleine Goldcluster	*Microfluidic Synthesis and Catalytic Application of PVP-Stabilized ~1 nm Gold Clusters*
	J.Michael Köhler	**CF** (SAR-Mischer); SF	Au, Ag	NaBH₄ oder Ascorbinsäure als Reduktionsmittel sowie Verwendung von Polyvinylalkohol & Natriumhydrogencarbonat	*Preparation of metal NP with varied composition for catalytic applications in microreactors*
	Jörg Wagner	**CF**; 3 SAR-Mischer	Ag, Au	NP-Synthese mit NaBH₄ und direkte Thiolmodifizierung; in-situ UV-VIS Messung; Reaktorfouling (Einfluss von pH & Silanisierung); Gesamtflussrate 3,33 – 66,67µl/s	*Microfluidic generation of metal NP by borohydride reduction*
2009	Suhanya Duraiswamy	SF	anisotrope AuNP	Picoliter Segmente für Stäbchen, Sphären und Hundeknochen	*Droplet-based microfluidic synthesis of anisotropic metal nanocrystals*
2010	Laura L. Lazarus	**CF**; Flowfokusierung	Au	Synthese mit Tetraflurboroate	*Flow-focused synthesis of monodisperse gold nanoparticles using ionic liquids on a microfluidic platform*
	Sung-Yi Yang	**CF**; durch PDMS integrierte Pumpe & Mischer	Au	wirbelbasierte Mischung und verschieden große AuNP-Herstellung	*Size-controlled synthesis of gold nanoparticles using a micro-mixing system*
	Koji Sugano	**CF**; Y-Mischer mit Piezobaserter Pumpe	Au	Herstellung frequenzabhängig großer AuNP	*Mixing speed-controlled gold nanoparticle synthesis with pulsed mixing microfluidic system*
	Gomez-de Pedro	**CF**; Keramikreaktor	Au	Keramik-Reaktor zur AuNP-Herstellung	*Continuous flow synthesis of nanoparticles using ceramic microfluidic devices*
2010	Jörg Polte	**CF**	Au Seeds	zeitaufgelöste Studien zur Nanopartikelfomierung (Nukleation < 200ms)	*Nucleation and growth of Au NP studied via in situ small angle X-ray scattering at ms time resolution*
	Suhanya Duraiswamy	SF	Au Hüllen & Inseln	über SF erzeugte Au-Hüllen und Nanoinseln auf Silicapartikeln	*Plasmonic Nanoshell Synthesis in Microfluidic Composite Foams*
	D.V. Ravi Kumar	**CF**; Spirale aus Polymer und Stahl	Ag	Nutzung von verschiedenen Biologischen Surfaktanten zur Reduktion und zum Stabilisieren	*Continuous flow synthesis of functionalized silver nanoparticles using bifunctional biosurfactants*

Jahr	Erstautor	Methode	Material	Besonderheit	Titel
2011	Victor Sebastian Cabeza	**SF**	Au	Reverse- und Normalphasen SF Goldpartikelsynthese	Size-Controlled Flow Synthesis of Gold Nanoparticles using a SF microfluidic platform
	A. M. Nightingale	**SF**	Ag	Durchflussrohr als Spule durch Ölbad (T<250°C); auch andere NP hergestellt (z.B. TiO$_2$ CdSe)	A stable droplet reactor for high temperature nanocrystal synthesis
	Andrea Knauer	**SF**	Au@Ag	Multihüllensynthese mittels SF; in-situ UV-VIS Messung	Au/Ag/Au double shell NP with narrow size distribution obtained by continuous micro segmented flow synthesis
	Jamal Frouni	**CF**; T-Mixer & Kapillare	Au	1,8 nm AuNP mit Turkevich-Methode	Highly controlled synthesis of nanometric gold particles by citrate reduction using the short mixing, heating and quenching times achievable in a microfluidic device
2012	Kyoung G. Lee	**SF**	Au	Kombination aus Hydrogel & rekombinanten E.Coli zur AuNP-Synthese	In Vitro Biosynthesis of Metal Nanoparticles in Microdroplets
	Laura L. Lazarus	**SF**	Au; Ag	Herstellung von Au & Ag Seeds im Zweiphasensystem in der organischen Phase	Two-Phase Microfluidic Droplet Flows of Ionic Liquids for the Synthesis of Gold and Silver Nanoparticles
	G.A. Patil	**CF**; Y-Mixer	Ag Seeds	Ag Seeds mittels Y-Mixer unter Verwendung von CTAB & SDS	Continuous synthesis of functional silver nanoparticles using microreactor: Effect of surfactant and process parameters
	D.V. Ravi Kumar	**SF**; Spiralkapillare	Ag	Gas-Flüssig; Flüssig-Flüssig Segmente	Segmented flow synthesis of Ag nanoparticles in spiral microreactor: Role of continuous and dispersed phase
	Krzysztof Paclawski	**CF**; mehrere T-Verbinder	Au	Reduktion von Au(III) mit Glucose und PVP zur Stabilisierung; Kinetik und Temperatureinstellung	Gold nanoparticles formation via gold(III) chloride complex ions reduction with glucose in the batch and in the flow microreactor systems
	Li Sun	**CF**; miniaturisiertes Durchflussrohr (Kapillare)	Au/Ag-Verbund NP	Verweilzeit von 3 min; Ölbad bei 140° bis 160° C; Synthese in Oleylamin und Octadecene	One-step synthesis of monodisperse Au–Ag alloy nanoparticles in a microreaction system
	Andrea Knauer	**SF**	Ag Seeds & Prismen	Seedsynthese (26,8µl/s) und Wachstum (3,33µl/s) im SF (300µl Segmente); Einfluss von AgNO$_3$- und Seedkonzentration	Microsegmented flow-through synthesis of Ag Nanoprisms with exact tunable optical properties
2013	Samuel E. Lohse	**CF**; miniaturisiertes Durchflussrohr (>>mm) mit Y-Verbinder	Au Sphären & Stäbchen	Protokoll von Murphy (CTAB Stäbchen und Sphären) für einfachen Laboraufbau mit sehr großen Kanälen → *Millifluidik*	A Simple Millifluidic Benchtop Reactor System for the High-Throughput Synthesis and Functionalization of Gold Nanoparticles with Different Sizes and Shapes
	Hakim Mehenni	**SF** (Kommerzielles *Flowsyn Multi-X system*)	Au Sphären & Würfel	Verweilschleife bei 150°C; Verwendung von Natriumhydrosulfid, Eisennitrat & Fluorinierte Flüssigkeit (FC-70), mehrfaches Waschen nötig	Rapid continuous flow synthesis of high-quality silver nanocubes and nanospheres
	Andrea Knauer	**SF**	Ag Prismen	Kombinatorik für Partikelparameterscreening; in-situ UV-VIS Messung	Screening of Multiparameter Spaces for Silver Nanoprism Synthesis by Microsegmented Flow Technique
	Andrea Knauer	**SF**	Ag Prismen	Erzeugung und Parametertuning von Prismen in Polymeren	Micro continuous flow-through synthesis of triangular silver nanoprisms and their incorporation in complexly composed polymer microparticles
2014	D.V. Ravi Kumar	**CF**; miniaturisiertes PTF Durchflussrohr (Kapillare)	Au Dreiecke	mit und ohne Surfaktant; Temperaturgradient innerhalb d. Reaktors	Microfluidic platform for continuous flow synthesis of triangulargold nanoplates
	Suhanya Duraiswamy	Kombination aus **CF** und **SF**	Au Stäbchen-Quaderförmige Nanopartikel	Komplexe Plattform zur vollständig mikrofluidischen Synthese (CF) und Wachstum (SF) von AuNP; mindere Ausbeute und Formschärfe	Dual-Stage Continuous-Flow Seedless Microfluidic Synthesis of Anisotropic Gold Nanocrystals

Jahr	Erstautor	Methode	Material	Besonderheit	Titel
2015	Qiang Fu	CF	Au Seeds (Nanoplättchen)	PDMS-Chip mit 3 Kanälen: Querschnitt 400 x 400µm; Länge 3cm; Verwendung von CTAC	A microfluidic-based controllable synthesis of rolled or rigid ultrathin gold nanoplates
	Razwan Baber	CF; koaxialer Durchflussreaktor	Ag Seeds	Bei Raumtemperatur Reduktion von $AgNO_3$ durch $NaBH_4$ ohne Surfaktant; Durchmesser: 556 & 798µm (innere Kapillare); 2mm (äußerer Kanal); 16µl/s → 230µl/s	Synthesis of silver nanoparticles in a microfluidic coaxial flow reactor
	Matthias Thiele	CF: SAR, T-Mischer; DFM	Ag Seeds (Prismen)	Etablieren einer mikrofluidischen Vormischeinheit und Kombination verschiedener Mischer	High-Throughput Synthesis of Uniform Silver Seed Particles by a Continuous Microfluidic Synthesis Platform
2016	Laura Uson	CF; Kaskadenartige T-Verbinder	Au Stäbchen	Kaskadenartige über T-Verbindungen aufgebaute PTFE Schlauchplattform (Durchlaufzeit 35min; 4,7µl/s), Ohne Zwischenstop von Seed → Rod → PEG Funktionalisierung;	Continuous microfluidic synthesis and functionalization of gold nanorods
	Matthias Thiele	CF (DFM); SF	Au Seeds und Würfel	Direkter Vergleich zwischen Batch, SF und CF; CTA^+ zum Kanalpassivieren; Kinetik und FOM	Gold nanocubes – Direct comparison of synthesis approaches reveals the need for a microfluidic synthesis setup for a high reproducibility
2017	Matthias Thiele	CF; DFM	Au Seeds, Sphären, Würfel & Stäbchen	Plattform zur effizienten (Ressourcen & Zeit) parallelen Herstellung verschiedener NP-Formen und Größen; Parameterscreening (Br^-, F^-, Cl^-, I^-)	Combination of microfluidic high-throughput production and parameter screening for efficient shaping of gold nanocubes using Dean-flow mixing

Danksagung

Mein besonderer Dank geht an dieser Stelle an die universitäre Betreuung durch **Prof. Volker Deckert**. Weiterhin möchte ich mich auch bei **Prof. Wolfgang Fritzsche** als Abteilungsleiter sowie **Frau Dr. Andrea Csáki** als Arbeitsgruppenleiterin für die Betreuung, das Ermöglichen von Reisen und Auslandsaufenthalten, sowie die generelle Einführung in die wissenschaftliche Gemeinschaft danken. In diesem Zusammenhang seien auch **Dr. Robert Müller, Dr. Ondra Stranik** sowie **Dr. Thomas Henkel** genannt, die mich durch rege Diskussionen und konstruktive Vorschläge motivieren konnten und durch die Bereitstellung von Labormaterial und Chemikalien unterstützt haben. Darüber hinaus bedanke ich mich bei der gesamten **Abteilung Nanobiophotonik** für die professionelle und freundschaftliche Zusammenarbeit. Insbesondere möchte ich dabei **Stefanie Hentschel** sowie **Jacqueline Jatschka** für die Bereitstellung, Erklärung und Messung von DNA- und LSPR-Verfahren benennen sowie zusätzlich **Eileen Heinrich**, **Cornelia Reuter** und später **Sophie Thamm** für ein angenehmes und erfrischend heiteres Büroklima, für das Korrektur lesen und die Möglichkeit fachlicher Diskussionen. Auch **Dr. Andreas Wolff** sei in diesem Zusammenhang gedankt.

Darüber hinaus gilt mein ganz herzlicher Dank **André Dathe** und **David Zopf**, mit denen ich zahlreiche Gedankenexperimente durchgehen konnte und die immer ein offenes Ohr für meine (oft verrückten) Ideen hatten und mir somit fachlich wie auch privat immer zur Seite standen. Dies betrifft auch meine ehemaligen Kollegen **Steffen Trautmann** und **Isabell Götz.**

Besonderer Dank auch an **Franka Jahn,** die teils stundenlang für mich an den Elektronenmikroskopen saß, um die besten „Schnappschüsse von Nanopartikeln" für mich zu bekommen.

Vielen Dank auch an die MRT-Abteilung und **Prof Köhler** von der TU-Ilmenau**,** der stets ein offenes Ohr für mich hatte und mir mit seinen Ideen und Vorschlägen Motivation gegeben hat. Mein besonderer Dank gilt an dieser Stelle auch Frau **Dr. Andrea Knauer**, mit der ich eine Zeitlang auf dem Gebiet der Mikrofluidik und der Au-Nanowürfel zusammenarbeiten durfte und die mich oft für das Thema motivieren und begeistern konnte.

Bedanken möchte ich mich auch bei **Chandan Singh, Stefan Hoffman und Markus Tauscher** für ihre Hilfe bei Versuchen und deren Vorbereitung danken. Zu guter Letzt möchte ich die Gelegenheit nutzen, mich auch ganz herzlich bei meiner **Familie** und meiner Freundin **Franziska Döring** zu bedanken, die mir immer zur Seite standen und mich jederzeit unterstützt haben.

Curriculum Vitae

Personal information

Name	Matthias Thiele
Address	Günthergasse 70, 99428 Nohra, Germany
Nationality	German
Date/ place of birth	18.08.1986 / Weimar
Mobile number	0049 173 39 35 352
E-Mail	matthiasthiele@outlook.de

Education

Since 06/ 2014	**FSU-Jena faculty of Chemistry and Earth Sciences**
	PhDcandidate at the Institute of Physical Chemistry
2009 - 2013	**Technical University-Ilmenau/ Ernst-Abbe-Hochschule Jena/ iba-Heiligenstadt (cooperative study)**
	Master study of Miniaturized Biotechnology
2006 - 2009	**Ernst-Abbe-Hochschule Jena**
	Bachelor study of Biotechnology at the Department of Medical Engineering and Biotechnology
2005 - 2006	Military service
1997 - 2005	**Marie-Curie Gymnasium Bad Berka/ Blankenhain**
	A-Levels (Abitur)

Work and Residence Experiences

2013 – 2017	**Leibniz Institute of Photonic Technology Jena**
	Scientist at Department of Nanobiophotonics
12/ 2016	**American University, Cairo (Egypt)**
	- Organization of the practical workshop *Biosensing with Plasmonic Nanomaterials*
	- Hold two lectures and gave two practical courses about Nanoparticles, Microfluidics and Biosensing
10 - 11/ 2016	**CIC biomaGUNE San Sebastian (Spain)**
	- Research stay at the Department of Bionanopalsmonics (Scholarship by COST and ESMI)
	- Experiments concerning the Project: *Microfluidic synthesis of multishell plasmonic nanoparticles for LSPR-spectroscopy*

	- Attended *International Conference on Self-Assembly in Confined Spaces*
05/ 2015	**Universidade Nova de Lisboa, Lisbon (Portugal)**
	- Guest researcher at the Chemistry Department
	- Theoretical calculations on nanoparticle growth
06 - 07/2014	**University of Porto, Porto (Portugal)**
11/ 2013	- Guest researcher at the Department of Chemistry and Biochemistry
	- Synthesis of anisotropic nanoparticles
	- Guest speaker at *International Conference on Advanced Nanomaterials* (Aveiro)
06/ 2014	**CEA saclay, Paris (France)**
	- Guest researcher at Saclay Institute of Matter and Radiation
	- Material characterization based on PPP-Project
12/ 2013	**Nanoscience Center, Jyväskylä (Finland)**
10/ 2012	- Guest researcher at the group of Molecular Electronics and Plasmonics
	- DNA-conjugation of nanoparticles and assembling experiments
	- Guest speaker AquaTest-Workshop
01 - 03/2011	**Ege University, Izmir (Turkey)**
	- Erasmus student at the Department of Biochemistry
	- Practical report and lab experiences about functionalization of QD

Personal Skills and Competences

Languages	German (native speaker)
	English (expert level)
	French (starter level)
Driving	A1; A; B; C1 (clean)
Interests	Sport: (Mountain-)biking, crossfit, running, climbing
	Living life: Volunteer firefighter, trainer for indoor cycling

…………………………
Place, Date

………………………
Signature

Erklärungen

Selbstständigkeitserklärung

Ich erkläre, dass ich die vorliegende Arbeit selbstständig und unter Verwendung der angegebenen Hilfsmittel, persönlichen Mitteilungen und Quellen angefertigt habe.

……………………………
Ort, Datum

…………………………
Matthias Thiele

Erklärung zu den Eigenanteilen der Promovendin sowie der weiteren Doktoranden/ Doktorandinnen als Koautoren an den Publikationen und Zweitpublikationsrechten bei einer kumulativen Dissertation

Für alle in dieser kumulativen Dissertation verwendeten Manuskripte liegen die notwendigen Genehmigungen der Verlage („Reprint permissions") für die Zweitpublikation vor. Die Co-Autoren der in dieser kumulativen Dissertation verwendeten Manuskripte sind sowohl über die Nutzung, als auch über die oben angegebenen Eigenanteile der weiteren Doktoranden/Doktorandinnen als Koautoren an den Publikationen und Zweitpublikationsrechten bei einer kumulativen Dissertation informiert und stimmen dem zu. Die Anteile der Co-Autoren an den Publikationen sind vor der jeweiligen Publikation aufgeführt.

……………………………
Ort, Datum

…………………………
Matthias Thiele